

DISSERTATION

THE STUDY AND REAL-TIME IMPLEMENTATION OF ATTENUATION
CORRECTION FOR X-BAND DUAL-POLARIZATION WEATHER RADARS

Submitted by

Yuxiang Liu

Department of Electrical and Computer Engineering

In partial fulfillment of the requirements

For the Degree of Doctor of Philosophy

Colorado State University

Fort Collins, Colorado

Spring 2008

UMI Number: 3321294

INFORMATION TO USERS

The quality of this reproduction is dependent upon the quality of the copy submitted. Broken or indistinct print, colored or poor quality illustrations and photographs, print bleed-through, substandard margins, and improper alignment can adversely affect reproduction.

In the unlikely event that the author did not send a complete manuscript and there are missing pages, these will be noted. Also, if unauthorized copyright material had to be removed, a note will indicate the deletion.

UMI[®]

UMI Microform 3321294

Copyright 2008 by ProQuest LLC.

All rights reserved. This microform edition is protected against unauthorized copying under Title 17, United States Code.

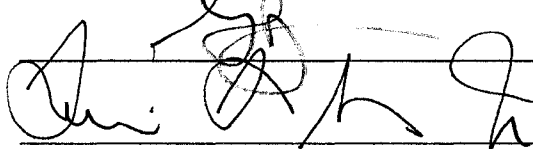
ProQuest LLC
789 E. Eisenhower Parkway
PO Box 1346
Ann Arbor, MI 48106-1346

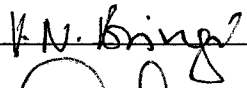
COLORADO STATE UNIVERSITY

December 5, 2007

WE HEREBY RECOMMEND THAT THE DISSERTATION PREPARED UNDER OUR SUPERVISION BY YUXIANG LIU ENTITLED THE STUDY AND REAL-TIME IMPLEMENTATION OF ATTENUATION CORRECTION FOR X-BAND DUAL-POLARIZATION WEATHER RADARS BE ACCEPTED AS FULFILLING IN PART REQUIREMENTS FOR THE DEGREE OF DOCTOR OF PHILOSOPHY.

Committee on Graduate Work

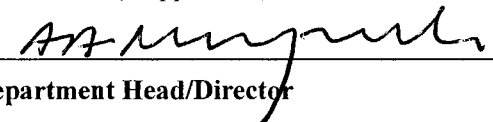




Adviser



Co-Adviser (if applicable)



Department Head/Director

ABSTRACT OF DISSERTATION

THE STUDY AND REAL-TIME IMPLEMENTATION OF ATTENUATION CORRECTION FOR X-BAND DUAL-POLARIZATION WEATHER RADARS

Attenuation of electromagnetic radiation due to rain or other wet hydrometeors along the propagation path is a well-recognized phenomenon that has been studied extensively in both the radar meteorology community as well as the satellite/terrestrial radio wave propagation community. Recently, there has been a tremendous interest in the use of short range dual-polarization X-band radar systems for hydrology due to lower system cost compared with the much more expensive S-band (~ 3 GHz) systems (WSR-88D) operated by the US National Weather Service. This interest has been due to advances in dual-polarization radar research which show that the specific attenuation (A_h) and differential attenuation (A_{dp}) between horizontal (h) and vertical polarized waves (v) caused by oblate, highly oriented raindrops can be estimated using the specific differential phase measurement (K_{dp}). This advance leads to correction of the radar measured reflectivity (Z_h) and the differential reflectivity (Z_{dr}) due to path attenuation. This thesis addresses via theory, simulations and data analyses the accuracy and optimal estimation of attenuation-correction procedures at X-band (~ 10 GHz) frequency. A primary driving force has been the real-time implementation of the procedures developed herein to the first generation of X-band dual-polarized Doppler radar network

(Integration Project 1, IP1) operated by the NSF Center for Collaborate Adaptive Sensing of the Atmosphere (CASA).

The attenuation problem can be formulated within an estimation framework. For the rain attenuation estimation, we first formulate a parametric model based on the A_h - K_{dp} and A_h - Z_h relationships. The parameters in the two relationships are not set *a priori* but rather estimated based on the consistency between the K_{dp} and Z_h in rain medium. This consistency is achieved by minimizing the model output and the measured differential propagation phase (Φ_{dp}) in a least-squares sense. By estimating the parameters based on the consistency, one can reduce the uncertainties inherent in the A_h - K_{dp} and A_h - Z_h relationships due to changes in temperature, rain drop shapes, and to a lesser extent, large variations in the drop size distribution (DSD) along the propagation path. Secondly, we extend the consistency principle to vertically polarized radar variables and an estimation model of the path-integrated differential attenuation is subsequently derived. With the estimated parameters, the path-integrated attenuation and differential attenuation can be used to correct the Z_h and Z_{dr} , respectively. Finally, we provide a preliminary method to address the mixed-phase (rain co-existing with wet ice) attenuation problem by which one can separately estimate the attenuation caused by rain and wet ice particles along the propagation path.

We evaluate our improved method for correcting the Z_h and the Z_{dr} for rain attenuation using simulations and X-band radar data. In the simulations, we apply the method to radar variables generated from constant DSD profiles and variable DSD profiles. We also

evaluate the performance under ideal and noisy situations. It is shown that our method is able to adjust the parameters according to the changes in temperature, drop shapes, and a certain class of DSD with very fast convergence. Both Z_h and Z_{dr} are corrected to a very good degree of accuracy by comparing the corrected values with the simulation input values. The X-band radar data are obtained from the National Institute of Earth Science and Disaster Prevention (NIED), Japan, and from CASA IP1. The improved method accurately corrects NIED's data when compared with ground truth calculated from *in situ* disdrometer-based DSD measurements for a Typhoon event. We have implemented, in real-time, the improved method in all the CASA IP1 radar nodes. The corrected Z_h PPI scan from the CASA IP1 network radars shows good agreement with the nearly-coincident Z_h PPI scan measured by a nearby un-attenuated WSR-88D S-band radar system. One additional advantage is that the estimation of the specific attenuation at the horizontal polarization (A_h) and the specific differential attenuation (A_{dp}) is independent of any systematic offsets in the h- or v-channels of the radar.

We also evaluate our preliminary method that separately estimates rain and wet ice attenuation using microphysical outputs from a previous supercell simulation using the CSU-RAMS (Regional Atmospheric Modeling System). The retrieved rain and wet ice specific attenuation fields were found to be in close correspondence to the 'true' fields calculated from the simulation. The wet ice attenuation field is useful in studying the A - Z relationship for wet ice, which can help improve the profiling algorithms used in Tropical Rainfall Measuring Mission (TRMM) or being proposed for the Global Precipitation Measurement (GPM) mission. The concept to correct rain and wet ice attenuation

separately can be also applied to the CASA IP1 network with additional constraint information possibly provided by the WSR-88D network.

Yuxiang Liu
Department of Electrical and Computer Engineering
Colorado State University
Fort Collins, CO 80523
Spring 2008

ACKNOWLEDGEMENTS

This work was supported by the Engineering Research Center program of the National Science Foundation under award number 0313747.

I'd like to thank my adviser Dr. V.N. Bringi and co-adviser Dr. V. Chandrasekar for the support and guidance over the years of my graduate study. I am very lucky to be one of their students. I'd like to thank my aunt, Dr. Li Liu, who also studied under Dr. V.N. Bringi and Dr. V. Chandrasekar and graduated from the same program. It was she who introduced me to my advisers and it was my advisers who led me with great patience and encouragement through the wonderful world of dual-polarization radar remote sensing. Without them, I would not have been able to complete my humble work that eventually resulted in this dissertation.

I'd like to thank Dr. Louis Scharf and Dr. Graeme Stephens for being on my committee and for their constructive criticisms and suggestions that contribute to finalize this dissertation. I'd like to also thank Dr. M. Maki of NIED, Japan, for providing their MP-X radar and disdrometer data.

I'd like to thank all the CASA scientists and engineers, who are certainly among the most talented and hard-working people I have ever worked with. I have benefited in many ways from working with them. I'd like to thank, especially, Dr. G.J. Huang, Dr. Y. Wang and Dr. D. Moisseev for their discussions and helps on the subjects of research in this dissertation.

DEDICATION

To my parents, Shisheng Liu and Yuliu Guan, and to my grandfather, Shousheng Liu, for
being a continuous source of inspiration.

To my wife, Yanyan Wang, for being a continuous source of support.

To my daughter, Jade Hanyu Liu.

In memory of my grandmother, Baiying Li.

TABLE OF CONTENTS

ABSTRACT OF DISSERTATION.....	iii
ACKNOWLEDGEMENTS.....	vii
DEDICATION	viii
TABLE OF CONTENTS	ix
LIST OF TABLES	xi
LIST OF FIGURES.....	xii
LIST OF SYMBOLS	xvi
1 INTRODUCTION.....	1
1.1 Overview.....	1
1.2 Organization of this dissertation.....	3
1.3 Instruments and testbeds	5
1.3.1 CASA IP1.....	5
1.3.2 MP-X radar	9
1.3.3 CP-2 radar	10
2 THEORETICAL BACKGROUND AND RELATED WORK.....	13
2.1 Scattering matrix	14
2.2 Transmission matrix and propagation effects.....	17
2.3 Radar range equation.....	20
2.4 Related work on rain attenuation correction techniques	27
2.5 Related work on rain differential attenuation correction techniques.....	33
2.6 Related work on attenuation correction for mixed-phase region.....	36
3 OPTIMAL ESTIMATION OF RAIN ATTENUATION AND CORRECTION OF REFLECTIVITY	38
3.1 Mathematical considerations for modeling the attenuation.....	38
3.2 Parameter estimation.....	40
3.2.1 Basic form.....	42
3.2.2 Form using constraint on the Hitschfeld and Bordan method.....	45
3.2.3 Trade-off studies and our finalized form.....	48
3.2.4 Minimization scheme	52
3.2.5 Stability of the algorithm	62
3.3 Simulation results.....	63
3.3.1 Constant DSD case.....	65
3.3.2 Variable DSD case.....	74
3.3.3 Sensitivity of the parameter α_h on temperature	76
3.3.4 Error introduced by using fixed α_h	77
3.4 Results using radar measurements	86
3.4.1 A typhoon case study using the MP-X radar data	86
3.4.2 Implementing the improved algorithm for the CASA IP1	92
3.4.3 Case study for the CASA IP1: comparison with nearby WSR-88D radar measurement	96
3.4.4 Seasonal results from the CASA IP1 testbed: Spring, Summer, and Autumn 2007.....	99
4 OPTIMAL ESTIMATION OF RAIN DIFFERENTIAL ATTENUATION AND CORRECTION OF DIFFERENTIAL REFLECTIVITY	112
4.1 Rethinking the estimation of the A_{dp} and correction of Z_{dr}	112

4.2 The A_h - A_v approach for estimation of A_{dp} and correction of Z_{dr}	114
4.3 Stability of the algorithm.....	119
4.4 Simulation results.....	125
4.4.1 Constant DSD case.....	125
4.4.2 Variable DSD case.....	132
4.4.3 Sensitivity of the parameter α_v on temperature	133
4.4.4 Error introduced by using fixed α_h and α_v	134
4.5 Results using radar measurements	140
4.5.1 A Typhoon case study using MP-X radar data	140
4.5.2 Seasonal results from the CASA IP1 testbed: Spring, Summer, and Autumn 2007	145
5 SEPARATELY ESTIMATE A_h DUE TO RAIN AND WET ICE: A PRIOR SUPERCELL SIMULATION USING THE CSU-RAMS MODEL	161
5.1 Estimating wet ice and rain attenuation separately	161
5.2 Formulation of the mixed-phase attenuation estimation algorithm	164
5.3 Simulation results.....	167
6 SUMMARY AND SUGGESTIONS FOR FUTURE WORK.....	175
6.1 Summary	175
6.2 Suggestions for future work	178
Appendix A: Derivation of the Hitschfeld and Bordan Method.....	181
Appendix B: Derivation of Testud et al.'s Method	185
Appendix C: Drop shape models used in this dissertation.....	189
REFERENCES.....	191

LIST OF TABLES

Table 1.1 System Characteristic of the CASA IP1 radar node (Source: IP1 System Requirements Documents, Revision 3, March 2005.).....	7
Table 1.2 System characteristics of the MP-X radar (Courtesy M. Maki of NIED).....	9
Table 1.3 System characteristics of the CP-2 radar (Courtesy Tom Keenan of BMRC)	12
Table 3.1 Estimated α_h , mean error (intrinsic – retrieved), and RMSE evaluated with several drop shape models in the literature. Constant DSD. No measurement errors.	73
Table 3.2 Estimated α_h , mean error (intrinsic – retrieved), and RMSE evaluated with several drop shape models in the literature. Constant DSD. Gaussian noises with zero means are added to the measurements. $\sigma_n(Z_h)=0.8$ dBZ, $\sigma_n(\Phi_{dp})=3$ deg.	73
Table 3.3 Estimated α_h , mean error (intrinsic – retrieved), and RMSE evaluated with several drop shape models in the literature. Variable DSD. No measurement errors.	84
Table 3.4 Estimated α_h , mean error (intrinsic – retrieved), and RMSE evaluated with several drop shape models in the literature. Variable DSD. Gaussian noises with zero means are added to the measurements. $\sigma_n(Z_h)=0.8$ dBZ, $\sigma_n(\Phi_{dp})=3$ deg.	84
Table 3.5 Estimated α_h , mean error (intrinsic – retrieved), and RMSE evaluated with the Pruppacher and Beard (1970) drop shape model at environmental temperature of 0°C, 10°C, 20°C, and 30°C, respectively. Variable DSD. No measurement errors.	85
Table 3.6 The CASA IP1 case studies start date/time, end date/time (all UTC) and storm type information.	102
Table 4.1 Estimated α_h and α_v , mean error(intrinsic – retrieved), and RMSE evaluated with several drop shape models in the literature. Constant DSD. No measurement errors.	131
Table 4.2 Estimated α_h and α_v , mean error (intrinsic – retrieved), and RMSE evaluated with several drop shape models in the literature. Constant DSD. Gaussian noises with zero means are added to the measurements. $\sigma_n(Z_h)=0.8$ dBZ, $\sigma_n(Z_{dr})=0.2$ dB, $\sigma_n(\Phi_{dp})=3$ deg.....	131
Table 4.3 Estimated α_h and α_v , mean error (intrinsic – retrieved), and RMSE evaluated with several drop shape models in the literature. Variable DSD. No measurement errors.	138
Table 4.4 Estimated α_h and α_v , mean error (intrinsic – retrieved), and RMSE evaluated with several drop shape models in the literature. Variable DSD. Gaussian noises with zero means are added to the measurements. $\sigma_n(Z_h)=0.8$ dBZ, $\sigma_n(Z_{dr})=0.2$ dB, $\sigma_n(\Phi_{dp})=3$ deg.....	138
Table 4.5 Estimated α_h and α_v , mean error (intrinsic – retrieved), and RMSE evaluated with the Pruppacher and Beard (1970) drop shape model at environmental temperature of 0°C, 10°C, 20°C, and 30°C, respectively. Variable DSD. No measurement errors.	139

LIST OF FIGURES

Figure 1.1 Photograph of the prototype CASA IP1 radar seated next to the CSU-CHILL S-band radar during the calibration and test in the Summer of 2005.	7
Figure 1.2 One of the four CASA IP1 radars being installed at the Cyril, Oklahoma site.	8
Figure 1.3 Schematic showing locations of the four nodes of the CASA IP1 network and its coverage near four cities in Oklahoma, namely Chickasha, Cyril, Lawton, and Rush Springs.	8
Figure 1.4 The MP-X mobile transportable radar (Courtesy of M. Maki of NIED).....	10
Figure 1.5 CP-2 radar being installed near Brisbane. The X-band system is yet to be installed (Courtesy of Tom Keenan of BMRC).	11
Figure 1.6 Topography surrounding Brisbane with areas (hatched) under flooding threat. The CP-2 radar site will be near Ipswich, about 30 km south west of Brisbane (Courtesy of Tom Keenan of BMRC). ..	11
Figure 3.1 Range profiles of the intrinsic Z_h , the attenuated Z_h , and the corrected Z_h . The profiles are based on a constant exponential DSD profile and the Pruppacher and Beard (1970) drop shape model.	69
Figure 3.2 Range profiles of the intrinsic A_h and the retrieved A_h . The profiles are based on a constant exponential DSD profile and the Pruppacher and Beard (1970) drop shape model.	69
Figure 3.3 (a) Range profiles of the intrinsic Φ_{dp} and the reconstructed Φ_{dp} . The intrinsic Φ_{dp} is calculated by taking range integration of the intrinsic K_{dp} generated from a constant DSD profile and the Pruppacher and Beard 1970 drop shape model. The reconstructed Φ_{dp} is calculated by evaluating the non-linear model at each iteration of α_h . (b) Enlarged intrinsic Φ_{dp} and reconstructed Φ_{dp} profiles in the dashed square in the upper figure panel.	70
Figure 3.4 Range profiles of the intrinsic Z_h , the attenuated Z_h , and the corrected Z_h . The profiles are based on a constant exponential DSD profile and the Pruppacher and Beard (1970) drop shape model. Measurement noise is added to the attenuated Z_h	71
Figure 3.5 Range profiles of the intrinsic A_h and the retrieved A_h . The profiles are based on a constant exponential DSD profile and the Pruppacher and Beard (1970) drop shape model. Estimated A_h is retrieved from the noisy measurements of Z_h and Φ_{dp}	71
Figure 3.6 (a) Range profiles of the measured Φ_{dp} and the reconstructed Φ_{dp} . The intrinsic Φ_{dp} is calculated by taking range integration of the intrinsic K_{dp} generated from a constant DSD profile and the Pruppacher and Beard (1970) drop shape model. Then Gaussian noise is added to the intrinsic Φ_{dp} to form the measured Φ_{dp} . The reconstructed Φ_{dp} is calculated by evaluating the non-linear model at each iteration of α_h . (b) Enlarged measured Φ_{dp} and reconstructed Φ_{dp} profiles in the dashed square in the upper figure panel.	72
Figure 3.7 N_w profile used in the variable DSD case study.	78
Figure 3.8 D_0 profile used in the variable DSD case study.	78
Figure 3.9 Range profiles of the intrinsic Z_h , the attenuated Z_h , and the corrected Z_h . The profiles are based on a variable DSD range profile and the Pruppacher and Beard (1970) drop shape model.	79

Figure 3.10 Range profiles of the intrinsic A_h and the retrieved A_h . The profiles are based on a variable DSD range profile and the Pruppacher and Beard (1970) drop shape model.79

Figure 3.11 (a) Range profiles of the intrinsic Φ_{dp} and the reconstructed Φ_{dp} . The intrinsic Φ_{dp} is calculated by taking range integration of the intrinsic K_{dp} generated from a variable DSD profile and the Pruppacher and Beard (1970) drop shape model. The reconstructed Φ_{dp} is calculated by evaluating the non-linear model at each iteration of α_h . (b) Enlarged intrinsic Φ_{dp} and reconstructed Φ_{dp} profiles in the dashed square in the upper figure panel.80

Figure 3.12 Profile of difference of the intrinsic Z_h – the corrected Z_h . The profile is based on a variable DSD range profile and the Pruppacher and Beard (1970) drop shape model. The corrected Z_h is obtained by correcting the noisy measured Z_h for attenuation.81

Figure 3.13 Profile of difference of the intrinsic A_h – the estimated A_h . The profile is based on a variable DSD range profile and the Pruppacher and Beard (1970) drop shape model. The estimated A_h is computed by the non-linear model at the converged α_h under condition of noisy measurements.....81

Figure 3.14 (a) Range profiles of the measured Φ_{dp} and the reconstructed Φ_{dp} . The intrinsic Φ_{dp} is calculated by taking range integration of the intrinsic K_{dp} generated from a variable DSD profile and the Pruppacher and Beard (1970) drop shape model. Then Gaussian noise is added to the intrinsic Φ_{dp} to form the measured Φ_{dp} . The reconstructed Φ_{dp} is calculated by evaluating the non-linear model at each iteration of α_h . (b) Enlarged measured Φ_{dp} and reconstructed Φ_{dp} profiles in the dashed square in the upper figure panel.82

Figure 3.15 Corrected Z_h with *a priori* fixed α_h value in error.83

Figure 3.16 A PPI scan of (a) the measured Z_h and (b) the corrected Z_h , observed at the elevation angle of 2.5 deg, at 01:59:54 LST, September 11 2001. The black line is the radar ray at azimuth angle of 294 deg. The three squares indicate the locations of the three *in situ* disdrometers, respectively.....89

Figure 3.17 Range profiles of the measured Z_h , the corrected Z_h using Park et al. (2005) method, and the corrected Z_h using the improved method along the azimuth angle of 294° for the Typhoon event at 01:59:54 LST September 11 2001. The asterisks (*) denote the mean values calculated from DSD data collected with the three *in situ* disdrometers, respectively.90

Figure 3.18 Histogram of the optimized coefficient α_h for radar rays spanning azimuth angles from 280° to 310° for the Typhoon event at 01:59:54 LST September 11 2001.90

Figure 3.19 Intensity scatterpot of K_{dp} vs. Z_h after attenuation correction. The black line is the empirical K_{dp} - Z_h relationship based on T-matrix calculation using the *in situ* disdrometer DSD data.91

Figure 3.20 Flowchart of the CASA IP1 dual-polarization attenuation-correction algorithm.....93

Figure 3.21 IP1 Reflectivity maps at 07:37:31 May 8 2007 and WSR-88D reflectivity map at 07:37:24 May 8 2007. (a) IP1 reflectivity before attenuation correction (b) IP1 reflectivity after attenuation correction (c) WSR-88D (KTLX) reflectivity.....98

Figure 3.22 Histograms of the estimated parameter α_h for the events listed in Table (3.6). 103

Figure 3.23 The mean values and standard deviations of the estimated parameter α_h plotted along the date of the events. 109

Figure 3.24 Cumulative distribution of path-integrated attenuation for the cases in Table (3.6) from rays below 6 deg elevation angle. 111

Figure 4.1 A_h vs. A_v relationships at X-band derived based on four different drop shape models in the literature. Black solid lines are the least squares fit to A_h and A_v values calculated from approximated 8000 measured DSDs for each drop shape model. Sample points are shown as black dots for the Pruppacher and Beard (1970) linear model. The cross-correlation coefficient between A_h and A_v is 0.9997.	115
Figure 4.2 Range profiles of the intrinsic Z_{dr} , the attenuated Z_{dr} , and the corrected Z_{dr} . The profiles are based on a constant exponential DSD profile and the Pruppacher and Beard (1970) drop shape model.	129
Figure 4.3 Range profiles of the intrinsic A_{dp} and the retrieved A_{dp} . The profiles are based on a constant exponential DSD profile and the Pruppacher and Beard (1970) drop shape model.....	129
Figure 4.4 Range profiles of the intrinsic Z_{dr} , the attenuated Z_{dr} , and the corrected Z_{dr} . The profiles are based on a constant exponential DSD profile and the Pruppacher and Beard (1970) drop shape model. Measurement noise is added to the attenuated Z_{dr}	130
Figure 4.5 Range profiles of the intrinsic A_{dp} and the retrieved A_{dp} . Profiles are based on a constant exponential DSD profile and the Pruppacher and Beard (1970) drop shape model. The estimated A_{dp} is retrieved from the noisy measurements of Z_h , Z_{dr} and Φ_{dp}	130
Figure 4.6 Range profiles of the intrinsic Z_{dr} , the attenuated Z_{dr} , and the corrected Z_{dr} . The profiles are based on a variable DSD range profile and the Pruppacher and Beard (1970) drop shape model.	135
Figure 4.7 Range profiles of the intrinsic A_{dp} and the retrieved A_{dp} . The profiles are based on a variable DSD range profile and the Pruppacher and Beard (1970) drop shape model.	135
Figure 4.8 Profile of difference of the intrinsic Z_{dr} – the corrected Z_{dr} . The profile is based on a variable DSD range profile and the Pruppacher and Beard (1970) drop shape model. The corrected Z_{dr} is obtained by correcting the noisy measured Z_{dr} for attenuation.	136
Figure 4.9 Profile of difference of the intrinsic A_{dp} – the estimated A_{dp} . The profile is based on a variable DSD range profile and the Pruppacher and Beard (1970) drop shape model. The estimated A_{dp} is computed by the non-linear model with the converged α_h and α_v under condition of noisy measurements.....	136
Figure 4.10 Corrected Z_{dr} with fixed α_h and α_v values in error.....	137
Figure 4.11 A PPI scan of (a) the measured Z_{dr} (b) the corrected Z_{dr} observed at the elevation angle of 2.5 deg, at 01:59:54 LST, September 11 2001. The black line is the radar ray at azimuth angle of 294 deg. The three squares indicate the locations of the three <i>in situ</i> disdrometers, respectively.	142
Figure 4.12 Range profiles of the measured Z_{dr} , the corrected Z_{dr} using Park et al. (2005) method, and the corrected Z_{dr} using the A_h - A_v method along the azimuth angle of 294° for the Typhoon event at 01:59:54 LST September 11 2001. The asterisks (*) denote the mean values calculated from DSD data collected with the three <i>in situ</i> disdrometers, respectively.	143
Figure 4.13 Histogram of the optimized coefficient α_v for radar rays spanning azimuth angles from 280° to 310° for the Typhoon event at 01:59:54 LST September 11 2001.	143
Figure 4.14 Scatter plot of Z_{dr} vs. Z_h before (grey dots) and after attenuation correction (black dots).	144
Figure 4.15 Histograms of the estimated parameter α_v for the events listed in Table (3.6).	147
Figure 4.16 2-D histograms of the estimated parameters α_h vs. α_v for the events listed in Table (3.6).	153

Figure 4.17 The mean values and standard deviations of the estimated parameter α_h and α , plotted along the date of the events. 159

Figure 5.1 Vertical cross-section of contours of specific attenuation (A_h) of rain and hail at X-band. Dash line is the hail A_h contour. Solid line is the rain A_h contour. The intrinsic X-band Z_h (in dBZ) is plotted as background. 171

Figure 5.2 Range profiles of the DWR along the slant path at 25° elevation angle, the ‘true’ total PIA, the ‘true’ rain PIA, and the estimated rain PIA. 171

Figure 5.3 Range profiles of the $Z_h(S)$, the attenuated (or ‘measured’) $Z_h(X)$, and the $Z_h(X)$ corrected for rain only attenuation (a) at 25 deg elevation angle (b) at 0.5 deg elevation angle. 172

Figure 5.4 Contours of specific attenuation of rain in the vertical section. (a) the ‘true’ values from the RAMS microphysical output, (b) the retrieved values. 173

Figure 5.5 Contours of specific attenuation of the wet hail in the vertical section. (a) the ‘true’ values from the RAMS microphysical output, (b) the retrieved values calculated from the first proposed method. 173

Figure 5.6 Profiles of the attenuated (or ‘measured’) $Z_h(X)$, the $Z_h(X)$ after correction for rain attenuation, the $Z_h(X)$ after correction for both rain and wet hail attenuation, and the ‘intrinsic’ $Z_h(X)$ 174

Figure 5.7 Contours of specific attenuation of the wet hail in the vertical section. (a) the ‘true’ values from the RAMS microphysical output, (b) the retrieved values calculated from the second proposed method. 174

LIST OF SYMBOLS

\vec{E}^0 : Complex vector quantity, the electric field at origin, whose magnitude and direction depend on time in general.	14
\vec{E}^i : Complex vector quantity, the incident electric field, whose magnitude and direction depend on time in general.	14
\hat{i} : Real unit vector quantity, the propagation direction of the incident electromagnetic wave at a point of interest.	14
\vec{r} : Real vector quantity, the range vector indicating a point of interest.	14
k_0 : Real scalar quantity, the wave number of the free space.	14
$(\hat{r}, \hat{\theta}, \hat{\phi})$: The real unit vectors that a 3-dimensional spherical coordinate system is defined with.	14
E_h^i : Real scalar quantity, amplitude of the horizontal polarized component of a polarized electric field, a function of time.	15
E_v^i : Real scalar quantity, amplitude of the vertically polarized component of a polarized electric field, a function of time.	15
E_0 : Real scalar quantity, amplitude of \vec{E}^0	15
\hat{e}_i : Real unit vector quantity, the unit linear polarization vector.	15
\hat{h} : Real unit vector quantity, the horizontal direction.	15
\hat{v} : Real unit vector quantity, the vertical direction.	15
$\vec{f}(\hat{s}, \hat{i})$: Complex vector quantity, scattering amplitude of a dielectric particle.	16
\hat{s} : Real unit vector quantity, the scattered wave direction.	16
\vec{E}^s : Complex vector quantity, the scattered electric field when waves encounter discontinuity of permittivity in space.	16
\vec{E}^r : Complex vector quantity, the back-scattered electric field.	16
S_{BSA} : 2 x 2 matrix with complex scalar elements, scattering matrix in back scattering alignment.	17

\mathbf{T} : 2 x 2 matrix with complex scalar elements, the transmission matrix.	18
k_{eff}^h, k_{eff}^v : Complex scalar quantities, effective wave numbers of medium at h polarization and v polarization, respectively.	19
n : Real scalar quantity, number of dielectric particles per cubic meters.	19
A_h, A_v : Real scalar quantities, the specific attenuation at h polarization and v polarization, respectively.	19, 20
A_{dp} : Real scalar quantity, the differential attenuation between h polarization and v polarization.	20
K_{dp} : Real scalar quantity, the specific differential propagation phase between h polarization and v polarization.	20
$\text{Im}\{\cdot\}$: Operator, a real function that gives the imaginary part of a complex number.	20
$\text{Re}\{\cdot\}$: Operator, a real function that gives the real part of a complex number.	20
V : Complex scalar quantity, the received voltage due to the back-scattered electric field.	21
\vec{h} : Real vector quantity, the effective antenna length.	21
$G(\theta, \phi)$: Real function, the antenna gain function.	22
M_h, M_v : Complex scalar quantity, the input plane wave complex amplitudes at h polarization and v polarization, respectively.	21
P_h^t, P_v^t : Real scalar quantity, the average peak powers transmitted by the antenna at h polarization and v polarization, respectively.	21
P_h^{co} : Real scalar quantity, the co-polar received power at h polarization.	22
σ_{hh} : Real scalar quantity, the back-scattered radar cross section.	22
PIA_h : Real scalar quantity, the one-way path-integrated attenuation at h polarization. ...	23
Ψ_{dp} : Real scalar quantity, the two-way differential total phase.	23
Φ_{dp} : Real scalar quantity, the two-way differential propagation phase.	23
δ_{co} : Real scalar quantity, the differential back-scattered phase.	23

θ_b, ϕ_b : Real scalar quantity, 3-dB beamwidths of a Gaussian antenna pattern.	25
K : Complex scalar quantity, the dielectric factor of a particle.	25
Z : Real scalar quantity, the radar reflectivity factor.	26
D : Real scalar quantity, the spherical particle diameter.	26
$N(D)$: Real function, the drop size distribution.	26
Z_{dr} : Real scalar quantity, the differential reflectivity.	27
Z_m : Real scalar quantity, the measured value of radar reflectivity.	28
Z_e : Real scalar quantity, the intrinsic value of radar reflectivity.	28
α : Real scalar quantity, the coefficient of the A - Z_e power-law relationship.	28
b : Real scalar quantity, the exponent of the A - Z_e power-law relationship.	28
α : Real scalar quantity, the coefficient of the A - K_{dp} linear relationship.	29
Φ_{dp}^{fil} : Real scalar quantity, the range-filtered differential propagation phase.	32
Φ_{dp}^c : Real scalar quantity, the reconstructed differential propagation.	32
$Z_{dr,m}$: Real scalar quantity, the measured value of the differential reflectivity.	33
$Z_{dr,e}$: Real scalar quantity, the intrinsic value of the differential reflectivity.	34
β : Real scalar quantity, the coefficient of the A_{dp} - K_{dp} linear relationship.	34
$\tilde{\beta}$: Real scalar quantity, the estimated value of β	35
$\tilde{\alpha}$: Real scalar quantity, the estimated value of α	36
κ : Real scalar quantity, the coefficient of K_{dp} - Z_e power-law relationship.	41
\tilde{Z}_e : Real scalar quantity, the estimated value of the intrinsic reflectivity.	42
\tilde{A} : Real scalar quantity, the estimated value of the specific attenuation.	42
\tilde{K}_{dp} : Real scalar quantity, the estimated value of the specific differential phase.	42

\tilde{PIA} : Real scalar quantity, the estimated value of the one-way path-integrated attenuation.	43
$\tilde{\Phi}_{dp}$: Real scalar quantity, the estimated value of the two-way differential propagation phase.	43
Δr : Real scalar quantity, the range resolution of a pulsed radar.	43
i : Integer scalar quantity, the index of i^{th} element of a vector.	43
\tilde{f} : Real vector function, the difference between a measured N-dimensional quantity and the estimated N-dimensional quantity.	44
F : Real function, the cost function that determines the goodness of the estimation.	44
$\text{argmin}(\cdot)$: Real function, the function that gives the parameters than minimize a given cost function.	44
\tilde{a} : Real quantity, the estimated value of the coefficient in the A - Z_e power-law relationship.	46
\tilde{PIA} : Real quantity, the estimated value of the PIA	46
\mathbf{J} : Real matrix, the Jacobian of \tilde{f}	56
\mathbf{F}'' : Real matrix, the Hessian of F	57
\mathbf{I} : Real matrix, the identity matrix.	60
α_v : Real scalar quantity, the coefficient of the A_v - K_{dp} linear relationship.	114
a_v : Real scalar quantity, the coefficient of the A_v - Z_v power-law relationship.	116
b_v : Real scalar quantity, the exponent of the A_v - Z_v power-law relationship.	116
DWR : Real scalar quantity, the dual-wavelength ratio.	162
Z_S : Real scalar quantity, the measured reflectivity at S-band.	163
Z_X : Real scalar quantity, the measured reflectivity at X-band.	163
A_{ice} : Real scalar quantity, the specific attenuation caused by ice particles.	165
Z_{ice} : Real scalar quantity, the reflectivity caused by ice particles.	165

1 INTRODUCTION

1.1 Overview

Since post-World War II, there has been a proliferation of radar technologies for various civilian applications. The invaluable capability to detect and profile distributed targets at long range makes radars ideal tools for weather surveillance. Doppler, polarimetric, dual-wavelength and other principles are employed and advanced technologies (e.g., phased array antenna, pulse compression) have been or are being actively pursued for weather applications (Doviak and Zrníc (1993), Bringi and Chandrasekar (2001)). The established WSR-88D national radar networks (Crum and Albery (1993)) in the United States, the recent Tropical Rainfall Measuring Mission (TRMM) as a joint-effort between the Japanese and the U.S. space agencies (Kummerow et al. (2000)), and the first spaceborne cloud radar, CloudSat led by the science team in the Colorado State University (Stephens et al. (2002)) are all considered milestones in the development of radar technologies on earth or in space.

A distinct feature of the aforementioned platforms of radar remote sensing technologies is that they are all capable of very large scale (national or global) observation. However, on the Earth's surface, because of the curvature of the Earth, a long-range (typically 300 km) radar (e.g., WSR-88D) is constantly under-sampling the atmosphere below about 2 km in a big portion of its planned scans. From space, the vertical sampling is greatly improved because of the advantage of the vertical look angle, but the horizontal sampling is

degraded (e.g., TRMM has a 4 km by 4 km horizontal footprint at nadir) due to the cost and size constraint of the antenna. The information in the lower troposphere is deemed very important for the study and prediction of local hazardous weather events, such as flash floods and tornadoes.

As an effort to address the poor spatial resolution of the lower troposphere using traditional long-range ground radar techniques, the Center for Collaborative and Adaptive Sensing of the Atmosphere (CASA) was launched in 2003 by the National Science Foundation and its four partner universities (McLaughlin et al. (2005)). The CASA approach to improve the spatial resolution of the lower troposphere over its coverage area is to employ low-cost, end-user-driven, and dense radar networks formed by short range (typically < 40 km) X-band radar systems, called Distributed Collaborative and Adaptive Sensing nodes (DCAS). The first generation of the DCAS system (called, IP1) is deployed in Oklahoma and has been operational as of April 2007.

It is recognized that there are underlying fundamental challenges for taking the CASA approach (Chandrasekar et al. (2004)), such as the range-velocity ambiguity (unambiguous range = $\frac{c \cdot (PRT)}{2}$; Nyquist velocity = $\frac{\lambda}{4(PRT)}$; where c is velocity of light and PRT is pulse repetition time) and the increased attenuation caused by precipitation particles due to the use of higher frequencies (X-band). Bharadwaj and Chandrasekar (2006) discussed and resolved the range-velocity ambiguity problem. Lim et al. (2004) derived a technique to correct radar reflectivity for attenuation using combined measurement of radar networks. Liu et al. (2006) derived an improved algorithm to

correct reflectivity and differential reflectivity for rain attenuation.

In this dissertation, we focus on the study and real-time implementation of attenuation correction for X-band dual-polarization weather radars. This work is primarily developed and evaluated during the course of the CASA IP1 but the data from other radar systems (e.g., the MP-X radar) operated by NIED, Japan are also studied.

1.2 Organization of this dissertation

We organize this dissertation into six chapters and three appendices.

Chapter 1: The overview and the organization of the dissertation are given in this chapter. The instruments that this work uses are also introduced (in the next section).

Chapter 2: The theoretical background of electromagnetic radiation and interaction with the precipitating particles is presented, especially as it relates to estimating (correcting) attenuation. The historical work on correcting the attenuation caused by rain and other precipitating particles is also summarized.

Chapter 3: A general mathematical framework to estimate the specific attenuation at horizontal polarization based on the consistency between the reflectivity and the specific differential propagation phase is presented. Then a more explicit form is derived based on previous work by Hitschfeld and Bordan (1954) and the constraint from the differential

propagation phase. The problem can be viewed as a parameter estimation problem in a parametric model. Various optimization schemes are discussed. The results obtained by using simulations, the MP-X radar data, and the CASA IP1 data are presented.

Chapter 4: The methodology presented in chapter 3 is extended to estimate the specific differential attenuation and to correct the differential reflectivity for rain attenuation. The results obtained by using simulations, the MP-X radar data, and the CASA IP1 data are also presented.

Chapter 5: Chapters 3 and 4 describe techniques for the attenuation and differential attenuation correction for the rain medium only. In chapter 5, we study attenuation due to the mix-phase region defined herein as rain mixed with wet ice particles. We use the microphysical outputs (rain and hail) from a prior supercell simulation using the CSU-RAMS model to study two proposed approaches to the mixed-phase attenuation problem which involves separately estimating the attenuation due to rain and the wet ice. The two proposed mixed-phase attenuation correction methods are applicable to the (e.g. CP-2) dual-wavelength radar configuration or the CASA IP1/WSR-88D configuration.

Chapter 6: In the last chapter of the dissertation, we summarize our work and suggest possible methods to further the work completed in this dissertation.

In the appendices, we give supplemental derivations of some of the formulations presented in the dissertation and other related materials. In appendix A, we give the

derivation of the Hitschfeld and Bordan (1954) method. In appendix B, we give an independent and simple derivation of the Testud et al. (2000) method. In appendix C, we summarize the drop shape models used in the simulation study in chapters 3 and 4.

1.3 Instruments and testbeds

1.3.1 CASA IP1

The CASA IP1 radars are designed and built completely within CASA. All four partner universities, namely, the University of Massachusetts in Amherst; Colorado State University; the University of Oklahoma; and the University of Puerto Rico all took part in the preliminary and critical design phases. The lead university, the University of Massachusetts in Amherst built the hardware and the control network components. One of the partner universities, Colorado State University, developed most of the radar signal processing algorithms. The CASA IP1 radars are now installed in four cities in Oklahoma, namely, Chickasha, Cyril, Lawton, and Rush Springs. It has been fully operational as of April 2007. The day-to-day operation is organized by the University of Oklahoma jointly with the other three partner universities.

Each of the four radars has the identical design and operates in the same configuration (X-band frequency). They all have the Doppler and dual-polarization capability. Table (1.1) lists the main characteristics of the radars.

Fig. 1.1 shows the prototype IP1 radar next to the CSU-CHILL S-band radar facility in Greeley, Colorado. The foreground is the CSU-CHILL radar's radome which is about 17 meters in height, while that of the CASA IP1 prototype located a few meters behind is only about 2.4 meters in height. The main factor in this large difference in size is the antenna.

Fig. 1.2 shows one of the four radar nodes of IP1 being installed at the site in Cyril, OK in Summer 2006. Fig. 1.3 shows the network topology of the four radar nodes with each node operating with a maximum range of 30 km (however it has been extended to 40 km as of June, 2007).

Table 1.1 System Characteristic of the CASA IP1 radar node (Source: IP1 System Requirements Documents, Revision 3, March 2005.)

Frequency	9.41 GHz
Peak Power	25 kW
Pulse Repetition Frequency	≤ 3.33 kHz
Pulse Length	0.6 – 1.5 μ s
Polarization	Horizontal and Vertical
Minimum Detectable Signal	-107 dBm
Receiver Dynamic Range	70 dB
Transmitter Tube	Magnetron
Antenna diameter	1.5 m
Beam Width	2 deg
Antenna Gain	38 dB

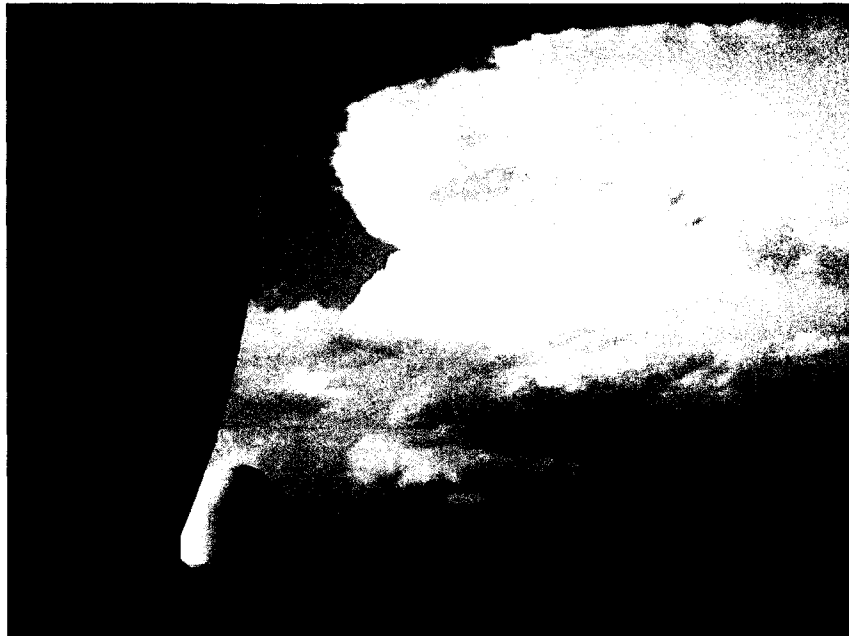


Figure 1.1 Photograph of the prototype CASA IP1 radar seated next to the CSU-CHILL S-band radar during the calibration and test in the Summer of 2005.

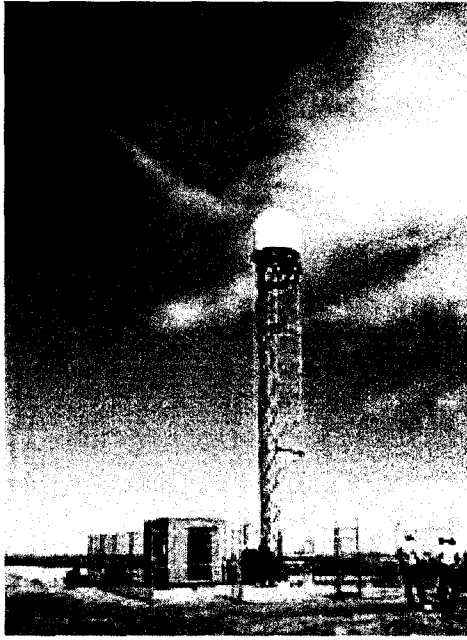


Figure 1.2 One of the four CASA IP1 radars being installed at the Cyril, Oklahoma site.

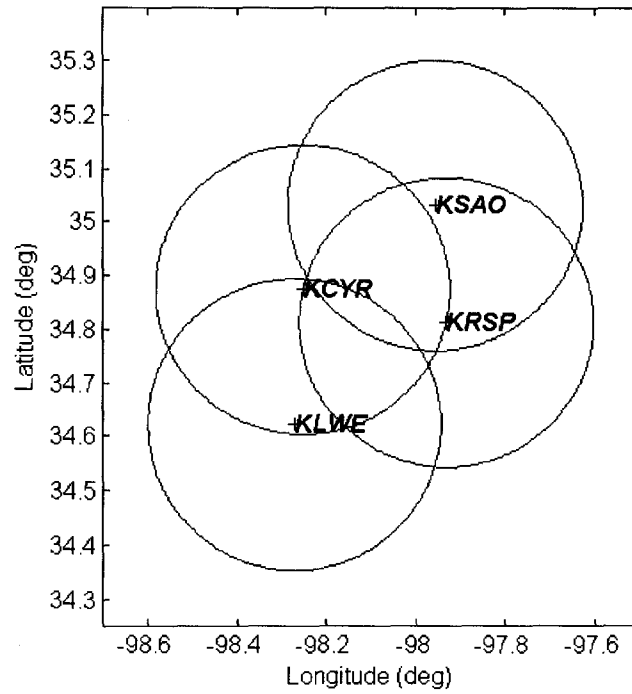


Figure 1.3 Schematic showing locations of the four nodes of the CASA IP1 network and its coverage near four cities in Oklahoma, namely Chickasha, Cyril, Lawton, and Rush Springs.

1.3.2 MP-X radar

The MP-X radar is a Doppler, dual-polarization X-band radar operated by the National Institute of Earth Science and Disaster Prevention (NIED), Japan. Table (1.2) lists its main characteristics. Fig. 1.4 shows the MP-X radar installed on a mobile transportable platform. The radar was installed near the Tsukuba area for a validation experiment during 2001. There are also other ground instruments like rain gauges and disdrometers in the nearby area which provide ground truth measurements of rainfall rate and particle size information.

Table 1.2 System characteristics of the MP-X radar (Courtesy M. Maki of NIED)

Frequency	9.375 GHz
Antenna Type	Circular Parabola
Antenna Diameter	2.1 m
Antenna Gain	41.6 dB
Beam Width	1.3 deg
Receiver Dynamic Range	83 dB
Transmitter Tube	Magnetron
Peak Power	50 kW
Pulse Length	0.5 μ s
Pulse Repetition Frequency	\leq 1800 Hz
Polarization	Horizontal and Vertical
Minimum Detectable Signal	-110 dBm
Observation Range	80 km

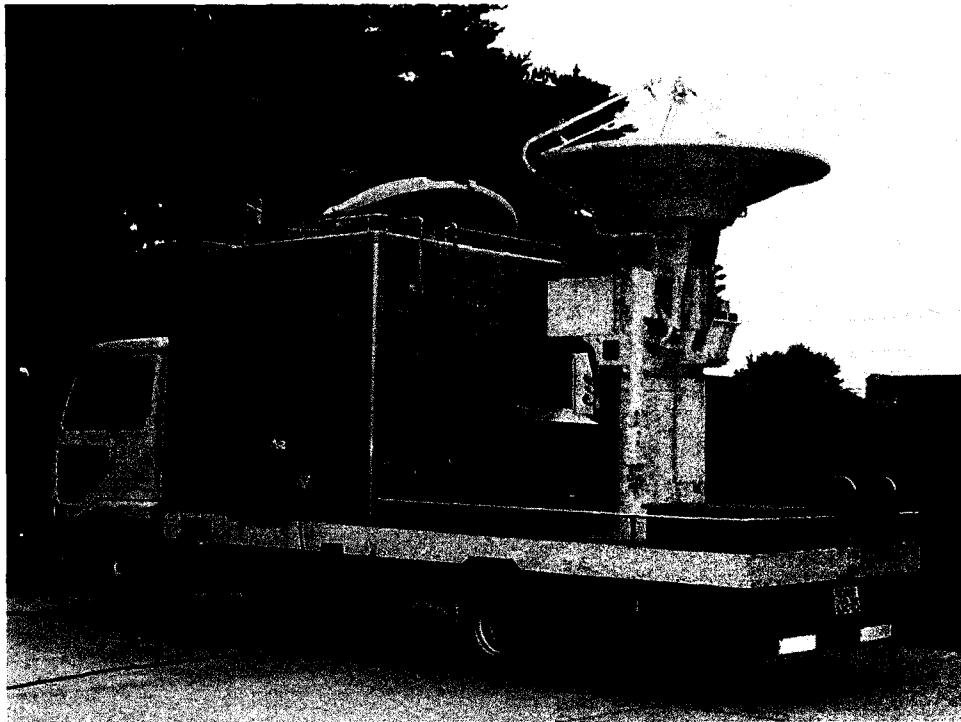


Figure 1.4 The MP-X mobile transportable radar (Courtesy of M. Maki of NIED)

1.3.3 CP-2 radar

The CP-2 radar is a dual-wavelength (S, X-band) radar with full dual-polarization capability at S-band. As yet we do not have data from this radar but our dual-wavelength radar simulations using the RAMS simulated supercell provides a basis for our proposed method of separately estimating the rain and wet ice attenuation in the mixed phase region. We provide some details of the radar here in anticipation of using our methodology in the near future (Nov 2007-March 2008). The radar is installed near Brisbane, Australia and is operated by the Bureau of Meteorology Research Centre (BMRC), Australia. Table (1.3) lists the main characteristics of the CP-2 radar. Fig. 1.5 shows a photograph taken when the radar was being installed early 2007. Fig. 1.6 shows the topology of the surrounding near the radar site.

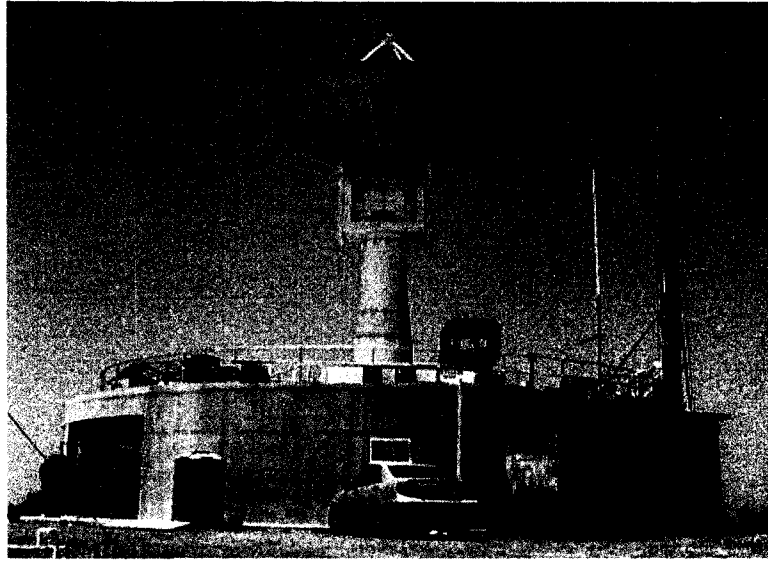


Figure 1.5 CP-2 radar being installed near Brisbane. The X-band system is yet to be installed (Courtesy of Tom Keenan of BMRC).

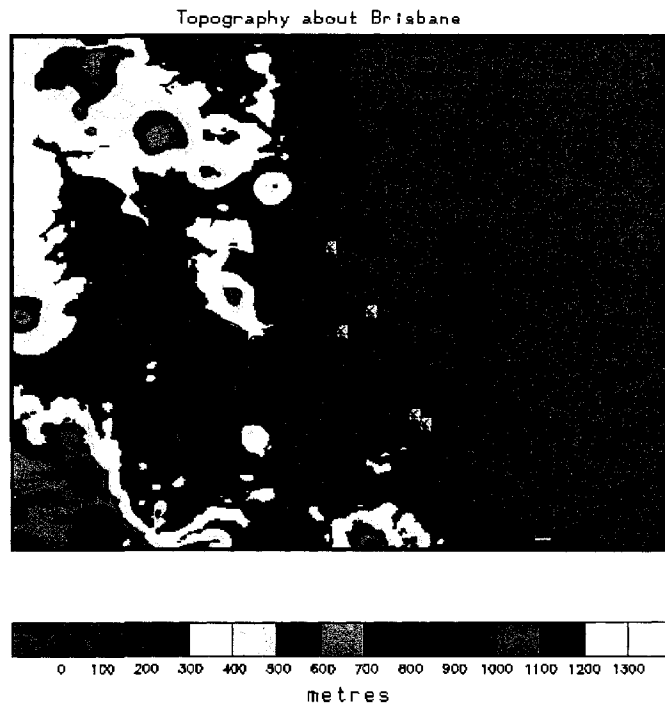


Figure 1.6 Topography surrounding Brisbane with areas (hatched) under flooding threat. The CP-2 radar site will be near Ipswich, about 30 km south west of Brisbane (Courtesy of Tom Keenan of BMRC).

Table 1.3 System characteristics of the CP-2 radar (Courtesy Tom Keenan of BMRC)

Characteristic	CP2 S-Band	CP2 X-band
Wavelength (cm)	10.7	3.2
Peak Power (kW)	1000	200
Pulse length(ms)	0.17-1.0	1.0
PRF (s^{-1})	<1700	<1000
Antenna Type	Centre feed paraboloid	Two cassegrain paraboloids
Feed Type	Potter horn	Rectangular Waveguide
Beamwidth (degrees)	0.93	0.94
Az coverage (degrees)	360	360
EI Coverage (degrees)	90	90
Polarisations radiated	LIN H, LIN V	LIN H
Simultaneous 2 channel reception	N	Y
Polarisation Received	Copolar to TX	LIN H & LIN V
Max Sidelobe level (dB)	-21	~-30
Max Antenna Linear X-POL lobes (dB)	-21	-36
Polarisation Control Method	Ferrite Switch	NA
Polarisation Control rate	Pulse by pulse	NA
Channel to Channel Isolation (db) ex Antenna	>30	>30
Doppler Capability	Y	N
Number of Range Gates	1024	1024
Range Resolution (m)	> 30 typically 150	> 30 typically 150
Polarisation Quantities measured	Z, Z_{dr} , Φ_{dp} , ρ_{HV}	Z, LDR,

2 THEORETICAL BACKGROUND AND RELATED WORK

Doppler radars are considered indispensable tools for remote sensing of the atmosphere, detecting and tracking of commercial or military objects, and so on. The theory and techniques of Doppler weather radars can be found in Doviak and Zrnic (1993). In addition to the Doppler techniques, radar polarimetry (e.g., linear or circular polarization) is considered an invaluable tool that provides much desired additional information, particularly the shape and orientation information of the precipitating particles. The advantages can be largely attributed to the abilities to classify hydrometeor types and to improve rainfall rate estimation. The theory and techniques of polarimetric radars can be found in Bringi and Chandrasekar (2001). For meteorological applications using radar systems at attenuating frequencies, the invaluable shape information of the raindrops provided by the polarimetric techniques is the key to many rain attenuation-correction algorithms applied to C band dual-polarized radars (Testud et al. (2000), Bringi et al. (2001)) and X band dual-polarized radars (Matrosov et al. (2005), Park et al. (2005)).

This chapter is intended to survey the background and theoretical basis of attenuation-correction (estimation) techniques. Beginning with the scattering matrix, the wave equation is described for the scattering of a particle in free space. For scattering over a homogenous precipitating path containing uniformly distributed oblate raindrops, the transmission matrix will be used to characterize the propagation effects along the path, including the attenuation, the differential attenuation and the differential propagation phase between the h and v -polarization states. Then the radar range equation is provided.

In the end different techniques to correct (estimate) the attenuation and the differential attenuation will be briefly presented in a chronological order so that a historical review is provided. .

2.1 Scattering matrix

The electromagnetic field radiated by an antenna is a spherical wave described by:

$$\vec{E}^i(\vec{r}) = \vec{E}^0 \frac{e^{-jk_0 \hat{i} \cdot \vec{r}}}{\hat{i} \cdot \vec{r}} \quad (2.1)$$

where k_0 is the wave number of free space, \vec{r} is the range vector (e.g., $\vec{r} = (r, \theta, \phi)$ in a spherical coordinate system), \hat{i} is the incident direction (unit vector) which is orthogonal to both the electric and the magnetic field, the superscript i (e.g., as in \vec{E}^i) denotes ‘incident’, and the superscript 0 (e.g., as in \vec{E}^0) denotes origin. Note that we use the arrow to denote vectors and the hat to denote unit vectors.

Now consider a spherical coordinate system specified by the triplet (r, θ, ϕ) . The unit vectors in the spherical coordinate system satisfy the orthogonal relations as follows:

$$\hat{r} = \hat{\theta} \times \hat{\phi} \quad (2.2a)$$

$$\hat{\phi} = \hat{r} \times \hat{\theta} \quad (2.2b)$$

$$\hat{\theta} = \hat{\phi} \times \hat{r} \quad (2.2c)$$

where ‘ \times ’ denotes the conventional vector cross product.

For linearly polarized waves, the unit linear polarization vector \hat{e}_i , that defines the direction of the incident electric field, can be decomposed into two orthogonal components at the horizontal (\hat{h}) direction and the vertical (\hat{v}), respectively, as:

$$\hat{e}_i = \frac{E_h^i}{E_0} \hat{h} + \frac{E_v^i}{E_0} \hat{v} \quad (2.3)$$

where E_h^i and E_v^i are the horizontal and vertical components, respectively and are both real here. However, in general they can be complex, resulting in circular polarization or elliptical polarization (Chapter 3, Brongi and Chandrasekar (2001)). E_0 is the real amplitude of \bar{E}^0 .

Conventionally, in the forward scattering direction, the horizontal and vertical unit vectors are same as the unit vectors $\hat{\phi}$ and $\hat{\theta}$ in the spherical coordinate system, respectively.

Thus we define:

$$\hat{h} = \hat{\phi} \quad (2.4a)$$

$$\hat{v} = \hat{\theta} \quad (2.4b)$$

In other words, the horizontal and vertical directions depends on $\hat{\phi}$ and $\hat{\theta}$, respectively.

Note that the two directions can be different than the literal meanings of the words

‘horizontal’ (i.e., parallel to the ground) and ‘vertical’ (i.e., perpendicular to the ground). With above definitions, the incident wave direction can be described in the spherical coordinate system as:

$$\hat{i} = \hat{v}_i \times \hat{h}_i = \hat{\theta}_i \times \hat{\phi}_i \quad (2.5)$$

where the subscript i denotes given values for the incident wave’s direction.

Assume the wave interacts with a dielectric particle in free space. In the far-field, the scattered wave from a dielectric particle can be expressed as:

$$\bar{E}^s(\bar{r}) = \bar{f}(\hat{s}, \hat{i}) \frac{e^{-jk_0 r}}{r} \quad (2.6)$$

where $\bar{f}(\hat{s}, \hat{i})$ is the complex vector scattering amplitude of the particle (Chapter 1, Brongi and Chandrasekar (2001)), the vector \bar{r} locates a position in the far-field and $r = |\bar{r}|$. Also, \hat{s} and \hat{i} are unit vectors along the direction of scattering and incidence, respectively. The superscript ‘s’ (e.g., as in \bar{E}^s) denotes ‘scattering’.

Combining eqs. (2.1), (2.3), and (2.6), in the back-scattering direction (i.e., $\hat{s} = -\hat{i}$) the back-scattered wave can be described by the complex scattering matrix \mathbf{S}_{BSA} , where the subscript BSA denotes ‘back scattering alignment’, as:

$$\bar{E}^r(r) = \frac{e^{-jk_0 r}}{r} [E_h^i \quad E_v^i] \mathbf{S}_{BSA} \begin{bmatrix} \hat{h} \\ \hat{v} \end{bmatrix} \quad (2.7)$$

where r is the distance from the particle along the back-scattering direction and the superscript ' r ' (e.g., as in \vec{E}^r) denotes back-scattering. Note that we use bold type to denote matrices.

The complex scattering matrix \mathbf{S}_{BSA} fully characterizes the response of the dielectric particle excited by the incident wave and is defined as:

$$\mathbf{S}_{BSA} = \begin{bmatrix} S_{hh} & S_{hv} \\ S_{vh} & S_{vv} \end{bmatrix} \quad (2.8)$$

where the double subscript denotes 'receiving-transmitting' polarization, e.g., hv denotes receiving at horizontal polarization after transmitting at vertical polarization.

2.2 Transmission matrix and propagation effects

The scattering matrix in eq. (2.7) described the relationship of the back-scattered electric field and the incident electric field for a particle in free space. When the propagation path is filled with distributed dielectric particles, propagation effects should be considered. The propagation effects can be described using the transmission matrix which replaces the spherical wave phase term e^{-jk_0r} by :

$$\vec{E}^r(r) = \frac{1}{r} [E_h^i \quad E_v^i] \mathbf{S}_{BSA} \mathbf{T} \begin{bmatrix} \hat{h} \\ \hat{v} \end{bmatrix} \quad (2.9)$$

where \mathbf{T} is the 2x2 transmission matrix defined as:

$$\mathbf{T} = \begin{bmatrix} T_{hh} & T_{hv} \\ T_{vh} & T_{vv} \end{bmatrix} \quad (2.10)$$

For detailed expressions of the elements of \mathbf{T} refer to section 4.2 of Bringi and Chandrasekar (2001). Eq. (2.9) describes the one-way propagation effects when the wave is back-scattered by the particle. The incident field radiated from the source, whose horizontal and vertical components are E_h^i and E_v^i , are also under the propagation effects. Therefore the spherical wave phase term in eq. (2.1) should be also replaced. Replacing the term in eq. (2.1) and substituting it into eq. (2.9) give the back-scattered wave electric field with the two-way propagation effects as follows:

$$\bar{E}^r(r) = \frac{1}{r^2} [E_h^0 \quad E_v^0] \mathbf{TS}_{BSA} \mathbf{T} \begin{bmatrix} \hat{h} \\ \hat{v} \end{bmatrix} \quad (2.11)$$

where now r is the distance between the receiver (collocated with the source) and the particle. Note that all terms in the above equation are complex except r , \hat{h} , and \hat{v} .

It is worth noting that the scattering matrix \mathbf{S}_{BSA} is the property of the dielectric particle, while the transmission matrix \mathbf{T} is the property of the propagation path (forward direction) which is filled with dielectric particles.

For simplicity, consider a propagation path which is filled with uniformly distributed spheroids whose symmetric axis are parallel with \hat{h} or \hat{v} (i.e., canting angle is 0). Under

such conditions, the solution of the transmission matrix is very simple as follows (Chapter 4, Brongi and Chandrasekar (2001)):

$$T = \begin{bmatrix} T_{hh} & 0 \\ 0 & T_{vv} \end{bmatrix} = \begin{bmatrix} e^{-jk_{eff}^h r} & 0 \\ 0 & e^{-jk_{eff}^v r} \end{bmatrix} \quad (2.12)$$

where $k_{eff}^{h,v}$ is the effective complex wave number of the medium that fills the path for h or v polarization. It is given as:

$$k_{eff}^h = k_0 + \frac{2\pi n}{k_0} \hat{h} \cdot \bar{f}(\hat{i}, \hat{i}) \quad (2.13a)$$

$$k_{eff}^v = k_0 + \frac{2\pi n}{k_0} \hat{v} \cdot \bar{f}(\hat{i}, \hat{i}) \quad (2.13b)$$

where n is the number of spheroids per cubic meters and \bar{f} is the complex vector scattering amplitude (see eq. (2.6)).

Now, we can define the specific attenuation, the differential attenuation, and the specific differential propagation phase as:

$$A_h = 20 \log_{10}(e^{\text{Im}\{k_{eff}^h\}}) \cdot 10^3 \quad (2.14a)$$

$$= 8.686 \times 10^3 \cdot \text{Im}\{k_{eff}^h\} \quad (2.14b)$$

$$= 8.686 \times 10^3 \cdot \frac{2\pi n}{k_0} \cdot \text{Im}\{\hat{h} \cdot \bar{f}(\hat{i}, \hat{i})\} \quad (2.14c)$$

$$A_v = 8.686 \times 10^3 \cdot \text{Im}\{k_{eff}^v\} \quad (2.15a)$$

$$= 8.686 \times 10^3 \cdot \frac{2\pi n}{k_0} \cdot \text{Im}\{\hat{v} \cdot \bar{f}(\hat{i}, \hat{i})\} \quad (2.15b)$$

$$A_{dp} = A_h - A_v \quad (2.16a)$$

$$= 8.686 \times 10^3 \cdot \text{Im}\{k_{eff}^h - k_{eff}^v\} \quad (2.16b)$$

$$= 8.686 \times 10^3 \cdot \frac{2\pi n}{k_0} \cdot \text{Im}\{\hat{h} \cdot \bar{f}(\hat{i}, \hat{i}) - \hat{v} \cdot \bar{f}(\hat{i}, \hat{i})\} \quad (2.16c)$$

$$K_{dp} = 10^3 \cdot \text{Re}\{k_{eff}^h - k_{eff}^v\} \quad (2.17a)$$

$$= 10^3 \cdot \frac{2\pi n}{k_0} \cdot \text{Re}\{\hat{h} \cdot \bar{f}(\hat{i}, \hat{i}) - \hat{v} \cdot \bar{f}(\hat{i}, \hat{i})\} \quad (2.17b)$$

In eqs. (2.14)-(2.17), k_0 is in m^{-1} , \bar{f} in m , n in m^{-3} . Then A_h , A_v , and A_{dp} are in dB km^{-1} , K_{dp} in rad km^{-1} .

It is clear that at a given time, K_{dp} contributes to the phase difference between the two characteristic waves (h , v) due to the medium in the propagation path while A_h and A_v contributes to the loss in power in the two characteristic waves, respectively.

2.3 Radar range equation

For an ideal antenna the (received) voltage equation due to the back-scattered electric field \bar{E}^r can be written as (Sinclair (1950)):

$$V = \frac{1}{\sqrt{2Z_0}} \bar{h} \cdot \vec{E}^r \quad (2.18)$$

where Z_0 is the impedance of free space and \bar{h} is the effective antenna length defined as:

$$\bar{h}(\theta, \phi) = \frac{\lambda}{\sqrt{4\pi}} \hat{e} \sqrt{G(\theta, \phi)} \quad (2.19)$$

where λ is the wavelength, $G(\theta, \phi)$ is the antenna gain function, and \hat{e} is the unit polarization vector.

It is clear that the received voltage depends on the polarization of the antenna and the polarization of the back-scattered electric field. For linear polarization we assume the two polarizations are matched and the received voltages at the h and v ports of the antenna can be expressed as:

$$\begin{bmatrix} V_h \\ V_v \end{bmatrix} = \frac{\lambda G(\theta, \phi)}{4\pi r^2} \mathbf{TS}_{BSA} \mathbf{T} \begin{bmatrix} M_h \\ M_v \end{bmatrix} \quad (2.20)$$

where M_h and M_v are the input plane wave complex amplitudes whose magnitudes are proportional to $\sqrt{P_h^t}$ and $\sqrt{P_v^t}$, respectively. Here, P_h^t and P_v^t are the 'pulse' powers transmitted by the antenna.

Given the propagation conditions described earlier for eq. (2.12), the transmission matrix \mathbf{T} and the scattering matrix are diagonal. Eq. (2.20) can be simplified as follows:

$$\begin{bmatrix} V_h \\ V_v \end{bmatrix} = \frac{\lambda G(\theta, \phi)}{4\pi r^2} \begin{bmatrix} T_{hh} & T_{hv} \\ T_{vh} & T_{vv} \end{bmatrix} \begin{bmatrix} S_{hh} & S_{hv} \\ S_{vh} & S_{vv} \end{bmatrix} \begin{bmatrix} T_{hh} & T_{hv} \\ T_{vh} & T_{vv} \end{bmatrix} \begin{bmatrix} M_h \\ M_v \end{bmatrix} \quad (2.21a)$$

$$= \frac{\lambda G(\theta, \phi)}{4\pi r^2} \begin{bmatrix} T_{hh} & 0 \\ 0 & T_{vv} \end{bmatrix} \begin{bmatrix} S_{hh} & 0 \\ 0 & S_{vv} \end{bmatrix} \begin{bmatrix} T_{hh} & 0 \\ 0 & T_{vv} \end{bmatrix} \begin{bmatrix} M_h \\ M_v \end{bmatrix} \quad (2.21b)$$

$$= \frac{\lambda G(\theta, \phi)}{4\pi r^2} \begin{bmatrix} T_{hh}^2 S_{hh} & 0 \\ 0 & T_{vv}^2 S_{vv} \end{bmatrix} \begin{bmatrix} M_h \\ M_v \end{bmatrix} \quad (2.21c)$$

The co-polar received power then can be simplified and calculated as:

$$P_h^{co} = V_h^* V_h = \frac{\lambda^2 G(\theta, \phi)^2}{(4\pi)^2 r^4} |T_{hh}|^4 |S_{hh}|^2 P_h' \quad (2.22a)$$

$$= \frac{\lambda^2 G(\theta, \phi)^2 P_h'}{(4\pi)^3 r^4} \left| e^{-jk_{eff}^h r} \right|^4 (2\pi |S_{hh}|^2) \quad (2.22b)$$

$$= \frac{\lambda^2 G(\theta, \phi)^2 P_h'}{(4\pi)^3 r^4} \left| e^{-j(\text{Re}\{k_{eff}^h\} + j\text{Im}\{k_{eff}^h\})r} \right|^4 \sigma_{hh} \quad (2.22c)$$

$$= \frac{\lambda^2 G(\theta, \phi)^2 P_h'}{(4\pi)^3 r^4} e^{4\text{Im}\{k_{eff}^h\}r} \sigma_{hh} \quad (2.22d)$$

$$= \frac{\lambda^2 G(\theta, \phi)^2 P_h'}{(4\pi)^3 r^4} \cdot 10^{\frac{2PIA_h}{10}} \cdot \sigma_{hh} \quad (2.22e)$$

where σ_{hh} is the back-scattered radar cross section (in m^2) at h polarization of the particle,

PIA_h is the one-way path-integrated attenuation (in dB) at h polarization. The σ_{hh} is

defined as:

$$\sigma_{hh} = 4\pi |S_{hh}|^2 \quad (2.23)$$

For the homogenous path assumption, PIA_h is defined as:

$$PIA_h(r) = A_h r \quad (2.24)$$

where A_h is the specific attenuation (in dB km⁻¹) at h polarization defined in eq. (2.14).

The two-way differential total phase is defined as:

$$\Psi_{dp}(r) = \arg(V_h^*(r)V_v(r)) \quad (2.25a)$$

$$= \arg(T_{hh}^{*2}S_{hh}^*T_{vv}^2S_{vv}) \quad (2.25b)$$

$$= \arg(e^{j2(k_{eff}^h - k_{eff}^v)r}) + \arg(S_{hh}^*S_{vv}) \quad (2.25c)$$

$$= \Phi_{dp}(r) + \delta_{co}(r) \quad (2.25d)$$

$$= 2K_{dp}r + \delta_{co}(r) \quad (2.25e)$$

where Φ_{dp} is the two-way differential propagation phase, δ_{co} is the differential back-scattered phase.

Although eq. (2.22) is deduced assuming a homogenous path with spheroids aligned at zero canting angle, it can be extended for an inhomogeneous path (i.e., a path with particles with different sizes and shapes) and for non-zero canting angles. In such conditions, the transmission \mathbf{T} is no longer diagonal and it varies along the range. However, it is acceptable to approximate the inhomogeneous path using 'piece-wise' homogeneous sections. This would result in a more general representation of eq. (2.20) as:

$$\begin{bmatrix} V_h \\ V_v \end{bmatrix} = \frac{\lambda G(\theta, \phi)}{4\pi r^2} \mathbf{T}_1 \mathbf{T}_2 \cdots \mathbf{T}_{n-1} \mathbf{T}_n \mathbf{S}_{BSA} \mathbf{T}_n \mathbf{T}_{n-1} \cdots \mathbf{T}_2 \mathbf{T}_1 \begin{bmatrix} M_h \\ M_v \end{bmatrix} \quad (2.26)$$

where $\mathbf{T}_1, \mathbf{T}_2, \dots, \mathbf{T}_{n-1}, \mathbf{T}_n$, are the transmission matrices of the n homogeneous sections.

The spatial variability of the precipitation occurs at all scales, but the radar resolution volume is typically non-uniformly filled with precipitation. (non-uniform beam filling especially at long ranges > 60 km for a 1 deg beam). Typical convective scales for precipitation are on the order of 500 – 1000 m whereas radar gates are typically spaced 150 m apart. Hence, the high ‘frequency’ gate-to-gate variability is due to random fluctuations and should be filtered with, for example, a FIR (finite impulse response) range filter with 6-dB bandwidth roughly equal to 1 km.

In general, eq. (2.26) is very hard to solve and approximations are usually made for different situations to obtain analytical results in terms of the state variables (e.g., mean canting angle, spheroid shape model, etc., see Bringi and Chandrasekar (2001)). Therefore, in general the transmission \mathbf{T} from the net-effect of all n sections is non-diagonal. Nonetheless, in similar fashion as shown in the previous simplified conditions in eq. (2.21), we can still write the radar range equation as eq. (2.22) but the attenuation term must be modified as:

$$PIA_h(r) = \sum_{i=1}^n A_h(i) \Delta r \quad (2.27a)$$

$$= \int_0^r A_h(r) dr \quad (2.27b)$$

where now A_h is a function of range.

Similarly, the differential propagation phase in eq. (2.25) should be modified as:

$$\Phi_{dp}(r) = 2 \sum_{i=1}^n K_{dp}(i) \Delta r \quad (2.28a)$$

$$= 2 \int_0^r K_{dp}(r) dr \quad (2.28b)$$

So far we have defined the radar equation for a single particle. Now consider a pulsed radar with the pulse width T . At any given time the received voltage (complex) is the sum of the return of all the particles illuminated by the transmitted energy in the resolution volume. The resolution volume is defined as the volume enclosed by the antenna pattern and the distance that the leading edge of the pulse travels in $T/2$. The radar equation for the distributed particles in the resolution volume is given here as (Bringi and Chandrasekar (2001)):

$$P_r(r) = \frac{P_t G_0^2}{(4\pi)^3} \cdot \frac{cT}{2} \cdot \frac{\pi \theta_b \phi_b}{8 \ln 2} \cdot \frac{\pi^5 |K|^2}{\lambda^2} \cdot \frac{1}{r^2} \cdot Z(r) \cdot 10^{-\frac{2PIA(r)}{10}} \quad (2.29a)$$

$$= C \cdot \frac{1}{r^2} \cdot Z(r) \cdot 10^{-\frac{2PIA(r)}{10}} \quad (2.29b)$$

In eq. (2.29), the antenna pattern function $G(\theta, \phi)$ is approximated by a Gaussian function and its 3-dB beamwidths at two orthogonal directions are θ_b and ϕ_b , respectively. K is the dielectric factor of the particle (usually assumed to be water), c is speed of light in free space, C is a constant termed ‘radar constant’, and $Z(r)$ is the radar reflectivity factor at range r defined as:

$$Z(r) = \int_0^{\infty} D^6 N(D, r) dD \quad (2.30)$$

where D is the spherical particle diameter (in mm), $N(D)$ is the drop size distribution (DSD). $N(D)$ has the unit of $\text{m}^{-3} \text{mm}^{-1}$ and $N(D) dD$ is the number of spherical particles per unit volume having diameters $[D, D+ dD]$.

Note that in going from eq. (2.22) to eq. (2.29) the Rayleigh scattering is also assumed under which we have:

$$\sigma_i = \frac{\pi^5 |K|^2}{\lambda^4} D_i^6 \quad (2.31)$$

where σ_i is the back-scattered radar cross section for i th particle in the resolution volume and D_i is the diameter of the i th particle.

Eq. (2.29) is given for single polarization (usually assumed to be horizontal), and reflectivity and back-scattered radar cross section in eqs. (2.30) and (2.31) are defined as quantities independent of polarization. However, note that spherical shape was assumed but the shape of actual precipitating particles can differ from spherical. In such case the

reflectivity and back-scatter radar cross section will be different between h and v polarizations. The differential reflectivity is defined as:

$$Z_{dr} = \frac{Z_h}{Z_v} \quad (2.32)$$

2.4 Related work on rain attenuation correction techniques

It is clear that the reflectivity (Z) as defined in eq. (2.30) has statistical information of the precipitation, in particular the 6th moment of the DSD. This quantity can be measured by the radar. However, as evident in eq. (2.29b), the received power at the antenna is a function of the reflectivity (Z), the path-integrated attenuation (PIA), and the range (r) (the radar constant C can be calculated and adjusted by various radar calibration techniques). It is easy to calculate r with a pulsed radar because the timing can be accurately determined and the sampling time will readily give the range as $r=ct/2$. It is the combination of the propagation effects due to the path and the back-scattered reflectivity at a given resolution volume that makes it difficult to separate and estimate Z and PIA , since they are both mixed together in the received power. The PIA is a quantity to be resolved before we can make any physical interpretation of Z at a given range. For example, Z is often used to infer rainfall rate directly with a power-law equation (e.g., $Z = aR^b$).

Estimation and correction of attenuation has been an active research area in radar meteorology since the inception of meteorological radars because there is a great need to

separate the propagation effects over the path and the back-scattered reflectivity from the volume target of interest. The framework of the estimation techniques can be expressed by the following basic equations:

$$Z_m(r) = \frac{P_r r^2}{C} \quad (2.33)$$

$$Z_e(r) = Z_m(r) 10^{\frac{2PIA(r)}{10}} \quad (2.34a)$$

$$= Z_m(r) e^{0.46 \int_0^r A(s) ds} \quad (2.34b)$$

where Z_m is the ‘measured’ reflectivity directly converted from the received power, and Z_e is the ‘intrinsic’ or ‘true’ reflectivity, A is the specific attenuation (≥ 0 dB km⁻¹) defined in eq. (2.14) (or eq. (2.15) for ν polarization). The polarization subscript is dropped here for the ease of notation but it should be kept in mind that the respective quantities are in a certain polarization (either h or ν states)

Hitschfeld and Bordan (1954) first proposed and developed a technique to estimate specific attenuation at each range gate. Their technique assumes that A - Z_e has a power-law relationship as:

$$A(r) = aZ_e^b(r) \quad (2.35)$$

Substituting this equation into eq. (2.34b), it can be solved (as an ordinary differential equation (ODE), e.g., see appendix A) to obtain the intrinsic reflectivity as a function of

the measured reflectivity and the range only. Using our notation, Hitschfeld and Bordan's original solution can be re-expressed as:

$$Z_e(r) = Z_m(r) \left(1 - 0.46ab \int_0^r Z_m^b(s) ds \right)^{\frac{1}{b}} \quad (2.36)$$

It was pointed out that eq. (2.36) is unstable and contains potentially large errors (Hitschfeld and Bordan (1954)). The error arises from two sources: the parameter error (in a and b) and the calibration error (in C when Z_m is calculated from eq. (2.33)). Both errors can propagate with range. Hitschfeld and Bordan (1954) suggested that eq. (2.36) be calibrated (constrained) with rain gauge measurements.

Hitschfeld and Bordan's method was limited by the single-polarized radar in use at the time it was developed. However, it has become a building-block for many other new attenuation estimation techniques using additional information that a dual-polarization radar provides. The specific differential propagation phase (K_{dp}) defined in eq. (2.17) is deemed to be an important quantity that can be related to attenuation directly under certain conditions.

Bringi et al. (1990) showed that in the rain medium the specific differential propagation phase (K_{dp} , in deg/km) is related to the specific attenuation at h polarization (k_h , in dB/deg) for frequencies below 20 GHz as:

$$A_h(r) = \alpha K_{dp}^{\epsilon} (r) \quad (2.37)$$

where ε lies in the range 0.97 to 1.02 for 5.5 to 19.35 GHz (see Table (7.1) in Bringi and Chandra (2001) taken from Jameson (1992)). Only at 3.0 GHz is the exponent close to 0.85. At X band the exponent is approximately unity, resulting a linear relationship between A_h and K_{dp} .

Using the relationship ($\varepsilon = 1$) and recalling that Φ_{dp} is the range integral of K_{dp} (see: eq. (2.28)), the intrinsic reflectivity can be calculated as:

$$Z_e(r) = Z_m(r) e^{0.23\alpha(\Phi_{dp}(r) - \Phi_{dp}(0))} \quad (2.38)$$

In theory it is simple to retrieve A_h and correct Z_e for attenuation using eqs. (2.37) and (2.38). But in practice Φ_{dp} is calculated from Ψ_{dp} in which there is another component δ_{co} (see eq. (2.25)). In addition, the measurement uncertainty contributes random fluctuation in Ψ_{dp} . Therefore, before applying the above attenuation estimation technique, one should filter Ψ_{dp} first and remove δ_{co} (Hubbert and Bringi (1995)). The difficulty in retrieval of K_{dp} should be also noted here for the same reasons since K_{dp} is retrieved by differentiating Ψ_{dp} with respect to range.

As mentioned earlier, Hitschfeld and Bordan's method can be made stable using the constraint from an independent measurement of PIA . In fact, this technique has been extended for single-polarized space-borne K_u -band radar on a satellite (TRMM; Iguchi et al. (2000)). For TRMM, the PIA can be inferred from the surface reference technique

(Iguchi et al. (2000)) or from the microwave radiometer technique (Kummerow and Giglio (1994)). Based on the same principle, Testud et al. (2000) proposed a method to estimate A_h for C-band dual-polarized radars, where the PIA is now given by $\alpha\Delta\Phi_{dp}$. Their solution is given as (Testud et al. (2000); see also, appendix B):

$$A_h(r) = \frac{Z_m^b(r)(e^{0.23cb\Delta\Phi_{dp}} - 1)}{I(r_1, r_2) + (e^{0.23cb\Delta\Phi_{dp}} - 1)I(r, r_2)} \quad (2.39)$$

where, r_1 is the range of the leading edge of the rain cell, r_2 is the range of the far end of the rain cell, $\Delta\Phi_{dp}$ is the increment of the differential propagation phase across the rain cell (i.e., $\Phi_{dp}(r_2) - \Phi_{dp}(r_1)$), and $I(r_1, r_2)$ is a quantity defined as:

$$I(r_1, r_2) = \int_{r_1}^{r_2} 0.46bZ_m^b(s)ds \quad (2.40)$$

One advantage of using Testud et al's method is the avoidance of filtering Ψ_{dp} and retrieving K_{dp} since only the difference of Φ_{dp} at both end of the rain cell is needed (but keep in mind that the A_h - K_{dp} relationship in eq. (2.37) is still implied). It is also arguably better to retrieve A_h in the sense of improving the spatial resolution since K_{dp} is not directly used but Z_m . However, in term of the error characteristic for a given range profile, Testud et al's method gives similar performance as the direct Φ_{dp} method (Gorgucci and Chandrasekar (2005)). It is clear that the $A(r)$ retrieved using both methods is immune to the calibration error, i.e., independent of the radar constant C . This is an advantage to be noted since it eliminates one source of error from the original Hitschfeld and Bordan's method.

Unfortunately, the parameterization error is still not removed. In the direct Φ_{dp} method this error is in the linear coefficient α in eq. (2.37). In Testud's method the error is in both α and the exponent b in eq. (2.35) (note that the coefficient a in eq. (2.35) is canceled out by assuming the drop concentration parameter (N_w) in the gamma DSD is constant along the path).

In order to mitigate this problem, Bringi et al. (2001) proposed an extension of Testud et al.'s method that reduces the uncertainty in the linear coefficient α in eq. (2.37). They proposed to use the 'self-consistency' between the derived (reconstructed) Φ_{dp} and the measured Φ_{dp} to minimize a cost function defined as,

$$Error(\alpha) = \sum_{j=0}^i \left| \Phi_{dp}^{filt}(r_j) - \Phi_{dp}^c(r_j, \alpha) \right| \quad (2.41)$$

where $\Phi_{dp}^{filt}(r_j)$ is the filtered version of the measured Φ_{dp} profile (Hubbert and Bringi (1995)) at range gate r_j , and $\Phi_{dp}^c(r_j, \alpha)$ is the reconstructed Φ_{dp} profile defined as:

$$\Phi_{dp}^c(r, \alpha) = 2 \int_{r_1}^r \frac{A(s, \alpha)}{\alpha} ds; r_1 \leq r \leq r_2 \quad (2.42)$$

This method provides a means to exploit the correlation between Z_e and K_{dp} in the rain medium. The optimal α is retrieved in a sense that it minimizes the sum of the absolute error between the reconstructed Φ_{dp} and the filtered Φ_{dp} . This method has been evaluated

for the BMRC C-pol radar (Bringi et al. (2001)) and later been modified for the MPX X-band polarimetric radar (Park et al. (2005)).

In addition to the methods summarized above, there are also other reported methods to estimate and correct attenuation. Hogan (2007) reported a method based on variational scheme to retrieve the coefficient of a reflectivity-rain rate ($Z-R$) relationship and incorporate very moderate S-band attenuation in his formulation. But he did not show the case where the attenuation is much more severe (e.g., at X-band). L'Ecuyer and Stephens (2002) reported an estimation-based precipitation retrieval method for CloudSat millimeter wave space-borne radar (94 GHz). Because the size-over-wavelength factor is large in such high frequency for the precipitating particle, the Rayleigh approximation no longer applies to the $Z-R$ relationship. Their work addressed the non-directly-invertible problem of the $Z-R$ relationship at 94 GHz using an optimal approach and considering constraints as well.

2.5 Related work on rain differential attenuation correction techniques

The differential reflectivity defined in eq. (2.32) is measured by the radar by taking the ratio of the measured Z_h vs. the measured Z_v . In general, it is affected by the differential attenuation over the propagation path as:

$$Z_{dr,m}(r) = Z_{dr,e}(r) \cdot 10^{\frac{1}{10}(2PIA_h(r) - 2PIA_v(r))} \quad (2.43a)$$

$$= Z_{dr,e}(r) \cdot 10^{-\frac{1}{5} \int_0^r A_{dp}(s) ds} \quad (2.43b)$$

$$= Z_{dr,e}(r) \cdot e^{-0.46 \int_0^r A_{dp}(s) ds} \quad (2.43c)$$

where $Z_{dr,m}$ is the measured differential reflectivity, $Z_{dr,e}$ is the ‘intrinsic’ or ‘true’ differential reflectivity, and A_{dp} is the specific differential attenuation defined in eq. (2.16).

Therefore, we have a similar problem as discussed in section 2.4 when we invert eq. (2.43) to separate the true differential reflectivity from the differential attenuation. The differential attenuation should be estimated and corrected before the true Z_{dr} can be used. For example, Z_{dr} is used to improve the rainfall rate estimation (Seliga and Bringi (1976)) and classify hydrometeor types (Zrnić et al (1993), Liu and Chandrasekar (2000)).

Ryzhkov and Zrnić (1995) proposed to correct the measured Z_{dr} for rain medium using:

$$\Delta Z_{dr}(r) = Z_{dr,m}(r) - Z_{dr,e}(r) \quad (2.44a)$$

$$= -\beta(\Phi_{dp}(r) - \Phi_{dp}(0)) \quad (2.44b)$$

where ΔZ_{dr} , $Z_{dr,m}$, and $Z_{dr,e}$ are in dB, β is in dB/deg.

The assumption in using eq. (2.44) is that the rain medium is uniform such that the decreasing trend in the measured Z_{dr} can be attributed to the differential attenuation only.

Then β can be estimated by fitting a straight line into the measured $Z_{dr} - \Phi_{dp}$ pairs.

After β is estimated Z_{dr} (in dB) can be corrected as:

$$\tilde{Z}_{dr,e}(r) = Z_{dr,m}(r) + \tilde{\beta}(\Phi_{dp}(r) - \Phi_{dp}(0)) \quad (2.45)$$

where the notation ‘ $\tilde{}$ ’ denotes the estimated quantities.

Smyth and Illingworth (1998) proposed that the true Z_{dr} at the edge of the rain cell is 0 dB because the shape of the raindrops is spherical there in light drizzle conditions. Based on this assumption, they proposed to estimate β as:

$$\Delta Z_{dr}(r_m) = Z_{dr,m}(r_m) - Z_{dr,e}(r_m) \quad (2.46a)$$

$$= Z_{dr,m}(r_m) - 0 \quad (2.46b)$$

$$= -\beta(\Phi_{dp}(r_m) - \Phi_{dp}(0)) \quad (2.46c)$$

$$\tilde{\beta} = \frac{-Z_{dr,m}(r_m)}{\Phi_{dp}(r_m) - \Phi_{dp}(0)} \quad (2.46d)$$

However, there is no guarantee that such region exists in a radar range profile for the 0 dB assumption to be valid. In such case that this 0 dB assumption cannot be established, the true Z_{dr} should be estimated by other means. Bringi et al. (2001) proposed to estimate the true Z_{dr} using a linear Z_h - Z_{dr} (linear when Z_h is in dBZ and Z_{dr} in dB) relationship with the true Z_h estimated first with the self-consistent method discussed in section 2.4. After the true Z_{dr} is estimated in this way, the β can be estimated as:

$$\tilde{\beta} = \frac{\tilde{Z}_{dr,e} - Z_{dr,m}(r_m)}{\Phi_{dp}(r_m) - \Phi_{dp}(0)} \quad (2.47)$$

where $\tilde{Z}_{dr,e}$ is the estimated true Z_{dr} by using the linear Z_h - Z_{dr} relationship.

They also proposed to retrieve a ‘high-resolution’ version of A_{dp} (as opposed to filtering the Φ_{dp} and get K_{dp} which is smoothed along the range) as:

$$\tilde{A}_{dp}(r) = \tilde{\beta} \tilde{K}_{dp}(r) \quad (2.48a)$$

$$= \tilde{\beta} \cdot \frac{\tilde{A}_h(r)}{\tilde{\alpha}} \quad (2.48b)$$

where $\tilde{\beta}$ is estimated from eq. (2.47), $\tilde{\alpha}$ and \tilde{A}_h are estimated from the self-consistent method discussed in section 2.4.

2.6 Related work on attenuation correction for mixed-phase region

The previous sections 2.4 and 2.5 describe primarily the existing techniques for correction of the Z_h and Z_{dr} for the A_h and A_{dp} , respectively, in the rain medium. It is common that other precipitating particles than rain drops, such as graupel or hail can coexist with rain, especially in a deep convective storms. These particles will also cause attenuation on the electromagnetic radiation by the radar. In such event, because the particles are in different thermodynamic phases, sometimes even in the transition between the solid phase to the liquid (mixed-phase), the attenuation is more difficult to estimate. The attenuation due mixed-phase particles can be significant. Bringi et al. (1984) used a differential reflectivity radar to detect hails. There are attempts to avoid the region where the attenuation may be a problem using a polarization diversity and dual-

wavelength radar (Barge and Humphries (1980)) and to correct for the total attenuation using a dual-wavelength radar (Tuttle and Rinehart (1983)). However, there have been less attempts to separately estimate the rain and the wet-ice attenuation. Such separation can resolve the mixed-phase zone in deep convection.

3 OPTIMAL ESTIMATION OF RAIN ATTENUATION AND CORRECTION OF REFLECTIVITY

We have reviewed several correction (estimation) techniques for attenuation at h -polarization in rain in section 2.4. In this chapter, we primarily consider the aspects that can improve the accuracy of the A_h estimation and its computational efficiency. A general mathematical framework for the improved technique will be presented. The implementation of the improved technique has been tested on simulated data and real data collected by the MPX dual-polarized Doppler radar. The implementation of this technique has been running in real time in the CASA IP1 dual-polarized Doppler radar network. Both the simulation results and the results using radar data will be presented here.

3.1 Mathematical considerations for modeling the attenuation

In section 2.4 it was shown that the attenuation can be formulated as functions of radar measurables, such as the measured reflectivity and the differential propagation phase in addition to parameterized relations in eqs. (2.35) and (2.37). Therefore, the accuracy of the estimation of attenuation mainly depends on three factors: the accuracy of the form of the function in representing the attenuation, the accuracy of parameters in the function, and the accuracy and precision of the measurement data.

Recall from chapter 2 that there are basically two forms to estimate the attenuation: the power law form as a function of the true reflectivity (eq. (2.35)) and the linear form as a

function of the specific differential phase (eq. (2.37)). The underlying physics in using the power law form is that (a) the extinction cross section which is responsible for the attenuation, and the back-scatter cross section which is responsible for the reflectivity can both be approximated as power law functions of the drop diameter under the Rayleigh scattering approximation (Bringi and Chandrasekar (2001)); (b) the DSD can be approximated with an exponential distribution or a gamma distribution so that the power law form is retained when both the extinction cross section and the back-scatter cross section are summed over all the particles inside the radar resolution cell (Ulbrich (1983)). The above two approximations are applicable to the rain medium for frequencies at and below X-band.

The underlying physics in using the linear form is that (a) the specific differential propagation phase is a function of the rainwater content and the mass-weighted mean diameter of the rain drops (Bringi et al. (2001)); (b) the extinction cross section is approximately the same DSD moment (4th moment) as the specific differential propagation phase (Bringi and Chandrasekar (2001)).

Although the physical justifications of using the power law and the linear functions are valid, the actual values of the parameters (in particular, a and α) used in the corresponding functions are not constant but sensitive to many factors such as the DSD, the drop shape, the operating frequency of the radar, and the drop temperature (dielectric constant). It is important to estimate them accurately for the platform and conditions in which they are used. In addition, the ability to cope with noise in the measurement data is

also an important factor to be considered.

3.2 Parameter estimation

For our discussion, the power law function (eq. (2.35)) and the linear function (eq. (2.37)) are given here again as:

$$A_h(r) = aZ_{h,e}^b(r) \quad (3.1)$$

$$A_h(r) = \alpha K_{dp}(r) \quad (3.2)$$

If the radar variables A_h , $Z_{h,e}$, and K_{dp} are known, the parameters a , b , and α can be computed directly (i.e., for a and b in eq. (3.1) we need two linearly independent pairs of $(A_h, Z_{h,e})$ and for α in eq. (3.2) we need only one pair of (A_h, K_{dp})). This is considered one-point estimation in which large error can exist because its ability to cope with noise and natural variance in the data is poor.

From scattering theory, we can compute all the radar variables (e.g., A_h , $Z_{h,e}$, K_{dp} , and Z_{dr} , etc.) if the state variables of the radar and the precipitation are known. In particular, the operating frequency of the radar, the type of the precipitation, the DSD, the shape, the canting angle distribution, and the temperature are sufficient to determine values of the radar variables. With the state variables given we can compute the values of the radar variables using T-matrix technique (Barber and Hill (1990)).

For a given operating frequency and a given precipitation type, the DSD, the drop shape, and the temperature are the state variables that are most likely to change. In order to cope with the natural variation in the state variables, it is necessary to vary them for the applicable platform and conditions and generate sufficiently many of A_h , $Z_{h,e}$, and K_{dp} values for the parameter estimation. With sufficiently many realizations of the three radar variables, eq. (3.1) and eq. (3.2) become over-determined. In this case, we can use linear least-squares fitting on each of the equations (for eq. (3.1) we can take log on both sides first) to estimate the parameters. Note that the estimation is obtained only for given sets of state variables, which are subsets of all possible combinations of the state variables.

However in reality we seldom know *a priori* the specific subset of state variables for the current conditions. Therefore, it is desirable to seek and formulate an instantaneous estimation scheme based on the actual measurement data instead of the *a priori* computation based on given values of the state variables. Notice that by equating the right side of eq. (3.1) and eq. (3.2) we have:

$$K_{dp}(r) = \frac{\alpha}{\alpha} Z_{h,e}^b(r) \quad (3.3 a)$$

$$= \kappa Z_{h,e}^b(r) \quad (3.3 b)$$

where κ is the coefficient in the K_{dp} - $Z_{h,e}$ relationship.

We state that eq. (3.3) is the consistency between the K_{dp} and $Z_{h,e}$ in the rain medium in which they result in the same amount of specific attenuation. Therefore, it is clear that the task of the instantaneous estimation is to estimate A_h from which the $Z_{h,e}$ is corrected and

is consistent with the K_{dp} as in eq. (3.3).

3.2.1 Basic form

Consider vectors of measurement data of $Z_{h,m}$, K_{dp} (strictly speaking K_{dp} is a ‘derived’ quantity from measurement of Φ_{dp}). We have $Z_{h,m} \in \mathbb{R}^N$ and $K_{dp} \in \mathbb{R}^N$, where N is the maximum gate number. At the radar receiver, discrete digital voltage is sampled from the continuous received voltage after a pulse is transmitted and processed into $Z_{h,m}$, Φ_{dp} , and K_{dp} data at each resolution cell along the range. The range resolution is given as Δr . Here, we allow the parameters associated with eq. (3.1), eq. (3.2) and eq. (3.3) to vary with range and generalize them to vectors, i.e., now $\vec{a} \in \mathbb{R}^N$, $\vec{b} \in \mathbb{R}^N$, $\vec{\alpha} \in \mathbb{R}^N$, and $\vec{\kappa} \in \mathbb{R}^N$. These vectors form the parameter space $(\vec{a}, \vec{b}, \vec{\alpha}, \vec{\kappa})$. Note that the dimension of parameter space is only $3 \times N$ (instead of $4 \times N$) because $\kappa = \frac{a}{\alpha}$.

Without loss of generality, we assume that the rain cell is encountered at gate 1 and ends at gate N . Initially, we have (for our discussion the h polarization subscript will be dropped here but is kept in mind):

$$\tilde{Z}_e[1] = Z_m[1] \tag{3.4 a}$$

$$\tilde{A}[1] = a[1] \tilde{Z}_e[1]^{b[1]} \tag{3.4 b}$$

$$\tilde{K}_{dp}[1] = \frac{\tilde{A}[1]}{\alpha[1]} \tag{3.4 c}$$

$$= \frac{a[1]}{\alpha[1]} \cdot \tilde{Z}_e[1]^{b[1]} \quad (3.4d)$$

$$= \kappa[1] \tilde{Z}_e[1]^{b[1]} \quad (3.4e)$$

$$P\tilde{I}A[1] = \tilde{A}[1] \cdot \Delta r \quad (3.4f)$$

$$\tilde{\Phi}_{dp}[1] = \tilde{K}_{dp}[1] \cdot \Delta r \quad (3.4g)$$

where the notation ‘ $\tilde{}$ ’ denotes the modeled (or estimated) values.

With the initialization using eq (3.4), the rest of the sequence ($i \in \mathbb{Z}$ and $i \in [2, N]$) of the modeled radar observables can be generated in the following order:

$$\tilde{Z}_e[i] = Z_m[i] \cdot 10^{0.2P\tilde{I}A[i-1]} \quad (3.5a)$$

$$\tilde{A}[i] = a[i] \tilde{Z}_e[i]^{b[i]} \quad (3.5b)$$

$$\tilde{K}_{dp}[i] = \kappa[i] \tilde{Z}_e[i]^{b[i]} \quad (3.5c)$$

$$P\tilde{I}A[i] = P\tilde{I}A[i-1] + \tilde{A}[i] \cdot \Delta r \quad (3.5d)$$

$$\tilde{\Phi}_{dp}[i] = \tilde{\Phi}_{dp}[i-1] + \tilde{K}_{dp}[i] \cdot \Delta r \quad (3.5e)$$

It can be seen that if we know all the parameters precisely then each modeled radar observable can be derived. However, *a priori* information of the parameters is hard to obtain very precisely. By coupling the modeled K_{dp} and Z_e based on the consistency discussed in the previous chapter, we derived the modeled Φ_{dp} (as in eq. (3.5e)) which can be matched to the measured Φ_{dp} . Hence, we here define a vector function $\tilde{f}(\vec{a}, \vec{b}, \vec{\alpha})$

$\in \mathbb{R}^{3N} \rightarrow \mathbb{R}^N$ as the difference between the measured Φ_{dp} ($\Phi_{dp}[i]$) and the modeled (estimated) Φ_{dp} ($\tilde{\Phi}_{dp}[i]$). The i^{th} element of $\vec{f}(\bar{a}, \bar{b}, \bar{\alpha})$ is described by:

$$f[i] = \Phi_{dp}[i] - \tilde{\Phi}_{dp}[i] \quad (3.6)$$

where $\tilde{\Phi}_{dp}[i]$ is estimated from eq. (3.4g) and eq. (3.5e). Note that the parameters $(\bar{a}, \bar{b}, \bar{\alpha}, \bar{\kappa})$ are implicit in the expressions.

In principle, the estimation of the parameters in the parameter space $(\bar{a}, \bar{b}, \bar{\alpha}, \bar{\kappa})$ can be obtained by minimizing $\vec{f}(\bar{a}, \bar{b}, \bar{\alpha})$ in a least-squares sense using a cost function defined as follows:

$$F = \frac{1}{2} \sum_{i=1}^N (f[i])^2 = \frac{1}{2} \vec{f}^T \cdot \vec{f} = \frac{1}{2} \|\vec{f}\|^2 \quad (3.7)$$

where $F \in \mathbb{R}^N \rightarrow \mathbb{R}$.

The estimation is the solution in the parameter space such that the following equation is satisfied:

$$(\tilde{\bar{a}}, \tilde{\bar{b}}, \tilde{\bar{\alpha}}, \tilde{\bar{\kappa}}) = \arg \min_{(\bar{a}, \bar{b}, \bar{\alpha}, \bar{\kappa})} (F) \quad (3.8)$$

3.2.2 Form using constraint on the Hitschfeld and Bordan method

A particular form of the true reflectivity estimation is given in eq. (2.36), which is the Hitschfeld and Bordan method. As discussed in section 2.4, a constraint on the total PIA can be used to make the method stable. Consider if the PIA at the end of the radar beam is known from some other source, we have from eq. (2.37) (also, see appendix A):

$$Z_e(r_N) = Z_m(r_N)(1 - 0.46ab \int_{r_l}^{r_N} Z_m^b(s) ds)^{\frac{1}{b}} \quad (3.9a)$$

$$= Z_m(r_N)10^{0.2PIA(r_N)} \quad (3.9b)$$

where r_l is the range at which the rain cell is encountered and r_N is the range at which the rain cell ends. Note that without loss of generality, the lower limit of the integral is changed from 0 to r_l because any previous PIA caused by any rain cells before r_l can be separated from eq. (3.9a) (see appendix A).

Solving eq. (3.9) for the parameter a we have (by equating eq. (3.9a) and eq. (3.9b)):

$$a = \frac{1 - 10^{-0.2bPIA(r_N)}}{0.46b \int_{r_l}^{r_N} Z_m^b(s) ds} \quad (3.10)$$

The $PIA(r_N)$ can be determined from several sources depending on the platform: (a) from a rain gauge by converting ground rain rate to the true reflectivity (Hitschfeld and Bordan (1954)) for a singly-polarized radar; (b) from the surface reference by taking difference between the back-scattered cross section of the earth surface in rain and no-rain region

for a space-borne radar (Iguchi et al. 2000); (c) from Φ_{dp} by converting Φ_{dp} to PIA (Bringi et al. (1990)) for a dual-polarized radar.

In case (c) , the $PIA(r_N)$ can be converted by (recall eq. (3.2), eq (2.27) and eq. (2.28)):

$$P\tilde{I}A(r_N) = \alpha \cdot \frac{\Phi_{dp}(r_N) - \Phi_{dp}(r_1)}{2} \quad (3.11)$$

Substitute eq. (3.11) into eq. (3.10) we have an estimate of the parameter a as:

$$\tilde{a} = \frac{1 - 10^{-0.1b\alpha(\Phi_{dp}(r_N) - \Phi_{dp}(r_1))}}{0.46b \int_1^N Z_m^b(s) ds} \quad (3.12)$$

Substitute eq. (3.12) into eq. (3.9a), the true reflectivity at range $[r_1 \dots r_N]$ is estimated as:

$$\tilde{Z}_e(r_i) = Z_m(r_i) (1 - 0.46\tilde{a}b \int_1^i Z_m^b(s) ds)^{\frac{1}{b}} \quad (3.13a)$$

$$= Z_m(r_i) \left(1 - \frac{\int_1^i Z_m^b(s) ds}{\int_1^N Z_m^b(s) ds} \cdot (1 - 10^{-0.1b\alpha(\Phi_{dp}(r_N) - \Phi_{dp}(r_1))})\right)^{\frac{1}{b}} \quad (3.13b)$$

From eq. (3.13b), the PIA at range $[r_1 \dots r_N]$ is estimated as:

$$P\tilde{I}A(r_i) = -\frac{5}{b} \log_{10} \left\{ 1 - \frac{\int_{r_1}^{r_i} Z_m^b(s) ds}{\int_{r_1}^{r_N} Z_m^b(s) ds} \cdot (1 - 10^{-0.1b\alpha(\Phi_{dp}(r_N) - \Phi_{dp}(r_i))}) \right\} \quad (3.14)$$

Finally, using eq. (3.1) the specific attenuation at range $[r_1 \dots r_N]$ is estimated as:

$$\tilde{A}(r_i) = \tilde{a} \tilde{Z}_e^b(r_i) \quad (3.15a)$$

$$= \frac{1 - 10^{-0.1b\alpha(\Phi_{dp}(r_N) - \Phi_{dp}(r_i))}}{0.46b \int_{r_1}^{r_N} Z_m^b(s) ds} \cdot \tilde{Z}_e^b(r_i) \quad (3.15b)$$

$$= \frac{Z_m^b(r_i)(1 - 10^{-0.1b\alpha(\Phi_{dp}(r_N) - \Phi_{dp}(r_i))})}{0.46b \int_{r_1}^{r_N} Z_m^b(s) ds - (1 - 10^{-0.1b\alpha(\Phi_{dp}(r_N) - \Phi_{dp}(r_i))}) \cdot 0.46b \int_{r_1}^{r_i} Z_m^b(s) ds} \quad (3.15c)$$

It shall be noted that although the solution (eq. (3.15c)) for the specific attenuation is the same as the solution of Testud et al (2000) (eq. (2.39) and eq. (2.40)), the derivation here is from a completely different angle. Eq. (3.15c) is given here only for completeness and is not needed in computing the specific attenuation. It is obvious that before reaching eq. (3.15c), the specific attenuation can already be retrieved from eq. (3.15a) with the estimated \tilde{a} (from eq. (3.12)), b (given as a constant) and the estimated \tilde{Z}_e (from eq. (3.13b)). Also to be noted that for the purpose of solely estimating Z_e (i.e., attenuation correction), eq. (3.13b) is sufficient.

It is clear that the parametric model as in eq. (3.14) of the path-integrated attenuation is independent of the potential system offset in the measured reflectivity as the offset is

cancelled out in the calculation. This feature is also applicable to the specific attenuation estimated by eq. (3.15). Such feature is desirable because the attenuation-correction procedure can be made independent of the system calibration procedure.

3.2.3 Trade-off studies and our finalized form

In section 3.2.1 and section 3.2.2 we presented two frameworks for estimation of attenuation and correction for the reflectivity, without explicitly knowing the DSD at each radar resolution volume (or, equivalently, range gate).

In the basic form presented in section 3.2.1, we give the most freedom to the parameterization because we allow each parameter to vary with range (similar to estimating the DSD at each range gate). This however, should be considered again more carefully in terms of two issues: under-determined and computational stability.

We will address the computational stability later in section 3.2.5. Here we will discuss the under-determined issue. This can be seen easily because there are not enough constraints to give a unique solution for eq. (3.8). In fact, we have N equations from eq. (3.6) but we need to solve them for at least $3N$ unknowns (recall eq. (3.5)). The solutions are under-determined. Moreover, it is not realistic to retrieve the parameters independently for each gate because noise is inevitably in the measurement data. The under-determined solution tends to over-fit the measured Φ_{dp} and follows the undesired trend of the noise in our simulation (not shown here). After all, only the solution that results valid attenuation

estimation (one that at least does not contradict with physical observations, e.g., attenuation should never be negative) should be used to correct the reflectivity for attenuation. Therefore, the dimensions of the parameter space should be reduced to resolve the under-determined issue. Hogan (2007) proposed a technique to lower the dimensions of the parameter space by resolution (in range) inter-conversion between the lower dimensional parameter space and the higher dimensional data space.

In addition to lower the dimension of each parameter, reducing the number of the parameters should be also considered. As discussed in section 3.1, the parameters can be derived if actual DSD, drop shape and temperature are known. Using scattering simulations the parameter b at X-band has been shown to be 0.78 by Park et al. (2005) for the gamma DSD. Moreover, Testud et al. (2000) have shown that the exponent b is independent of μ (the shape parameter of the gamma DSD). It has been also reported that there is only very moderate variation in b for a given frequency and temperature (Tuttle and Rinehart (1983)). Therefore, we can specify b as a known constant and remove it from the parameterization.

Having taken an opposite approach to estimating parameters at every gate, in section 3.2.2 we derived eqs. (3.13), (3.14), and (3.15) with the parameter space significantly reduced. The parameter b is given (e.g., 0.78), the parameter a is assumed to be an unknown constant at every gate and is tied to the parameter α through eq. (3.12). The parameter α is the only parameter that remains to be estimated using the least squares minimization. With these assumptions the form of the estimation is greatly simplified, by

which we gain insights into the dependency of the parameters on one and another in the estimators for the true reflectivity, the PIA , and the specific attenuation (see eqs. (3.13), (3.14), and (3.15)).

To estimate the parameter α using the measurement data, we should also invoke the consistency between the K_{dp} and $Z_{h,e}$ in the rain medium defined in eq. (3.3). Since a is already estimated through eq. (3.12), which is a function of the parameter α , the estimation problem is further reduced to only one-dimensional problem. It is amazing that the parameter space can be simplified from (a, b, α, κ) to α for the rain medium with the $PIA(r_N)$ converted from Φ_{dp} and other constraints based on scattering simulations. Here we select the parameterization form introduced in section 3.2.2 as our finalized parameterization form. The relationships of the parameters are summarized here for completeness as:

$$a = g(\alpha) = \frac{1 - 10^{-0.1b\alpha(\Phi_{dp}(r_N) - \Phi_{dp}(r_1))}}{0.46b \int_{r_1}^{r_N} Z_m^b(s) ds} \quad (3.16a)$$

$$b = 0.78 \quad (3.16b)$$

$$\kappa = \frac{a}{\alpha} = \frac{g(\alpha)}{\alpha} \quad (3.16c)$$

Therefore, the objective of the estimation of α is to compute the optimal value of κ such that the consistency is satisfied at every range gate. It is obvious that in the presence of the measurement noise the consistency can be satisfied in a least squares sense (or

other metric such as the absolute norm, see eq. (2.41), Bringi et al. (2001)). The least-squares solution can be obtained by minimizing the cost function defined in eq. (3.7). However, now the vector function \bar{f} in eq. (3.7) can be expressed explicitly without the induction procedure shown in eqs. (3.4) and (3.5) because the estimated $\tilde{\Phi}_{dp}[i]$ is directly calculable by eq. (3.14) as:

$$\tilde{\Phi}_{dp}[i] = \frac{2P\tilde{I}A[i]}{\alpha} + \Phi_{dp}[1] \quad (3.17a)$$

$$= \frac{10}{\alpha} \log_{10} \left\{ \left(1 - \frac{\sum_{s=1}^i Z_m^b[s] \Delta r}{\sum_{s=1}^N Z_m^b[s] \Delta r} \cdot \left(1 - 10^{-0.1b\alpha(\Phi_{dp}[N] - \Phi_{dp}[1])} \right) \right)^{-\frac{1}{b}} \right\} + \Phi_{dp}[1] \quad (3.17b)$$

Note that the variables now are presented in vector forms.

For completeness, the cost function is given here again as:

$$F = \frac{1}{2} \sum_{i=1}^N (f[i])^2 = \frac{1}{2} \bar{f}^T \cdot \bar{f} = \frac{1}{2} \|\bar{f}\|^2 \quad (3.18a)$$

where

$$f[i] = \Phi_{dp}[i] - \tilde{\Phi}_{dp}[i] \quad (3.18b)$$

where $\tilde{\Phi}_{dp}[i]$ is defined in eq. (3.17) and $\Phi_{dp}[i]$ is the measurement data of differential propagation phase. Note that the parameter α is implicit in $\tilde{\Phi}_{dp}[i]$ and hence \bar{f} . Also note that although we are using the same $\tilde{\Phi}_{dp}[i]$, \bar{f} , and F notations, they are different functions (constructed differently) than the ones defined by eqs. (3.5), (3.6) and (3.7).

The estimation of $\tilde{\alpha}$ is given here as:

$$\tilde{\alpha} = \arg \min_{\alpha}(F) \tag{3.19}$$

As we can see, the minimization is reduced to only estimate one scalar parameter, namely, the α .

Using the estimated $\tilde{\alpha}$, the corrected reflectivity (Z_e) at every range gate can be readily calculated from eq. (3.13b). The specific attenuation (A) follows immediately using eq. (3.15a) with the estimated $\tilde{\alpha}$ and \tilde{Z}_e .

3.2.4 Minimization scheme

There are many techniques available to solve the least-squares minimization problem described by eq. (3.7) or eq. (3.18) (e.g., Chong and Zak (2001)). In particular, the steepest decent, Newton's method, the Gauss-Newton method, and the Levenberg-Marquardt method (Levenberg (1944), Marquardt (1963)) are popular techniques for the problem. In this section, we will briefly review some of the aforementioned minimization techniques, in particular, the Newton's method, the Gauss-Newton method, and the Levenberg-Marquardt method. The intent here is to describe a general methodology for least-squares minimization without particularly referring to the model of estimating the attenuation. This linkage will be described later at the end of this section.

In general, we are interested in a real function $f(x_1, x_2, \dots, x_M)$ which is parameterized with M unknown real parameters, i.e., x_1, x_2, \dots, x_M . This function maps the M -dimensional parameter space onto the real line. The mapping describes a relationship between the known input (implicit in $f(\cdot)$) and the known outcome (also implicit in $f(\cdot)$). If we have more than one input-outcome pair, we will have N real functions, i.e., f_1, f_2, \dots, f_N (e.g., as in eq. (3.18b)) that all use x_1, x_2, \dots, x_M as parameters. We define the M -dimensional parameter vector as:

$$\bar{x} = \begin{bmatrix} x_1 \\ x_2 \\ \vdots \\ x_M \end{bmatrix}$$

where $\bar{x} \in \mathbb{R}^M$, and the N -dimensional vector function as:

$$\vec{f}(\bar{x}) = \begin{bmatrix} f_1(x_1, x_2, \dots, x_M) \\ f_2(x_1, x_2, \dots, x_M) \\ \vdots \\ f_N(x_1, x_2, \dots, x_M) \end{bmatrix} = \begin{bmatrix} f_1(\bar{x}) \\ f_2(\bar{x}) \\ \vdots \\ f_N(\bar{x}) \end{bmatrix}$$

where $\vec{f}(\bar{x}) \in \mathbb{R}^M \rightarrow \mathbb{R}^N$. Note that the arrow on top of a notation denotes a column vector.

We further define a cost (also known as ‘objective’) function as:

$$F(\bar{x}) = \frac{1}{2} \|f(\bar{x})\|^2$$

where $\|\cdot\|$ denotes the 2-norm of a vector.

The objective of the least-squares minimization is to derive a parameter vector $\tilde{\bar{x}}$ (from all the possible \bar{x} in the M-dimensional parameter space) such that the cost function $F(\bar{x})$ is minimized. This can be described as:

$$F(\tilde{\bar{x}}) = \min F(\bar{x}), \quad \bar{x} \in \mathbb{R}^M \tag{3.20}$$

where $\tilde{\bar{x}}$ is the desired parameter vector that minimize $F(\bar{x})$ in a least-squares sense (thus the name of the least-squares minimization).

In general, the least-squares minimization is difficult. Here we are interested in finding $\tilde{\bar{x}}$ over a local region of \bar{x} which leads to solving a less difficult problem. If the desired parameter vector $\tilde{\bar{x}}$ is an interior point in the local region, we have the necessary condition for $\tilde{\bar{x}}$ to be the solution of eq. (3.20) as:

$$\bar{F}'(\tilde{\bar{x}}) = \left. \frac{dF(\bar{x})}{d\bar{x}} \right|_{\bar{x}=\tilde{\bar{x}}} = \bar{0} \tag{3.21}$$

Note that the gradient, $\bar{F}'(\bar{x})$ is a vector having same dimensions as \bar{x} and $\bar{0}$ is a vector with all elements having 0 value.

To reach the minimum point $\tilde{\bar{x}}$ from an arbitrary initial point \bar{x} , we need to find the

feasible direction and the distance to $\tilde{\bar{x}}$. This is equivalent to finding a vector \bar{h} such that when \bar{x} is updated with \bar{h} , we reach $\tilde{\bar{x}}$ as :

$$F(\bar{x} + \bar{h}) = F(\tilde{\bar{x}}) \quad (3.22)$$

To find \bar{h} , we will use eq. (3.21). Expand $F(\bar{x} + \bar{h})$ at \bar{x} by Taylor expansion we have:

$$\bar{F}'(\tilde{\bar{x}}) = \bar{F}'(\bar{x} + \bar{h}) \quad (3.23a)$$

$$= \bar{F}'(\bar{x}) + \mathbf{F}''(\bar{x})\bar{h} + O(\|\bar{h}\|^2) \quad (3.23b)$$

where $O(\cdot)$ denotes the ‘order of’. Note that the bold typed notation denotes a matrix.

Since $\bar{F}'(\tilde{\bar{x}}) = \bar{0}$, by omitting the higher order terms we have:

$$\bar{F}'(\bar{x}) + \mathbf{F}''(\bar{x})\bar{h} = \bar{0} \quad (3.24a)$$

$$\mathbf{F}''(\bar{x})\bar{h} = -\bar{F}'(\bar{x}) \quad (3.24b)$$

The gradient $\bar{F}'(\bar{x})$ can be derived as:

$$\bar{F}'(\bar{x}) = \frac{dF(\bar{x})}{d\bar{x}} \quad (3.25a)$$

$$= \begin{bmatrix} \frac{\partial F(\bar{x})}{\partial x_1} \\ \frac{\partial F(\bar{x})}{\partial x_2} \\ \cdot \\ \cdot \\ \frac{\partial F(\bar{x})}{\partial x_M} \end{bmatrix} = \begin{bmatrix} \frac{\partial \frac{1}{2} \sum_{i=1}^N f_i^2(\bar{x})}{\partial x_1} \\ \frac{\partial \frac{1}{2} \sum_{i=1}^N f_i^2(\bar{x})}{\partial x_2} \\ \cdot \\ \cdot \\ \frac{\partial \frac{1}{2} \sum_{i=1}^N f_i^2(\bar{x})}{\partial x_M} \end{bmatrix} = \begin{bmatrix} \sum_{i=1}^N f_i(\bar{x}) \frac{\partial f_i(\bar{x})}{\partial x_1} \\ \sum_{i=1}^N f_i(\bar{x}) \frac{\partial f_i(\bar{x})}{\partial x_2} \\ \cdot \\ \cdot \\ \sum_{i=1}^N f_i(\bar{x}) \frac{\partial f_i(\bar{x})}{\partial x_M} \end{bmatrix} \quad (3.25b)$$

$$= \begin{bmatrix} \frac{\partial f_1(\bar{x})}{\partial x_1} & \frac{\partial f_2(\bar{x})}{\partial x_1} & \dots & \frac{\partial f_N(\bar{x})}{\partial x_1} \\ \frac{\partial f_1(\bar{x})}{\partial x_2} & \frac{\partial f_2(\bar{x})}{\partial x_2} & \dots & \frac{\partial f_N(\bar{x})}{\partial x_2} \\ \cdot & \dots & \dots & \cdot \\ \cdot & \dots & \dots & \cdot \\ \frac{\partial f_1(\bar{x})}{\partial x_M} & \frac{\partial f_2(\bar{x})}{\partial x_M} & \dots & \frac{\partial f_N(\bar{x})}{\partial x_M} \end{bmatrix} \begin{bmatrix} f_1(\bar{x}) \\ f_2(\bar{x}) \\ \cdot \\ \cdot \\ f_N(\bar{x}) \end{bmatrix} \quad (3.25c)$$

$$= \mathbf{J}(\bar{x})^T \vec{f}(\bar{x}) \quad (3.25d)$$

where $\mathbf{J}(\bar{x})$ is the Jacobian of $\vec{f}(\bar{x})$ defined as:

$$\mathbf{J}(\bar{x}) = \frac{d\vec{f}(\bar{x})}{d\bar{x}} = \mathbf{f}'(\bar{x}) = \begin{bmatrix} \frac{\partial f_1(\bar{x})}{\partial x_1} & \frac{\partial f_2(\bar{x})}{\partial x_1} & \dots & \frac{\partial f_N(\bar{x})}{\partial x_1} \\ \frac{\partial f_1(\bar{x})}{\partial x_2} & \frac{\partial f_2(\bar{x})}{\partial x_2} & \dots & \frac{\partial f_N(\bar{x})}{\partial x_2} \\ \cdot & \dots & \dots & \cdot \\ \cdot & \dots & \dots & \cdot \\ \cdot & \dots & \dots & \cdot \\ \frac{\partial f_1(\bar{x})}{\partial x_M} & \frac{\partial f_2(\bar{x})}{\partial x_M} & \dots & \frac{\partial f_N(\bar{x})}{\partial x_M} \end{bmatrix}^T \quad (3.26)$$

The matrix $\mathbf{F}''(\bar{x})$ in eq. (3.24) is the Hessian of $F(\bar{x})$ defined as:

$$\mathbf{F}''(\bar{x}) = \frac{d\bar{F}'(\bar{x})}{d\bar{x}} \quad (3.27a)$$

$$= d \begin{bmatrix} \frac{\partial F(\bar{x})}{\partial x_1} \\ \frac{\partial F(\bar{x})}{\partial x_2} \\ \cdot \\ \cdot \\ \frac{\partial F(\bar{x})}{\partial x_M} \end{bmatrix} / d\bar{x} = \begin{bmatrix} \frac{\partial^2 F(\bar{x})}{\partial x_1^2} & \frac{\partial^2 F(\bar{x})}{\partial x_1 \partial x_2} & \cdots & \frac{\partial^2 F(\bar{x})}{\partial x_1 \partial x_M} \\ \frac{\partial^2 F(\bar{x})}{\partial x_1 \partial x_2} & \frac{\partial^2 F(\bar{x})}{\partial x_2^2} & \cdots & \frac{\partial^2 F(\bar{x})}{\partial x_2 \partial x_M} \\ \cdot & \cdots & \cdots & \cdot \\ \cdot & \cdots & \cdots & \cdot \\ \frac{\partial^2 F(\bar{x})}{\partial x_1 \partial x_M} & \frac{\partial^2 F(\bar{x})}{\partial x_2 \partial x_M} & \cdots & \frac{\partial^2 F(\bar{x})}{\partial x_M^2} \end{bmatrix} \quad (3.27b)$$

From eq. (3.25b) we can express the elements in the Hessian as:

$$\frac{\partial^2 F(\bar{x})}{\partial x_i \partial x_j} = \frac{\partial \sum_{k=1}^N f_k(\bar{x}) \frac{\partial f_k(\bar{x})}{\partial x_i}}{\partial x_j} \quad (3.28a)$$

$$= \sum_{k=1}^N \frac{\partial f_k(\bar{x})}{\partial x_i} \cdot \frac{\partial f_k(\bar{x})}{\partial x_j} + \sum_{k=1}^N f_k(\bar{x}) \frac{\partial^2 f_k(\bar{x})}{\partial x_i \partial x_j} \quad (3.28b)$$

Therefore, the Hessian can also be expressed as:

$$(\mathbf{F}''(\bar{\mathbf{x}}))_{ij} = \left(\begin{array}{cccc} \left[\begin{array}{ccc} \frac{\partial f_1(\bar{\mathbf{x}})}{\partial x_1} & \frac{\partial f_2(\bar{\mathbf{x}})}{\partial x_1} & \dots & \frac{\partial f_N(\bar{\mathbf{x}})}{\partial x_1} \\ \frac{\partial f_1(\bar{\mathbf{x}})}{\partial x_2} & \frac{\partial f_2(\bar{\mathbf{x}})}{\partial x_2} & \dots & \frac{\partial f_N(\bar{\mathbf{x}})}{\partial x_2} \\ \cdot & \dots & \dots & \cdot \\ \cdot & \dots & \dots & \cdot \\ \cdot & \dots & \dots & \cdot \\ \frac{\partial f_1(\bar{\mathbf{x}})}{\partial x_M} & \frac{\partial f_2(\bar{\mathbf{x}})}{\partial x_M} & \dots & \frac{\partial f_N(\bar{\mathbf{x}})}{\partial x_M} \end{array} \right] \left[\begin{array}{ccc} \frac{\partial f_1(\bar{\mathbf{x}})}{\partial x_1} & \frac{\partial f_2(\bar{\mathbf{x}})}{\partial x_1} & \dots & \frac{\partial f_N(\bar{\mathbf{x}})}{\partial x_1} \\ \frac{\partial f_1(\bar{\mathbf{x}})}{\partial x_2} & \frac{\partial f_2(\bar{\mathbf{x}})}{\partial x_2} & \dots & \frac{\partial f_N(\bar{\mathbf{x}})}{\partial x_2} \\ \cdot & \dots & \dots & \cdot \\ \cdot & \dots & \dots & \cdot \\ \cdot & \dots & \dots & \cdot \\ \frac{\partial f_1(\bar{\mathbf{x}})}{\partial x_M} & \frac{\partial f_2(\bar{\mathbf{x}})}{\partial x_M} & \dots & \frac{\partial f_N(\bar{\mathbf{x}})}{\partial x_M} \end{array} \right]^T \\ + \\ \sum_{k=1}^N f_k(\bar{\mathbf{x}}) \frac{\partial^2 f_k(\bar{\mathbf{x}})}{\partial x_i \partial x_j} \end{array} \right)_{ij} \quad (3.29a)$$

$$= (\mathbf{J}(\bar{\mathbf{x}})^T \mathbf{J}(\bar{\mathbf{x}}))_{ij} + \sum_{k=1}^N f_k(\bar{\mathbf{x}}) \frac{\partial^2 f_k(\bar{\mathbf{x}})}{\partial x_i \partial x_j} \quad (3.29b)$$

It is clear that if we know the Jacobian and Hessian, we are ready to solve the step $\bar{\mathbf{h}}$ using eq. (3.24b). Solving the step this way is well known as Newton's method.

The second partial derivatives in the Hessian (see eq. (3.29)) can be omitted if we make a further approximation of $\bar{f}(\bar{\mathbf{x}} + \bar{\mathbf{h}})$ using Taylor expansion as:

$$\bar{f}(\bar{\mathbf{x}} + \bar{\mathbf{h}}) = \bar{f}(\bar{\mathbf{x}}) + \mathbf{f}'(\bar{\mathbf{x}})\bar{\mathbf{h}} + O(\|\bar{\mathbf{h}}\|^2) \quad (3.30a)$$

$$\bar{t}_{\bar{\mathbf{x}}}(\bar{\mathbf{h}}) = \bar{f}(\bar{\mathbf{x}}) + \mathbf{f}'(\bar{\mathbf{x}})\bar{\mathbf{h}} \approx \bar{f}(\bar{\mathbf{x}} + \bar{\mathbf{h}}) \quad (3.30b)$$

We define a function $T_{\bar{\mathbf{x}}}(\bar{\mathbf{h}})$ to approximate $F(\bar{\mathbf{x}} + \bar{\mathbf{h}})$ as:

$$T_{\bar{x}}(\bar{h}) = \frac{1}{2} \|\bar{t}_{\bar{x}}(\bar{h})\|^2 \approx \frac{1}{2} \|\bar{f}(\bar{x} + \bar{h})\|^2 = F(\bar{x} + \bar{h}) \quad (3.31)$$

Substitute eq. (3.30b) into eq. (3.31), we have:

$$T_{\bar{x}}(\bar{h}) = \frac{1}{2} \|\bar{t}_{\bar{x}}(\bar{h})\|^2 \quad (3.32a)$$

$$= \frac{1}{2} \bar{t}_{\bar{x}}(\bar{h})^T \bar{t}_{\bar{x}}(\bar{h}) \quad (3.32b)$$

$$= \frac{1}{2} (\bar{f}(\bar{x}) + \mathbf{f}'(\bar{x})\bar{h})^T (\bar{f}(\bar{x}) + \mathbf{f}'(\bar{x})\bar{h}) \quad (3.32c)$$

$$= \frac{1}{2} (\bar{f}(\bar{x})^T \bar{f}(\bar{x}) + \bar{f}(\bar{x})^T \mathbf{f}'(\bar{x})\bar{h} + \bar{h}^T \mathbf{f}'(\bar{x})^T \bar{f}(\bar{x}) + \bar{h}^T \mathbf{f}'(\bar{x})^T \mathbf{f}'(\bar{x})\bar{h}) \quad (3.32d)$$

Differentiating with respect to \bar{h} on both sides of eq. (3.32d) we have:

$$\bar{T}'_{\bar{x}}(\bar{h}) = \frac{dT_{\bar{x}}(\bar{h})}{d\bar{h}} \quad (3.33a)$$

$$= \frac{1}{2} (2\mathbf{f}'(\bar{x})^T \bar{f}(\bar{x}) + 2\mathbf{f}'(\bar{x})^T \mathbf{f}'(\bar{x})\bar{h}) \quad (3.33b)$$

$$= \mathbf{J}(\bar{x})^T \bar{f}(\bar{x}) + \mathbf{J}(\bar{x})^T \mathbf{J}(\bar{x})\bar{h} \quad (3.33c)$$

Differentiating with respect to \bar{h} on both sides of eq. (3.31), we have:

$$\bar{T}'_{\bar{x}}(\bar{h}) \approx \bar{F}'(\bar{x} + \bar{h}) = \bar{\mathbf{0}} \quad (3.34)$$

Combining eqs. (3.33c) and (3.34), the \bar{h} can be calculated using:

$$\mathbf{J}(\bar{x})^T \bar{f}(\bar{x}) + \mathbf{J}(\bar{x})^T \mathbf{J}(\bar{x}) \bar{h} = \bar{0} \quad (3.35a)$$

$$\mathbf{J}(\bar{x})^T \mathbf{J}(\bar{x}) \bar{h} = -\mathbf{J}(\bar{x})^T \bar{f}(\bar{x}) \quad (3.35b)$$

The above method is well known as the Gauss-Newton method. Comparing to Newton's method, it is clear that the Hessian on the left side of eq. (3.24b) is reduced to $\mathbf{J}(\bar{x})^T \mathbf{J}(\bar{x})$ by approximation. The Gauss-Newton method converges slower (having quadratic or linear convergence) than Newton's method (having always quadratic convergence) but it does eliminate the calculation of the second partial derivative terms in the Hessian (as in eq. (3.29b)).

The final method we are going to review here is the Levenberg-Marquardt method. This method can be considered as a 'damped' Gauss-Newton method with the following modification to the matrix on the left side of eq (3.35b):

$$(\mathbf{J}(\bar{x})^T \mathbf{J}(\bar{x}) + \mu \mathbf{I}) \bar{h} = -\mathbf{J}(\bar{x})^T \bar{f}(\bar{x}) \quad (3.36)$$

where μ is a non-negative scalar, and \mathbf{I} is the identity matrix.

The advantage of using the Levenberg-Marquardt is that it can be tuned from the steepest descent method (not reviewed here, see Chong and Zak (2001)) by using a large μ in the beginning gradually to the Gauss-Newton method by using a small μ in the end. This feature makes the minimization more robust and efficient, i.e., it begins with a slower but

more accurate minimization method initially and then switches to a faster one when it is approaching the desired parameter vector ($\tilde{\bar{x}}$). The Levenberg-Marquardt method is the method of our choice when we minimize our finalized cost function as described in the previous section.

We now derive the Jacobian for our particular estimation problem which reduces to a 1-dimensional problem with $\bar{x} = [\alpha]$. For our finalized formulation in eq. (3.18b), we give the expression of the elements in the Jacobian as:

$$\frac{\partial f_i}{\partial \alpha} = \frac{\partial \frac{10}{\alpha} \log_{10} \left\{ \left(1 - \frac{\sum_{s=1}^i Z_m^b[s] \Delta r}{N} \cdot (1 - 10^{-0.1b\alpha(\Phi_{dp}[N] - \Phi_{dp}[1])}) \right)^{\frac{1}{b}} \right\}}{\partial \alpha} \quad (3.37a)$$

$$= \frac{10}{\alpha^2} \left\{ \alpha \left(1 - \frac{\sum_{s=1}^i Z_m^b[s] \Delta r}{N} \cdot (1 - 10^{-0.1b\alpha(\Phi_{dp}[N] - \Phi_{dp}[1])}) \right)^{\frac{1}{b}} \cdot \frac{1}{\ln 10} \cdot \left(-\frac{1}{b} \left(1 - \frac{\sum_{s=1}^i Z_m^b[s] \Delta r}{N} \cdot (1 - 10^{-0.1b\alpha(\Phi_{dp}[N] - \Phi_{dp}[1])}) \right)^{\frac{1+b}{b}} \cdot \frac{\sum_{s=1}^i Z_m^b[s] \Delta r}{\sum_{s=1}^i Z_m^b[s] \Delta r} \cdot 10^{-0.1b\alpha(\Phi_{dp}[N] - \Phi_{dp}[1])} \cdot \ln 10 \cdot (-0.1b(\Phi_{dp}[N] - \Phi_{dp}[1])) - \log_{10} \left\{ \left(1 - \frac{\sum_{s=1}^i Z_m^b[s] \Delta r}{N} \cdot (1 - 10^{-0.1b\alpha(\Phi_{dp}[N] - \Phi_{dp}[1])}) \right)^{\frac{1}{b}} \right\} \right\} \quad (3.37b)$$

3.2.5 Stability of the algorithm

We addressed the under-determined issue in the discussion in section 3.2.3. We also pointed out the computational stability issue which we are going to discuss here.

In principle, the minimization scheme presented in section 3.2.4 can also be applied to the basic form described by the induction procedure in eqs. (3.4) and (3.5). For example, if we assume that parameters α and b are known constants (e.g., $\alpha = 0.25$, $b = 0.78$ based on calculation from a subset of state variables for X-band frequencies and rain), and the parameter a does not vary along the range, we can retrieve the parameter a using the similar minimization scheme (but the Jacobian will be different). This is a totally forward-directional procedure. Although the procedure will match theoretically the estimated $\tilde{\Phi}_{dp}$ to the measured Φ_{dp} , the numerical solutions of the estimated $\tilde{\Phi}_{dp}$ in the intermediate steps run into the risk of exceeding the floating point range (double precision) of a general purpose computer. As inherited in the original Hitschfeld and Bordan's method, even small error in the parameter a will cause the algorithm to fail totally. This can be further illustrated by the following equation:

$$PIA(r_i) = -\frac{5}{b} \log_{10} \left\{ 1 - 0.46ab \int_0^r Z_m^b(s) ds \right\} \quad (3.38)$$

It is evident that the stability of the PIA depends on, (a) the parameter a ; (b) length of the rain cell. These two factors could result in the integral exceeding unity and thus invalidate the retrieval of PIA . Based on our example, we were able to estimate the parameter a

consistently if the PIA is less than 10 dB. Otherwise, the calculation of the estimated $\tilde{\Phi}_{dp}$ tends to go beyond the range of floating point numbers (infinite), which fails the minimization process

Using the finalized form, the stability problem is resolved by constraining the final PIA first. As we can see in eq. (3.14), the value inside the logarithm will not become negative because it is guaranteed that the difference of Φ_{dp} is non-negative in rain. This ensures that in estimating the parameter α we will stay in the range of floating numbers.

3.3 Simulation results

It is an impossible task to simulate all possible occurrences of what a radar measures over its propagation path. Our goal of the simulation is to assess the validity of our estimation model discussed in section 3.2.3 and the performance of the minimization scheme discussed in section 3.2.4. The validity of the estimation model will be evaluated by the ability to estimate the ‘true’ values (simulation input) under the conditions and assumptions that the algorithm is developed. The performance of the minimization scheme will be evaluated by the convergence speed. The estimation model and the minimization scheme together are referred to ‘the improved algorithm’ (or simply ‘the algorithm’) from now on. Our simulation here is mainly to test the algorithm and answer the following research questions:

- 1) What is the effect of the assumption of the coefficient (α) in the A - Z relationship

being constant over the propagation path (or equivalently, N_w being constant)?

2) Based on the consistency of K_{dp} -Z defined in eq. (3.3), how well does our model do at estimating the coefficient (α) in the A - K_{dp} relationship when the shape of raindrops, the DSD, or the temperature changes?

3) How well does our model do in an ideal condition without any noise and in a more 'realistic' condition with simulated noise?

In order to answer above questions, we organize our simulations into two main categories: constant DSD profiles and variable DSD profiles. For each category, we further simulate situations where the shape of the raindrops or temperature changes. We also add simulated noise to our input observables.

The simulation is carried out under common state variables as follows:

- a) An operating frequency of 9.3 GHz (X-band);
- b) Range resolution of 100 meters;
- c) A 40 km propagation path filled with rain;
- d) A fixed environmental temperature of 20 °C unless specified otherwise;
- e) A Gaussian canting angle distribution with mean canting angle equal to 0° and standard deviation equal to 5°;
- f) Exponential DSD model (equivalently gamma DSD model with shape parameter (μ) equal to 0).

With the common state variables, and the specified DSD profile and drop shape for each case of the simulation, we generate simulation input which are regarded as ‘true’ values for the following radar observables: the intrinsic reflectivity ($Z_{h,e}$) at h polarization, the specific differential propagation phase (K_{dp}), the specific attenuation (A_h), the differential phase (Φ_{dp} , by integrating K_{dp} along the path), the PIA (by integrating A_h along the path), and the measured reflectivity ($Z_{h,m}$) at h polarization (by subtracting the PIA from the intrinsic $Z_{h,e}$). The algorithm operates on the measured $Z_{h,m}$ and Φ_{dp} only and estimate the intrinsic $Z_{h,e}$, the A_h , and the K_{dp} . They are considered as the output of the algorithm and therefore will be compared with the simulation input for evaluation.

3.3.1 Constant DSD case

The parameters of the exponential DSD are set to constants ($N_v=7409 \text{ mm}^{-1}\text{mm}^{-3}$, $D_0=1.55 \text{ mm}$) over the propagation path. This represents uniform rain for the full path. First we test the algorithm with the drop shape model of Pruppacher and Beard (1970) and then extend the analysis to cover more drop shape models that exist in the literature.

For the specified drop shape model, first we evaluate the algorithm in the ideal situation where there are absolutely no measurement errors in any radar variables. Fig. 3.1 shows the range profile of the intrinsic Z_h , the measured (attenuated) Z_h , and the corrected Z_h (output by the algorithm). Fig. 3.2 shows the intrinsic A_h and estimated A_h . Because the DSD parameters are constant and there are no measurement errors, the range profiles of above intrinsic values appear to be straight lines parallel to the range axis, indicating

uniform rain medium. Also as shown in Fig. 3.3 Φ_{dp} range profile appears to be a slant line with constant slope, indicating constant K_{dp} along the path. Shown in Fig. 3.1, the attenuated Z_h is decreasing along range at a constant slope because of the accumulating attenuation over the path (*PIA*). The output of the algorithm, the corrected Z_h profile matches the simulation input, the intrinsic Z_h well, with a small difference at the end of the beam (about 0.2 dB). The difference is the result of slightly under-estimated A_h profile shown in Fig. 3.2. The difference, however, only account for 0.5% of the intrinsic Z_h , which is small considering the signal propagates over a path of 40 km long.

Fig. 3.3 illustrates the minimization process discussed in section 3.2.4. The minimization achieves convergence after just a few iterations (typically 4 iterations). The reconstructed (estimated) Φ_{dp} profile calculated from the coefficient α_h when converged matches the intrinsic Φ_{dp} profile very well. The optimized parameter α_h (0.19283 dB/deg) that the algorithm estimated as a result of the minimization, is used sequentially to obtain the output shown earlier, i.e., the corrected Z_h (in Fig. 3.1) and the estimated A_h (in Fig. 3.2).

We go on and test the algorithm with some other drop shape models available in the literature, in order to evaluate if the algorithm indeed is able to follow and adapt to the change of the drop shape. The test results are presented using metrics of merit such as mean error and RMSE, and listed in Table (3.1). For the drop shape models we used, the coefficient α_h retrieved by the algorithm ranges from 0.16583 to 0.36707 dB/deg. The range agrees with the calculation based on the simulation input well (not shown here). Such wide range of variation indeed indicates that the possibility of large bias error

introduced by using *a priori* fixed α_h . Table (3.1) shows that the algorithm is indeed able to adjust the coefficient to the change of drop shape based on the measured data only. As we can see in Table (3.1), the mean error and RMSE values show good performance for coefficient retrieval results for all drop shape models studied here. Over the 40 km path, the mean error shows acceptable underestimation about 0.07 dB of Z_h . The RMSE show values that are much smaller than typical measurement errors on Z_h (e.g., 0.8 dBZ).

We consider measurement errors in the next run of the simulation. We assume the attenuated Z_h is now measured by a ‘real’ radar which is subject to noise. To simulate the noisy measured Z_h , we first attenuate the intrinsic Z_h and then add independent white Gaussian noise to each gate. The measured Φ_{dp} is assumed to have additive independent white Gaussian (phase) noise also. The mean of noises for the two measurements are assumed to be all 0. The standard deviation of the noise added to Z_h is assumed to be 0.8 dB, while that for the Φ_{dp} is 3 deg. The parameters of the Gaussian noise model are representative for a typical operational radar.

Following similar analytical steps in earlier analysis, Fig 3.4 and Fig. 3.5 show retrieval results under the specified noisy environment. The same Pruppacher and Beard (1970) drop shape model is used. As we can see with the presence of noise in the measured Z_h , the corrected Z_h and the estimated A_h are also noisy. Nonetheless, the retrievals appear to be free of biases despite the noisy measurements. Also, it is noticeable in Fig. 3.6 that the estimated Φ_{dp} does follow the trend of the true Φ_{dp} in a least-squares sense. This indicates that the parameter α_h can be estimated reliably under the Gaussian noise

condition.

Again, similar metrics of merit are computed and organized in Table (3.2). Compared with Table (3.1) which obtained in the ideal condition without noise, the close values of retrievals of parameter α_h indeed show the algorithm is stable under the simulated noisy condition. The mean error chart shows small but acceptable biases. The RMSE chart does show degrade in performance because of noise. However, recalling the standard deviations of measurement noise of Z_h (0.8 dB), the RMSE chart show that the algorithm will not further degrade the precision of the measurements.

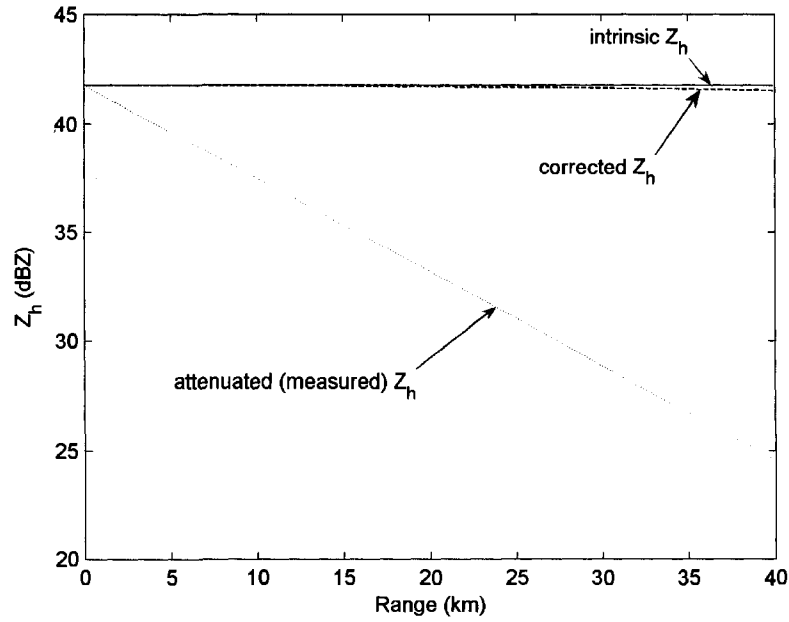


Figure 3.1 Range profiles of the intrinsic Z_h , the attenuated Z_h , and the corrected Z_h . The profiles are based on a constant exponential DSD profile and the Pruppacher and Beard (1970) drop shape model.

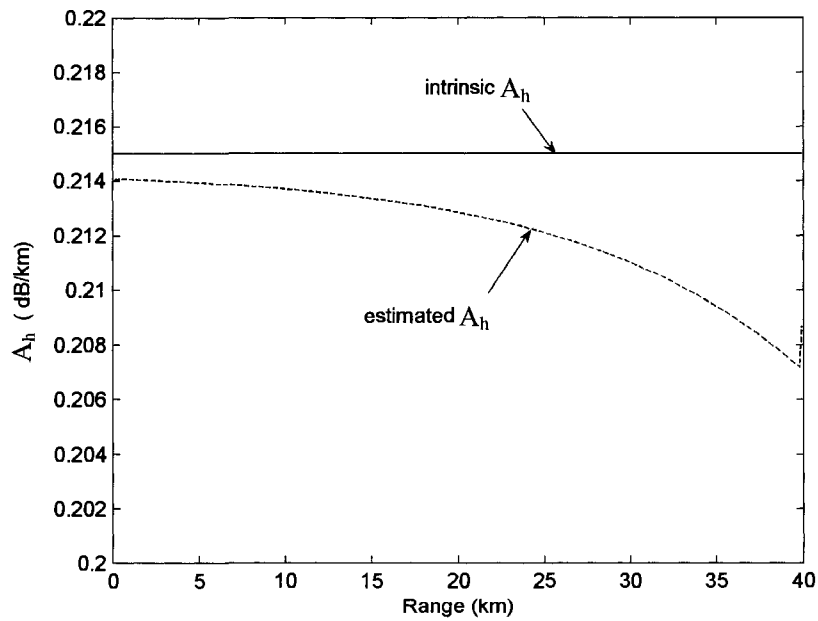


Figure 3.2 Range profiles of the intrinsic A_h and the retrieved A_h . The profiles are based on a constant exponential DSD profile and the Pruppacher and Beard (1970) drop shape model.

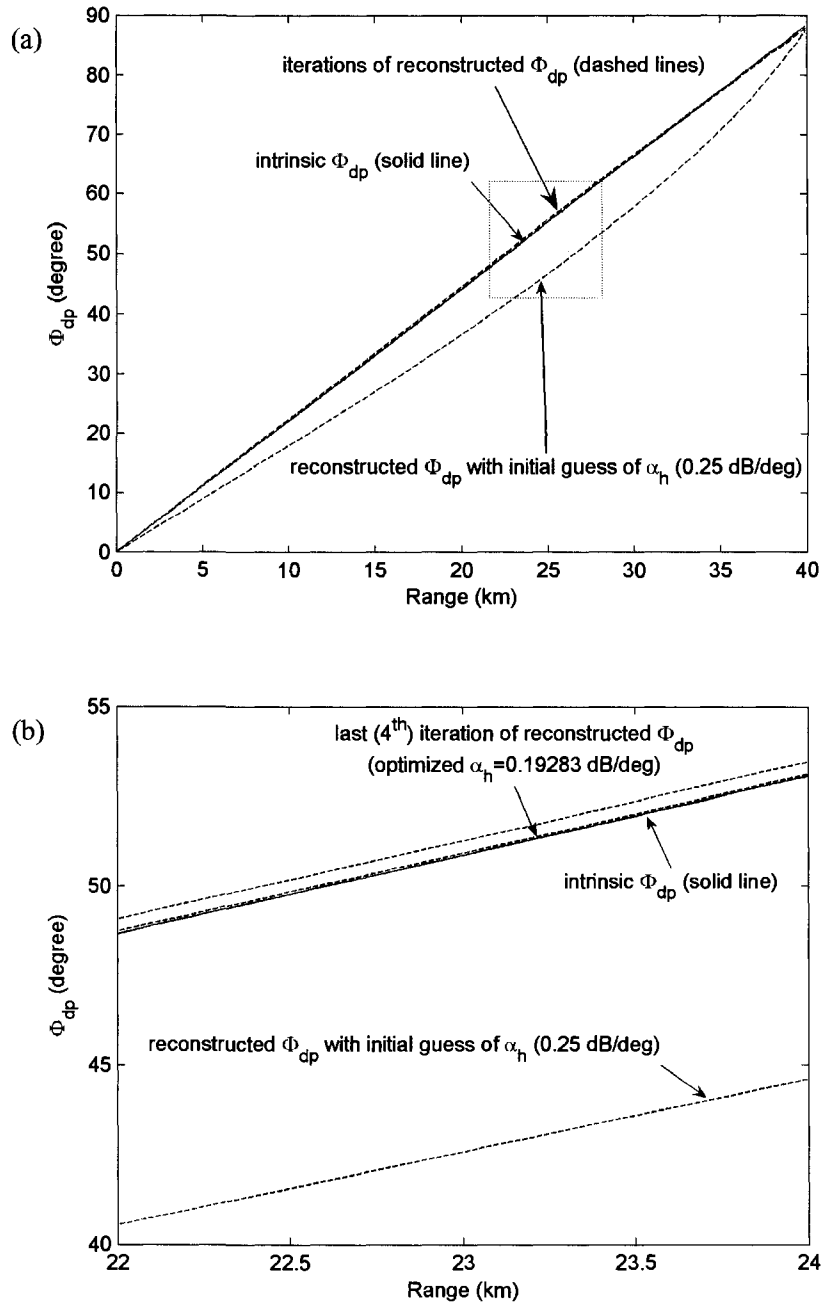


Figure 3.3 (a) Range profiles of the intrinsic Φ_{dp} and the reconstructed Φ_{dp} . The intrinsic Φ_{dp} is calculated by taking range integration of the intrinsic K_{dp} generated from a constant DSD profile and the Pruppacher and Beard 1970 drop shape model. The reconstructed Φ_{dp} is calculated by evaluating the non-linear model at each iteration of α_h . (b) Enlarged intrinsic Φ_{dp} and reconstructed Φ_{dp} profiles in the dashed square in the upper figure panel.

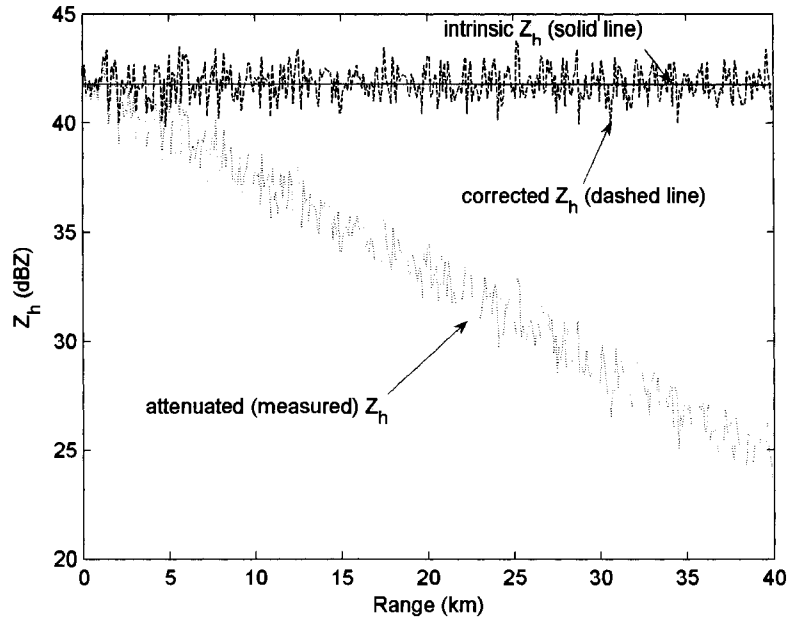


Figure 3.4 Range profiles of the intrinsic Z_h , the attenuated Z_h , and the corrected Z_h . The profiles are based on a constant exponential DSD profile and the Pruppacher and Beard (1970) drop shape model. Measurement noise is added to the attenuated Z_h .

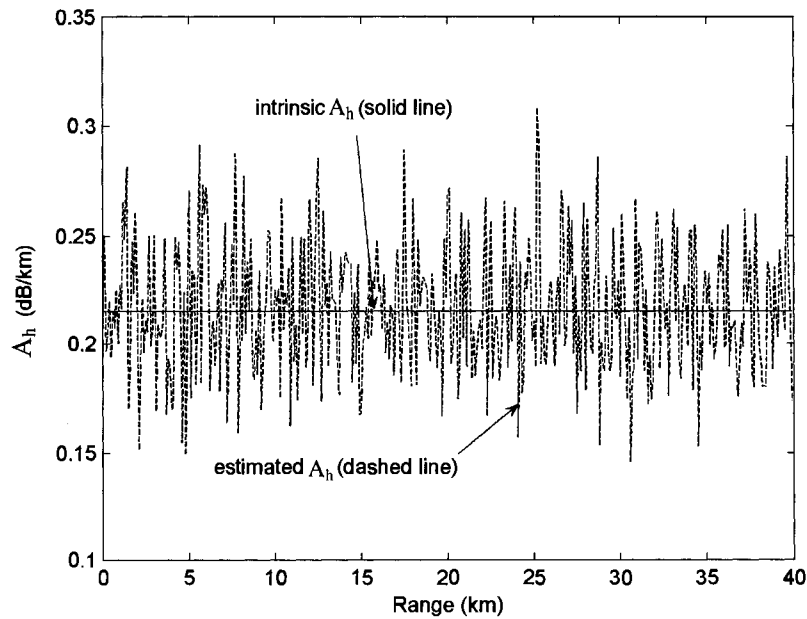


Figure 3.5 Range profiles of the intrinsic A_h and the retrieved A_h . The profiles are based on a constant exponential DSD profile and the Pruppacher and Beard (1970) drop shape model. Estimated A_h is retrieved from the noisy measurements of Z_h and Φ_{dp} .

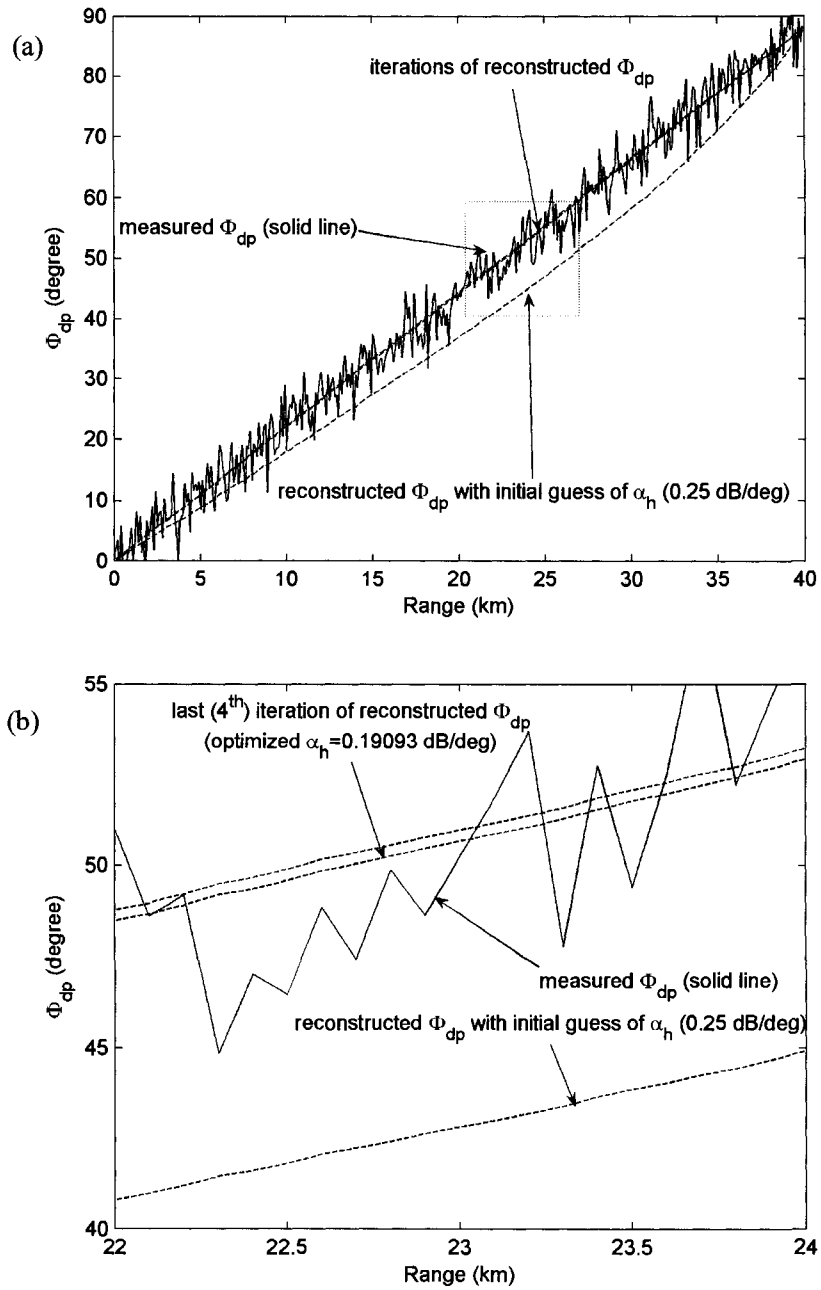


Figure 3.6 (a) Range profiles of the measured Φ_{dp} and the reconstructed Φ_{dp} . The intrinsic Φ_{dp} is calculated by taking range integration of the intrinsic K_{dp} generated from a constant DSD profile and the Pruppacher and Beard (1970) drop shape model. Then Gaussian noise is added to the intrinsic Φ_{dp} to form the measured Φ_{dp} . The reconstructed Φ_{dp} is calculated by evaluating the non-linear model at each iteration of α_h . (b) Enlarged measured Φ_{dp} and reconstructed Φ_{dp} profiles in the dashed square in the upper figure panel.

Table 3.1 Estimated α_h , mean error (intrinsic – retrieved), and RMSE evaluated with several drop shape models in the literature. Constant DSD. No measurement errors.

DROP SHAPE MODELS	ESTIMATED PARAMETER α_h (dB/deg)	MEAN ERROR		RMSE	
		Z_h (dBZ)	A_h (dB/km)	Z_h (dBZ)	A_h (dB/km)
Pruppacher and Beard 1970	0.19283	0.0733	0.00285	0.0957	0.00342
Beard and Chuang 1987	0.24511	0.0726	0.00282	0.0947	0.00337
Andsager et al. 1999	0.29094	0.0715	0.00277	0.0932	0.00330
Mixed model (linear for large drops, Brandes et al. 2002 for small drops), linear slope= 0.040mm^{-1}	0.36707	0.0697	0.00268	0.0908	0.00319
Mixed model (linear for large drops, Brandes et al. 2002 for small drops), linear slope= 0.060mm^{-1}	0.20121	0.0729	0.00284	0.0952	0.00340
Mixed model (linear for large drops, Brandes et al. 2002 for small drops), linear slope= 0.070mm^{-1}	0.16583	0.0748	0.00293	0.0978	0.00352

Table 3.2 Estimated α_h , mean error (intrinsic – retrieved), and RMSE evaluated with several drop shape models in the literature. Constant DSD. Gaussian noises with zero means are added to the measurements. $\sigma_n(Z_h)=0.8$ dBZ, $\sigma_n(\Phi_{dp})=3$ deg.

DROP SHAPE MODELS	ESTIMATED PARAMETER α_h (dB/deg)	MEAN ERROR		RMSE	
		Z_h (dBZ)	A_h (dB/km)	Z_h (dBZ)	A_h (dB/km)
Pruppacher and Beard 1970	0.19093	0.0800	0.00496	0.7908	0.03081
Beard and Chuang 1987	0.24563	0.0383	0.00240	0.81268	0.03159
Andsager et al. 1999	0.29512	0.0209	0.00018	0.81847	0.03151
Mixed model (linear for large drops, Brandes et al. 2002 for small drops), linear slope= 0.040mm^{-1}	0.36638	0.0086	0.03064	0.8203	0.03064
Mixed model (linear for large drops, Brandes et al. 2002 for small drops), linear slope= 0.060mm^{-1}	0.20167	0.0946	0.00237	0.8094	0.03149
Mixed model (linear for large drops, Brandes et al. 2002 for small drops), linear slope= 0.070mm^{-1}	0.16346	0.1537	0.00601	0.8204	0.03223

3.3.2 Variable DSD case

The previous constant DSD simulation is representative of the situation when the assumption of constant N_w along the path is met stringently, usually in highly uniform rain event. In this section, we extend the evaluation of the algorithm to more realistic variable DSD parameters along the propagation path. It should be noted again that in deriving our finalized estimation form discussed in sections 3.2.2 and 3.2.3, we assume the parameter a an unknown constant along the path so that it makes the form very simple. With the variable DSD simulation, we are going to evaluate the sensitivity of the algorithm under this assumption in spite of the DSD variation which would result non-constant parameter a 's over the path.

The variable DSD profile is generated by a mechanism described in Berne and Uijlenhoet (2005). Based on the mechanism, the parameters (N_w and D_0) of a exponential DSD are assumed to be a bivariate lognormal distribution. The means and standard deviations were obtained from DSD data from an intense storm that lasted about 45 minutes. After the initial generation of the N_w and D_0 parameters (at the first range gate), the DSD parameters along the path are assumed to follow a stationary vector auto-regressive process of order one. Based on this mechanism, a generated DSD profile is selected in our simulation. The N_w and D_0 profiles used here are plotted in Fig. 3.7 and Fig. 3.8, respectively. The radar variables are then calculated and the algorithm is run following similar procedure as described in the previous section.

We first evaluate the algorithm in the ideal situation without measurement errors. Fig. 3.9

and Fig. 3.10 show the retrievals under this condition for the Pruppacher and Beard (1970) drop shape model. Please note that the variation of the intrinsic Z_h and A_h is because of the DSD variation along the path. The corrected Z_h as well as the estimated A_h almost overlap visually with the intrinsic profiles, respectively, despite the N_w parameter is varying along the range. This indicates that the N_w constant approximation in the algorithm is fairly good for the purpose of attenuation correction. This statement is further strengthened by metrics of merit in Table (3.3). Both the mean error and RMSE are quiet acceptable for all the drop shape models studied.

The minimization process is also illustrated here as shown in Fig. 3.11. The Φ_{dp} profile is no longer a straight line because the K_{dp} is changing along the path. This change is a result of variable DSD along the path. The optimization converges quickly after 4 iterations, similar to the constant DSD case.

Next we evaluate the algorithm under noisy measurement condition similarly applied to the constant DSD profiles. Independent Gaussian noises are added to measured Z_h and Φ_{dp} . Instead of plotting both the simulation input and the algorithm output together in previous figures, we plot the difference between them here. As we can see in Fig. 3.12, the difference between the intrinsic Z_h and the corrected Z_h appears to be a random variable with mean equal to zero. The mean error and RMSE are available in Table (3.4). The mean error and RMSE are both increased because of noise, compared with the ideal situation. However they are relatively small considering the magnitude of the attenuation correction (about 16 dB PIA at 40 km). As Fig. 3.13 shows, the estimated A_h is sometimes

over-estimated or under-estimated (spikes) over a very short range (about a few hundred meters) otherwise they appear to be stable over the path.

The minimization once again shows insensitivity to the Gaussian measurement noises as the estimated (reconstructed) Φ_{dp} appears to only follow the global trend instead of the noise details in the measured Φ_{dp} profile, as Fig. 3.14 shows. Table (3.4) shows retrievals of α_h and metrics of merits for the estimated variables. This table shows that although noise is present, the algorithm still performs very well in agreement with previous observations in the previous section. Comparing Tables (3.3) and (3.4) with Tables (3.1) and (3.2) which obtained from constant DSD case, it shows that the N_v constant assumption does not affect the estimation of A_h and correction of Z_h in our simulation.

3.3.3 Sensitivity of the parameter α_h on temperature

We evaluate here the sensitivity of the parameter α_h due to the change of the environment temperature. Table (3.5) shows the estimated parameter α_h at different environmental temperatures for the Pruppacher and Beard (1970) drop shape model in an ideal condition. Four different environmental temperatures are used here, e.g., 0°C, 10°C, 20°C and 30°C, respectively. According to Table (3.5), the parameter is slightly sensitive to the change of the temperature but not as much sensitive as to the change of drop shape. This temperature insensitivity at X-band agrees with Jameson (1992). The metrics of merit for the estimated A_h and the corrected Z_h are shown in Table (3.5) for each temperature.

3.3.4 Error introduced by using fixed α_h

In the end of this simulation study we show the effect of using a fixed parameter α_h , estimated *a priori* and potentially in error. In this case, the optimization is not performed. We assume the fixed value deviates from the 'true' value by ± 0.05 dB/deg (about 20% error). The corrected Z_h is plotted for the constant DSD and the Pruppacher and Beard (1970) drop shape model in an ideal condition and shown in Fig. 3.15. It appears that the corrected Z_h is biased quite severely over the path. Therefore, we do not recommend using *a priori* fixed α_h to correct rain attenuation for X-band, unless it is known very accurately.

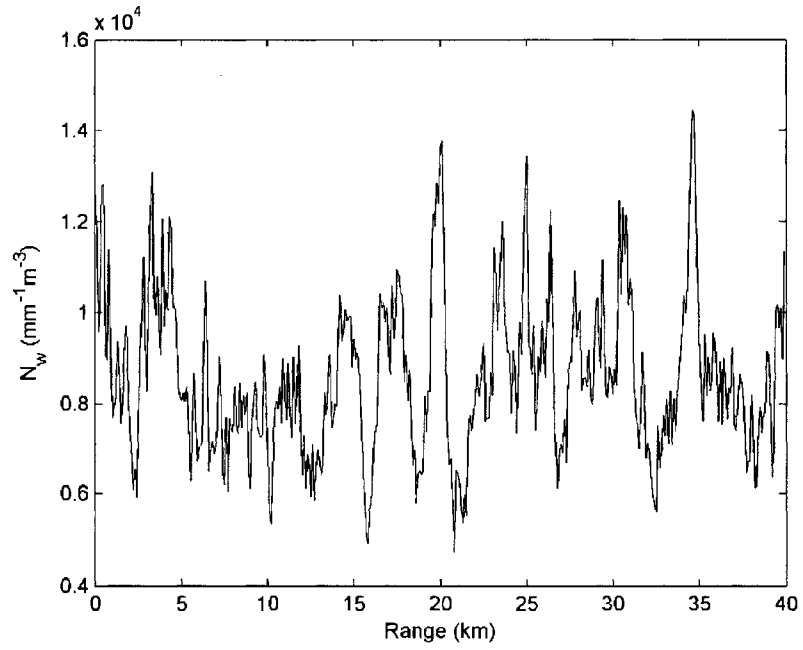


Figure 3.7 N_w profile used in the variable DSD case study.

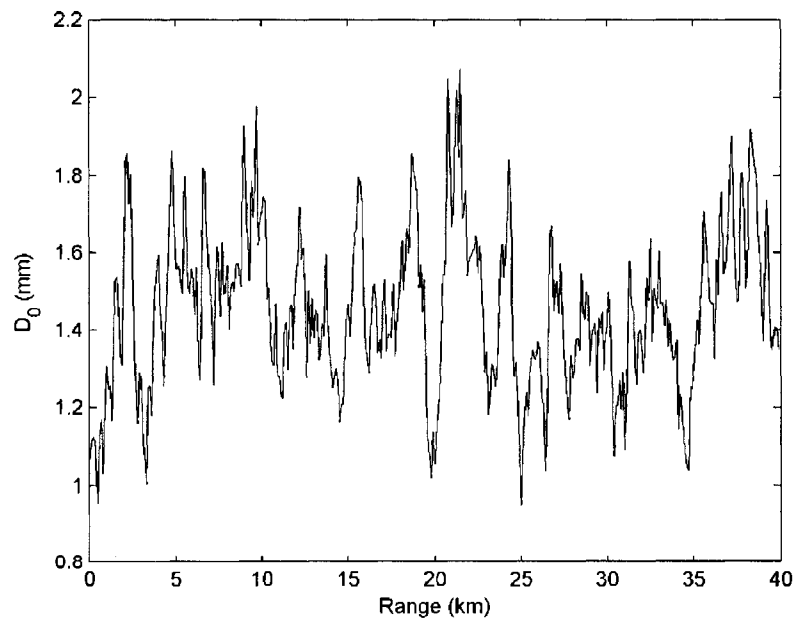


Figure 3.8 D_0 profile used in the variable DSD case study.

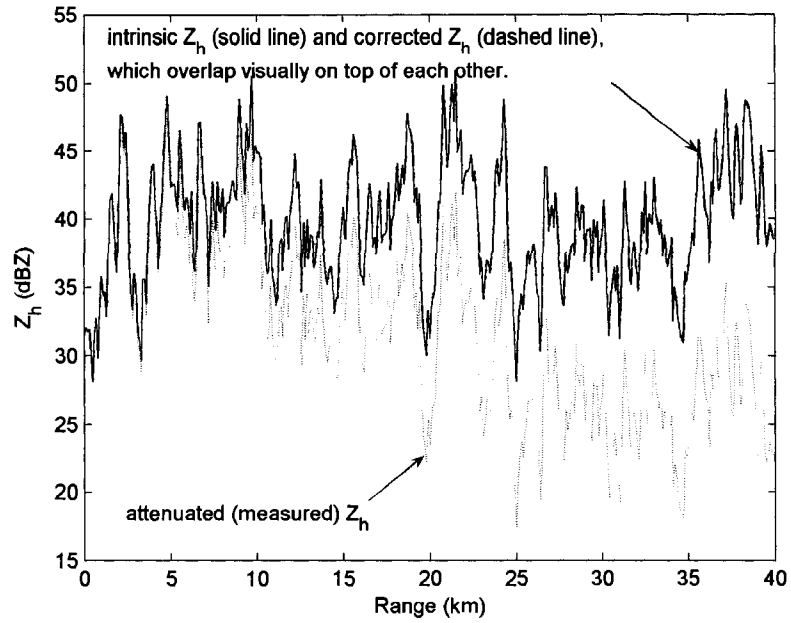


Figure 3.9 Range profiles of the intrinsic Z_h , the attenuated Z_h , and the corrected Z_h . The profiles are based on a variable DSD range profile and the Pruppacher and Beard (1970) drop shape model.

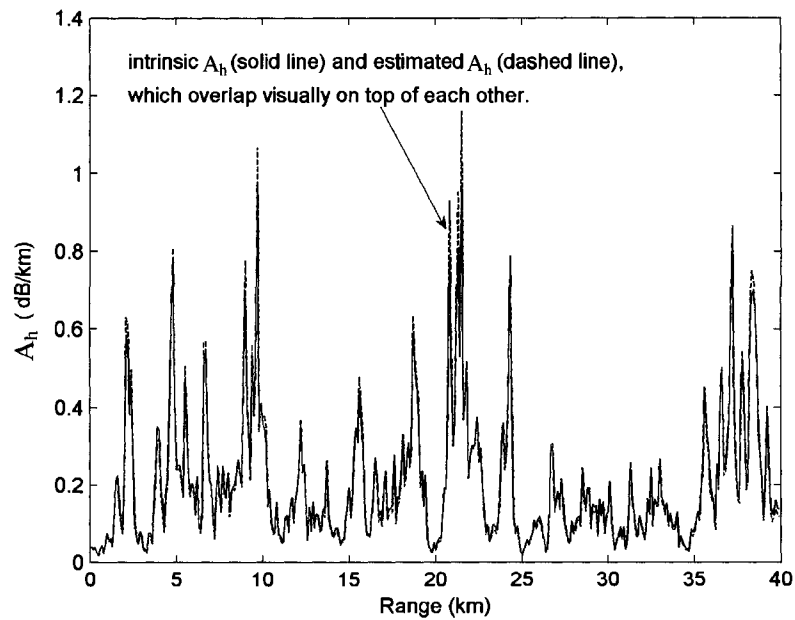


Figure 3.10 Range profiles of the intrinsic A_h and the retrieved A_h . The profiles are based on a variable DSD range profile and the Pruppacher and Beard (1970) drop shape model.

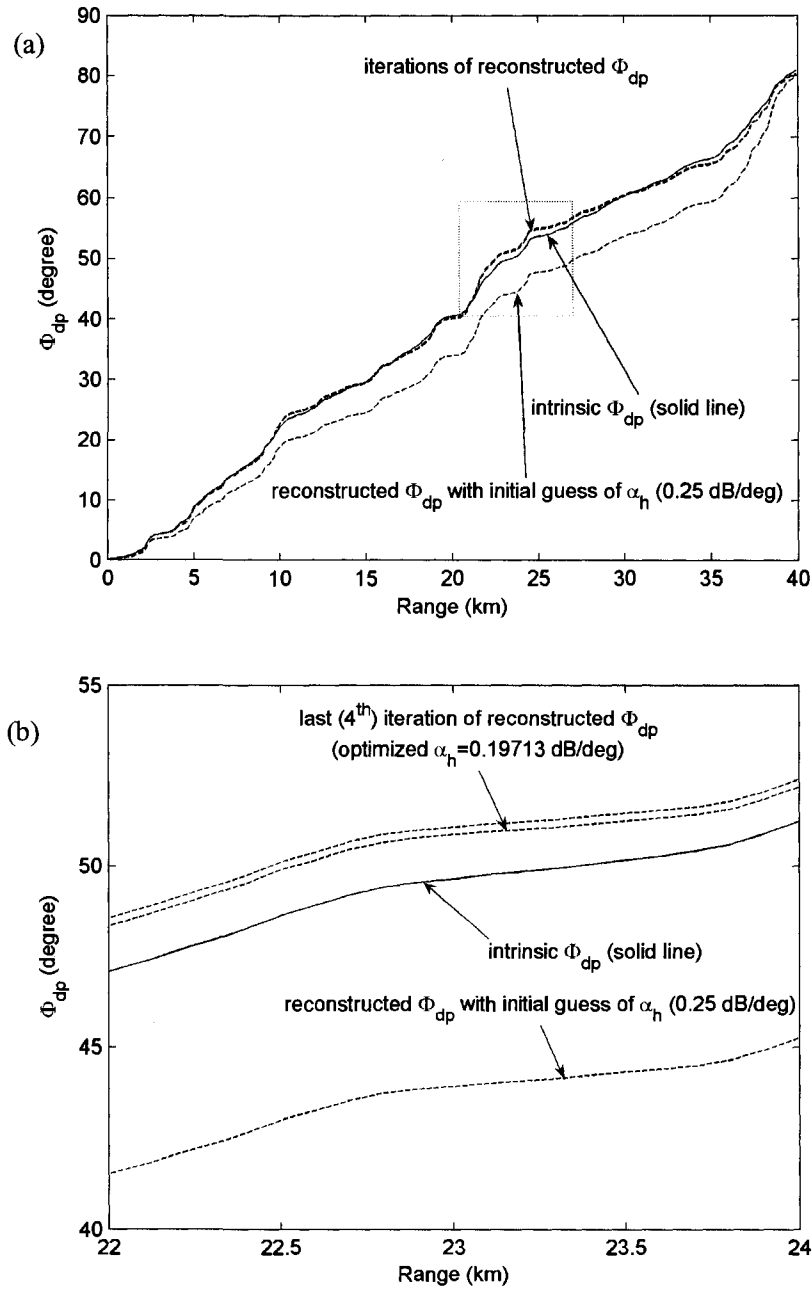


Figure 3.11 (a) Range profiles of the intrinsic Φ_{dp} and the reconstructed Φ_{dp} . The intrinsic Φ_{dp} is calculated by taking range integration of the intrinsic K_{dp} generated from a variable DSD profile and the Pruppacher and Beard (1970) drop shape model. The reconstructed Φ_{dp} is calculated by evaluating the non-linear model at each iteration of α_h . (b) Enlarged intrinsic Φ_{dp} and reconstructed Φ_{dp} profiles in the dashed square in the upper figure panel.

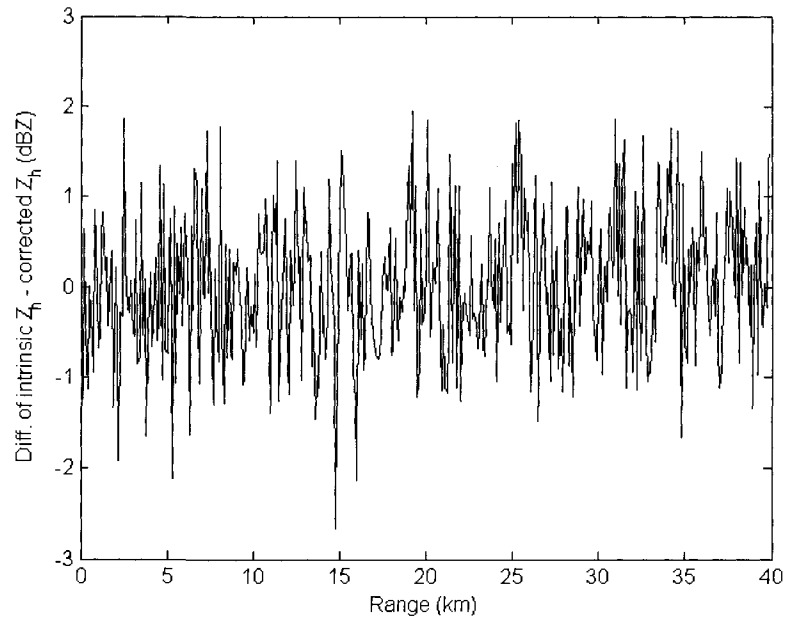


Figure 3.12 Profile of difference of the intrinsic Z_h – the corrected Z_h . The profile is based on a variable DSD range profile and the Pruppacher and Beard (1970) drop shape model. The corrected Z_h is obtained by correcting the noisy measured Z_h for attenuation.

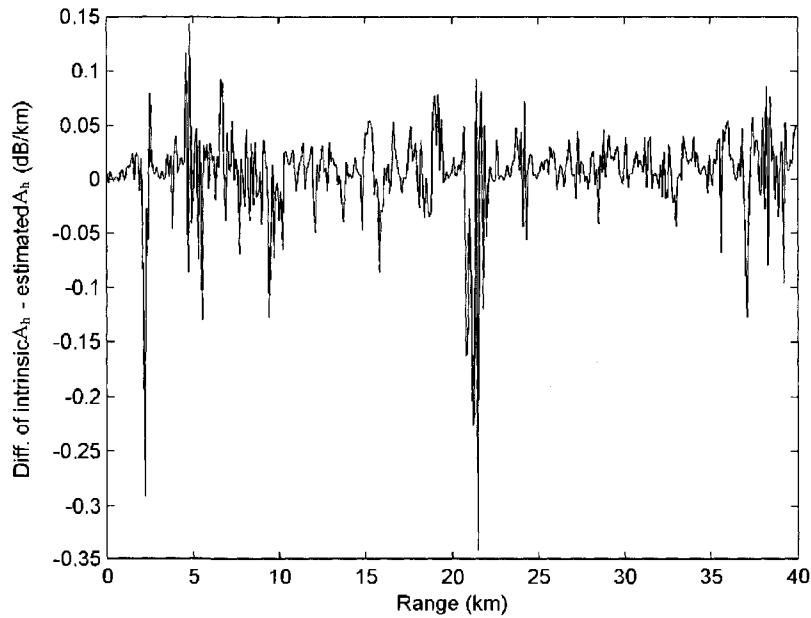


Figure 3.13 Profile of difference of the intrinsic A_h – the estimated A_h . The profile is based on a variable DSD range profile and the Pruppacher and Beard (1970) drop shape model. The estimated A_h is computed by the non-linear model at the converged α_h under condition of noisy measurements.

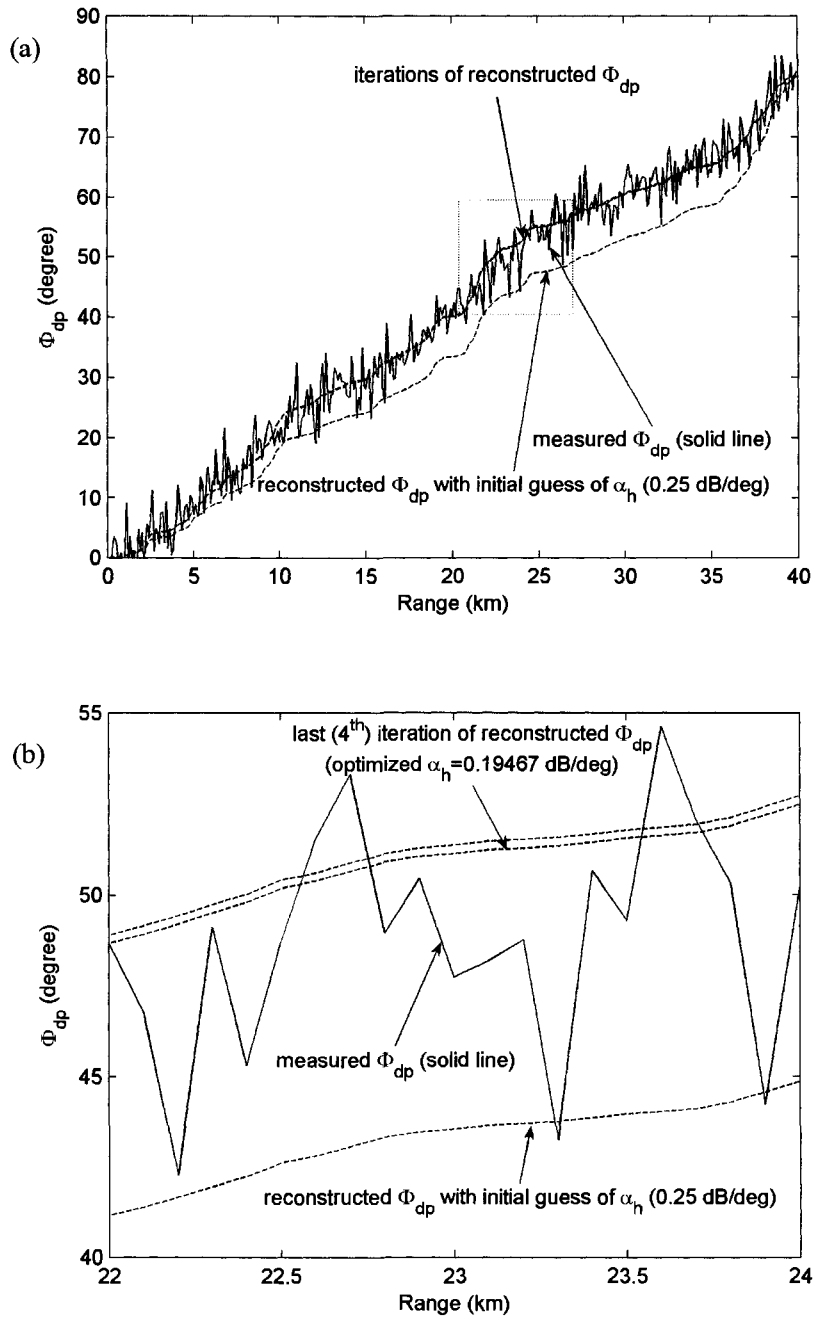


Figure 3.14 (a) Range profiles of the measured Φ_{dp} and the reconstructed Φ_{dp} . The intrinsic Φ_{dp} is calculated by taking range integration of the intrinsic K_{dp} generated from a variable DSD profile and the Pruppacher and Beard (1970) drop shape model. Then Gaussian noise is added to the intrinsic Φ_{dp} to form the measured Φ_{dp} . The reconstructed Φ_{dp} is calculated by evaluating the non-linear model at each iteration of α_h . (b) Enlarged measured Φ_{dp} and reconstructed Φ_{dp} profiles in the dashed square in the upper figure panel.

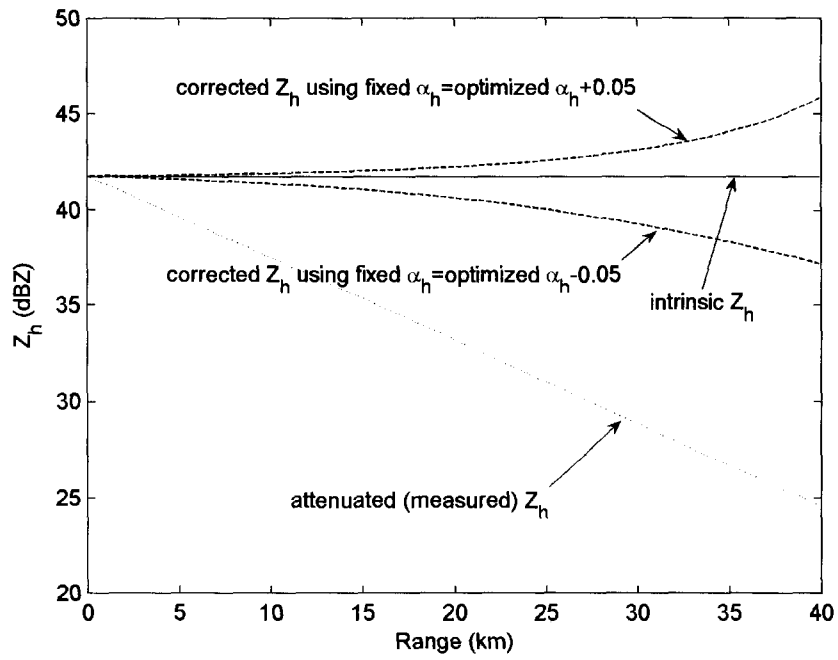


Figure 3.15 Corrected Z_h with *a priori* fixed α_h value in error.

Table 3.3 Estimated α_h , mean error (intrinsic – retrieved), and RMSE evaluated with several drop shape models in the literature. Variable DSD. No measurement errors.

DROP SHAPE MODELS	ESTIMATED PARAMETER	MEAN ERROR		RMSE	
		Z_h (dBZ)	A_h (dB/km)	Z_h (dBZ)	A_h (dB/km)
Pruppacher and Beard 1970	0.19713	0.0803	0.00293	0.1040	0.02159
Beard and Chuang 1987	0.24887	0.0850	0.00314	0.1100	0.02185
Andsager et al. 1999	0.29531	0.0842	0.00315	0.1099	0.02200
Mixed model (linear for large drops, Brandes et al. 2002 for small drops),linear slope= 0.040mm^{-1}	0.37739	0.0810	0.00300	0.1036	0.01908
Mixed model (linear for large drops, Brandes et al. 2002 for small drops),linear slope= 0.060mm^{-1}	0.20579	0.0796	0.00290	0.1031	0.02135
Mixed model (linear for large drops, Brandes et al. 2002 for small drops),linear slope= 0.070mm^{-1}	0.16933	0.0829	0.00303	0.1078	0.02270

Table 3.4 Estimated α_h , mean error (intrinsic – retrieved), and RMSE evaluated with several drop shape models in the literature. Variable DSD. Gaussian noises with zero means are added to the measurements. $\sigma_n(Z_h)=0.8$ dBZ, $\sigma_n(\Phi_{dp})=3$ deg.

DROP SHAPE MODELS	ESTIMATED PARAMETER	MEAN ERROR		RMSE	
		Z_h (dBZ)	A_h (dB/km)	Z_h (dBZ)	A_h (dB/km)
Pruppacher and Beard 1970	0.19467	0.2437	0.00541	0.8354	0.04053
Beard and Chuang 1987	0.24677	0.1292	0.00483	0.8180	0.04767
Andsager et al. 1999	0.29042	0.2003	0.00636	0.8226	0.03798
Mixed model (linear for large drops, Brandes et al. 2002 for small drops),linear slope= 0.040mm^{-1}	0.37461	0.1156	0.00439	0.7849	0.03859
Mixed model (linear for large drops, Brandes et al. 2002 for small drops),linear slope= 0.060mm^{-1}	0.20013	0.2519	0.00831	0.8325	0.03895
Mixed model (linear for large drops, Brandes et al. 2002 for small drops),linear slope= 0.070mm^{-1}	0.16842	0.1647	0.00413	0.8415	0.04625

Table 3.5 Estimated α_h , mean error (intrinsic – retrieved), and RMSE evaluated with the Pruppacher and Beard (1970) drop shape model at environmental temperature of 0°C, 10°C, 20°C, and 30°C, respectively. Variable DSD. No measurement errors.

DROP SHAPE MODEL AND TEMPERATURE	ESTIMATED PARAMETER	MEAN ERROR		RMSE	
	α_h (dB/deg)	Z_h (dBZ)	A_h (dB/km)	Z_h (dBZ)	A_h (dB/km)
Pruppacher and Beard 1970, 0°C	0.20245	0.0878	0.00320	0.1201	0.02866
Pruppacher and Beard 1970, 10°C	0.20186	0.0855	0.00312	0.1136	0.02546
Pruppacher and Beard 1970, 20°C	0.19713	0.0802	0.00293	0.1040	0.02159
Pruppacher and Beard 1970, 30°C	0.18790	0.0722	0.00262	0.0914	0.01731

3.4 Results using radar measurements

3.4.1 A typhoon case study using the MP-X radar data

We have briefly introduced the MP-X (X-band) dual-polarized Doppler radar operated by NIED, Japan in chapter 1. In this section, we present results obtained from the improved method applied to a storm event collected by the MP-X radar. The storm event is a Typhoon that passed through the Tsukuba area, Japan on Sep 11, 2001 where the MP-X radar was located. The Typhoon also passed through the area where three Joss impact-based disdrometers were located. The *in situ* measurements of the DSD from the three disdrometers provided us a means to independently validate the algorithm. The three disdrometers were placed on a straight line from the radar along the azimuth angle of 294 deg with respect to the radar, at 14.7, 21.5 and 27.5 km range, respectively (Park et al. (2005)). The radar ray at this azimuth angle and the locations of the disdrometers are indicated in the following radar images (Fig. 3.16).

Fig. 3.16(a) shows a plan position indicator (PPI) scan image of the measured Z_h at elevation angle 2.5 deg to avoid the ground clutter caused by the nearby hills. As seen in the figure, the intensive rain cell surrounding the area to the west of the radar is very likely to cause significant amount of attenuation. This is evident as we examine the corrected Z_h for the same scan, shown in Fig. 3.16(b). After the attenuation-correction, the corrected Z_h reveals the second intensive core beyond around 20 km to the north-west of the radar.

In order to validate the attenuation correction, we first calculate the intrinsic Z_h (by T-matrix method) from the 1-minute rain drop size spectra (histogram of the diameters) measured by the three disdrometers. The result is shown in Fig. 3.17. The calculated intrinsic Z_h values are shown in the figure asterisks, placed at the appropriate ranges where the disdrometers were located. Also shown in the figure is the result obtained from Park et al. (2005)'s method, as a comparison. The method described in Park et al. (2005) is basically an extension of Bringi et al. (2001) to the X-band radar (see also chapter 2). It appears that the corrected Z_h output by the improved method and the Park et al.'s method both agree with the disdrometer calculation very well in this case. Small difference in the correct Z_h between the two methods is observed. The difference results from very close α_h values estimated independent by the two methods. The value estimated by the improved method converges to 0.24294 dB/km, while the value estimated by Park et al.'s method is 0.25 dB/km. However, the numbers of iterations used to achieve the converged values are significantly different. As discussed in chapter 2, a 'brute force' minimization scheme is used for the Bringi et al.'s method because the cost function defined in eq. (2.41) is an absolute function. In Park et al's X-band extension to this method, the brute force minimization was performed in the intervals of [0.025 0.575] with a 0.025 step for this case. It takes all the 23 iterations to find the value that minimizes the absolute cost function. The improved method is based on the model defined by the least-squares error in section 3.2.3 and the minimization scheme discussed in section 3.2.4, which is carried out and implemented very efficiently. The numbers of iterations for the improved method to converge, as shown in the previous simulation sections, rarely exceeds four. In this case it took 4 iterations. Furthermore, it is worth noting that with a 0.025 step, the average error

in the estimated coefficient is ± 0.0125 with the brute force search which can lead to a relative error about 5% (assuming mean $\alpha_h=0.25$) in the estimation of the specific attenuation. It is important to minimize this kind of bias error. The error is avoided by the improved method since it searches for the minimizer over the continuous error curve (as opposed to searching only at some discrete intervals) in a least squares sense.

Fig. 3.18 shows the histogram of α_h obtained from the improved method. The histogram is obtained from radar rays spanning azimuth angles from 280° to 310° , where the attenuation is significant. The range and distribution of α_h is reasonable comparing the result obtained from the previous simulation. Fig. 3.19 shows K_{dp} - Z_h intensity plot after the attenuation correction by the improved method for the selected rays. The empirical curve for the K_{dp} - Z_h calculated independently from the *in situ* disdrometer data is also plotted. The close agreement between the radar data after the attenuation correction and the empirical curve is noted here.

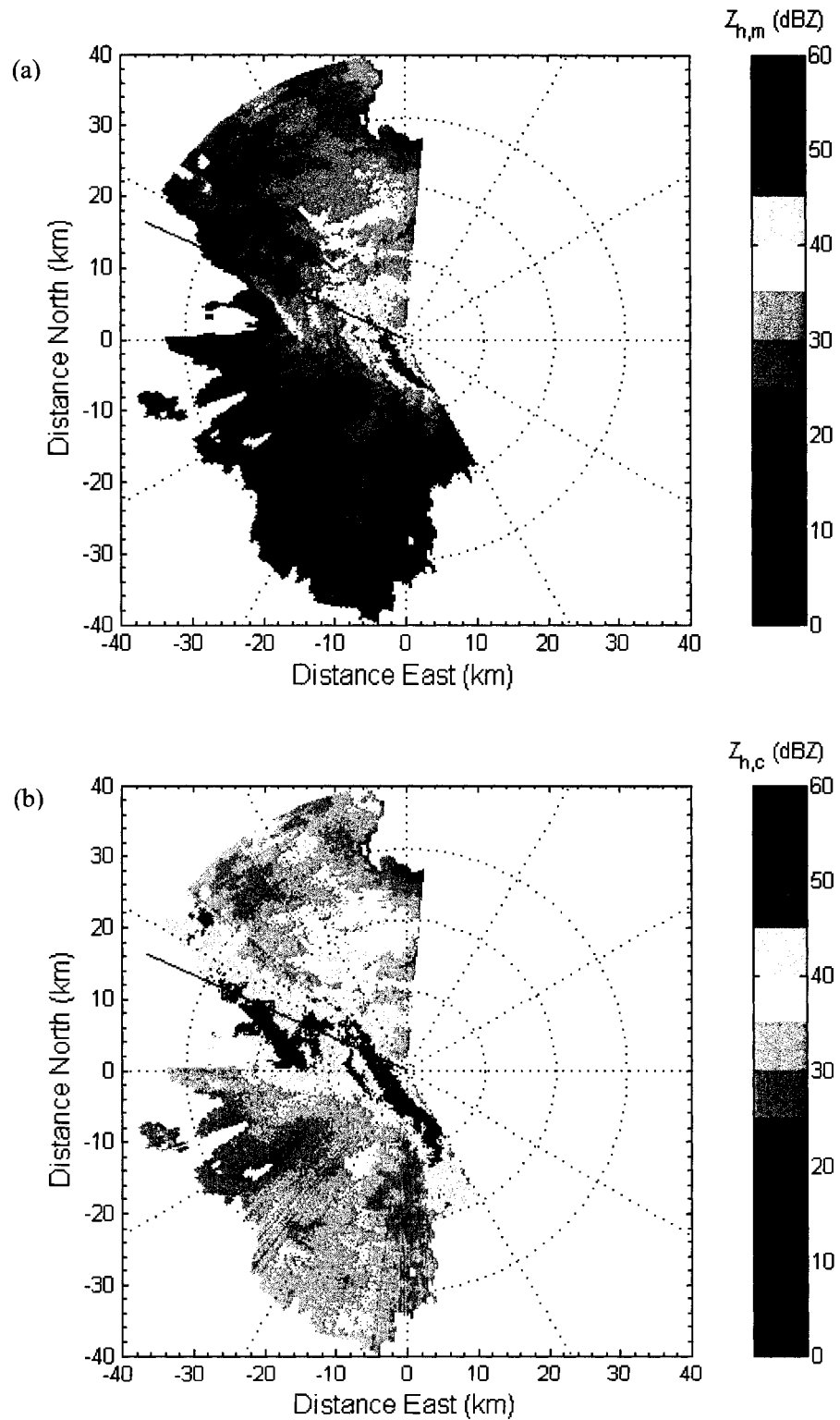


Figure 3.16 A PPI scan of (a) the measured Z_h and (b) the corrected Z_h , observed at the elevation angle of 2.5 deg, at 01:59:54 LST, September 11 2001. The black line is the radar ray at azimuth angle of 294 deg. The three squares indicate the locations of the three *in situ* disdrometers, respectively.

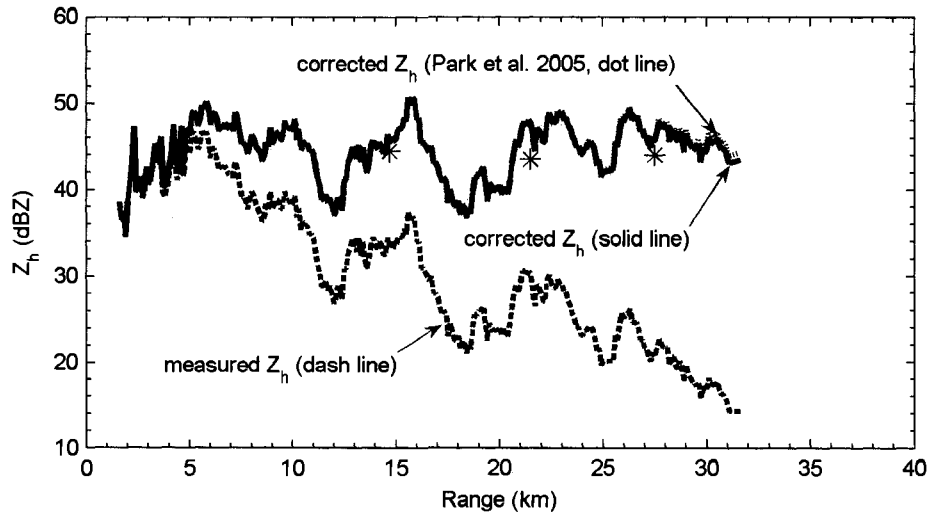


Figure 3.17 Range profiles of the measured Z_h , the corrected Z_h using Park et al. (2005) method, and the corrected Z_h using the improved method along the azimuth angle of 294° for the Typhoon event at 01:59:54 LST September 11 2001. The asterisks (*) denote the mean values calculated from DSD data collected with the three *in situ* disdrometers, respectively.

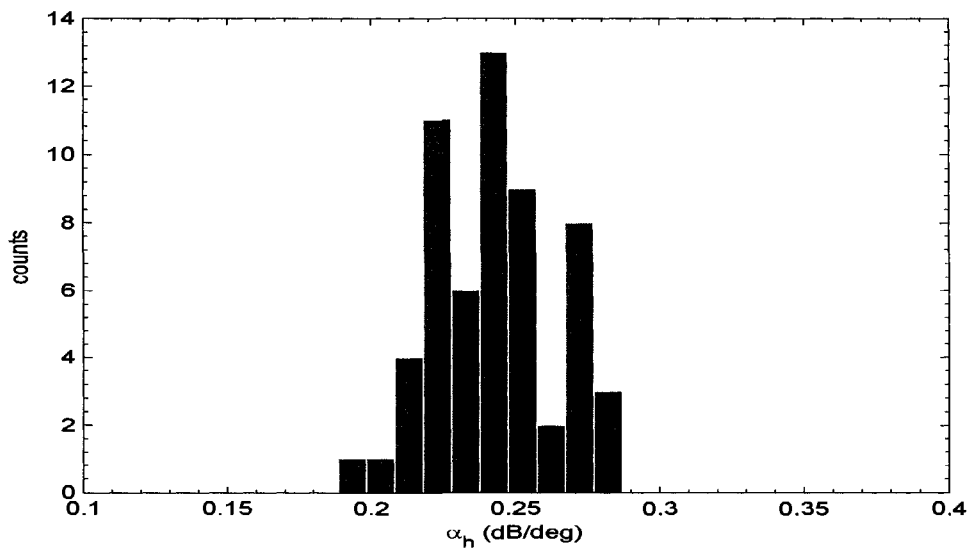


Figure 3.18 Histogram of the optimized coefficient α_h for radar rays spanning azimuth angles from 280° to 310° for the Typhoon event at 01:59:54 LST September 11 2001.

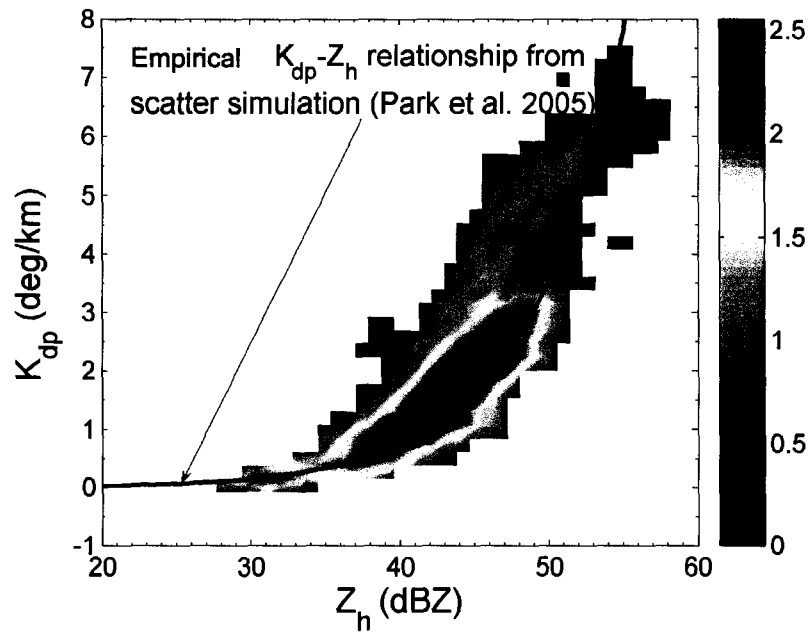


Figure 3.19 Intensity scatterplot of K_{dp} vs. Z_h after attenuation correction. The black line is the empirical K_{dp} - Z_h relationship based on T-matrix calculation using the *in situ* disdrometer DSD data.

3.4.2 Implementing the improved algorithm for the CASA IP1

The previous sections about the simulation study and the MP-X radar case study primarily focus on validating the improved algorithm in a post-analysis sense. It is desirable to investigate the algorithm more carefully when it is to be implemented for operational radar systems. In an operational environment, the real-time processing and robustness are considered two very important factors. Our motivation here is to make the improved algorithm run in real-time and robustly for the CASA IP1 so that any downstream algorithms that require the attenuation-corrected data will run seamlessly.

It has been noted that in the simulation study and the MP-X case study the improved algorithm performed well in terms of convergence speed. However, the data quality requirements for the algorithm to run successfully were only briefly investigated. Moreover, the connection of the algorithm to a real system was not mentioned. Here, we pay more attention to the CASA IP1 systems aspect in order to implement the algorithm efficiently and robustly. As a result of fine-tuning the implementation, we show our logic for the data quality control, the flow of the data, and other details of implementation in the flowcharts shown in Fig. 3.20. Note that the estimation of the differential specific attenuation (A_{dp}) and the correction for the differential reflectivity (Z_{dr}) is postponed to the next chapter but the functionality is still shown here in the flowchart as a complete system.

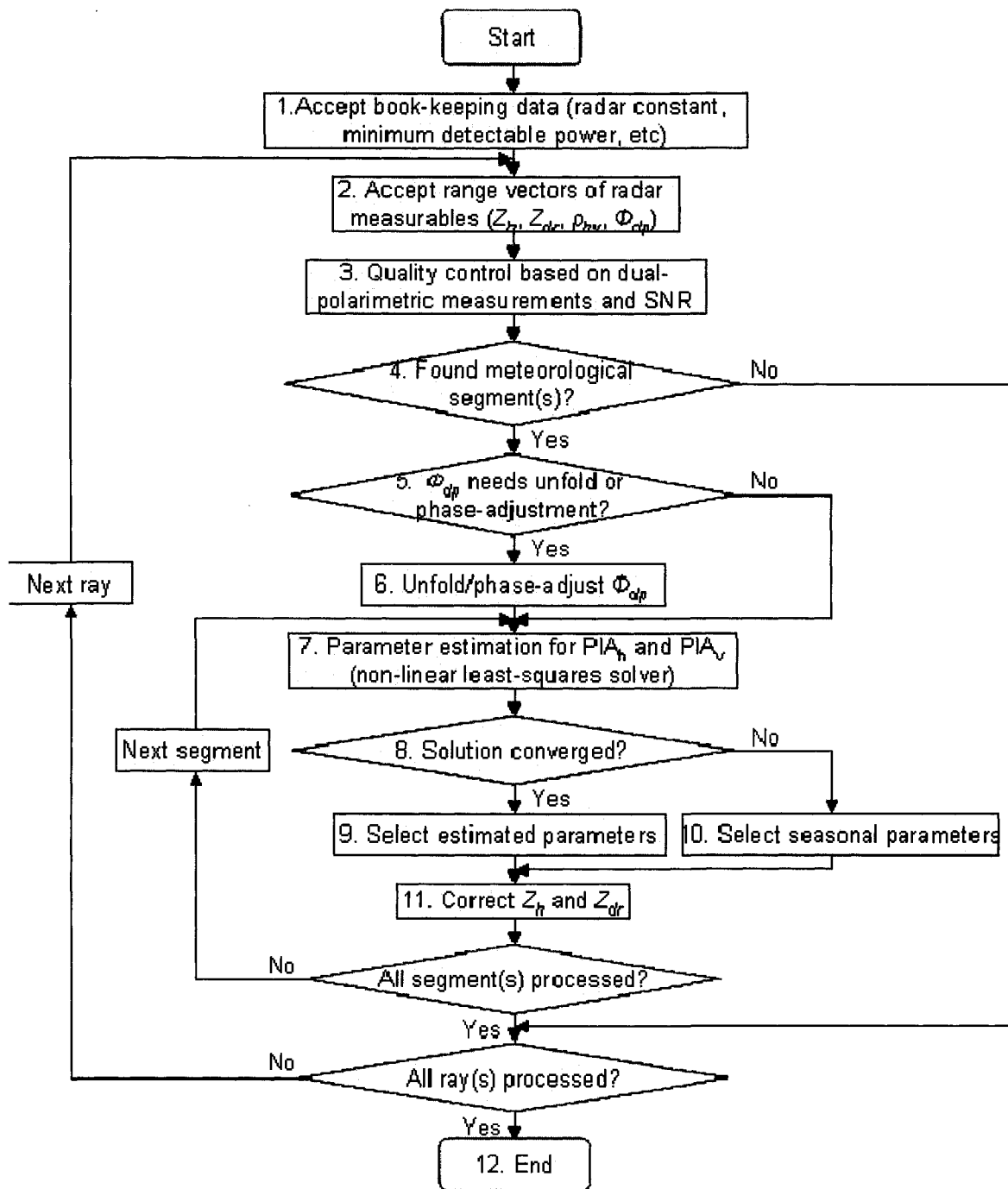


Figure 3.20 Flowchart of the CASA IP1 dual-polarization attenuation-correction algorithm.

We summarize briefly the descriptions for the numbered blocks in the above flowchart as follows:

1. The book-keeping data concerning the dual-polarization attenuation-correction are input from the lower level radar control system. Particularly, the start range and the range resolution of the data vectors is used to identify the first range gate, while the radar constant and the minimum detectable power are used to calculate the SNR at each range gate.
2. The radar measurables concerning the dual-polarization attenuation-correction are input from the lower level radar data management system. Particularly, the measured reflectivity at h -polarization (Z_h) and the measured differential reflectivity between the h - and v -polarizations (Z_{dr}) are the two quantities that need the attenuation-correction. The measured differential propagation phase (Φ_{dp}) is used in the objective function for the non-linear least squares solver (shown in block no. 7 later). The co-polar correlation coefficient (ρ_{hv}), the normalized coherent power (NCP), and the Φ_{dp} together provide dual-polarization information for block no.3.
3. The ρ_{hv} , the NCP, the Φ_{dp} , and the SNR together provide dual-polarization-based data quality control on a ray-by-ray basis. Based on these variables, an elaborate scheme is used to identify ‘meteorological segments’, which is defined here as a segment of range that has continuous precipitation.
4. For the definition of ‘meteorological segments’ please see block no.3.
5. If any meteorological segments are found, the first one will be used as a reference to check if the Φ_{dp} needs to be adjusted for prevention of phase-wrapping. It is desired to

adjust the system offset of the Φ_{dp} so that over the full range it is a continuous function in $[-\pi, \pi]$. After the system offset is adjusted, it is unusual that the Φ_{dp} needs unfolding but the mechanism to unfold is still there just in case.

6. Please see block no.5.
7. The parameter estimation for the parametric model of the path-integrated attenuation at h-polarization (PIA_h) and at v-polarization (PIA_v) is conducted in a least-squares sense by the solver. The solver is designed and coded very efficiently and is real-time.
8. An elaborated scheme is used to monitor the convergence of the solver and check the validity of the estimated parameters.
9. If the solution of the parameter estimation converged and valid, the estimated parameters will be used in the parametric model to compute the PIA_h and the PIA_v .
10. There is a possibility that the solution does not converge. In this case, *a priori* seasonally averaged parameters will be used (the seasonal average values are to be calculated and studied in the later section 3.4.4).
11. The measured Z_h and the measured Z_v are corrected using the estimated PIA_h and the estimated PIA_v , respectively. The measured Z_{dr} is then corrected using the corrected Z_h and the corrected Z_v .
12. Upon completion, the output is converted to netCDF format and the resources allocated at the start of the algorithm will be released.

Here in end of this section we verify that our implementation of the algorithm performs in real time. As we monitor the execution time of the software installed in the CASA IP1 radar nodes, the average time to complete processing a full PPI scan (about 360 beams) is

1-2 seconds, including the disk I/O, data quality control and other miscellaneous features described in the flowchart. At maximum, the average time to process a single ray is about 5 ms, which is only about 5% of the dwell time.

3.4.3 Case study for the CASA IP1: comparison with nearby WSR-88D radar measurement

The WSR-88D (S-band) radar networks provide national coverage for weather surveillance applications. The base production S-band reflectivity provides at least baseline references for the storm intensity and structure, with which we can compare the attenuation-corrected reflectivity of the CASA IP1.

In order to do a point-to-point comparison despite the fundamental differences in the configurations of the two radar networks, we derived a scheme to grid and merge the networked data from each individual node into a composite dataset on a geo-referenced frame. This scheme is termed ‘mosaic of radar data’ and more detailed is available in Liu et al. (2007).

Here, we present the mosaic images of a severe storm measured by the WSR-88D and the CASA IP1 coincidentally. The WSR-88D data are from the KTLX node in Oklahoma City, OK, which is some 100 km away from the CASA IP1.

Fig. 3.21 shows a storm over the center of IP1 testbed at around 07:37:31 May 8 2007 UTC. Fig. 3.21(a) shows the composite reflectivity from the four IP1 radars before

attenuation-correction. Fig. 3.21(b) shows the composite reflectivity after attenuation-correction. Fig. 3.21(b) is to be compared visually with Fig. 3.21(c) which shows the WSR-88D reflectivity at almost the same time from the KTLX radar. As Fig. 3.21(b) and Fig. 3.21(c) show, the two reflectivity maps show very similar storm intensity and structure although they are from two completely different systems operating at two different frequencies (~ 3 GHz and ~ 9.4 GHz). The improved spatial resolution of CASA data is also to be noted here.

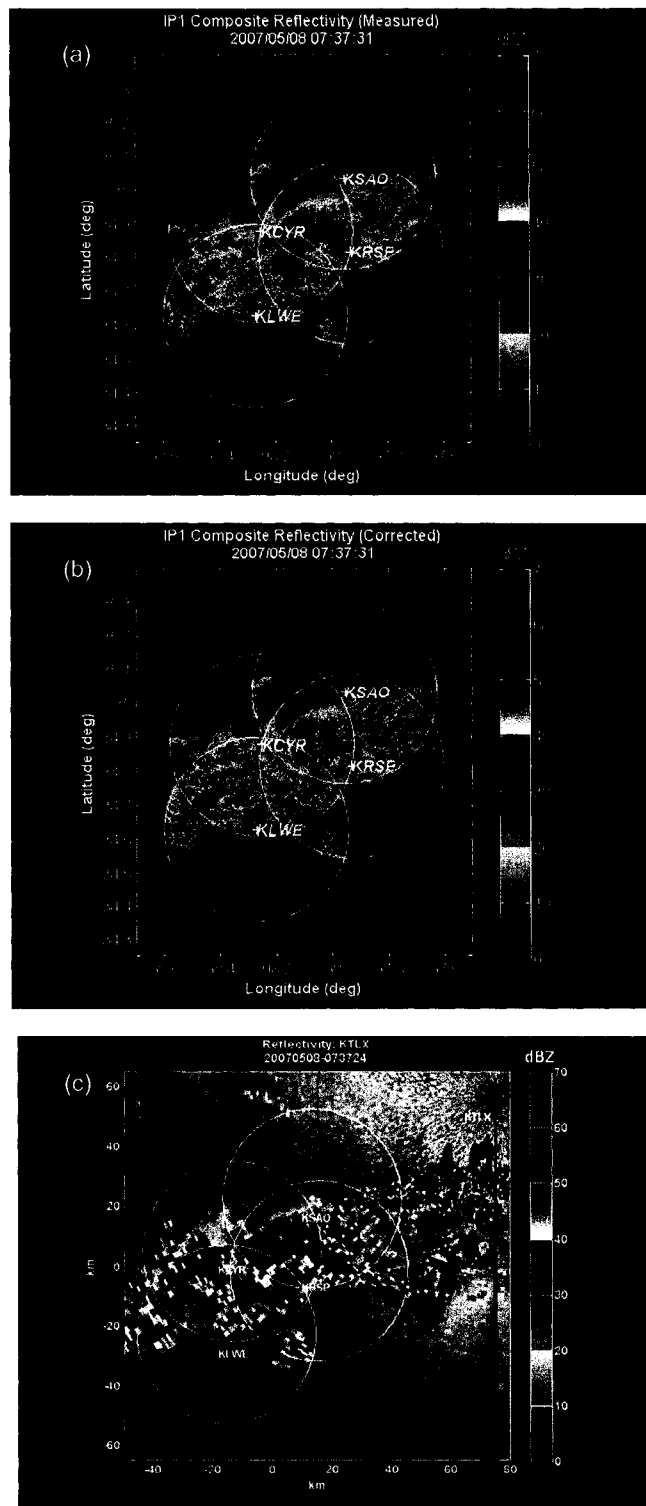


Figure 3.21 IP1 Reflectivity maps at 07:37:31 May 8 2007 and WSR-88D reflectivity map at 07:37:24 May 8 2007. (a) IP1 reflectivity before attenuation correction (b) IP1 reflectivity after attenuation correction (c) WSR-88D (KTLX) reflectivity.

3.4.4 Seasonal results from the CASA IP1 testbed: Spring, Summer, and Autumn 2007

The CASA IP1 testbed has collected and archived terabytes of radar data for a number of major storm events passing through the network as of April 2007, including a tornado. In this section, we analyze the statistics of the estimated parameter α_h and the estimated total path-integrated attenuation for a number of storms that occurred in the testbed in Spring, Summer, and Autumn, 2007, respectively.

We summarize information of the storm events analyzed for the statistics study in Table (3.6). The table lists the start date, start time, end date, end time approximately when each storm entered and exited the CASA IP1 coverage area. The type of each storm is also given. If there were more than one type of storm from the start time and end time, we also indicate this in the ‘type’ column.

As expected in Oklahoma, the storms are mostly convective. Hail particles, either dry or wet, are possible in strong convective events. The study of wet hail attenuation will be presented later in chapter 5.

First we present the statistics of the parameter α_h for each storm in order to understand the range of the variation of the parameter estimation, both physical and statistical in real storm events. As discussed in the simulation section, the physical variation is due to the natural variation in the DSD and the shape of raindrops and other environmental variables like temperature. The statistical variation is introduced due to the noise in the

system. It is hard to separate these two factors in the real data. However, the intrinsic distribution of the parameter for the instrument (the CASA IP1) and the governing process of the storm should be revealed by sufficient time-averaged histograms.

Fig. 3.22 shows the histograms of the estimated parameter α_h for each storm from the start time to the end time listed in the Table (3.6). In the figure, histograms from a given event are plotted in the same column, with each row showing the histogram from a particular radar node. It is clear that the distributions of the parameter α_h vary from event to event and from radar to radar. The variation is expected because, (a) each storm is different; (b) even in the same storm, the DSD and drop shape can vary spatially within the coverage area. For our purpose of attenuation-correction, it is important that the variation along the radar propagation path is compensated by estimating the parameter α_h through the self-consistent principle discussed earlier, in a least-squares sense.

Fig. 3.23 shows the mean values of the parameter α_h obtained from the histograms shown in Fig. 3.22. For each radar, the mean values and the standard deviations are plotted with the date as the x-axis (not uniformly spaced) to illustrate the trend of the mean values from event to event.

Next we show in Fig. 3.24 the cumulative distribution function of the total *PIA* for all the events listed in Table (3.6). It shows that the total *PIA* is less than 10.39 dB about 80% of time and is less than 17.76 dB about 90% of the time. The total *PIA* here is defined as the *PIA* at the last range gate containing precipitation on the propagation path, up to the

maximum unambiguous range of the radar. At X-band, it is possible that the radar radiated power is completely attenuated after some distance before reaching the maximum unambiguous range when the propagation path traverses a very intensive storm. In this case, the total *PIA* is defined here as the *PIA* up to the last range gate identified as ‘good quality’ data (see section 3.4.2), which can be smaller than that if the signal were not attenuated completely. Therefore, in such situation the statistics shown in Fig. 3.24 are not fully representative of the storm in the coverage area. When this happens, we observe that part of the storm is missed by one of the radars in the network. However, the other radars could observe the missing part of the storm provided that the storm is inside the overlapping region of the network and the paths from other radars are oriented such that they intercept the less intensive part of the storm complex (e.g., see the topology of the CASA IP1 in Fig. 1.3). This network approach is considered a core component of the CASA approach of sensing the atmosphere.

Table 3.6 The CASA IP1 case studies start date/time, end date/time (all UTC) and storm type information.

State Date	Start Time	End Date	End Time	Type(s) of Storm	Operating Node(s)
2007/04/10	22:46	2007/04/10	23:59	Isolated cells, convective	All
2007/04/11	00:00	2007/04/11	01:24	Isolated cells, convective	All
2007/04/24	16:10	2007/04/24	19:00	Squall line	KSAO, KCYR, KLWE
2007/04/27	17:42	2007/04/27	19:12	Isolated cells, convective	KSAO, KCYR, KLWE
2007/05/07	04:38	2007/05/07	17:58	Isolated cells(more intense), convective	All
2007/05/08	07:02	2007/05/08	10:58	Isolated cells(more severe), convective	All
2007/05/08	23:00	2007/05/09	04:40	Tornado at KLWE around 00:32:58, strong convective storm later	All
2007/05/10	22:02	2007/05/10	23:59	Isolated cells, convective	All
2007/06/10	20:02	2007/06/10	23:58	Isolated cells, convective	All
2007/06/14	06:00	2007/06/14	14:59	Strong convective	All
2007/06/20	04:00	2007/06/20	12:59	Strong Squall line	All
2007/06/21	03:00	2007/06/21	21:00	Isolated cells, convective	All
2007/10/03	00:00	2007/10/03	07:00	Isolated cells, convective	KLWE, KRSP
2007/10/15	00:00	2007/10/15	06:00	Squall line	KCYR, KLWE

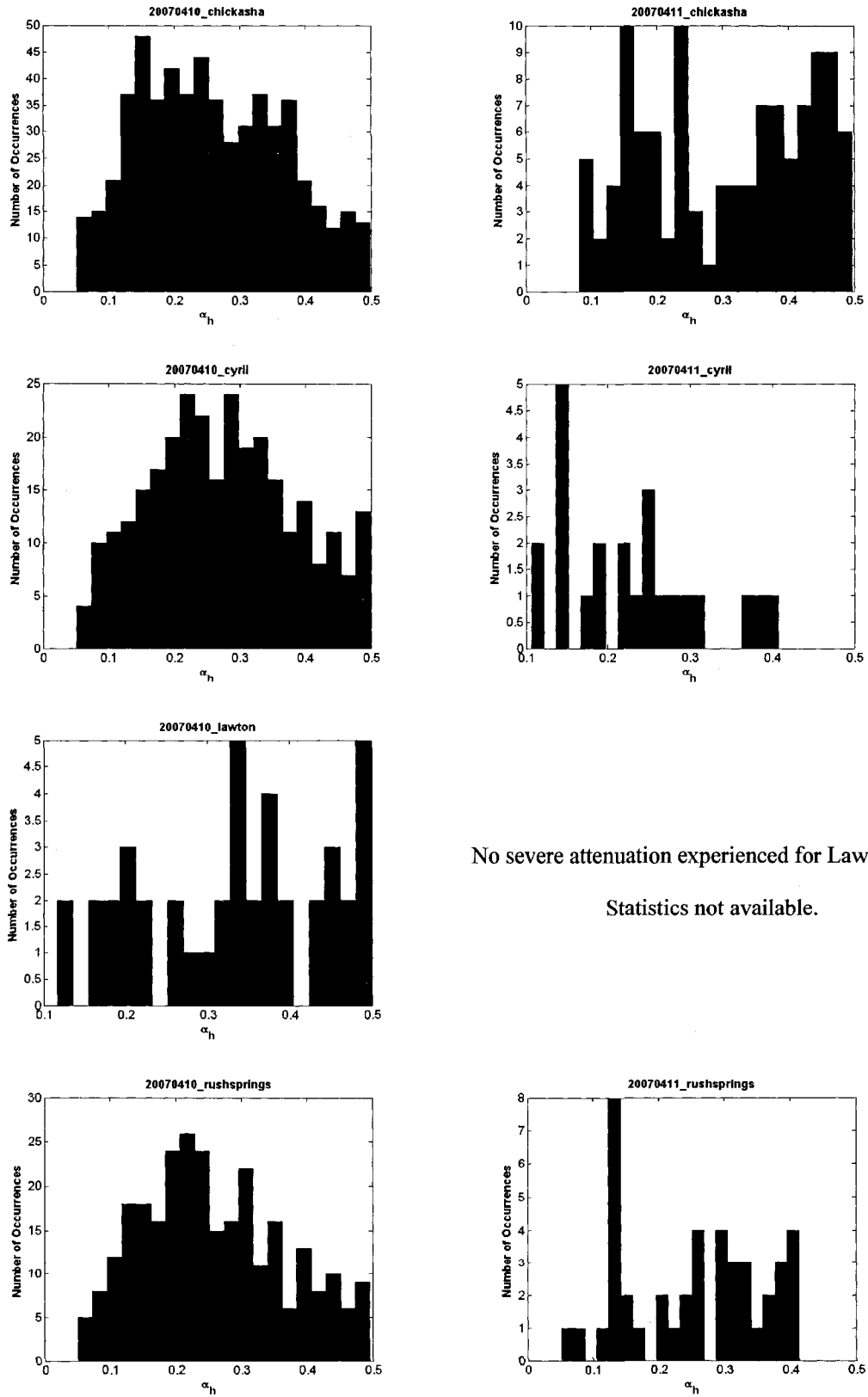
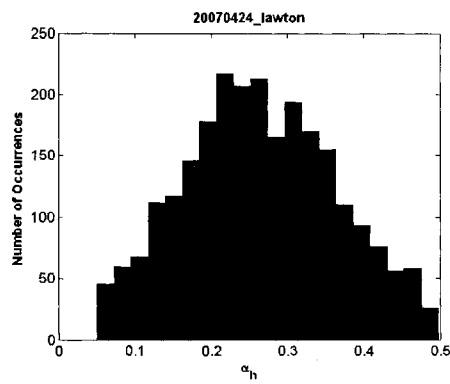
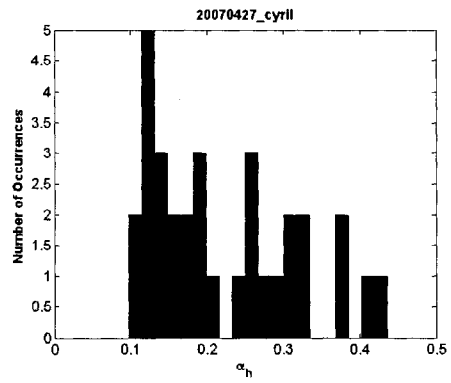
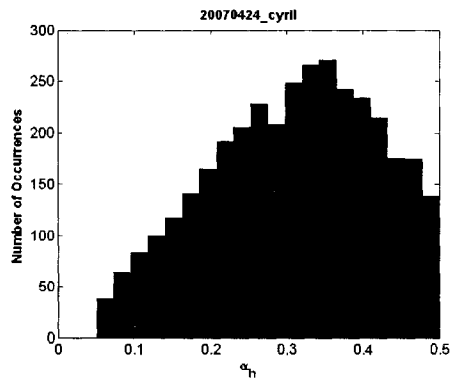
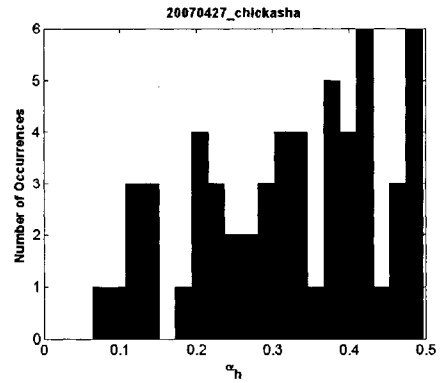
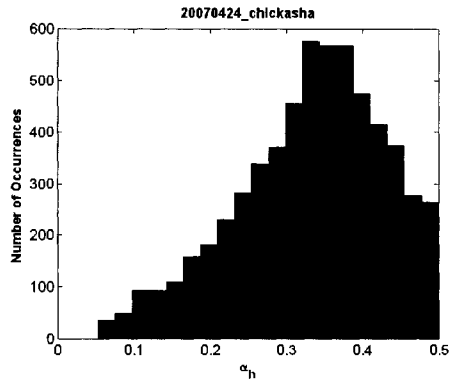


Figure 3.22 Histograms of the estimated parameter α_h for the events listed in Table (3.6).



No severe attenuation experienced for Lawton node.

Statistics not available.

Rush Springs node not operating for this case.

Rush Springs node not operating for this case.

Figure 3.22 (continued). Histograms of the estimated parameter α_h for the events listed in Table (3.6).

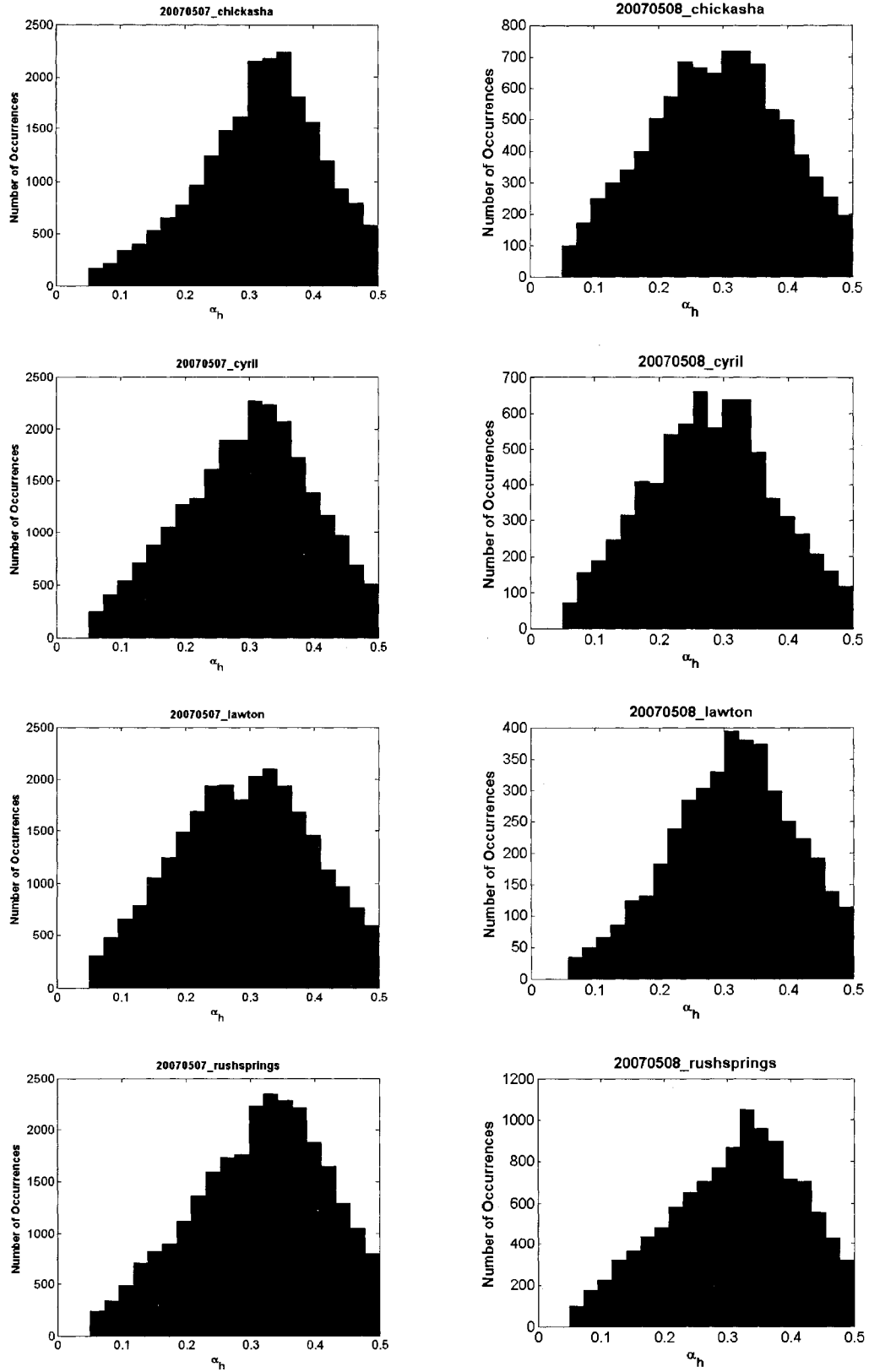


Figure 3.22 (continued). Histograms of the estimated parameter α_h for the events listed in Table (3.6).

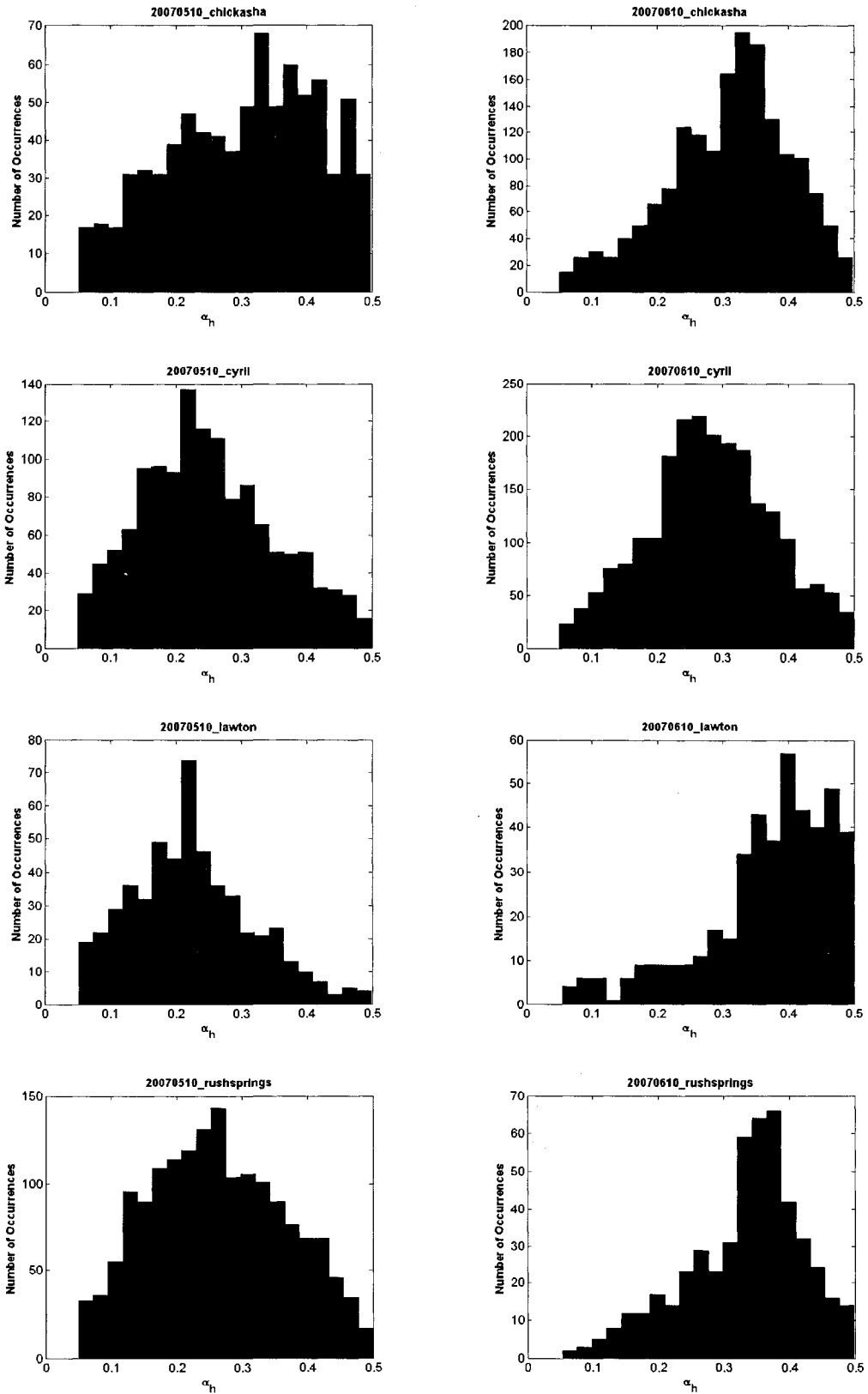


Figure 3.22 (continued). Histograms of the estimated parameter α_h for the events listed in Table (3.6).

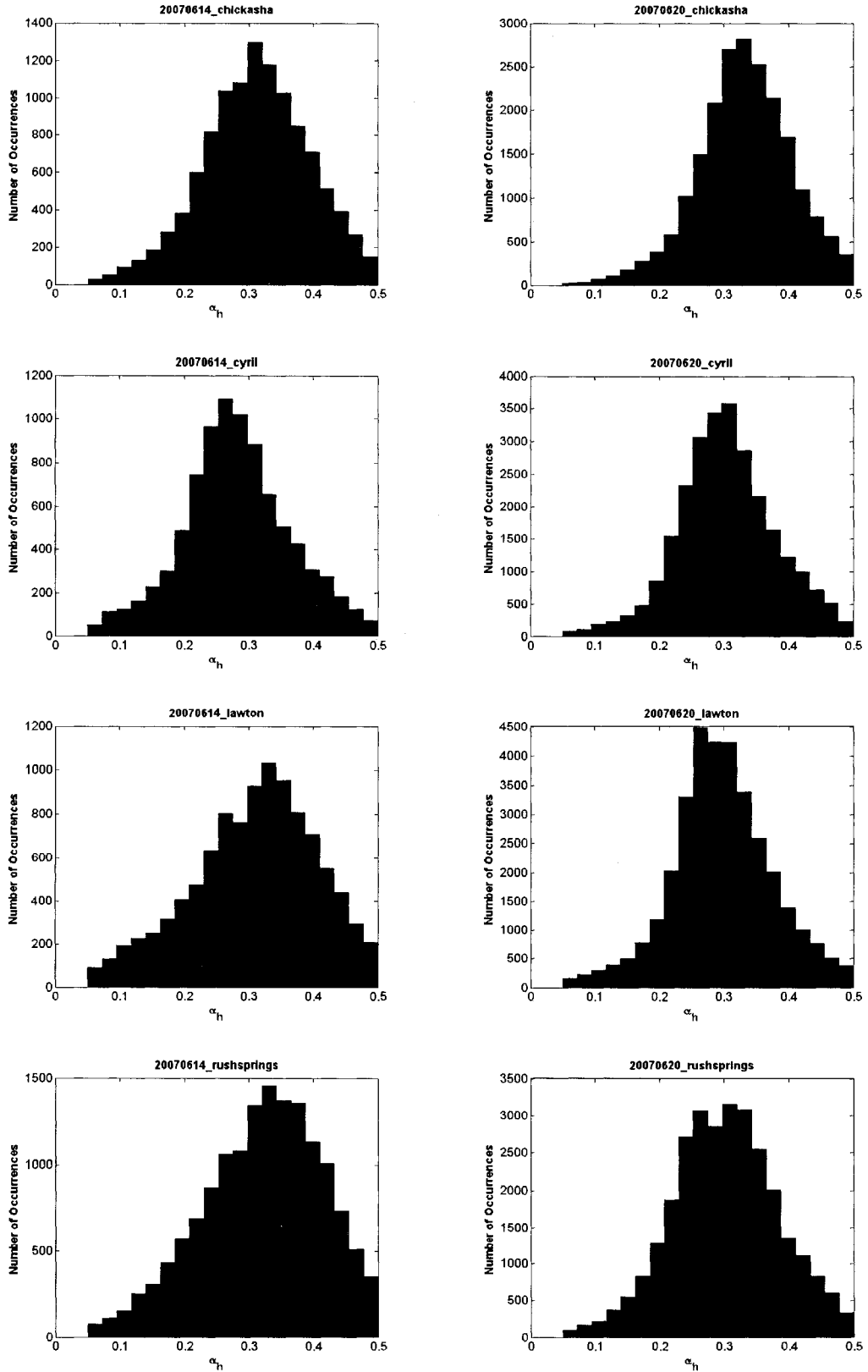


Figure 3.22 (continued). Histograms of the estimated parameter α_h for the events listed in Table (3.6).

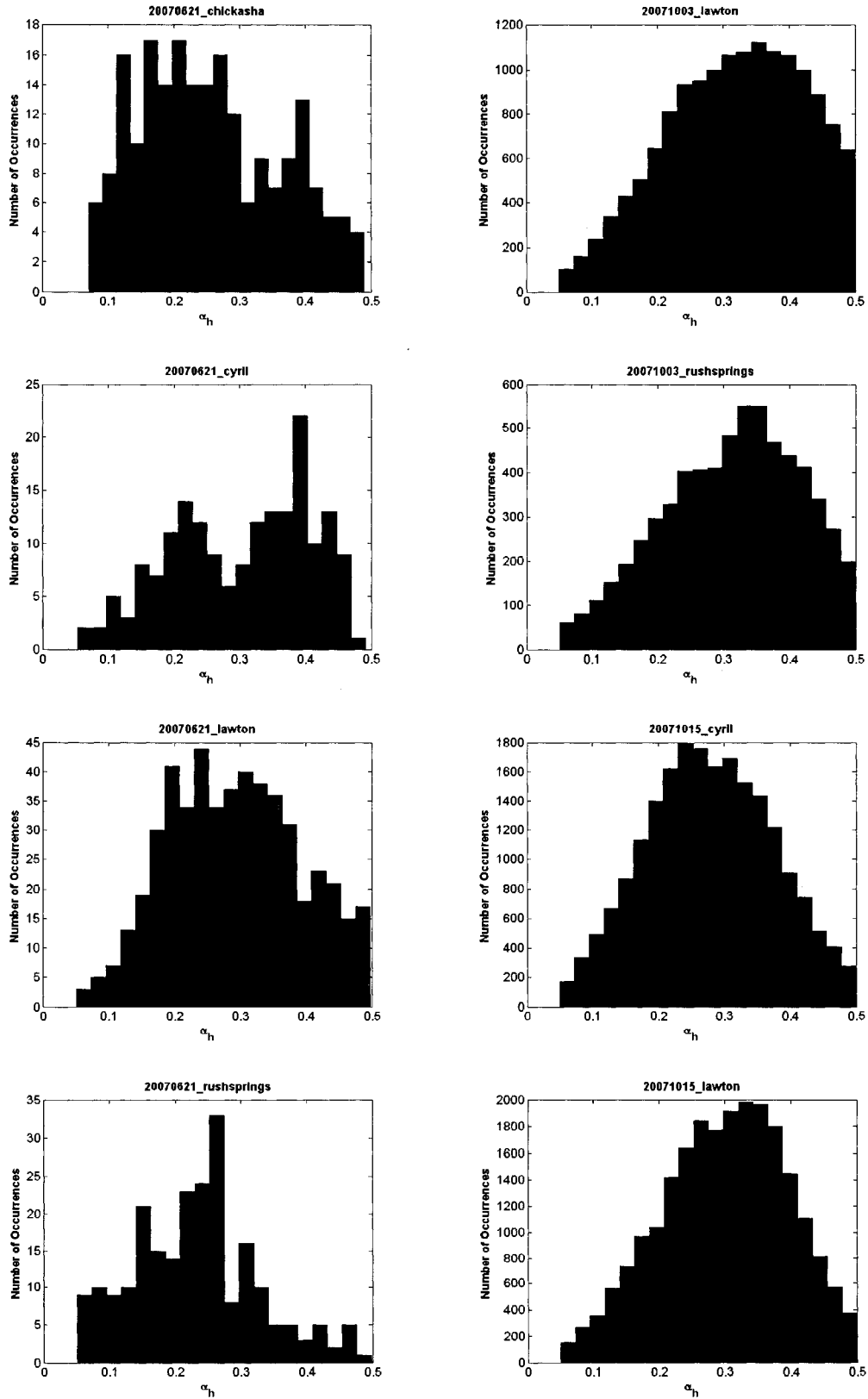


Figure 3.22 (continued). Histograms of the estimated parameter α_h for the events listed in Table (3.6).

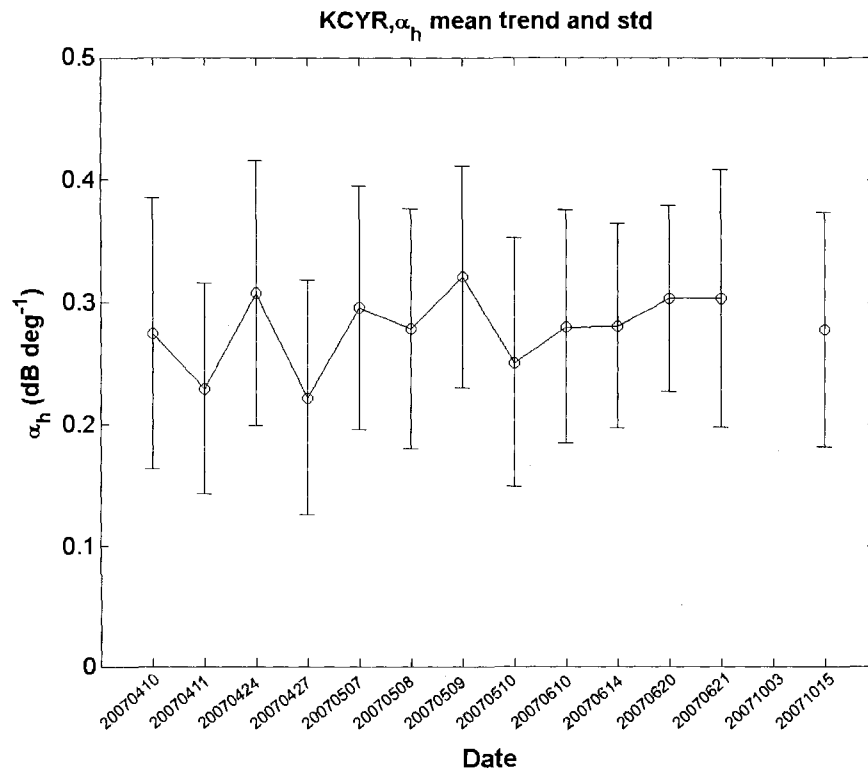
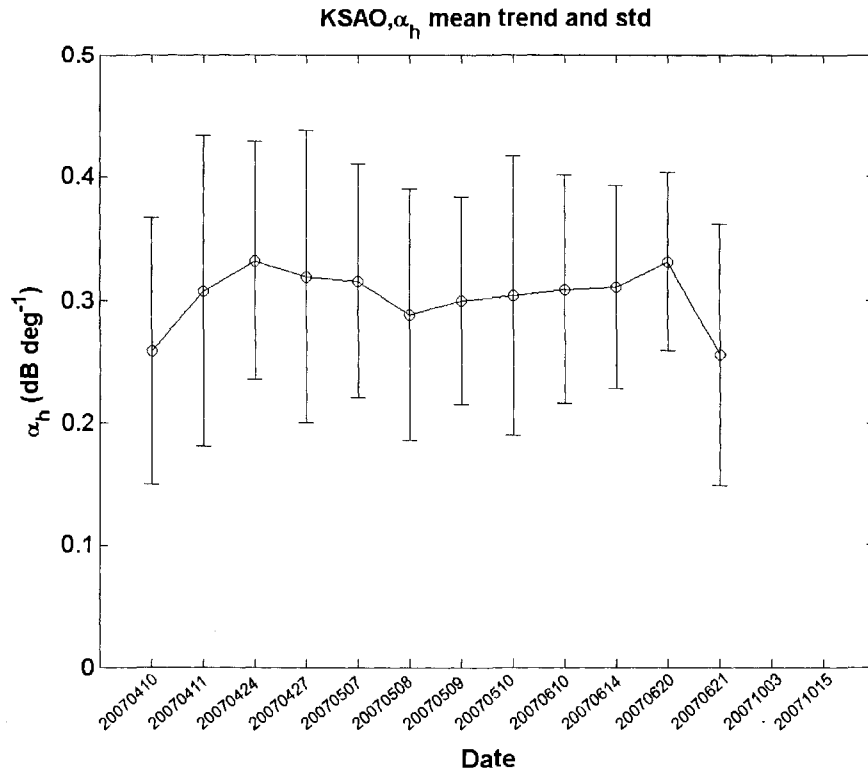


Figure 3.23 The mean values and standard deviations of the estimated parameter α_h plotted along the date of the events.

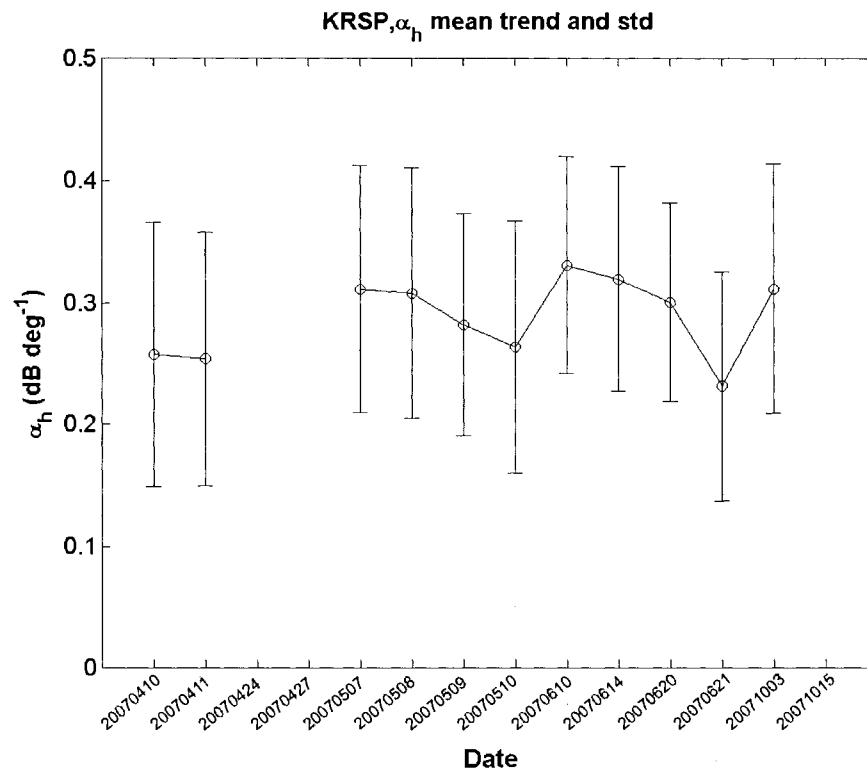
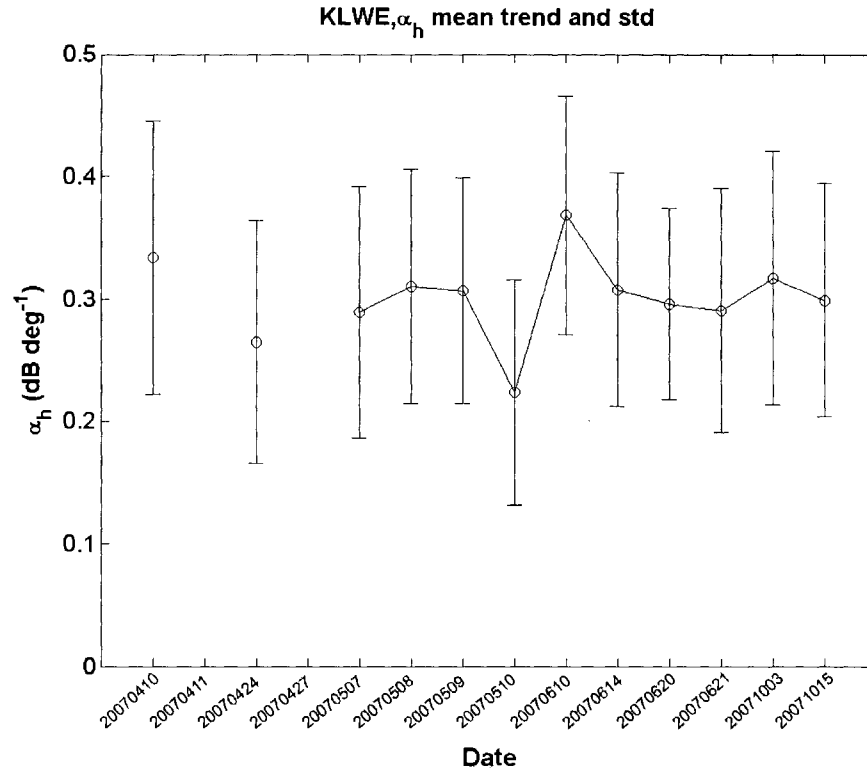


Figure 3.23 (continued) The mean values and standard deviations of the estimated parameter α_h plotted along the date of the events.

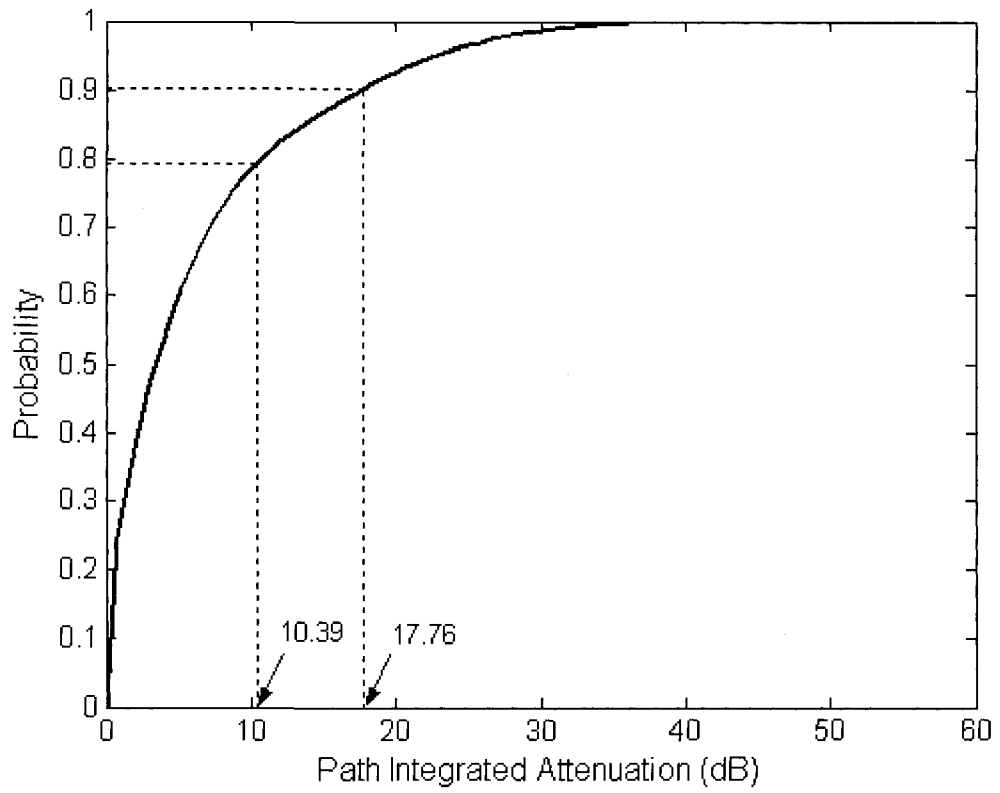


Figure 3.24 Cumulative distribution of path-integrated attenuation for the cases in Table (3.6) from rays below 6 deg elevation angle.

4 OPTIMAL ESTIMATION OF RAIN DIFFERENTIAL ATTENUATION AND CORRECTION OF DIFFERENTIAL REFLECTIVITY

In section 2.5 we reviewed several techniques for the estimation of the specific differential attenuation (A_{dp}) and the attenuation-correction for the differential reflectivity (Z_{dr}) for the rain medium. In this chapter, we are going to present a different approach for this problem. Following similar organization as chapter 3, first we present the mathematical framework. Based on this framework, we find that the principle of the minimization presented in chapter 3 can be reused here. We further test our implementation with simulation and the MPX dual-polarized Doppler radar. The implementation has been running in real time in the CASA IP1 dual-polarized Doppler radar network. Both the simulation results and the results using radar measurements will be presented here.

4.1 Rethinking the estimation of the A_{dp} and correction of Z_{dr}

Previously, the specific differential attenuation has been treated as a continuum, estimated either by the scaling of the estimated specific attenuation (see eq. (2.48b), Bringi et al. (2001)) or by the scaling of the differential propagation phase directly (see eqs. (2.44)-(2.47), Ryzhkov and Znić (1995), Smyth and Illingworth (1998)). However, this continuum can be broken down into two basic components, the specific attenuation at h polarization (A_h) and the specific attenuation at v polarization (A_v), resulting an alternative means to solving the differential attenuation correction problem. Similar to the differential reflectivity (Z_{dr}) which is measured by taking ratio of the reflectivity at h

polarization (Z_h measured through the h -port of the antenna) over the reflectivity at v polarization (Z_v measured through the v -port of the antenna), the A_{dp} fundamentally is the difference between the A_h and the A_v . (see eq. (2.16)). We have demonstrated the optimal estimation of A_h in the previous chapter. In this chapter, we are going to demonstrate an alternative approach to estimate the A_{dp} and correct the Z_{dr} by estimating the A_h and the A_v separately.

A large part of our motivation for taking this approach is to overcome some limitations caused by making assumptions about the ‘true’ Z_{dr} at the end of a rain cell. As we recall the discussion in section 2.5, to satisfy the assumptions about ‘true’ Z_{dr} one of the following two conditions must hold: (a) the rain drops are spherical at the end of the rain cell so that the ‘true’ Z_{dr} is 0 dB; (b) if such region can not be identified, the ‘true’ Z_{dr} can be predicted through a Z_h - Z_{dr} relationship. In the first case, the Z_{dr} has to be calibrated accurately, while in the second both the Z_h and the Z_{dr} . Otherwise, the resulting path-integrated differential attenuation ($PIDA$) will not be correct and thus the accuracy of the differential attenuation correction will degrade.

There are several techniques to calibrate Z_h and Z_{dr} (Gorgucci et al. (1999)). However, it is not common that they are calibrated on a day-to-day basis. The advantage to have the estimated PIA and the estimated $PIDA$ independent of the calibration error is obvious; the calibration error can be adjusted as a constant after the attenuation and differential attenuation correction. Because it is not necessary to rerun the attenuation and differential attenuation correction again on the data if the calibration error is to be corrected, it can

save a lot of post-processing time. Moreover, the retrieval of $PIDA$ and A_{dp} free of distortion caused by the calibration error is also highly desired.

We already know from chapter 3 the improved technique on the A_h (or PIA) estimation is independent of the Z_h calibration error. Based on above discussions, we are motivated to rethink the A_{dp} estimation and consider the A_h and the A_v approach. If we have the A_v also independent of the Z_v calibration error, it is easy to see that the A_{dp} (or the $PIDA$) will be independent of the Z_{dr} calibration error as well.

4.2 The A_h - A_v approach for estimation of A_{dp} and correction of Z_{dr}

In rain medium, the A_v is well-correlated with A_h and the relationship is linear based on T-matrix calculations. Fig. 4.1 shows the scatter plot of the A_h vs. the A_v for several drop shape models with a DSD subset of about 8000 measured DSD samples from disdrometers. It is evident that the cross-correlation coefficient is very high (0.9997) and the relationship is linear.

Similar to the A_h - K_{dp} relationship, the A_v is also well-correlated with the K_{dp} in rain medium (not shown here) and is linear with K_{dp} as:

$$A_v = \alpha_v K_{dp} \quad (4.1)$$

Note that in general the parameter α_v is less than α_h (termed α in previous chapters).

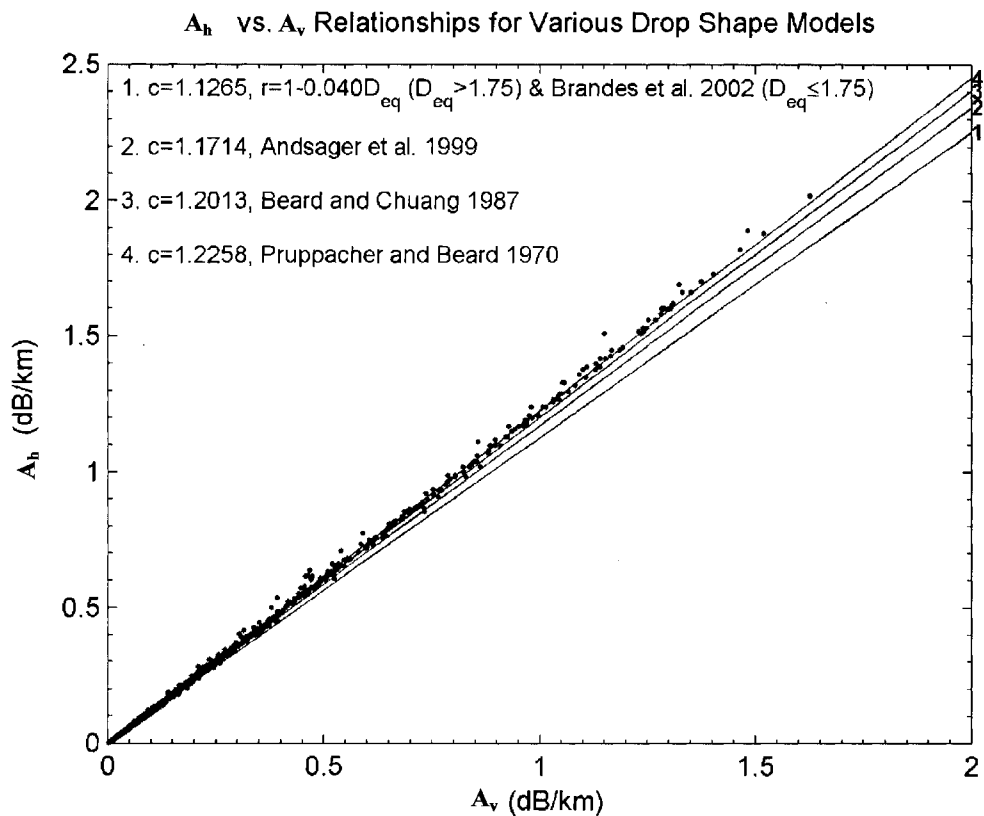


Figure 4.1 A_h vs. A_v relationships at X-band derived based on four different drop shape models in the literature. Black solid lines are the least squares fit to A_h and A_v values calculated from approximated 8000 measured DSDs for each drop shape model. Sample points are shown as black dots for the Pruppacher and Beard (1970) linear model. The cross-correlation coefficient between A_h and A_v is 0.9997.

Based on Hitschfeld and Bordan (1954), we assume the A_v is a power law function of the true Z_v as:

$$A_v = a_v Z_v^{b_v} \quad (4.2)$$

Note that in general the parameters a_v and b_v are different from the parameter a_h and b_h (termed a and b in previous chapters) in the A_h - Z_h relationship.

Based on eqs (4.1) and (4.2), following the exactly same derivation in section 3.2.2 we express the estimated parameter \tilde{a}_v as (see also eq. (3.12)):

$$\tilde{a}_v = \frac{1 - 10^{-0.1b_v\alpha_v(\Phi_{dp}(r_N) - \Phi_{dp}(r_1))}}{0.46b_v \int_1^N Z_{v,m}^{b_v}(s) ds} \quad (4.3)$$

The estimated $\tilde{Z}_{v,e}$ is expressed as (see also eq. (3.13b)):

$$\tilde{Z}_{v,e}(r_i) = Z_{v,m}(r_i) \left(1 - \frac{\int_1^i Z_{v,m}^{b_v}(s) ds}{\int_1^N Z_{v,m}^{b_v}(s) ds}\right) \cdot \left(1 - 10^{-0.1b_v\alpha_v(\Phi_{dp}(r_N) - \Phi_{dp}(r_1))}\right)^{\frac{1}{b_v}} \quad (4.4)$$

The estimated $P\tilde{I}A_\nu$ at ν polarization is expressed as (see also eq. (3.14)):

$$P\tilde{I}A_\nu(r_i) = -\frac{5}{b} \log_{10} \left\{ 1 - \frac{\int_1^i Z_{\nu,m}^{b_\nu}(s) ds}{\int_1^N Z_{\nu,m}^{b_\nu}(s) ds} \cdot (1 - 10^{-0.1b_\nu\alpha_\nu(\Phi_{dp}(r_N) - \Phi_{dp}(r_i))}) \right\} \quad (4.5)$$

The estimated \tilde{A}_ν is expressed as (see also eq. (3.15)):

$$\tilde{A}_\nu(r_i) = \tilde{a}_\nu \tilde{Z}_{\nu,e}^{b_\nu}(r_i) \quad (4.6a)$$

$$= \frac{Z_{\nu,m}^{b_\nu}(r_i)(1 - 10^{-0.1b_\nu\alpha_\nu(\Phi_{dp}(r_N) - \Phi_{dp}(r_i))})}{0.46b_\nu \int_1^N Z_{\nu,m}^{b_\nu}(s) ds - (1 - 10^{-0.1b_\nu\alpha_\nu(\Phi_{dp}(r_N) - \Phi_{dp}(r_i))}) \cdot 0.46b_\nu \int_1^i Z_{\nu,m}^{b_\nu}(s) ds} \quad (4.6b)$$

Based on the estimated $P\tilde{I}A_\nu$, we construct the estimated $\tilde{\Phi}_{dp,\nu}$ as (the subscript ν denotes that the estimation is from $P\tilde{I}A_\nu$; see also eq. (3.17)):

$$\tilde{\Phi}_{dp,\nu}[i] = \frac{2P\tilde{I}A_\nu[i]}{\alpha_\nu} + \Phi_{dp}[1] \quad (4.7a)$$

$$= \frac{10}{\alpha} \log_{10} \left\{ \left(1 - \frac{\sum_{s=1}^i Z_{\nu,m}^{b_\nu}[s] \Delta r}{\sum_{s=1}^N Z_{\nu,m}^{b_\nu}[s] \Delta r} \cdot (1 - 10^{-0.1b_\nu\alpha_\nu(\Phi_{dp}[N] - \Phi_{dp}[1])}) \right)^{\frac{1}{b_\nu}} \right\} + \Phi_{dp}[1] \quad (4.7b)$$

Note that the variables now are presented in vector forms.

Therefore, this results in exactly the same minimization form (but with different parameters and measurement) as eqs. (3.18) and (3.19) as:

$$f_v[i] = \Phi_{dp}[i] - \tilde{\Phi}_{dp,v}[i] \quad (4.8a)$$

$$F_v = \frac{1}{2} \sum_{i=1}^N (f_v[i])^2 = \frac{1}{2} \tilde{f}_v^T \cdot \tilde{f}_v = \frac{1}{2} \|\tilde{f}_v\|^2 \quad (4.8b)$$

where $\tilde{\Phi}_{dp,v}[i]$ is estimated from eq. (4.7).

The estimation of $\tilde{\alpha}_v$ is given here as:

$$\tilde{\alpha}_v = \arg \min_{\alpha_v} (F_v) \quad (4.9)$$

After the minimization converges (using the technique discussed in section 3.2.4), the estimation of $\tilde{Z}_{v,e}$, $P\tilde{I}A_v$, and \tilde{A}_v can be calculated by eqs. (4.4), (4.5) and (4.6), respectively.

Finally together with previously estimated $\tilde{Z}_{h,e}$, $P\tilde{I}A_h$, and \tilde{A}_h (estimated using the improved technique described in chapter 3), the estimated $\tilde{Z}_{dr,e}$, the estimated $P\tilde{I}DA$, and the estimated \tilde{A}_{dp} are given as follows, respectively:

$$\tilde{Z}_{dr,e}(r_i) = \frac{\tilde{Z}_{h,e}(r_i)}{\tilde{Z}_{v,e}(r_i)} \quad (4.10a)$$

$$P\tilde{I}DA(r_i) = P\tilde{I}A_h(r_i) - P\tilde{I}A_v(r_i) \quad (4.10b)$$

$$\tilde{A}_{dp}(r_i) = \tilde{A}_h(r_i) - \tilde{A}_v(r_i) \quad (4.10c)$$

4.3 Stability of the algorithm

It is well known that Z_{dr} is a function of the median volume diameter (D_0) of the DSD and can be directly inverted to retrieve D_0 at non-attenuating frequencies using the Rayleigh - Gans theory for the rain medium (Seliga and Bringi (1976)). It should be noted again here that the deviation of rain drop shape from sphere to oblate spheroid is the key observation that results in that the Z_{dr} , although estimated from dividing (or differentiating in logarithmic scale) two large numbers (Z_h and Z_v), is a meaningful measurement of the D_0 . Because of the oblate shape of the rain drops, Z_h and Z_v are correlated (through the geometry factor as a function of the drop shape; Seliga and Bringi (1976)). At attenuating frequencies when the differential attenuation is not negligible, it is important to maintain this correlation when we correct the measured Z_{dr} for the differential attenuation.

Using previously developed algorithms (e.g., Ryzhkov and Zrnić (1995), Smyth and Illingworth (1998), Bringi et al. (2001)), the correlation is maintained by using the measured Z_{dr} directly in the attenuation-correction algorithms. Here in our algorithm, we first calculate the measured Z_v from the measured Z_h and the measured Z_{dr} (i.e., $Z_v = Z_h - Z_{dr}$ if Z_h and Z_v in dBz and Z_{dr} in dB, or $Z_v = Z_h / Z_{dr}$ if Z_h and Z_v in $\text{mm}^6 \text{m}^{-3}$ and Z_{dr} without units). Then we run the core algorithm twice, first with the measured Z_h and then with the measured Z_v , so that the minimization of the cost functions and the attenuation corrections are performed independently. We will show next when we use eq. (4.10a) to estimate the intrinsic Z_{dr} , the high intrinsic correlation is still maintained.

Here we investigate the correlation of Z_h and Z_v after attenuation-correction using the A_h - A_v estimation algorithm. By expanding eq. (4.10a), we have:

$$\tilde{Z}_{dr,e}(r_i) = \frac{\tilde{Z}_{h,e}(r_i)}{\tilde{Z}_{v,e}(r_i)} \quad (4.11a)$$

$$= \frac{Z_{h,m}(r_i) \left(1 - \frac{\int_1^i Z_{h,m}^{b_h}(s) ds}{\int_1^N Z_{h,m}^{b_h}(s) ds} \cdot (1 - 10^{-0.1b_h\alpha_h(\Phi_{dp}(r_N) - \Phi_{dp}(r_i))})\right)^{\frac{1}{b_h}}}{Z_{v,m}(r_i) \left(1 - \frac{\int_1^i Z_{v,m}^{b_v}(s) ds}{\int_1^N Z_{v,m}^{b_v}(s) ds} \cdot (1 - 10^{-0.1b_v\alpha_v(\Phi_{dp}(r_N) - \Phi_{dp}(r_i))})\right)^{\frac{1}{b_v}}} \quad (4.11b)$$

$$= Z_{dr,m}(r_i) \cdot \frac{\left(1 - \frac{\int_1^i Z_{h,m}^{b_h}(s) ds}{\int_1^N Z_{h,m}^{b_h}(s) ds} \cdot (1 - 10^{-0.1b_h\alpha_h(\Phi_{dp}(r_N) - \Phi_{dp}(r_i))})\right)^{\frac{1}{b_h}}}{\left(1 - \frac{\int_1^i Z_{v,m}^{b_v}(s) ds}{\int_1^N Z_{v,m}^{b_v}(s) ds} \cdot (1 - 10^{-0.1b_v\alpha_v(\Phi_{dp}(r_N) - \Phi_{dp}(r_i))})\right)^{\frac{1}{b_v}}} \quad (4.11c)$$

$$= Z_{dr,m}(r_i) \cdot \frac{p_h(r_i)}{p_v(r_i)} \quad (4.11d)$$

Since both α_h and α_v are allowed to change and are related to a_h and a_v respectively, the estimated $\tilde{Z}_{dr,e}$ are not very sensitive to b_h and b_v . We assign them to the same value that found in Part et al. (2005) (e.g., $b_h = b_v = b = 0.78$).

It is evident that in eq. (4.11d) that using eq. (4.10a) to correct the differential attenuation for Z_{dr} does not alter the correlation in the measured Z_{dr} . Eq. (4.11d) shows that

fundamentally the measured Z_{dr} is implicit in the correction equation (eq. (4.10a)). The factor $\frac{p_h(r_i)}{p_v(r_i)}$ in eq. (4.11d) is the path-integrated differential attenuation factor (i.e., a ratio) converted from the *PIDA*, which decides the amount of the differential attenuation.

Hence, it is important that we make sure that eq. (4.11d) results in a valid candidate of the *PIDA*. Based on the microphysical properties of rain, a valid candidate of the *PIDA* must have $PIDA \geq 0$ dB and be a monotonically increasing function along the range. Here, we are going to prove that the functions $p_h(r_i)$ and $p_v(r_i)$ are both monotonically increasing functions of the range first, although this is quite self-evident. For the function $p_h(r_i)$ we know:

$$\Phi_{dp}(r_N) - \Phi_{dp}(r_1) > 0;$$

$$b = 0.78 > 0;$$

$$\alpha_h > 0;$$

$$Z_{h,m}(r) > 0 \quad \forall r \in [r_1, r_N].$$

Therefore, we have:

$$(1 - 10^{-0.1b_h\alpha_h(\Phi_{dp}(r_N) - \Phi_{dp}(r_1))}) > 0;$$

$$q_h(r_i) = \frac{\int_{r_1}^{r_i} Z_{h,m}^{b_h}(s) ds}{\int_{r_1}^{r_N} Z_{h,m}^{b_h}(s) ds} \text{ is a monotonically increasing function of } r_i;$$

$l_h(r_i) = 1 - q_h(r_i) \cdot (1 - 10^{-0.1b_h\alpha_h(\Phi_{dp}(r_N) - \Phi_{dp}(r_i))})$ is a monotonically decreasing function of r_i .

Therefore $p_h(r_i) = l_h(r_i)^{\frac{1}{b}}$ is a monotonically increasing function of r_i . (same for $p_v(r_i)$ following the similar proof). It is also easy to verify that $p_h(r_i) \geq 1 \forall r \in [r_1, r_N]$. The monotonically increasing trend and the greater than or equal to unity are two necessary conditions for any functions that are candidates to correct the attenuation for the measured Z_h (and the measured Z_v) of the rain medium. This is based on the physics that the specific attenuation is greater than or equal to zero (absorption of the electromagnetic energy by rain drop) and hence results in a monotonically increasing PIA greater than or equal to 0 dB.

Now we are going to deduce the necessary conditions for a candidate function to be a valid function for correcting the measured Z_{dr} of the rain medium. Because of the oblate rain drop shape, the energy is absorbed more at the h polarization aligned with the major axis of the rain drop spheroid than at the v polarization aligned with the minor axis of the rain drop spheroid. Hence after correcting for the differential attenuation we must have:

$$\tilde{Z}_{dr,e}(r_i) \geq Z_{dr,m}(r_i) \quad (4.12)$$

This is equivalent to:

$$\frac{p_h(r_i)}{p_v(r_i)} \geq 1 \quad (4.13)$$

Since we know:

$$p_h(r_i) \geq 1$$

$$p_v(r_i) \geq 1$$

$$-b < 0$$

If we ensure:

$$p_h^{-b}(r_i) \leq p_v^{-b}(r_i) \tag{4.14}$$

we will satisfy the inequality (4.13). Substitute $p_h(r_i)$ and $p_v(r_i)$ into inequality (4.14), we have:

$$1 - \frac{\int_1^i Z_{h,m}^b(s) ds}{\int_1^N Z_{h,m}^b(s) ds} \cdot (1 - 10^{-0.1b\alpha_h(\Phi_{dp}(r_N) - \Phi_{dp}(r_i))}) \leq 1 - \frac{\int_1^i Z_{v,m}^b(s) ds}{\int_1^N Z_{v,m}^b(s) ds} \cdot (1 - 10^{-0.1b\alpha_v(\Phi_{dp}(r_N) - \Phi_{dp}(r_i))})$$

$$\frac{\int_1^i Z_{h,m}^b(s) ds}{\int_1^N Z_{h,m}^b(s) ds} \cdot (1 - 10^{-0.1b\alpha_h(\Phi_{dp}(r_N) - \Phi_{dp}(r_i))}) \geq \frac{\int_1^i Z_{v,m}^b(s) ds}{\int_1^N Z_{v,m}^b(s) ds} \cdot (1 - 10^{-0.1b\alpha_v(\Phi_{dp}(r_N) - \Phi_{dp}(r_i))}) \tag{4.15}$$

Therefore, inequality (4.15) is a necessary condition that $\frac{p_h(r_i)}{p_v(r_i)}$ can be used to correct the measured Z_{dr} using eq. (4.11d).

It can be seen that to satisfy inequality (4.15), the parameters α_h and α_v should be carefully chosen. Because the quantities $Z_{h,m}$ and $Z_{v,m}$ are already determined after the radar finishes collecting data for a given range profile, the satisfaction of inequality (4.15) totally depends on the parameters α_h and α_v . In the minimization, there is no mechanism yet to ensure inequality (4.15) will be always satisfied (but empirically from our simulation and data analysis, it is often the case that the estimations of α_h and α_v satisfy the inequality). Therefore, it is important to test the estimated α_h and α_v to ensure that inequality (4.15) is satisfied. However, there is a quicker but less stringent criterion to test that solution eq. (4.11d) is valid than testing inequality (4.15). Recall that the specify attenuation at h and v polarization, respectively is related to the specific propagation phase as:

$$A_h = \alpha_h K_{dp} \quad (4.16)$$

$$A_v = \alpha_v K_{dp} \quad (4.17)$$

If we enforce that $\alpha_h \geq \alpha_v$, we will have:

$$A_{dp} = A_h - A_v = (\alpha_h - \alpha_v) K_{dp} \geq 0 \quad (4.18)$$

If we also enforce that $K_{dp} \geq 0$, eq. (4.18) will satisfy the requirement for the specific differential attenuation for the rain medium and hence the requirement for *PIDA*. Since our solution of eq. (4.11d) is derived from the two fundamental equations (i.e., eqs (4.1) and (4.2)), enforcing $\alpha_h \geq \alpha_v$ would increase greatly the possibility that inequality (4.15) is satisfied.

4.4 Simulation results

In the section we extend the same simulation setup used in section 3.3 to evaluate the A_h - A_v algorithm on simulated radar measurement profiles. Following the same procedure, the intrinsic Z_{dr} and the intrinsic A_{dp} are generated by the T-Matrix method for the constant DSD case and the variable DSD case. The measured Z_{dr} is then calculated from the above two variables along the range. Next the measured Z_{dr} , the measured Z_h , and the measured Φ_{dp} are ingested into the A_h - A_v algorithm where the estimated A_{dp} and the estimated intrinsic Z_{dr} are outputted. The estimation results are then compared with the simulation input and the performance of the A_h - A_v algorithm is evaluated through the mean error and the root squared mean error between the input and output for the whole range profile.

4.4.1 Constant DSD case

The constant DSD profile used here is the same as that in section 3.3.1. The organization of this section is similar to that of section 3.3.1. First, we evaluate the A_h - A_v algorithm for the Pruppacher and Beard (1970) drop shape model. The ideal situation with no

measurement errors will be evaluated first and later the more realistic situation with simulated Gaussian noise. Then the study is extended to include more drop shape models available in the literature and the metrics of merit such as mean error and RMSE are presented using tables.

Fig. 4.2 shows the intrinsic Z_{dr} , the measured (attenuated) Z_{dr} , and the corrected (estimated) Z_{dr} . As expected, the measured Z_{dr} appears decreasing along the path because of the monotonically increasing $PIDA$. The $PIDA$ is approximately 3 dB at 40 km. The estimated Z_{dr} (the algorithm output using eq. (4.10a)) appears to be a very good match when compared with the intrinsic Z_{dr} (the simulation input). Fig. 4.3 shows the intrinsic A_{dp} (the simulation input) and the estimated A_{dp} (the algorithm output). Note that the A_{dp} is estimated by eq. (4.10c) by separately estimate A_h and A_v first. The estimated A_{dp} is close to the intrinsic A_{dp} but slightly underestimated. However, the estimation remains valid (≥ 0) across the whole range. Using the minimization scheme, the parameter α_v is estimated to be 0.16363, which is smaller than the estimated α_h (0.19713) previously shown in section 3.3.1. This satisfies the requirement discussed earlier in the previous section, hence it results the valid estimation of A_{dp} .

The estimated Φ_{dp} by using Z_v and α_v as in eq. (4.7) is not shown here because of the similarity to estimated Φ_{dp} by using Z_h and α_h as in eq. (3.17) (see Fig. 3.3). Both eqs. (3.17) and (4.7) estimate the Φ_{dp} very well. This indicates that the minimization is indeed exploiting the consistency in the Z_h - K_{dp} discussed in chapter 3 and the consistency principle is also applicable to the Z_v - K_{dp} relationship. It is the consistency that enables the

parameter α_v to be retrieved consistently, satisfying the requirement discussed in the previous section. We will continue to see this observation as we progress with more simulation results.

It is expected as we alter the drop shape model the estimation will be able to adapt to such change. This is shown in Table (4.1). It is evident that the estimated parameter α_v changes with the drop shape model and it adapts to the measured Φ_{dp} in a least-squares sense. Such adaptation results the mean error and RMSE to remain consistently good across all the drop shape models tested here. The estimated parameter α_h from the previous result is also shown here next to the column of the estimated parameter α_v . It can be seen that these two estimated parameters are well apart from each other and meet the requirement discussed in the previous section.

Next we evaluate the A_h - A_v algorithm under some noisy environment. In addition to the Gaussian noise added to the measured Z_h and the measured Φ_{dp} that are described in section 3.3.1, we add Gaussian noise with 0 mean and a standard deviation of 0.2 dB to the measured Z_{dr} . This is shown in Fig. 4.4. The A_h - A_v algorithm performs quite well in this noisy situation, as the estimated (corrected) Z_{dr} shown also in Fig. 4.4 appears to align with the intrinsic Z_{dr} very well. The estimated A_{dp} for this case is shown with the intrinsic A_{dp} in Fig. 4.5. As expected the estimated A_{dp} is fluctuating around the intrinsic value along the range because of the noises both in the Z_h and Z_{dr} measurements. Nevertheless, the estimated A_{dp} appears to be unbiased which is very important for the corrected Z_{dr} to be used in estimating parameter D_0 of the DSD.

The parameter α_v for this case is estimated to be 0.15814 which is slightly lower than that for the case without noise. This is expected within the error. It is more important that the parameter α_h and the parameter α_v satisfy the requirement discussed in the previous section. They indeed satisfy the requirement as the parameter α_h is estimated to be significantly larger than the parameter α_v (see Table (4.2)).

Extending the analysis for other drop shape model, we list the mean error and RMSE for the algorithm output compared with the simulation input in the Table (4.2). Once again, the A_h - A_v algorithm appears to perform very well even under the noisy environment.

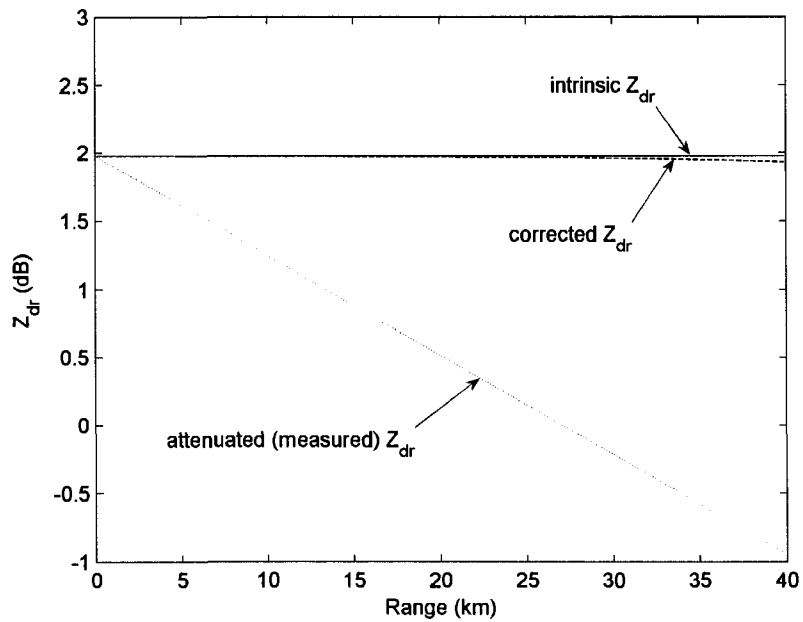


Figure 4.2 Range profiles of the intrinsic Z_{dr} , the attenuated Z_{dr} , and the corrected Z_{dr} . The profiles are based on a constant exponential DSD profile and the Pruppacher and Beard (1970) drop shape model.

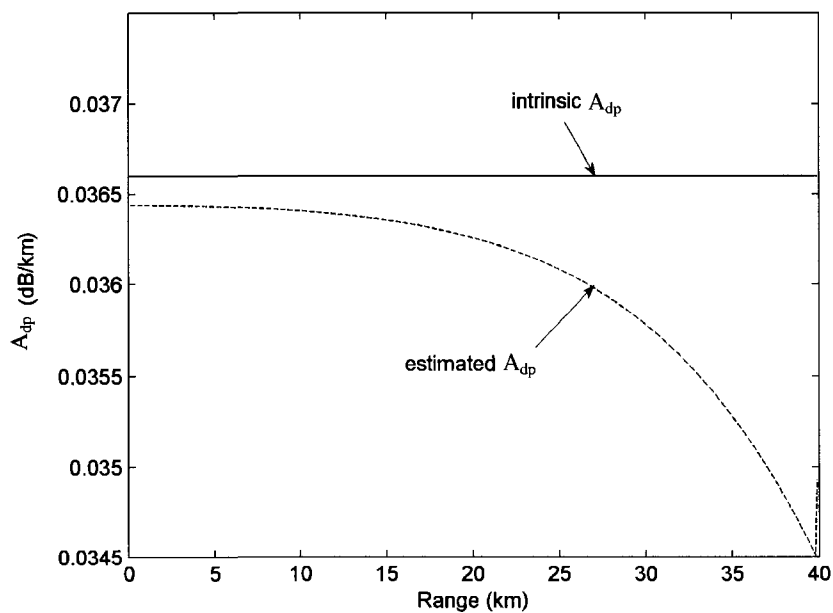


Figure 4.3 Range profiles of the intrinsic A_{dp} and the retrieved A_{dp} . The profiles are based on a constant exponential DSD profile and the Pruppacher and Beard (1970) drop shape model.

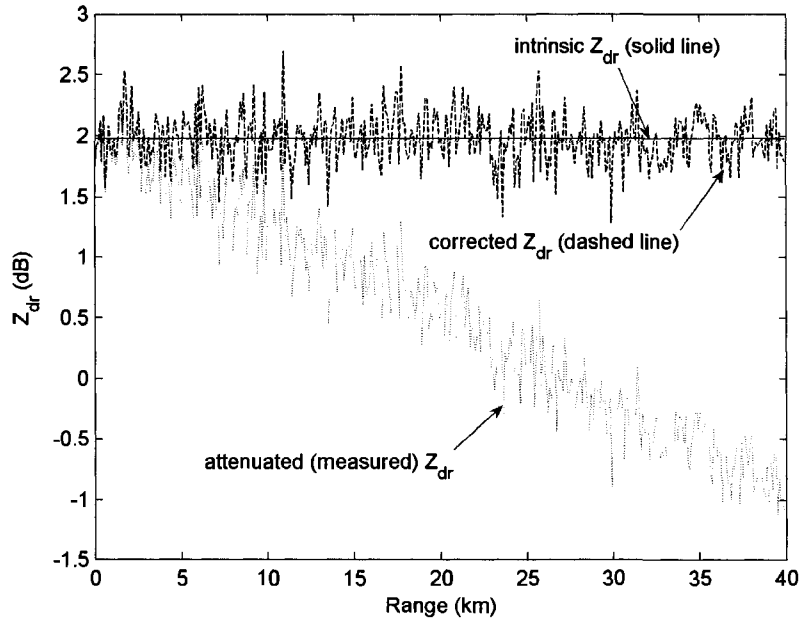


Figure 4.4 Range profiles of the intrinsic Z_{dr} , the attenuated Z_{dr} , and the corrected Z_{dr} . The profiles are based on a constant exponential DSD profile and the Pruppacher and Beard (1970) drop shape model. Measurement noise is added to the attenuated Z_{dr} .

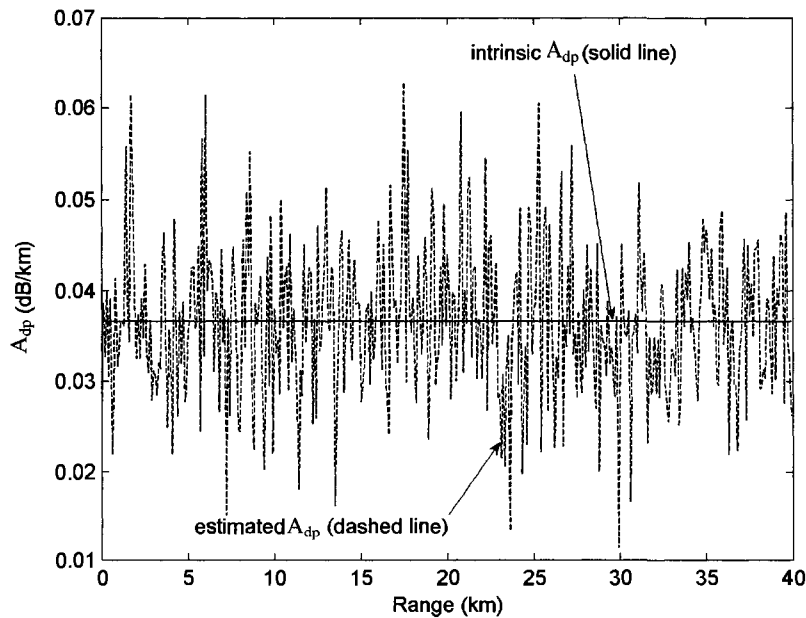


Figure 4.5 Range profiles of the intrinsic A_{dp} and the retrieved A_{dp} . Profiles are based on a constant exponential DSD profile and the Pruppacher and Beard (1970) drop shape model. The estimated A_{dp} is retrieved from the noisy measurements of Z_h , Z_{dr} and Φ_{dp} .

Table 4.1 Estimated α_h and α_v , mean error(intrinsic – retrieved), and RMSE evaluated with several drop shape models in the literature. Constant DSD. No measurement errors.

DROP SHAPE MODELS	ESTIMATED PARAMETERS		MEAN ERROR		RMSE	
	α_h (dB/deg)	α_v (dB/deg)	Z_{dr} (dB)	A_{dp} (dB/km)	Z_{dr} (dB)	A_{dp} (dB/km)
Pruppacher and Beard 1970	0.19283	0.16001	0.0127	0.00058	0.0174	0.00077
Beard and Chuang 1987	0.24511	0.20841	0.0111	0.00050	0.0151	0.00067
Andsager et al. 1999	0.29094	0.25354	0.0093	0.00042	0.0127	0.00055
Mixed model (linear for large drops, Brandes et al. 2002 for small drops),linear slope=0.040mm ⁻¹	0.36707	0.33269	0.0066	0.00029	0.0089	0.00037
Mixed model (linear for large drops, Brandes et al. 2002 for small drops),linear slope=0.060mm ⁻¹	0.20121	0.16840	0.0121	0.00055	0.0166	0.00073
Mixed model (linear for large drops, Brandes et al. 2002 for small drops),linear slope=0.070mm ⁻¹	0.16583	0.13289	0.0152	0.00070	0.0208	0.00093

Table 4.2 Estimated α_h and α_v , mean error (intrinsic – retrieved), and RMSE evaluated with several drop shape models in the literature. Constant DSD. Gaussian noises with zero means are added to the measurements. $\sigma_n(Z_h)=0.8$ dBZ, $\sigma_n(Z_{dr})=0.2$ dB, $\sigma_n(\Phi_{dp})=3$ deg.

DROP SHAPE MODELS	ESTIMATED PARAMETERS		MEAN ERROR		RMSE	
	α_h (dB/deg)	α_v (dB/deg)	Z_{dr} (dB)	A_{dp} (dB/km)	Z_{dr} (dB)	A_{dp} (dB/km)
Pruppacher and Beard 1970	0.19093	0.15814	0.0218	0.00062	0.1969	0.00788
Beard and Chuang 1987	0.24563	0.20920	0.0151	0.00074	0.1952	0.00816
Andsager et al. 1999	0.29512	0.25825	0.0381	0.00080	0.2002	0.00751
Mixed model (linear for large drops, Brandes et al. 2002 for small drops),linear slope=0.040mm ⁻¹	0.36638	0.33138	0.1911	0.00701	0.1911	0.00701
Mixed model (linear for large drops, Brandes et al. 2002 for small drops),linear slope=0.060mm ⁻¹	0.20167	0.16893	-0.0020	0.00063	0.1971	0.00790
Mixed model (linear for large drops, Brandes et al. 2002 for small drops),linear slope=0.070mm ⁻¹	0.16346	0.13079	0.0272	0.00104	0.2029	0.00829

4.4.2 Variable DSD case

It is well known that Z_{dr} is a function of the median volume diameter (D_0) of the DSD (Seliga and Bringi (1976)). In principle, the intrinsic Z_{dr} should not be affected by the N_w parameter of the DSD of the exponential form because it is cancelled out during the calculation. But since the N_w constant is fundamentally inherent by specifying a constant parameter a over the path and both Z_h and Z_v are corrected individually, it is necessary here again to revisit this problem for correcting Z_{dr} . In this section, similar to the section 3.3.2, we use the same variable DSD range profile to generate Z_{dr} and A_{dp} values in addition to the already available Z_h , A_h , and K_{dp} values obtained in section 3.3.2.

The Pruppacher and Beard (1970) drop shape is assumed first under ideal conditions. Fig. 4.6 shows the intrinsic Z_{dr} , the measured Z_{dr} , the estimated (corrected) Z_{dr} . Note that both the intrinsic Z_{dr} and the measured Z_{dr} are obtained from the simulation input, while the estimated (corrected) Z_{dr} is obtained by the A_h - A_v algorithm output. It is amazing that the estimated Z_{dr} follows the intrinsic Z_{dr} so closely that they cannot be distinguished visually. The good estimation of Z_{dr} results from the good estimation of the A_{dp} , which is shown in Fig. 4.7. Indeed, the A_{dp} estimated by taking the difference of A_h - A_v does follow very well the trend of the simulated intrinsic A_{dp} . It also stays positive along the whole range hence satisfies the requirement discussed in section 4.3.

Table (4.3) shows the mean error and RMSE when the algorithm is applied to several other drop shape models. The change both in the parameters α_h and α_v is as expected. More importantly, they change consistently and satisfy the requirement for using the A_h -

A_v algorithm. The mean error and RMSE remain very good across all the drop shape models tested here.

Similarly, the Gaussian noise (see previous section) is added next. Fig. 4.8 shows the difference of the intrinsic Z_{dr} minus the estimated (corrected) Z_{dr} . The standard deviation of the difference is estimated to be 0.2 dB, which is the same as the Gaussian noise added to the measured Z_{dr} . The estimated Z_{dr} appears to be unbiased since the mean of the difference is approximately 0 dB. Fig. 4.9 shows the difference of the intrinsic A_{dp} - the estimated (corrected) A_{dp} . The noisy appearance is noticed here and it is directly transferred from the noisy measured Z_h and the noisy measured Z_{dr} . Although it is not shown here, the estimated A_{dp} stays positive along the whole range hence satisfies the requirement discussed in section 4.3. The standard deviation of the difference is estimated to be about 0.01 dB/km.

The estimated parameters, the mean error and the RMSE of the Z_{dr} and A_{dp} are shown in the Table (4.4) for this case and other drop shape models. The mean error and the RMSE are slight degraded because of the noise but it is more important that the parameters are estimated consistently following the change of the drop shape model.

4.4.3 Sensitivity of the parameter α_v on temperature

We evaluate the sensitivity of the parameter α_v due to the change of the environment temperature here. Table (4.5) shows the estimated parameter α_v at different environmental

temperatures for the Pruppacher and Beard (1970) drop shape model in an ideal condition. Four different environmental temperatures are used here, e.g., 0°C, 10°C, 20°C and 30°C, respectively. As expected, the parameter α_v is slightly sensitive to the temperature similarly to that shown for α_h in section 3.3.3. However the range of the change is much less compared with that due to the change of the drop shape. The metrics of merit for the estimated A_{dp} and the corrected Z_{dr} are shown in Table (3.5) for each temperature.

4.4.4 Error introduced by using fixed α_h and α_v

In the end of this simulation study we show the effect of using fixed α_h and α_v , estimated *a priori* and potentially in error. In this case, the optimization is not performed. We assume the fixed values deviate from the ‘true’ values by ± 0.05 dB/deg (about 20% error). The corrected Z_{dr} is plotted for the constant DSD and the Pruppacher and Beard (1970) drop shape model in an ideal condition and shown in Fig. 4.10. The corrected Z_{dr} appears to be biased quite severely over the path. Therefore, we do not recommend using *a priori* fixed α_h and α_v to correct rain differential attenuation at X-band, unless it is known very accurately.

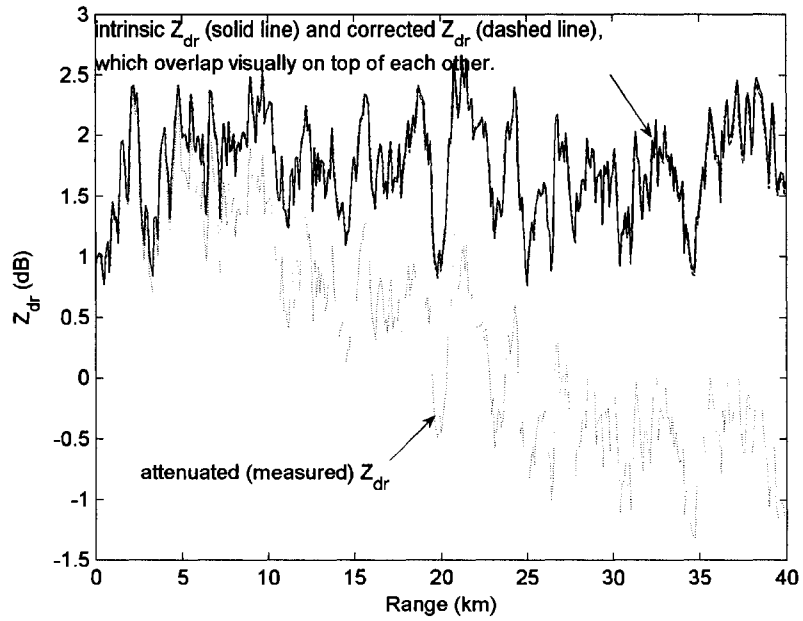


Figure 4.6 Range profiles of the intrinsic Z_{dr} , the attenuated Z_{dr} , and the corrected Z_{dr} . The profiles are based on a variable DSD range profile and the Pruppacher and Beard (1970) drop shape model.

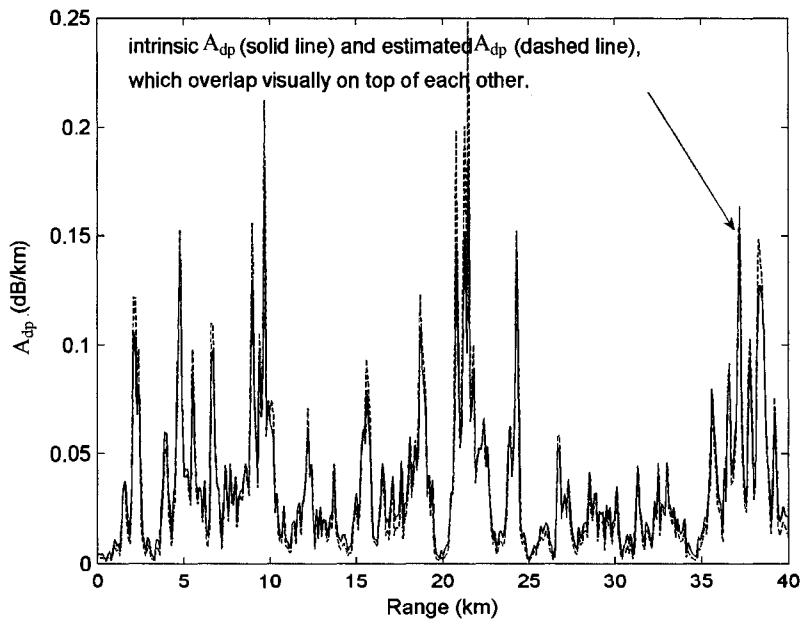


Figure 4.7 Range profiles of the intrinsic A_{dp} and the retrieved A_{dp} . The profiles are based on a variable DSD range profile and the Pruppacher and Beard (1970) drop shape model.

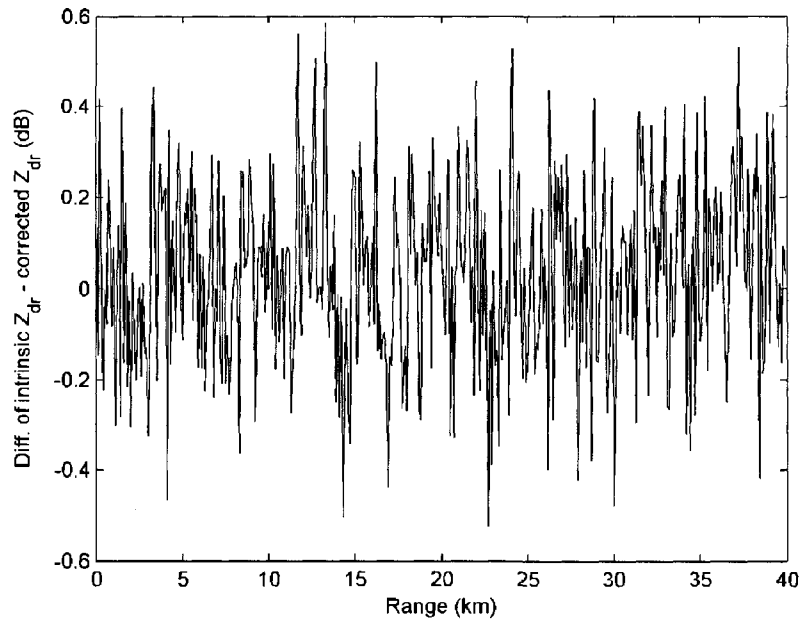


Figure 4.8 Profile of difference of the intrinsic Z_{dr} – the corrected Z_{dr} . The profile is based on a variable DSD range profile and the Pruppacher and Beard (1970) drop shape model. The corrected Z_{dr} is obtained by correcting the noisy measured Z_{dr} for attenuation.

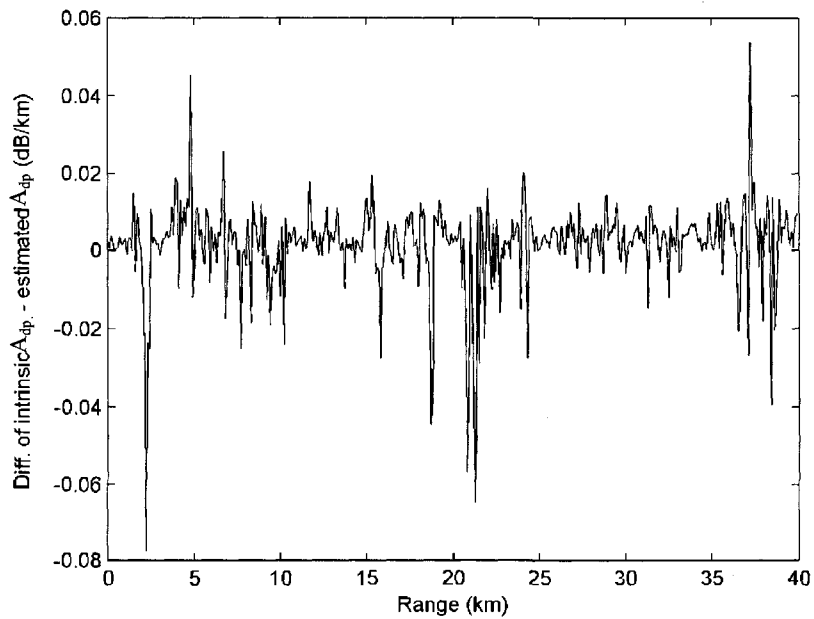


Figure 4.9 Profile of difference of the intrinsic A_{dp} – the estimated A_{dp} . The profile is based on a variable DSD range profile and the Pruppacher and Beard (1970) drop shape model. The estimated A_{dp} is computed by the non-linear model with the converged α_h and α_v under condition of noisy measurements.

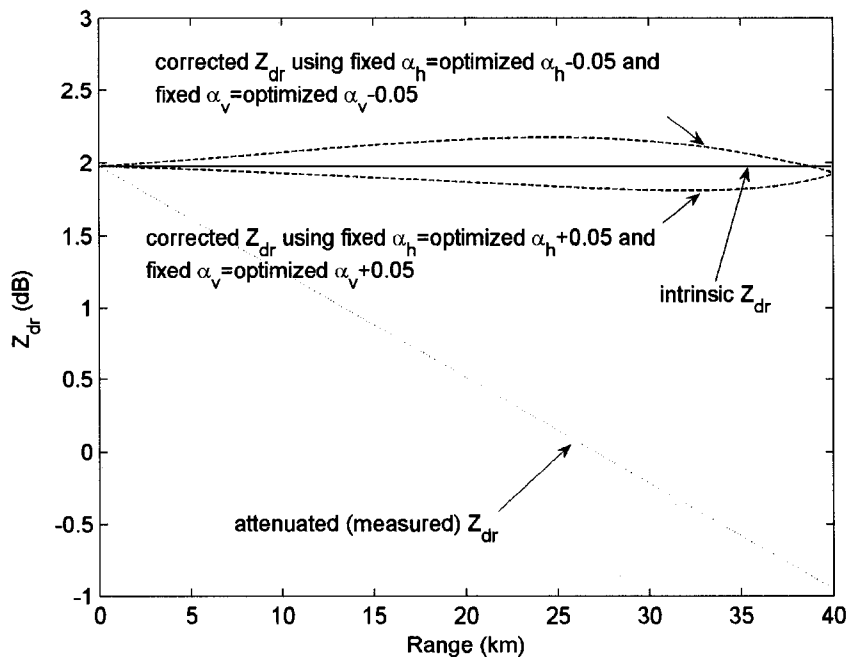


Figure 4.10 Corrected Z_{dr} with fixed α_h and α_v values in error.

Table 4.3 Estimated α_h and α_v , mean error (intrinsic – retrieved), and RMSE evaluated with several drop shape models in the literature. Variable DSD. No measurement errors.

DROP SHAPE MODELS	ESTIMATED PARAMETERS		MEAN ERROR		RMSE	
	α_h (dB/deg)	α_v (dB/deg)	Z_{dr} (dB)	A_{dp} (dB/km)	Z_{dr} (dB)	A_{dp} (dB/km)
Pruppacher and Beard 1970	0.19713	0.16363	0.0198	0.00077	0.0283	0.00745
Beard and Chuang 1987	0.24887	0.21121	0.0159	0.00064	0.0269	0.00890
Andsager et al. 1999	0.29531	0.25667	0.0120	0.00050	0.0250	0.00959
Mixed model (linear for large drops, Brandes et al. 2002 for small drops),linear slope=0.040mm ⁻¹	0.37739	0.34206	0.0093	0.00037	0.0112	0.00201
Mixed model (linear for large drops, Brandes et al. 2002 for small drops),linear slope=0.060mm ⁻¹	0.20579	0.17227	0.0189	0.00074	0.0266	0.00681
Mixed model (linear for large drops, Brandes et al. 2002 for small drops),linear slope=0.070mm ⁻¹	0.16933	0.13575	0.0242	0.00094	0.0359	0.01005

Table 4.4 Estimated α_h and α_v , mean error (intrinsic – retrieved), and RMSE evaluated with several drop shape models in the literature. Variable DSD. Gaussian noises with zero means are added to the measurements. $\sigma_n(Z_h)=0.8$ dBZ, $\sigma_n(Z_{dr})=0.2$ dB, $\sigma_n(\Phi_{dp})=3$ deg.

DROP SHAPE MODELS	ESTIMATED PARAMETERS		MEAN ERROR		RMSE	
	α_h (dB/deg)	α_v (dB/deg)	Z_{dr} (dB)	A_{dp} (dB/km)	Z_{dr} (dB)	A_{dp} (dB/km)
Pruppacher and Beard 1970	0.19467	0.16143	0.0325	0.00103	0.2041	0.01204
Beard and Chuang 1987	0.24677	0.20927	0.0325	0.00078	0.2060	0.01424
Andsager et al. 1999	0.29042	0.25221	0.0132	0.00078	0.1991	0.01339
Mixed model (linear for large drops, Brandes et al. 2002 for small drops),linear slope=0.040mm ⁻¹	0.37461	0.33863	-0.0193	0.00003	0.2041	0.00915
Mixed model (linear for large drops, Brandes et al. 2002 for small drops),linear slope=0.060mm ⁻¹	0.20013	0.16681	0.0355	0.00093	0.2065	0.01330
Mixed model (linear for large drops, Brandes et al. 2002 for small drops),linear slope=0.070mm ⁻¹	0.16842	0.13445	0.0152	0.00047	0.2110	0.01376

Table 4.5 Estimated α_h and α_v , mean error (intrinsic – retrieved), and RMSE evaluated with the Pruppacher and Beard (1970) drop shape model at environmental temperature of 0°C, 10°C, 20°C, and 30°C, respectively. Variable DSD. No measurement errors.

DROP SHAPE MODEL AND TEMPERATURE	OPTIMIZED COEFFICIENTS		MEAN ERROR		RMSE	
	α_h (dB/deg)	α_v (dB/deg)	Z_{dr} (dB)	A_{dp} (dB/km)	Z_{dr} (dB)	A_{dp} (dB/km)
Pruppacher and Beard 1970, 0°C	0.20245	0.17015	0.0194	0.00075	0.0291	0.00913
Pruppacher and Beard 1970, 10°C	0.20186	0.16901	0.0195	0.00076	0.0289	0.00853
Pruppacher and Beard 1970, 20°C	0.19713	0.16363	0.0198	0.00077	0.0283	0.00745
Pruppacher and Beard 1970, 30°C	0.18790	0.15401	0.0204	0.00078	0.0276	0.00606

4.5 Results using radar measurements

4.5.1 A Typhoon case study using MP-X radar data

The same Typhoon case studied in the previous chapter for validating the improvement of the A_h estimation and correction for Z_h is studied here again for the similar validation purpose but for the A_{dp} estimation and correction for Z_{dr} .

Fig. 4.11(a) shows a plan position indicator (PPI) scan image of the measured Z_{dr} at elevation angle 2.5 deg, which is the same scan as the one shown for Z_h in Fig. 3.16. The measured Z_{dr} becomes negative in the region where the strong A_h is estimated for Z_h (compared with Fig. 3.16). This agrees with our analysis of the A_{dp} characteristics in the previous sections that Z_h is attenuated more than Z_v in rain. Fig. 4.11(b) shows the corrected Z_{dr} by the A_h - A_v method. As expected, the corrected Z_{dr} reveals the second intensive core beyond around 20 km to the north-west of the radar consistent with the corrected Z_h shown in Fig. 3.16(b).

Fig. 4.12 shows the measured Z_{dr} , the corrected Z_{dr} using Park et al. (2005) method, and the corrected Z_{dr} using the A_h - A_v method plotted along the range at the same azimuth angle, 294 deg as the Z_h plotted in Fig. 3.17. The calculated values of the intrinsic Z_{dr} from DSD data collected by the three distrometers are also shown as three asterisks at the respective ranges where the distrometers were situated. The calculated intrinsic Z_{dr} values provide ground truth to validate and compare the two algorithms evaluated here. It is clear that Park et al. (2005) method and the A_h - A_v method both agree with the intrinsic Z_{dr}

values well, except that for the second nearest disdrometer there is about 0.45 dB discrepancy between the disdrometer and the corrected Z_{dr} by Park et al. (2005) method, while there is about 0.25 dB discrepancy between the disdrometer and the corrected Z_{dr} by the A_h-A_v method. Given the statistical variations in both the MP-X radar ($\sigma(Z_{dr}) \approx 0.2$ dB) and the Joss disdrometers, both discrepancies are acceptable. However, the advantage of correcting the Z_{dr} without the use of a Z_h-Z_{dr} empirical relationship (see section 4.1) is certainly welcome here, especially as there could be also potential Z_h or Z_{dr} calibration errors that needs to be corrected for (the data shown here were already calibrated: Park et al. (2005)). Perhaps, the 0.2 dB improvement by the A_h-A_v method over Park et al. (2005) method is the result of removing the potential error caused by using a Z_h-Z_{dr} empirical relationship. In fact, Park et al (2005 Part II) show the expected error in correcting Z_{dr} in their approach.

Fig. 4.13 shows the histogram of α_v obtained from the improved method. The histogram is obtained from radar rays spanning azimuth angles from 280° to 310° , the same region used for plotting Fig. 3.18. The range and distribution of α_v is reasonable comparing the result obtained from the previous simulation. Comparing to the Fig. 3.18, it is clear that the estimated α_v is smaller than the estimated α_h , which satisfies our requirement for the using the A_h-A_v method as discussed earlier in this chapter. To complete this Typhoon case study, the Z_{dr} vs. Z_h scatter plot is shown in Fig. 4.14 before and after the attenuation correction by the improved method for the selected rays. It is clear that after the correction, the scatter plot displays the expected relationship between the Z_{dr} and Z_h in rain very well.

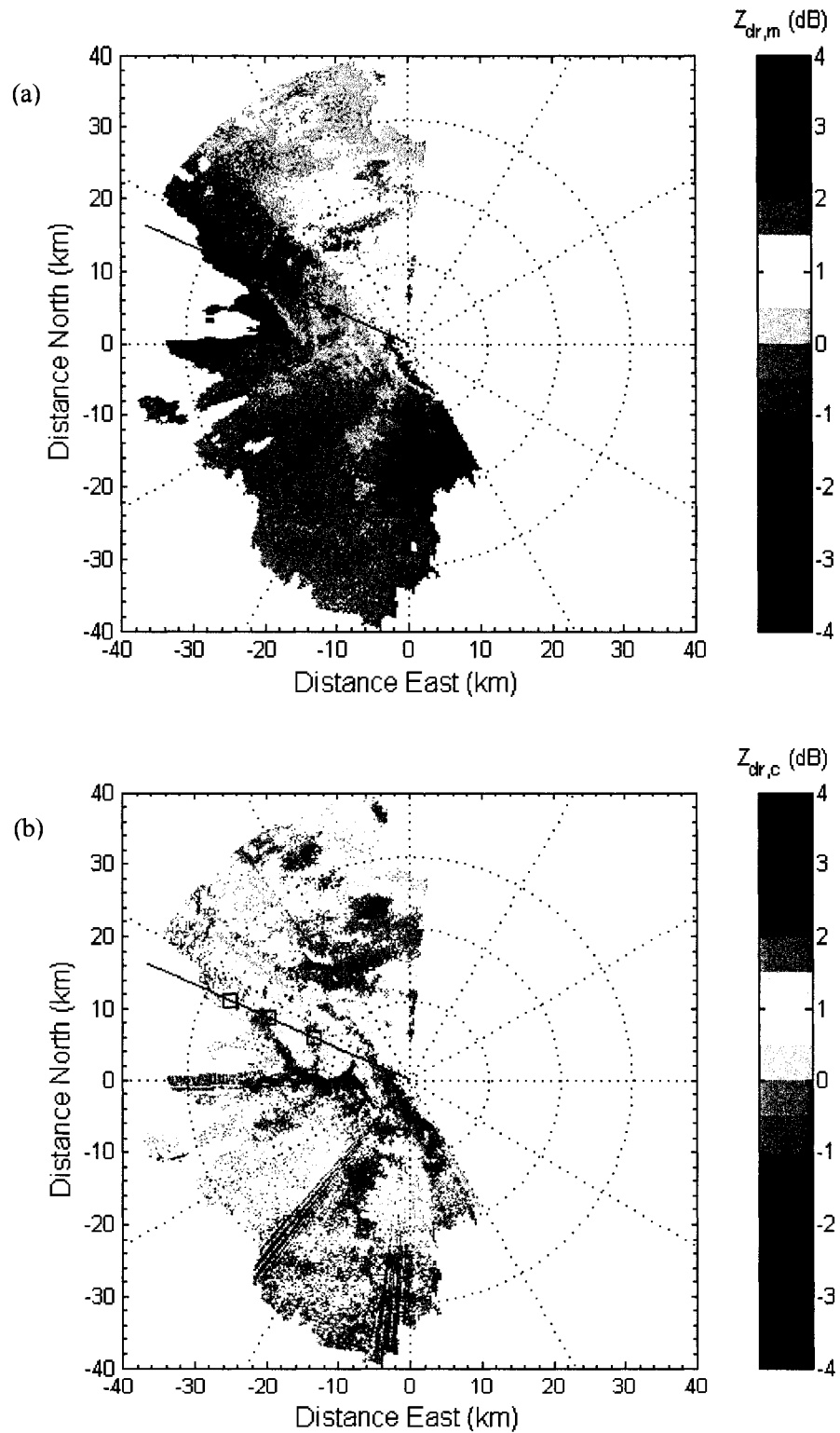


Figure 4.11 A PPI scan of (a) the measured Z_{dr} (b) the corrected Z_{dr} observed at the elevation angle of 2.5 deg, at 01:59:54 LST, September 11 2001. The black line is the radar ray at azimuth angle of 294 deg. The three squares indicate the locations of the three *in situ* disdrometers, respectively.

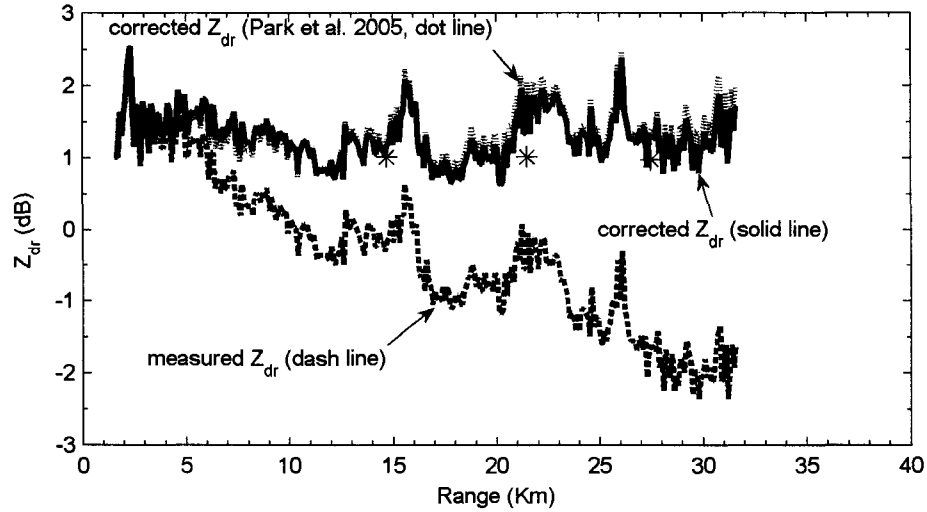


Figure 4.12 Range profiles of the measured Z_{dr} , the corrected Z_{dr} using Park et al. (2005) method, and the corrected Z_{dr} using the A_h - A_v method along the azimuth angle of 294° for the Typhoon event at 01:59:54 LST September 11 2001. The asterisks (*) denote the mean values calculated from DSD data collected with the three *in situ* disdrometers, respectively.

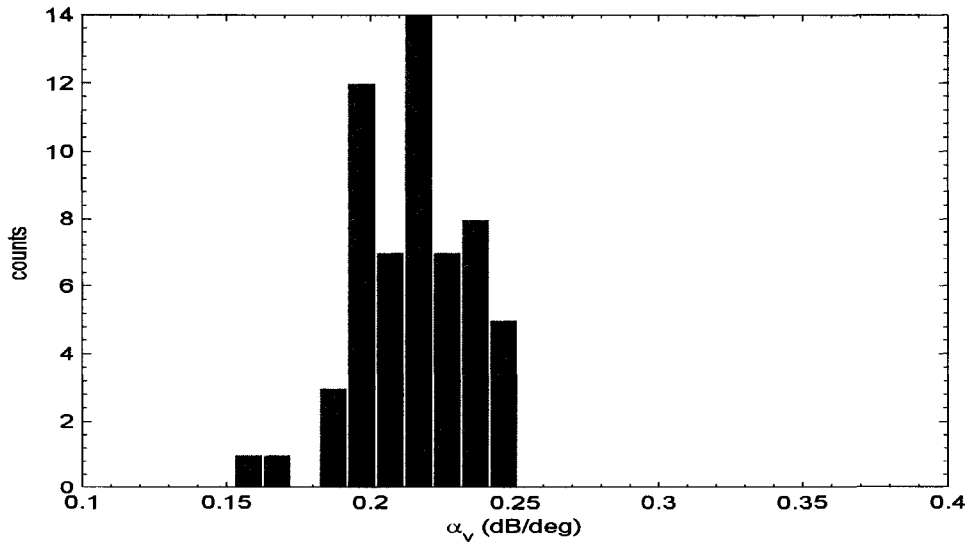


Figure 4.13 Histogram of the optimized coefficient α_v for radar rays spanning azimuth angles from 280° to 310° for the Typhoon event at 01:59:54 LST September 11 2001.

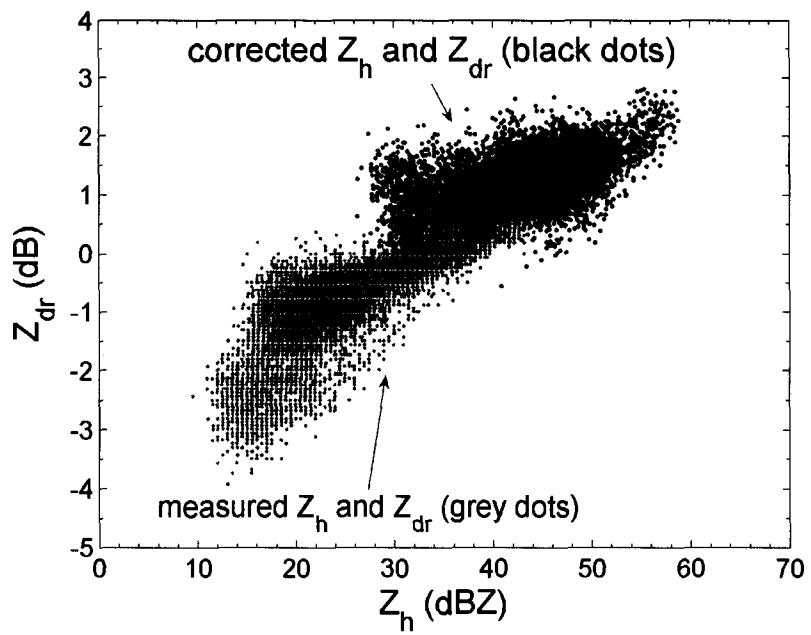


Figure 4.14 Scatter plot of Z_{dr} vs. Z_h before (grey dots) and after attenuation correction (black dots).

4.5.2 Seasonal results from the CASA IP1 testbed: Spring, Summer, and Autumn 2007

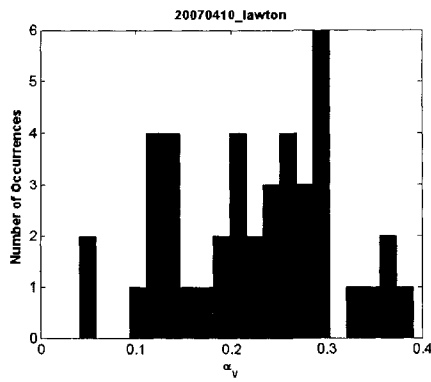
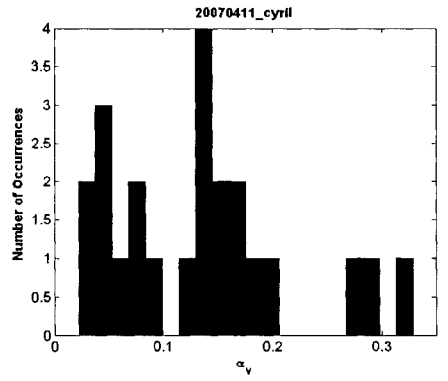
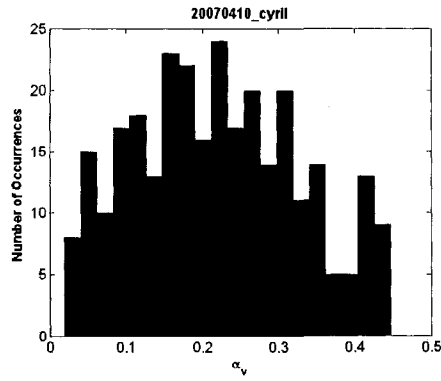
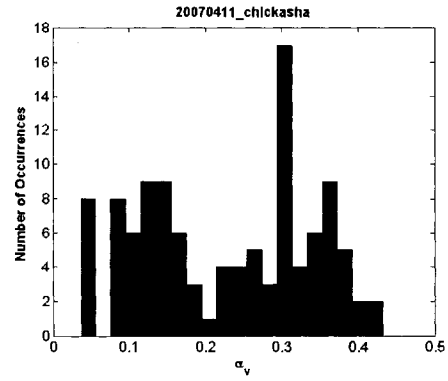
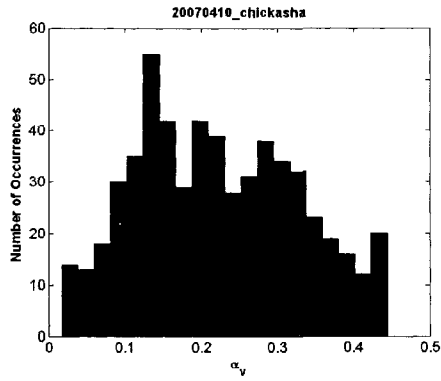
In section 3.4.4 we presented the statistical analysis for the estimated parameter α_h and the estimated total PIA for storm data collected by the CASA IP1 during the Spring, Summer and Autumn 2007. The Z_{dr} data were actually processed at the same time with the Z_h data but the analysis is postponed until the methodology is introduced in this chapter. Here, we present the similar statistical analysis for the estimated parameter α_v and the relationship between the estimated parameters α_h and α_v .

The storms studied here are the same as in section 3.4.4, the information of which is listed in Table (3.6). Fig. 4.15 shows the histograms of the estimated parameter α_v , organized similarly as Fig. 3.22 with the each column representing one event and each row representing one radar. Comparing the parameter α_v histograms to that of the α_h shown in Fig. 3.22, it is clear that they are similar that the parameter α_v histogram of a given radar in a given event appears a replica of that of the parameter α_h , except the range is shifted to the smaller side. To illustrate this effect more clearly, we plot the 2-D histograms of α_h vs. α_v in Fig. 4.16. The colors in the figure represent numbers of samples fall within small intervals and can be read from the colorbar. The linear regression for the parameters α_h vs. α_v is also shown in each scatter plot. The cross-correlation coefficients are calculated for each radar in each event and printed in each

figure panel. It is clear that the estimated parameters α_h and α_v exhibit very strong linear relation.

The strong linear relationship is supported by the fact that A_h and A_v are highly correlated (see Fig. 4.1) and an observation by Matrosov et al. (2002). In their paper, they used a fixed $A_{dp} - \Phi_{dp}$ linear relationship (see also section 2.5) to correct the Z_{dr} and showed that the coefficient (β) of this linear relationship changed very little from their simulation in rain. In fact, it is easy to see that the coefficient β is related to α_h and α_v by $\beta = \alpha_h - \alpha_v$. Because β is relatively stable, the difference of the estimated α_h minus estimated α_v should remain also relatively stable. This is shown by the strong linear relationship between α_h and α_v in the scatter plots. Furthermore, if the slope of the linear regression to a scatter plot of α_h vs. α_v is 1, it is clear that the intercept gives the estimated β directly. However, in our findings there is no significant proof that the coefficient β should be a constant.

Fig. 4.17 shows the mean values of the parameter α_v obtained from the histograms shown in Fig. 4.15. To compare with the mean trend of α_h shown in Fig. 3.23 in the previous chapter, both trends are shown in the same figure. For each radar, the mean values and the standard deviations are plotted with the date as the x-axis (not uniformly spaced) to illustrate the trend of the mean values from event to event. As expected, the mean values of α_h and α_v have strong correlation.



No severe attenuation experienced for Lawton node.

Statistics not available.

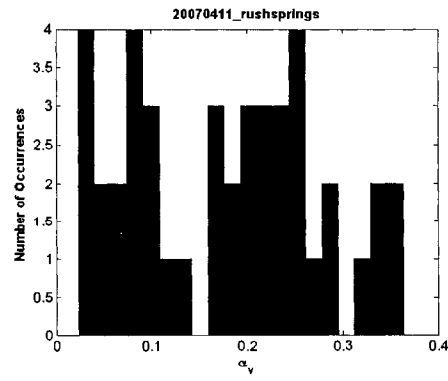
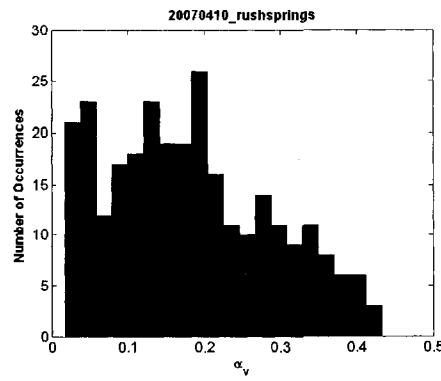
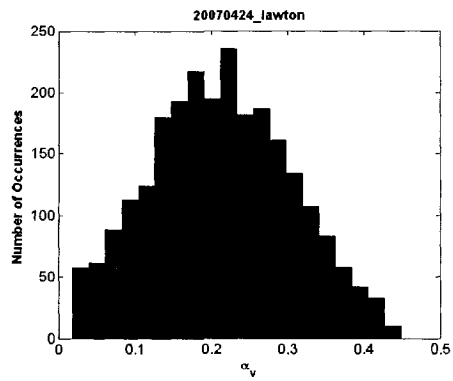
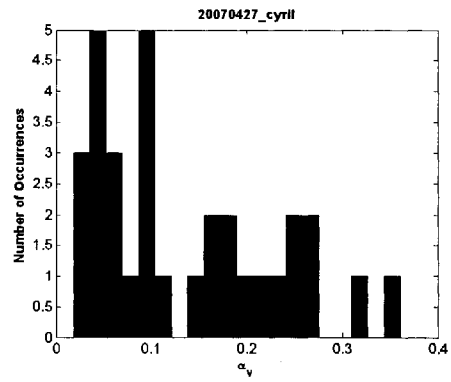
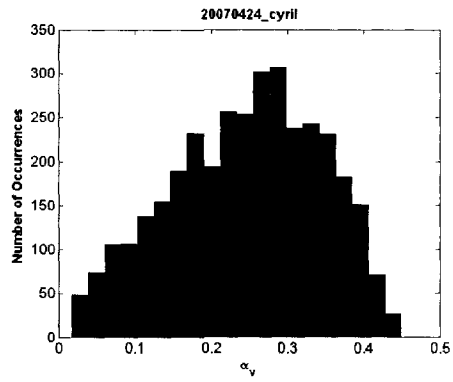
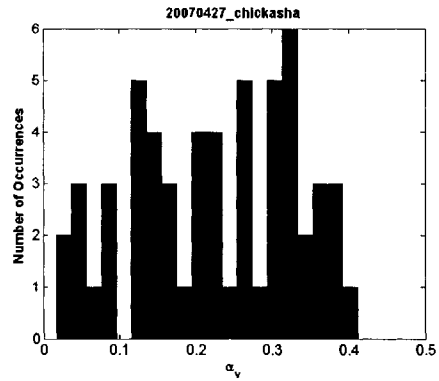
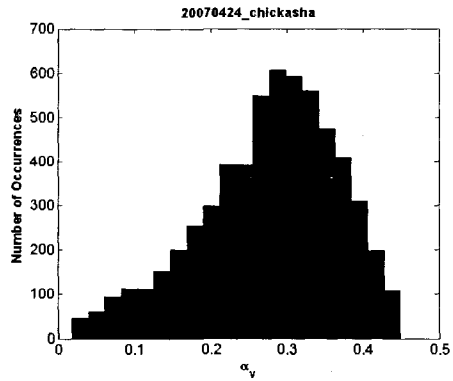


Figure 4.15 Histograms of the estimated parameter α_v for the events listed in Table (3.6).



No severe attenuation experienced for Lawton node.

Statistics not available.

Rush Springs node not operating for this case.

Rush Springs node not operating for this case.

Figure 4.15 (continued) Histograms of the estimated parameter α_v for the events listed in Table (3.6).

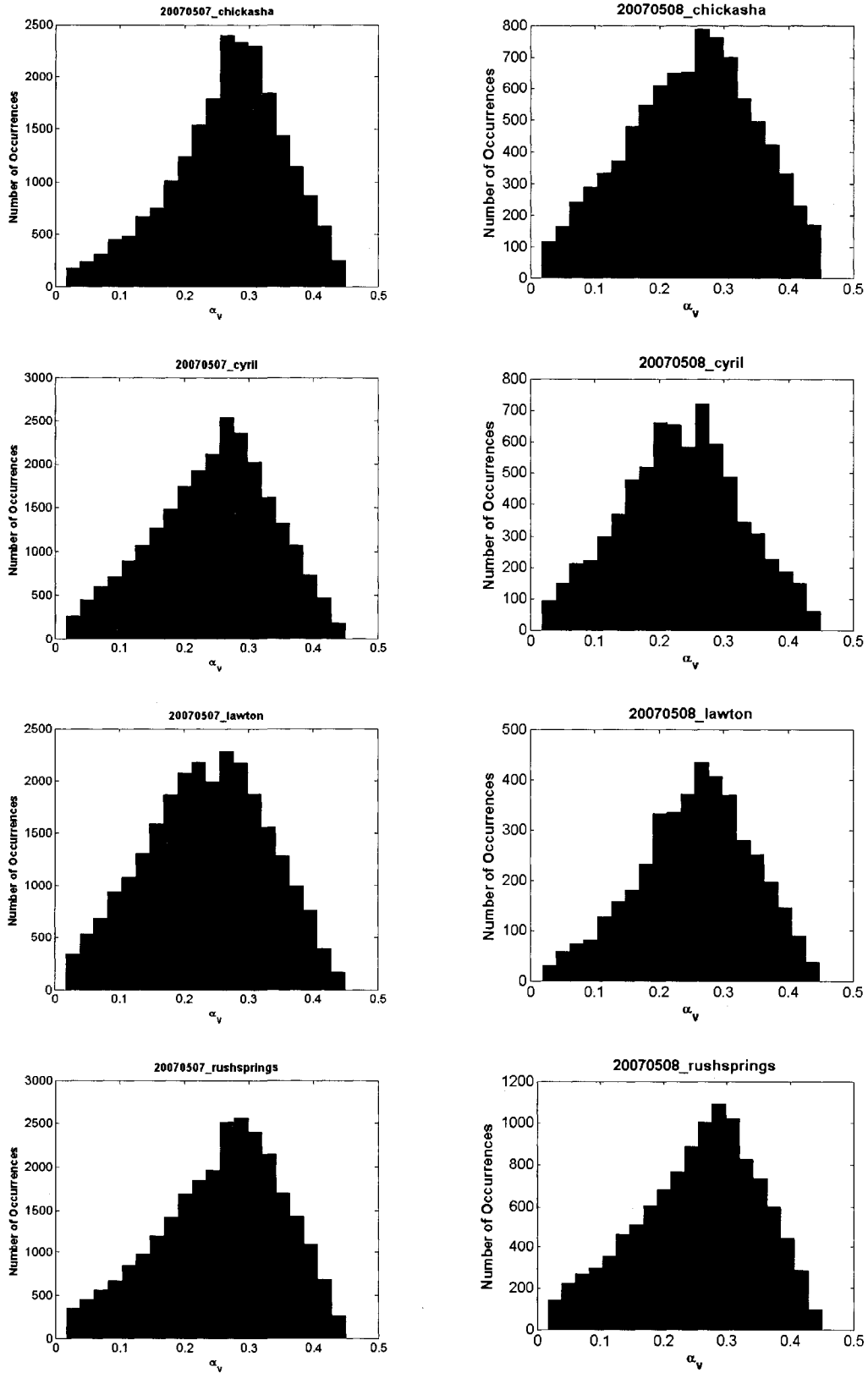


Figure 4.15 (continued) Histograms of the estimated parameter α_v for the events listed in Table (3.6).

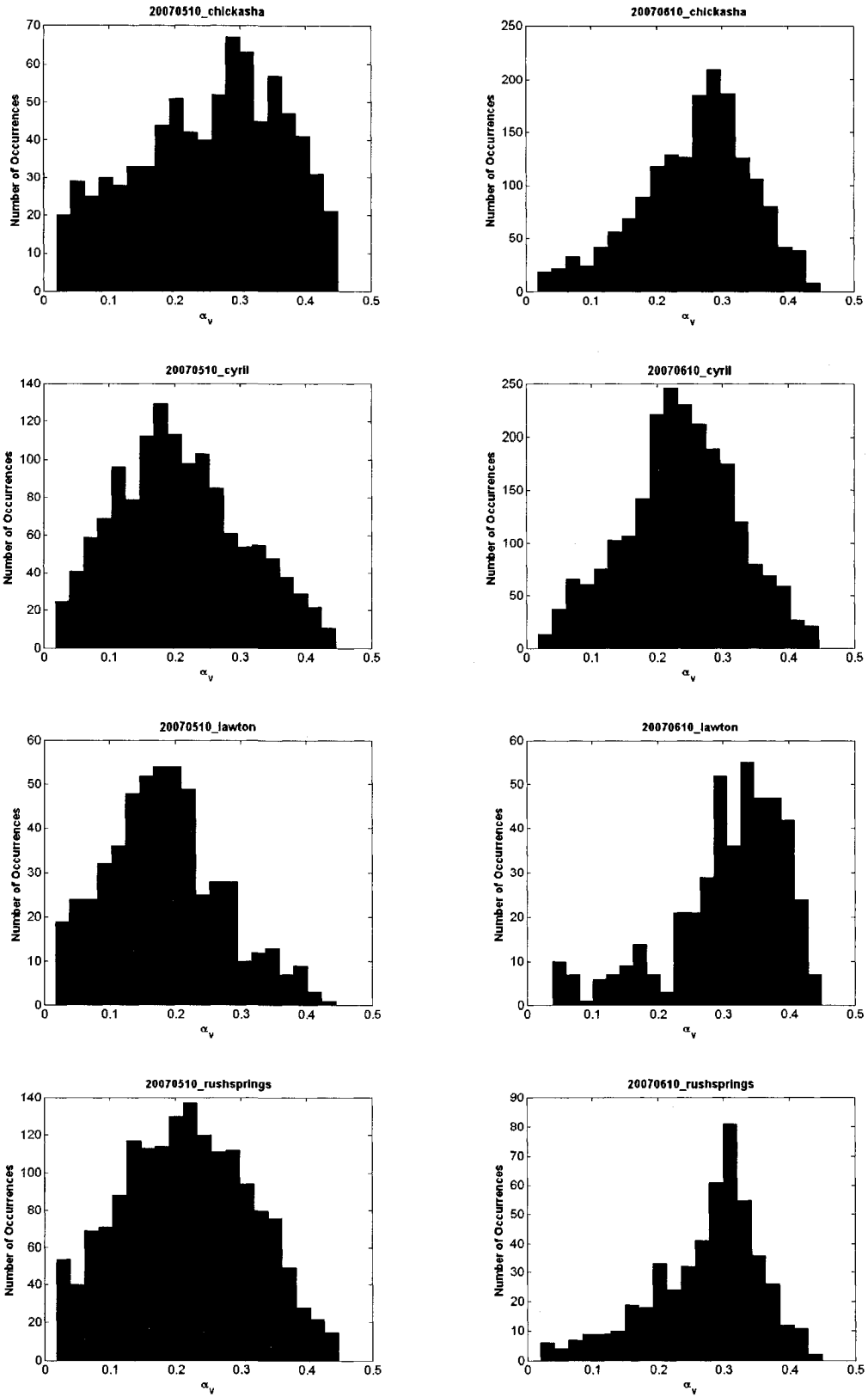


Figure 4.15 (continued) Histograms of the estimated parameter α_v for the events listed in Table (3.6).

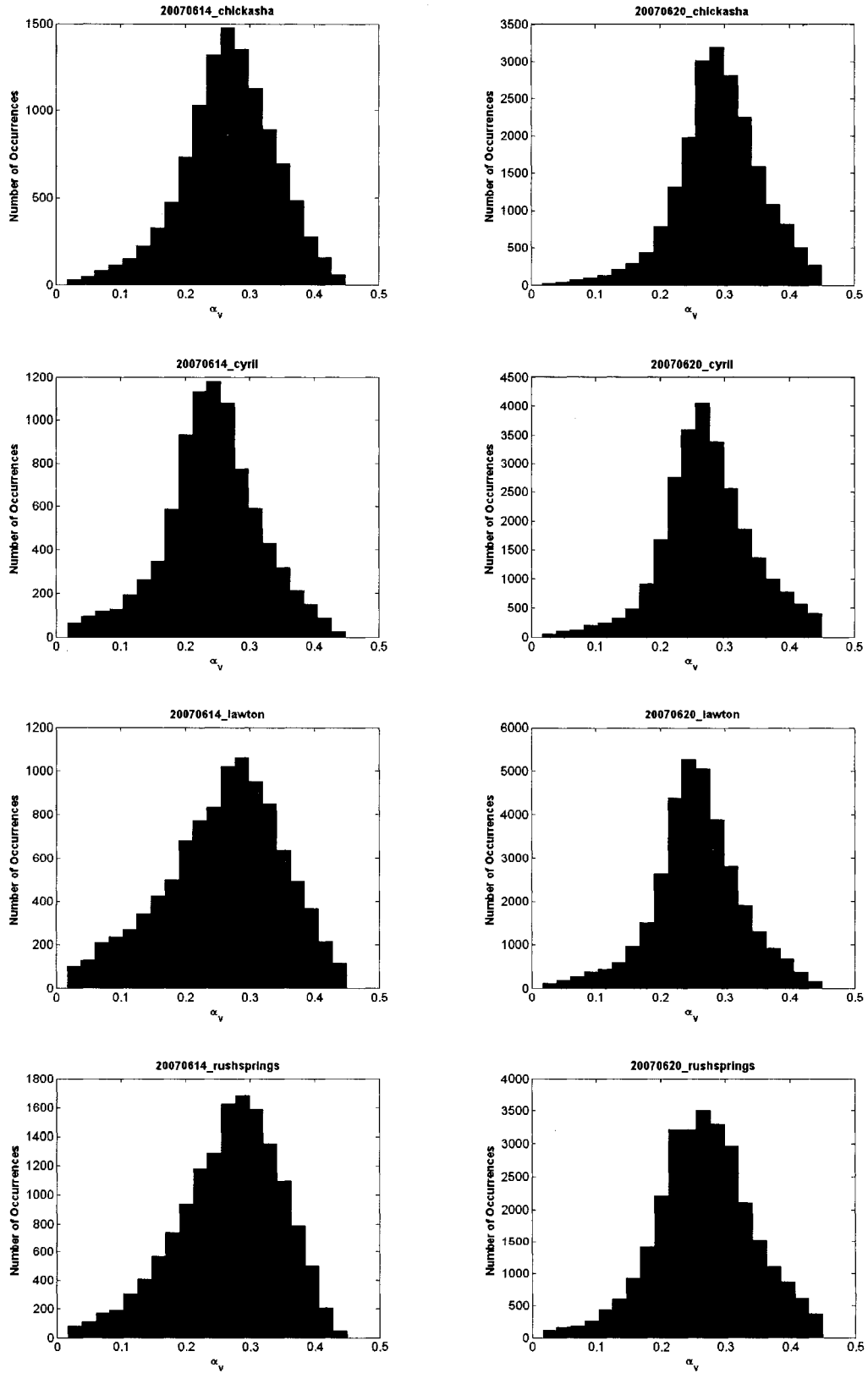


Figure 4.15 (continued) Histograms of the estimated parameter α_v for the events listed in Table (3.6).

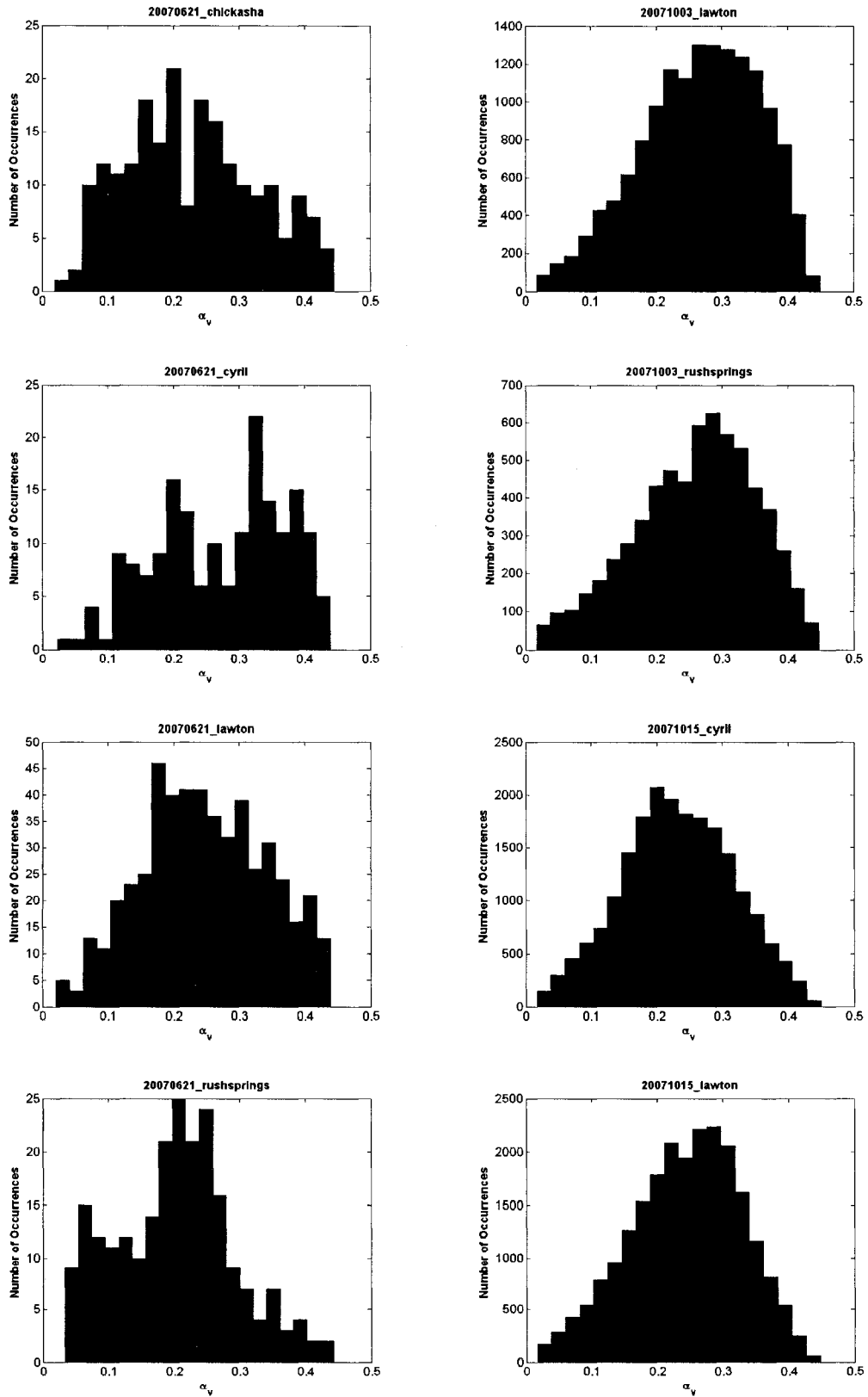


Figure 4.15 (continued) Histograms of the estimated parameter α_v for the events listed in Table (3.6).

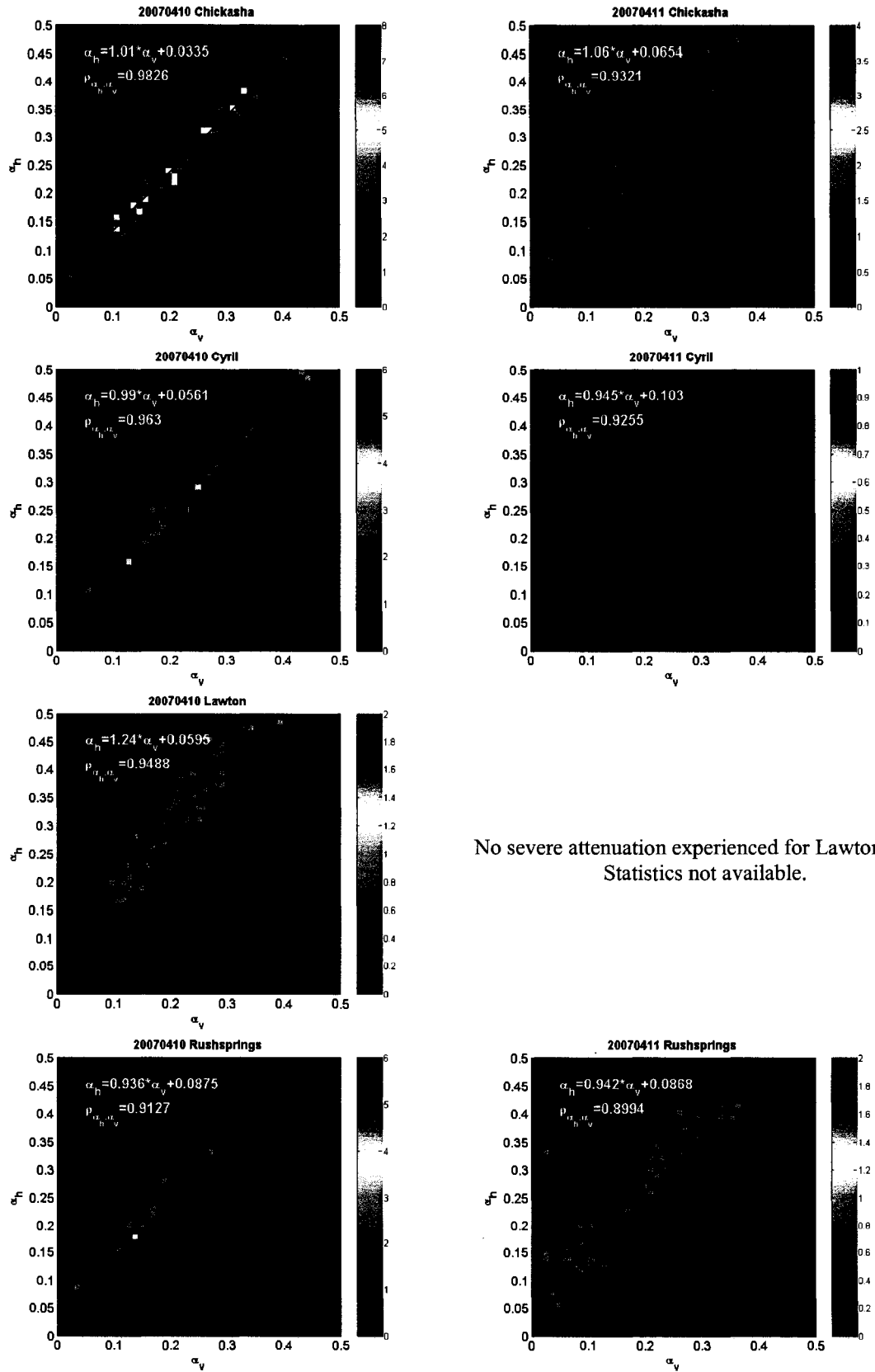
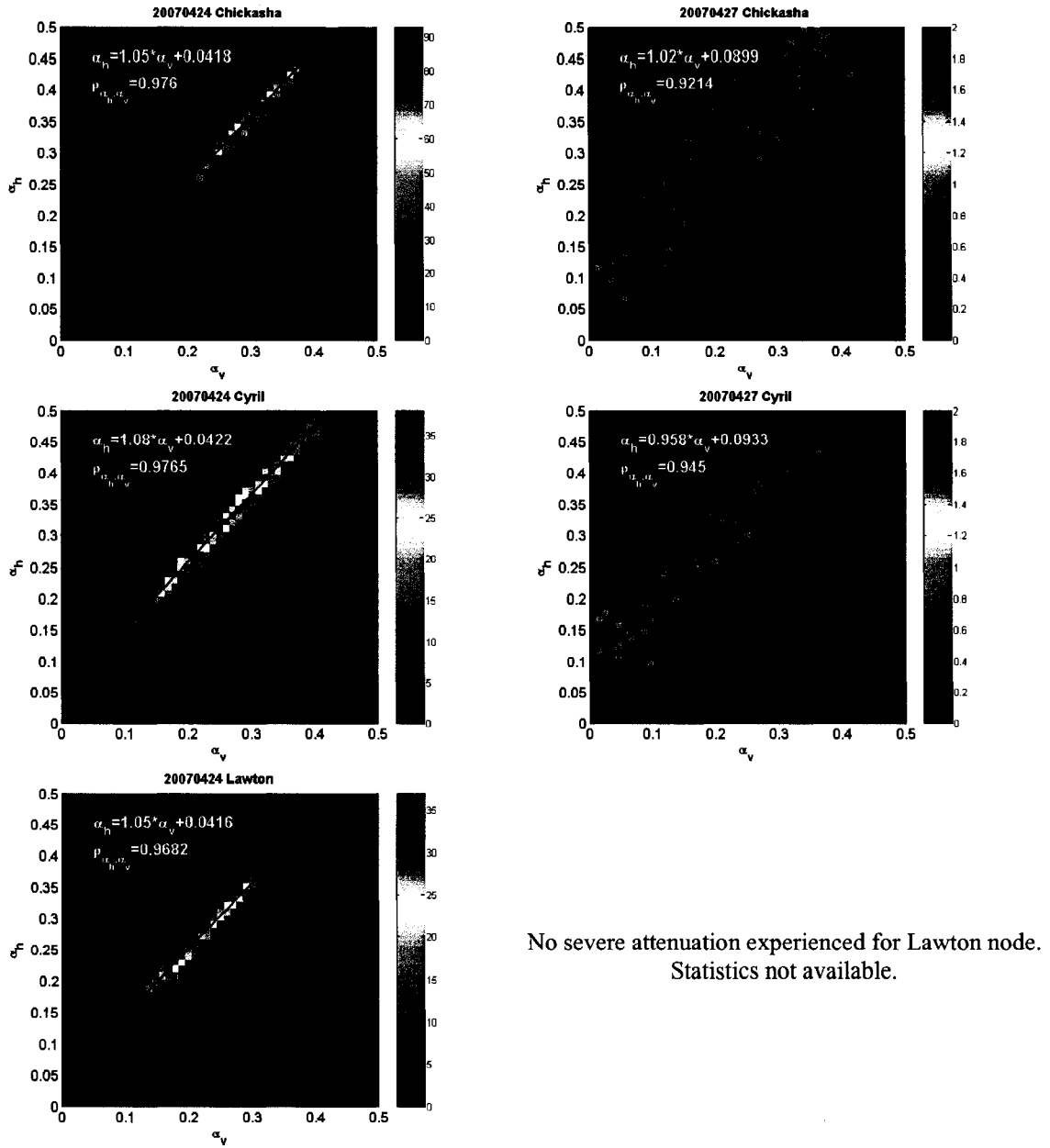


Figure 4.16 2-D histograms of the estimated parameters α_h vs. α_v for the events listed in Table (3.6).



Rush Springs node not operating for this case.

Rush Springs node not operating for this case.

Figure 4.16 (continued) 2-D histograms of the estimated parameters α_h vs. α_v for the events listed in Table (3.6).

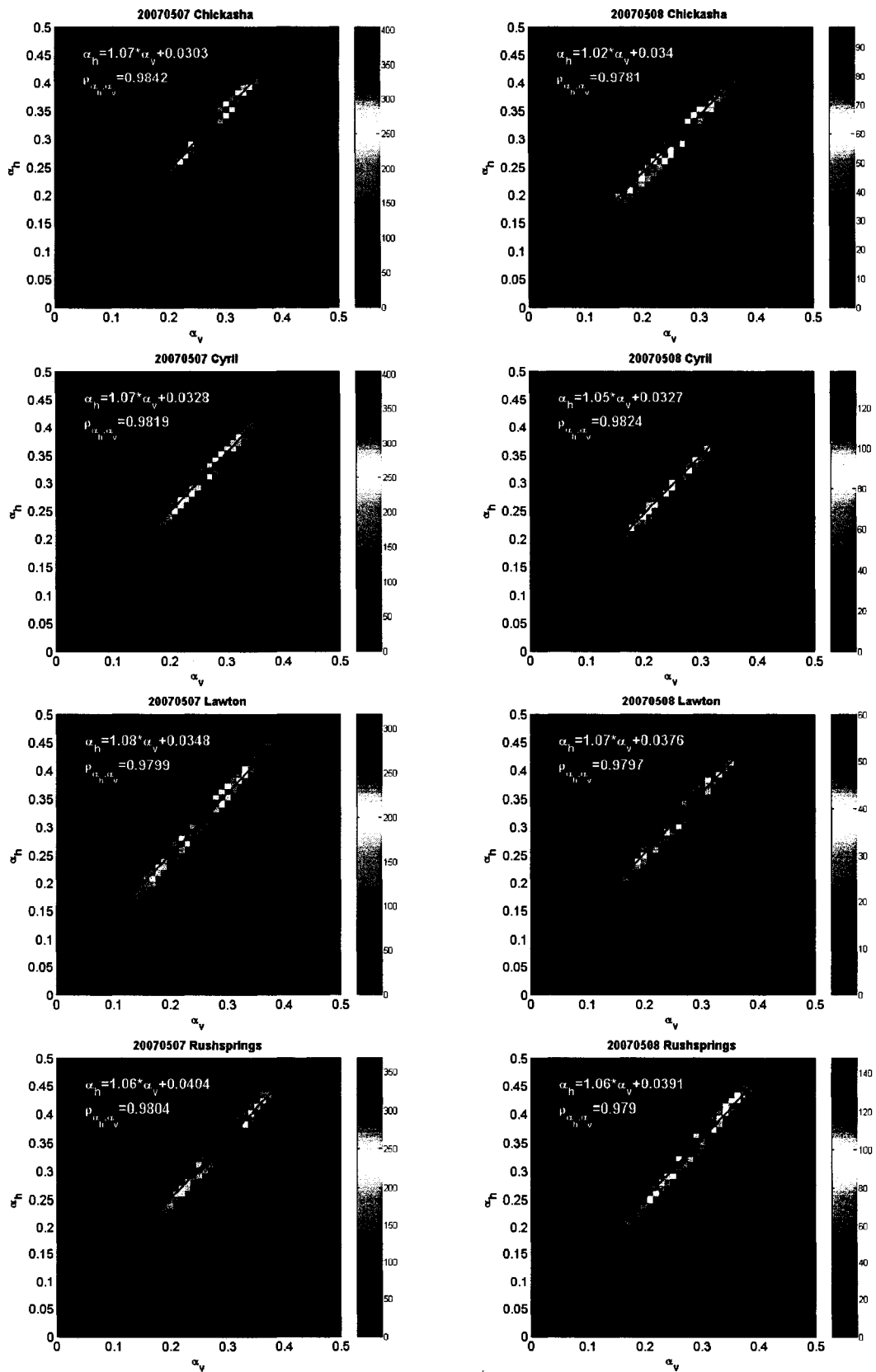


Figure 4.16 (continued) 2-D histograms of the estimated parameters α_h vs. α_v for the events listed in Table (3.6).

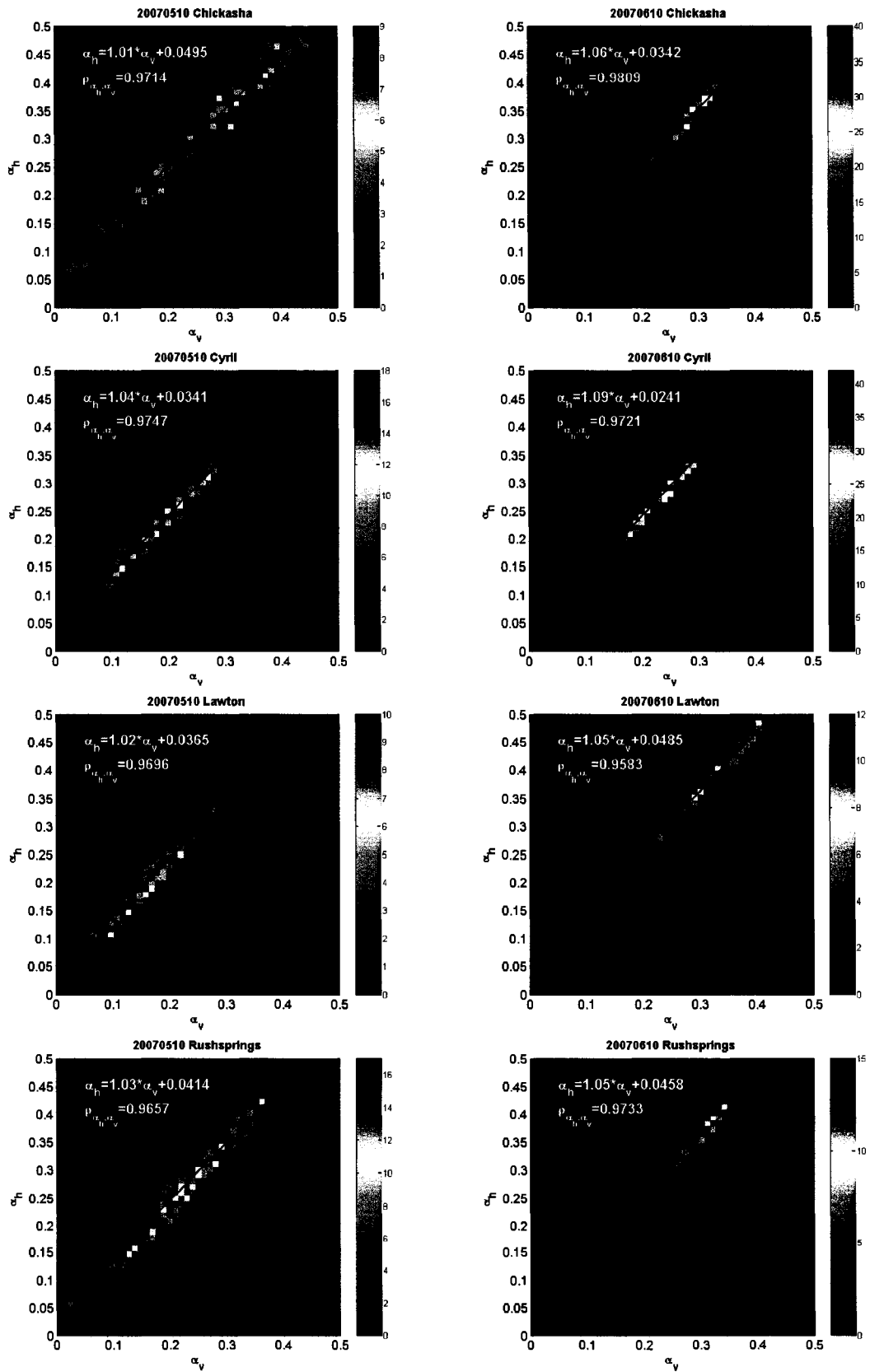


Figure 4.16 (continued) 2-D histograms of the estimated parameters α_h vs. α_v for the events listed in Table (3.6).

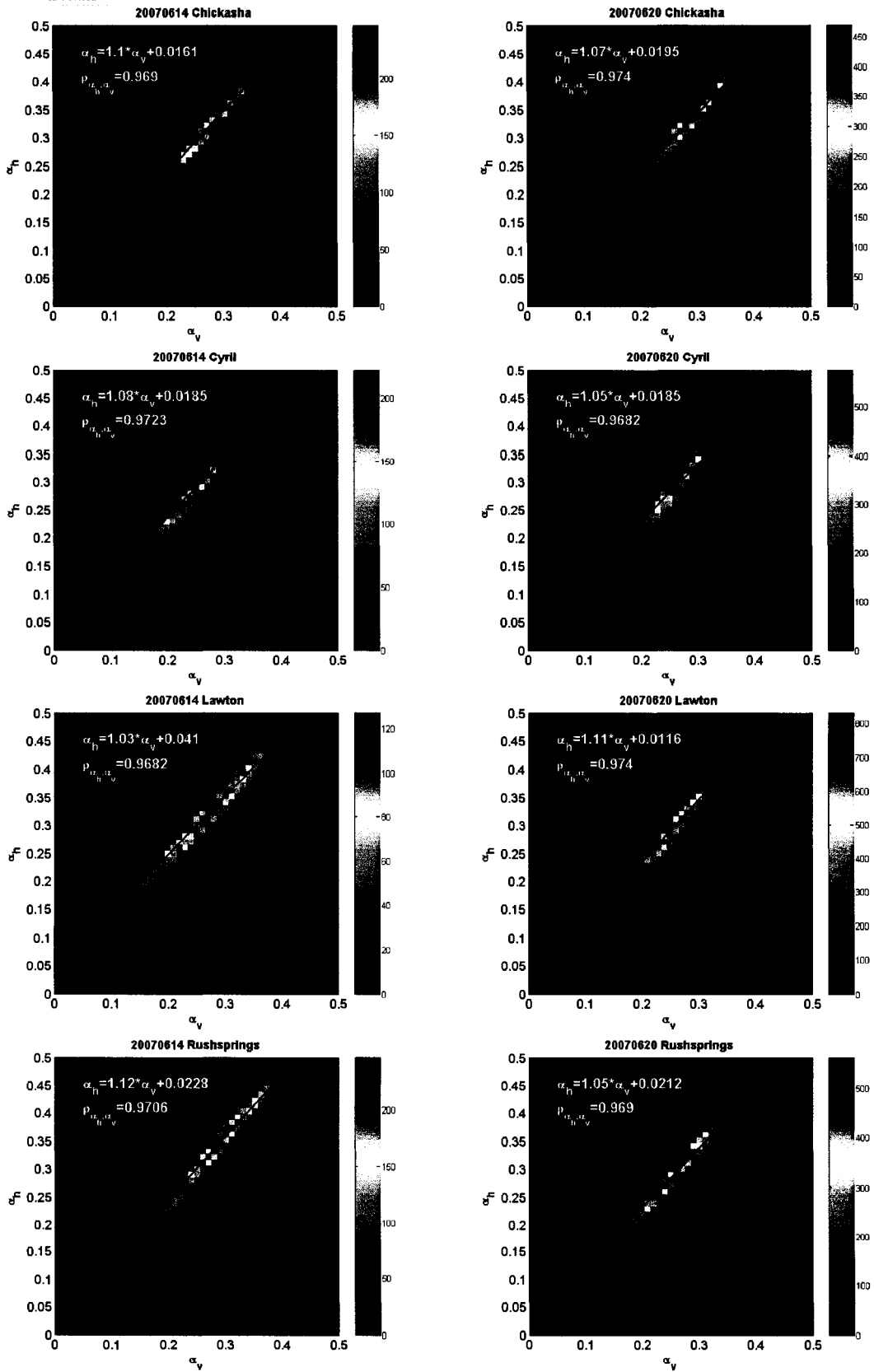


Figure 4.16 (continued) 2-D histograms of the estimated parameters α_h vs. α_v for the events listed in Table (3.6).

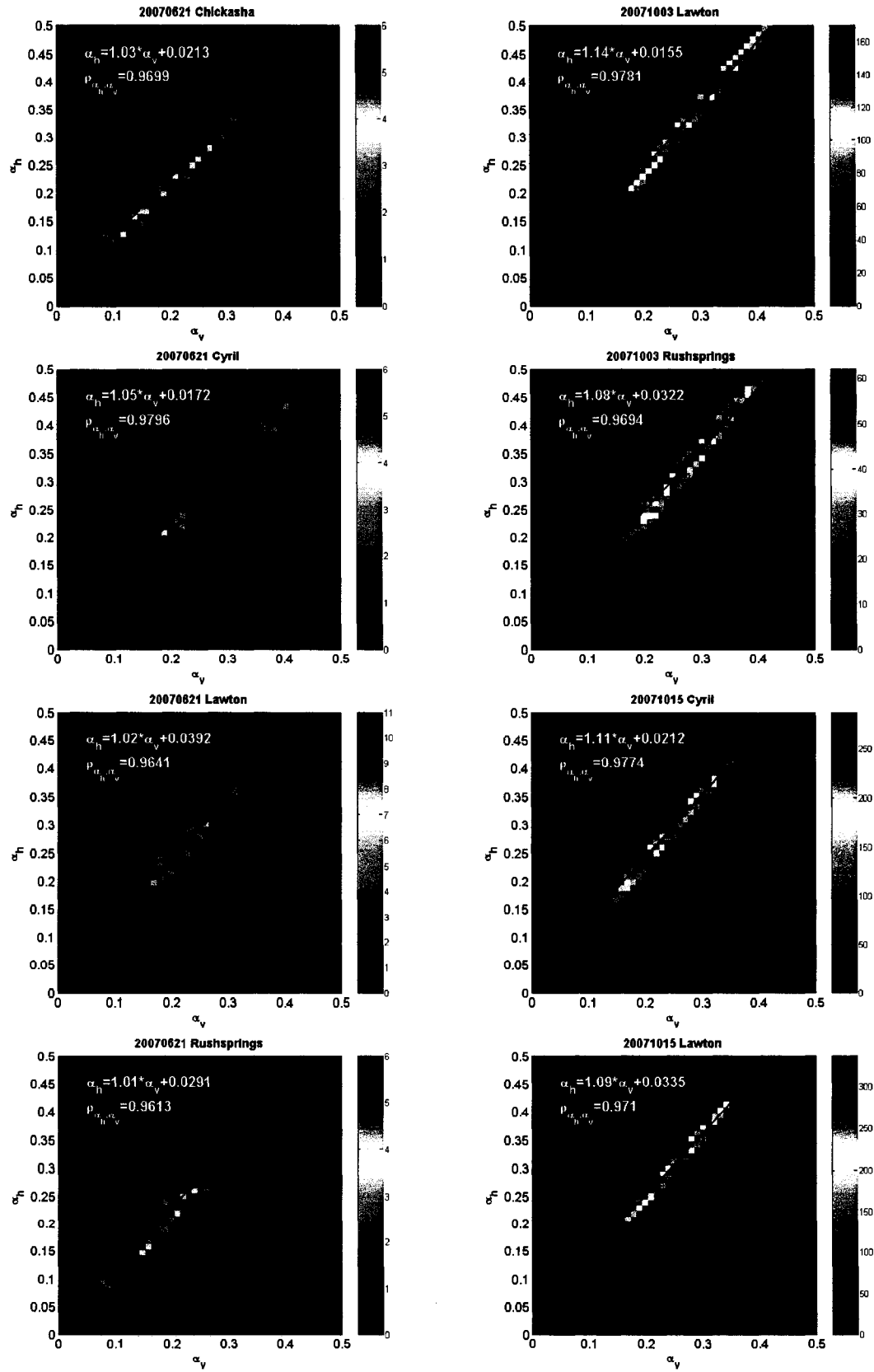


Figure 4.16 (continued) 2-D histograms of the estimated parameters α_h vs. α_v for the events listed in Table (3.6).

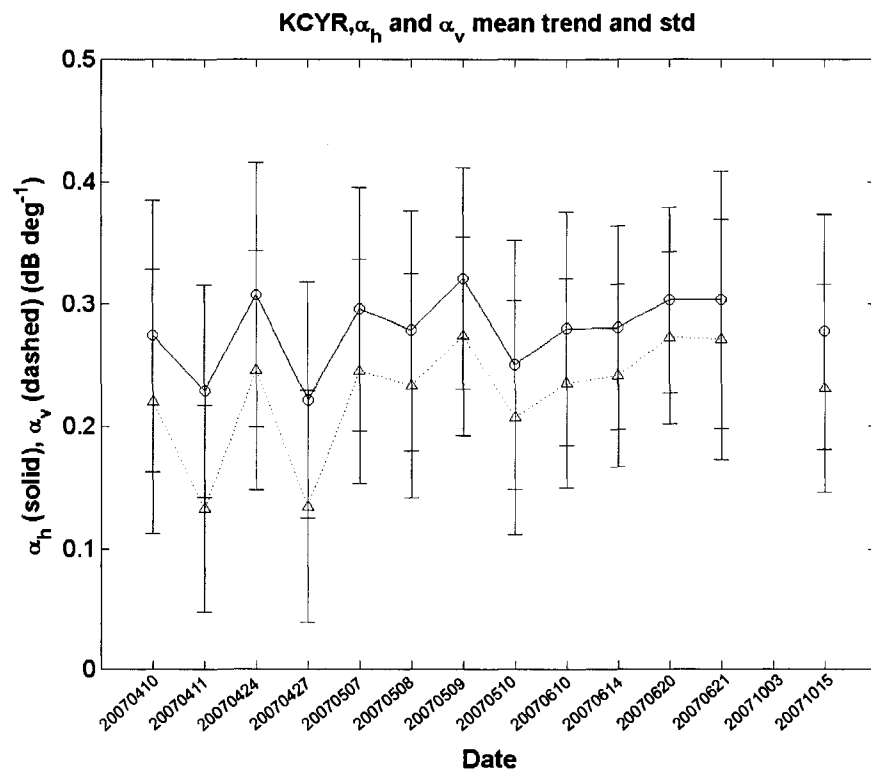
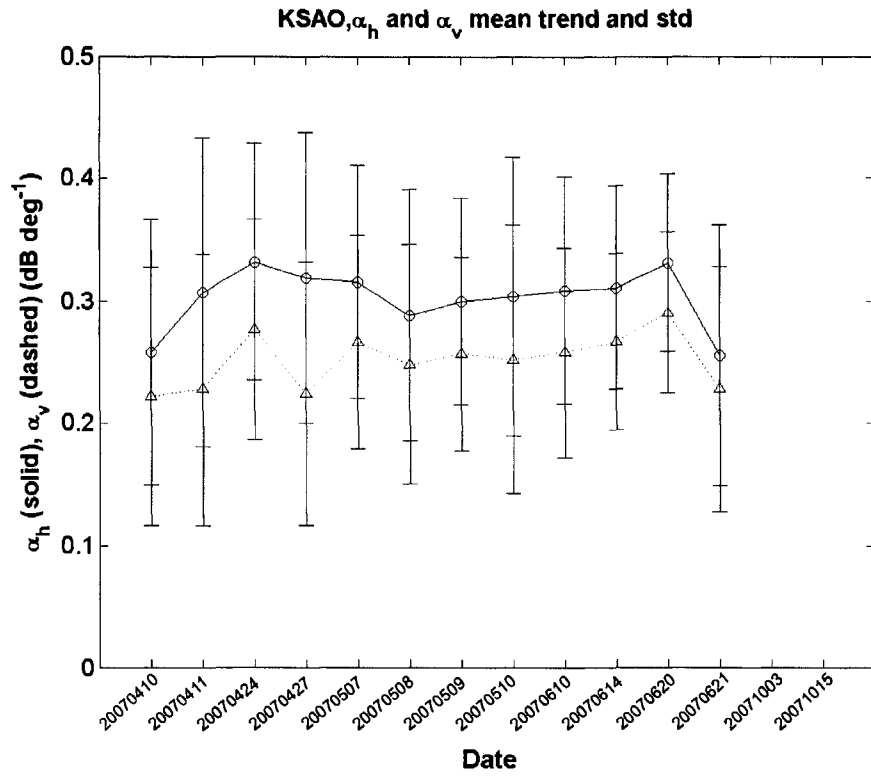


Figure 4.17 The mean values and standard deviations of the estimated parameter α_h and α_v plotted along the date of the events.

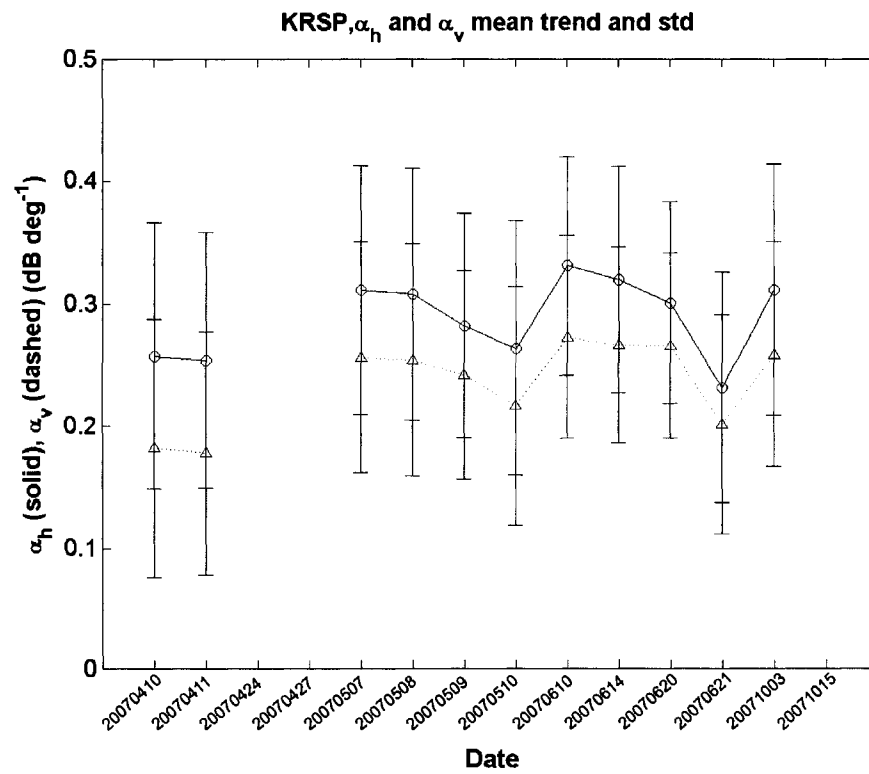
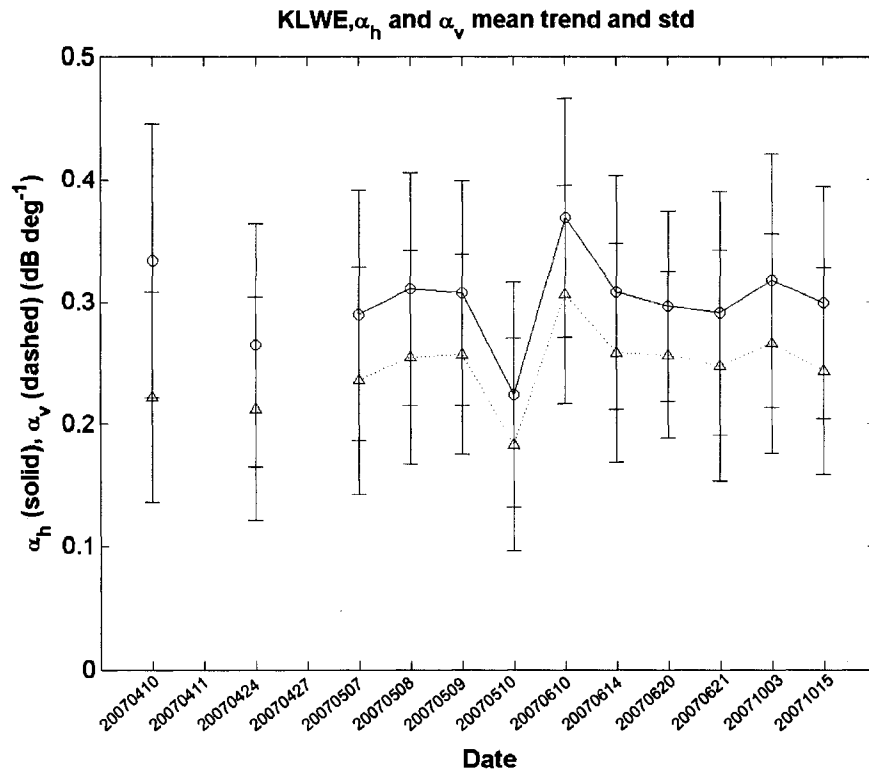


Figure 4.17 (continued) The mean values and standard deviations of the estimated parameter α_h and α_v plotted along the date of the events.

5 SEPARATELY ESTIMATE A_h DUE TO RAIN AND WET ICE: A PRIOR SUPERCELL SIMULATION USING THE CSU-RAMS MODEL

The last two chapters focused on the study and improvement of the estimation of the specific attenuation (A_h) and the specific differential attenuation (A_{dp}), respectively, for the rain medium. With the estimated A_h and the estimated A_{dp} , the reflectivity (Z_h) and the differential reflectivity (Z_{dr}) can be corrected. In this chapter, we extend the methodology to include the effect of the mixed-phase region, particular the attenuation effect caused by rain mixed with the wet ice particles (e.g., wet hail). This chapter focuses on methods to separately estimate the attenuation due to the rain and wet ice components. The methodology for estimating specific differential attenuation in the mixed-phase region will be suggested but has not been studied extensively here.

5.1 Estimating wet ice and rain attenuation separately

Previously developed attenuation estimation methods based on K_{dp} are well suited for the rain medium because the oblate spheroid shape model is maintained (in equilibrium) by the balance between gravitational, surface tension and aerodynamic forces (ref). In such a case, the difference of the real parts of the effective propagation constants between the two characteristic polarizations (K_{dp} , see chapter 2) appears to be positive along the range and results in monotonically increasing Φ_{dp} which is measurable by a dual-polarized radar. Because of the relatively stable spheroid shape during the fall, the K_{dp} is correlated with the imaginary part of the effective propagation constant which is responsible for the attenuation. Such a property is, in general, not valid in the mixed-phase region, where the

rain and other wet-ice particles (e.g., wet hail) coexist. The solid particles (or solid particles coated with water) do not exhibit the oblate spheroid shape or align their symmetric axis with one of the polarization states when they fall; instead, they can tumble and their shapes appear to be random in a given radar resolution volume. Therefore, the water-coated wet-ice particles contribute little to the K_{dp} due to their isotropic scattering (Bringi and Chandrasekar (2001)). However, they do contribute significantly to the attenuation. In such case, the K_{dp} -based attenuation correction methods will not be able to account for the attenuation by the wet-ice particles.

Here, we propose two methods to separately estimate the rain attenuation and the wet-ice attenuation for X-band dual-polarization radars. The principle of both methods is that the wet-ice attenuation is estimated by some other means than the K_{dp} . The first method assumes that a dual-wavelength radar (e.g. CP-2 S/X-band) is available with capability to transmit and receive dual-polarized waves at one frequency at least. In this case, the dual-wavelength ratio (DWR , defined next) at a far range gate (reference gate) will give the cumulative attenuation due to all particles up to that gate. Then the attenuation due to rain (A_r) can be estimated using the K_{dp} technique introduced earlier. If there is significant wet-ice attenuation, the path-integrated attenuation estimated by the K_{dp} method will be less than that estimated from the DWR . We attribute the difference to the wet-ice attenuation assuming that the Mie-scattering effect (e.g., hail-signal) has been avoided at the referenced gate. Since the range derivative of DWR at range r is equal to 2 times the specific total attenuation ($A_t(r)$) at range r (defined here as the sum of the specific attenuation due to rain and that due to the wet ice), the wet ice attenuation is retrieved by

simply taking the difference $A_t - A_r$. The *DWR* is defined as the ratio between the reflectivity from the longer wavelength (S-band here) to that from the shorter wavelength (X-band here):

$$DWR = \frac{Z_S}{Z_X} \quad (5.1)$$

where Z_S is the measured reflectivity at S-band, Z_X is the measured reflectivity at X-band.

The second method does not require the *DWR* at every range gate. Rather, the total path-integrated attenuation is retrieved from the reference gate and then is apportioned backward to the previous gates using the constrained Hitschfeld and Bordan method (see chapter 3). This quantity can be obtained by the *DWR* at the reference gate with the above radar system setup. Alternatively, it can also be obtained by at least one independent measurement of the un-attenuated reflectivity (e.g. at S-band) from a radar which does not necessarily have to be co-located with the X-band radar. The difference of the S-band reflectivity and X-band reflectivity after rain attenuation-correction at a matched resolution cell ($\Delta Z = 10 \log_{10}(Z_S(r)/Z_{Xr}(r))$), is used as a constraint to correct the reflectivity for attenuation due to wet ice, similar to the method discussed in section 3.2.2.

The above two proposed methods are for estimation of the specific attenuation at one given polarization. For the estimation of the specific differential attenuation between the two characteristic polarizations in the mixed phase, one can first identify the wet ice region by looking for the relatively flat appearance of the measured differential reflectivity profile. Because of the isotropic scattering of the wet-ice particles, the

reflectivity at horizontal polarization and vertical polarization should be the same and also should be attenuated by the same amount, resulting in the above observation. After such a region is identified, one can initially know the path-integrated differential attenuation by negating the measured differential reflectivity at that region, assuming that the differential calibration of the radar is correct. However, this is our initial suggestion and the estimation of the differential specific attenuation due to the mixed-phase region has not been studied extensively here.

5.2 Formulation of the mixed-phase attenuation estimation algorithm

The first proposed method has been described in the previous section. Here we focus on the formulation for the second proposed method.

In the mixed-phase region where rain is mixed with ice, the back-scattered signal is attenuated by both types of particles in the propagation path. Consider an X-band radar: the measured reflectivity at horizontal polarization is related to the intrinsic reflectivity attenuated by both particle types as follows (for our discussion the subscript ‘*h*’ for horizontal polarization is dropped for convenience):

$$Z_m(r) = \frac{Z_e(r)}{10^{0.2(PIA_{rain}(r)+PIA_{ice}(r))}} \quad (5.2)$$

where $PIA_{rain}(r)$ is the one-way path-integrated attenuation due to rain and $PIA_{ice}(r)$ is the one-way path-integrated attenuation due to wet ice.

We define the attenuated reflectivity ($Z_{a,ice}$) by only the wet-ice attenuation as:

$$Z_{a,ice}(r) = \frac{Z_e(r)}{10^{0.2PIA_{ice}(r)}} \quad (5.3)$$

Note that if we further attenuate $Z_{a,ice}$ by the rain attenuation (PIA_{rain}) we will get the measured reflectivity Z_m in the mixed-phase region as eq. (5.2).

With K_{dp} -based methods, the measured reflectivity can be corrected for rain attenuation. In other word, the PIA_{rain} can be estimated (e.g., using previously developed method in chapter 3); thus it is a known quantity in eq. (5.2). Therefore, $Z_{a,ice}$ can be estimated by:

$$\tilde{Z}_{a,ice}(r) = Z_m(r) \cdot 10^{0.2\tilde{PIA}_{rain}(r)} \quad (5.4)$$

To estimate the wet-ice attenuation, we assume that the ice specific attenuation can be related to the reflectivity contributed by wet ice only as a power-law relationship as:

$$A_{ice}(r) = a_{ice} Z_{ice}^{b_{ice}}(r) \quad (5.5a)$$

$$= a_{ice} (f(r) Z_e(r))^{b_{ice}} \quad (5.5b)$$

$$= a_{ice} f^{b_{ice}} Z_e^{b_{ice}}(r) \quad (5.5c)$$

$$= g Z_e^{b_{ice}}(r) \quad (5.5d)$$

In going from eq. (5.5a) to eq. (5.5b), we use the fraction of ice which is defined as the ratio between the intrinsic reflectivity of all particles and the intrinsic reflectivity of only the wet ice particles inside a radar resolution volume. In going from eq. (5.5b) to eq. (5.5c) we assume that the fraction of ice is a constant along the mix-phased region.

From eqs. (5.4) and (5.5d), the estimated intrinsic reflectivity (due to all particles) and the estimated path-integrated attenuation of wet ice (PIA_{ice}) can be derived similarly as that derived for rain in chapter 3. The estimated intrinsic reflectivity solution is given here as,

$$\tilde{Z}_e(r) = \tilde{Z}_{a,ice}(r) \cdot 10^{0.2PIA_{ice}(r)} \quad (5.6a)$$

$$= \frac{\tilde{Z}_{a,ice}(r)}{\left[1 - 0.46b_{ice}g \int_1^r \tilde{Z}_{a,ice}^{b_{ice}}(s)ds\right]^{1/b_{ice}}} \quad (5.6b)$$

We have already discussed in previous chapters that one uncertainty in using forms like (5.5d) is the coefficient g . For the wet ice particles, the large variability of DSD and water coat thickness will give rises to large family of A_{ice} - Z_{ice} relationships. In addition, the fraction of ice is not known. However, this can be remedied if an independent measurement of the ‘true’ reflectivity is known at range r_N . As discussed in the previous section, this independent measurement can be potentially obtained by the S-band reflectivity from a dual-wavelength radar system or from an S-band radar where the measurement of reflectivity can be matched in close space and time to some range gates of the X-band radar. After this quantity is established, we can constrain the solution of PIA_{ice} at range r_N as,

$$P\tilde{I}A_{ice}(r_N) = \Delta Z \quad (5.7)$$

where the ΔZ is defined as the difference (in dBZ) between the $Z_{a,ice}$ and the S-band reflectivity at the matched volume (assuming that the range gate, r_N , can be matched):

$$\Delta Z = 10 \log_{10} Z_S(r_N) - 10 \log_{10} Z_{a,ice}(r_N) \quad (5.8)$$

With the ΔZ , the coefficient g in eq. (5.5d) can be directly estimated as (also see section 3.2.2):

$$\tilde{g} = \frac{1 - 10^{-0.2b_{ice}\Delta Z}}{0.46b_{ice} \int_1^{r_N} Z_{a,ice}^{b_{ice}}(s) ds} \quad (5.9)$$

Now the estimated intrinsic reflectivity can be calculated with eqs (5.9) and (5.6b). The specific attenuation due to wet ice only can be calculated using eqs. (5.9) and (5.5d).

5.3 Simulation results

A previous supercell storm simulated using the CSU-RAMS model is used here to demonstrate our methodology (van den Heever, S.C. and W.R. Cotton (2004), see also: Huang et al. (2005)). The microphysical outputs from the single-moment RAMS supercell simulation used herein are the rain and hail mixing ratios. A vertical section of data was obtained from the RAMS simulation at the peak time of hail formation aloft. For

this cross-section, we derive using our own assumptions the exponential raindrop size distribution (assuming $N_0=8000 \text{ mm}^{-1} \text{ m}^{-3}$) and the types of the precipitation species (e.g., rain, dry hail, wet hail) at every spatial grid point. For rain, the D_0 parameter of the exponential DSD with the constant N_0 is derived from the rain mixing ratio and the mass of water. For hail we use the mass diameter output of the RAMS model and assume an exponential drop size distribution and then obtain N_0 from the hail mixing ratio and the mass of water. The hail is assumed wet if the grid point is below the 0 deg isotherm (set at about 6 km) or rain mixing ratio is non-zero. It is assumed dry if the grid point is above the 0 deg isotherm and the rain mixing ratio is zero. From this information, radar variables at X-band and S-band frequencies are calculated using the T-Matrix method for every grid point assuming shape, orientation and dielectric constant models. Radar measurement profiles are then simulated by placing an ‘imaginary’ radar at the corner of the grid which ‘measures’ the simulated storm with a Gaussian antenna beam function (3-dB beamwidth is 1 deg at both frequencies to mimic the CP2 radar beam).. The ‘measured’ Z_h profiles at various elevation angles are calculated by attenuating the intrinsic Z_h with rain and wet ice attenuation. The ‘measured’ Z_h , DWR , and Φ_{dp} are then input into the two proposed mixed-phase attenuation algorithms. The output variables, e.g., the corrected Z_h , the retrieved (estimated) rain specific attenuation (A_{rain}), the retrieved (estimated) wet ice attenuation (A_{ice}) are then compared with the intrinsic variables (the simulation input), respectively.

The intrinsic attenuation contours due to rain and wet ice in the cross-section are illustrated in Fig. 5.1. In the figure, the intrinsic reflectivity field at X-band is also plotted

in the background just to illustrate the intensity of the storm. The wet-ice attenuation contour shows that in the simulated supercell storm, the ice particles mainly exist at 2 km or higher, with the core at about 6 km. There is a large patch of overlapping area of rain and ice mixture region (mixed-phase) between 2 and 7 km. The ‘imaginary’ radar is placed at the corner at the (0, 0) coordinates. The radar is assumed to be dual-wavelength (S, X-band) and dual-polarized at S-band. Again, this is to simulate the NCAR CP-2 radar (Bringi and Hendry (1990)) which has already been installed and is currently operational in Brisbane, Australia.

Fig. 5.2 shows the path-integrated attenuation due to rain and wet ice along the slant range at 25° elevation angle, which passes through the cores of the rain and the wet ice. Over this path, the rain and wet ice each contributes almost the same amount of attenuation. Fig. 5.3 shows two radar reflectivity profiles, one measured at the same elevation angle and the other a much lower elevation angle (0.5°). At the higher elevation angle where the rain and wet ice particles coexist, the measured Z_h at S-band exceeds the rain attenuation corrected Z_h at X-band by ΔZ (about 25 dBZ) at the end of the beam. This is expected because we know the K_{dp} -based attenuation correction method is not able to account for the wet ice attenuation (see section 5.1).

Based on this supercell simulation the two proposed mixed-phase attenuation correction algorithms are evaluated. Here we present the result for the dual-wavelength (*DWR*) ratio method first. Fig. 5.4 shows the retrieved rain attenuation field and the ‘true’ rain attenuation field. For the simulation, we assume there is no dual-polarized capability at

X-band. Therefore, we convert simply the K_{dp} at S-band to the rain specific attenuation at X-band using a linear relationship ($A_{rain,X}=\alpha K_{dp,S}$). The value of the coefficient, $\alpha=0.95$ dB/deg, is calculated carefully for this event, therefore, there is no bias in the estimated coefficient. The K_{dp} is estimated from the filtered Φ_{dp} (Hubbert and Bringi (1995)). The estimated rain attenuation contour appears less sharp than the ‘true’ one. This is expected because there will be some smoothing effect on the estimated K_{dp} due to the filtering. Nonetheless, the difference is within ± 0.5 dB/km which is the expected error of the retrieval. Fig. 5.5 shows the retrieved contour of the wet ice attenuation compared with the ‘true’ one. Although there are some smoothing effects due to the filtering technique to overcome the noise, Figs. 5.4 and 5.5 show the close correspondence of the estimated specific attenuation contours as compared with the ‘true’ contours.

Next we evaluate the second method which uses the independent measurement of the unattenuated reflectivity at the end of the radar beam. Fig. 5.6 shows the slant range profile at the same 25° elevation angle. The ΔZ used in the constrained method is assumed to be known from the DWR at the end of the beam in this case (but the intermediate DWR at other gates are not used). Following the procedure described in section 5.3, Fig. 5.6 shows that the corrected (estimated) $Z_{h,X}$ matches the intrinsic $Z_{h,X}$ very well. Fig. 5.7 shows the retrieved wet-ice specific attenuation contour and the true wet-ice specific attenuation contour. Similar to the first method, the vertical structure of the retrieved contour closely corresponds to the true one. It is noticeable that the retrieved wet-ice contour in Fig. 5.7 has more details compared with the result obtained from the first method (Fig. 5.5) since there is no filtering involved in this case.

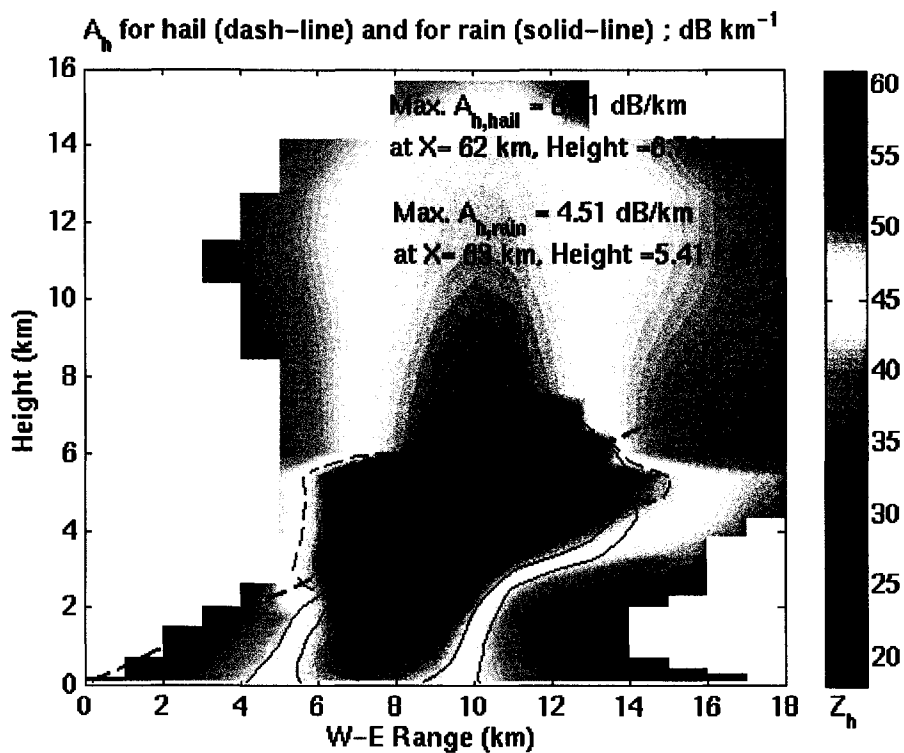


Figure 5.1 Vertical cross-section of contours of specific attenuation (A_h) of rain and hail at X-band. Dash line is the hail A_h contour. Solid line is the rain A_h contour. The intrinsic X-band Z_h (in dBZ) is plotted as background.

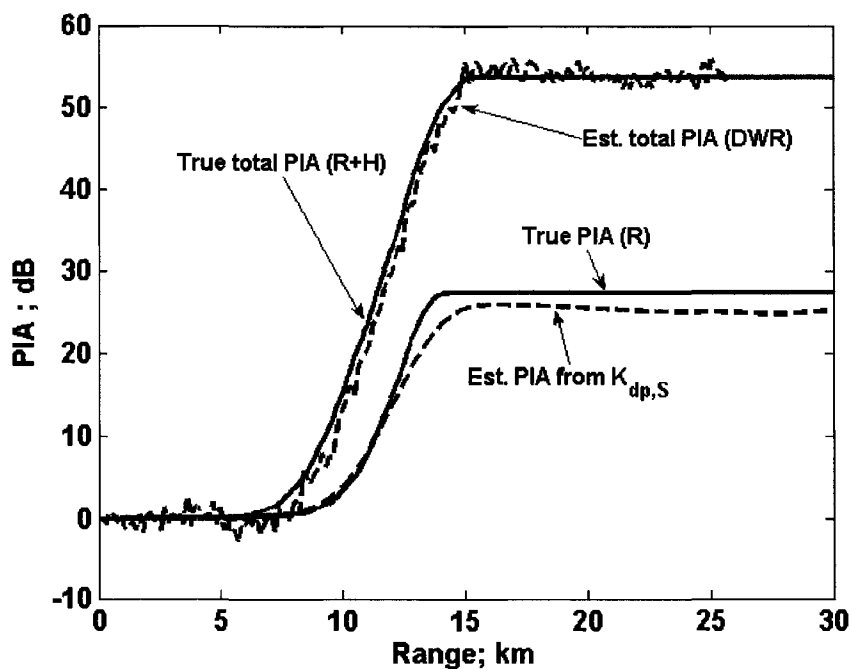


Figure 5.2 Range profiles of the DWR along the slant path at 25° elevation angle, the 'true' total PIA, the 'true' rain PIA, and the estimated rain PIA.

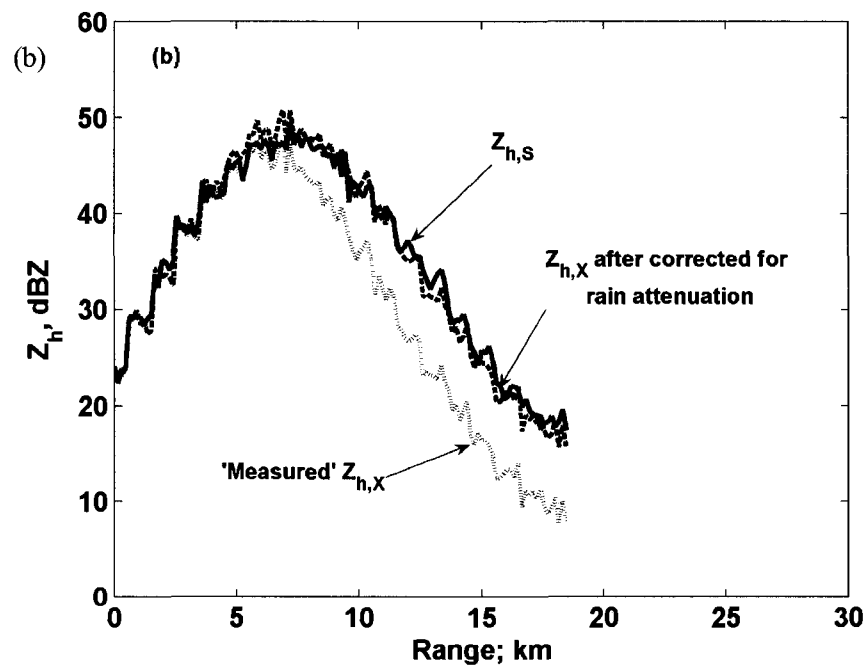
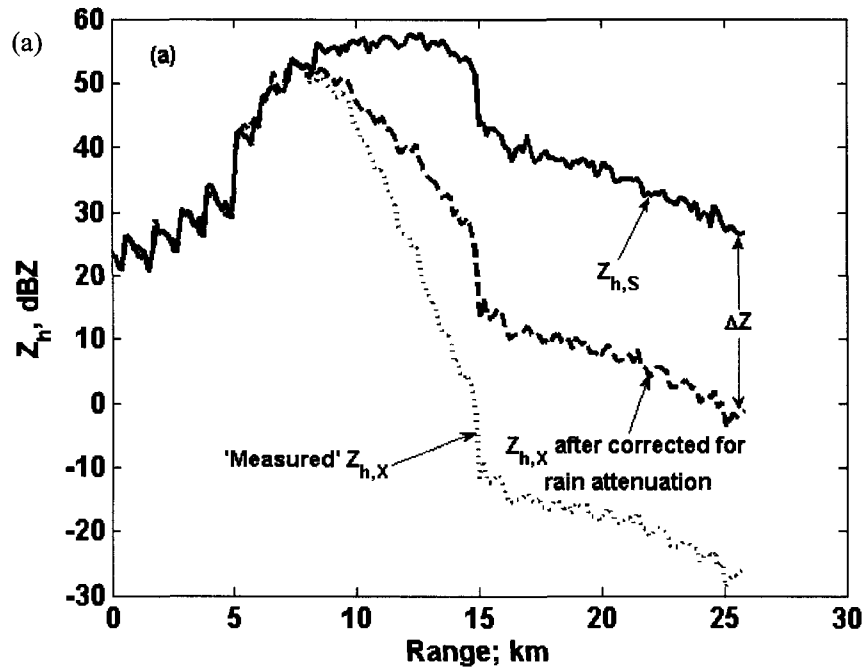


Figure 5.3 Range profiles of the $Z_h(S)$, the attenuated (or 'measured') $Z_h(X)$, and the $Z_h(X)$ corrected for rain only attenuation (a) at 25 deg elevation angle (b) at 0.5 deg elevation angle.

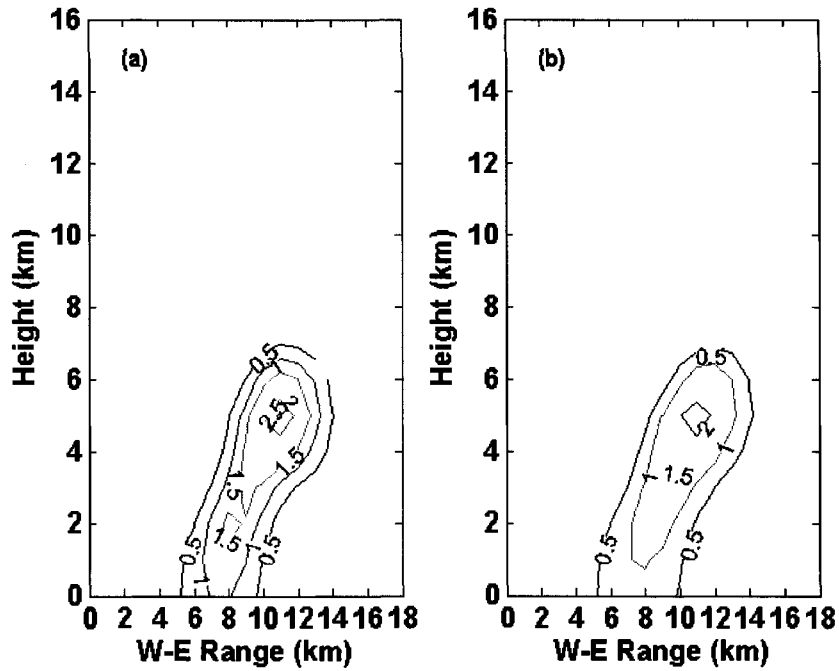


Figure 5.4 Contours of specific attenuation of rain in the vertical section. (a) the ‘true’ values from the RAMS microphysical output, (b) the retrieved values.

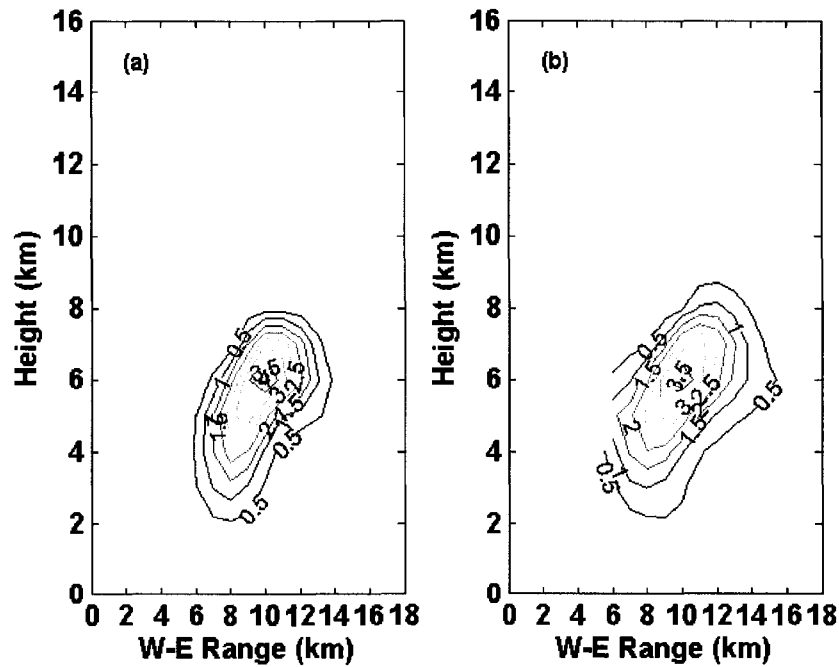


Figure 5.5 Contours of specific attenuation of the wet hail in the vertical section. (a) the ‘true’ values from the RAMS microphysical output, (b) the retrieved values calculated from the first proposed method.

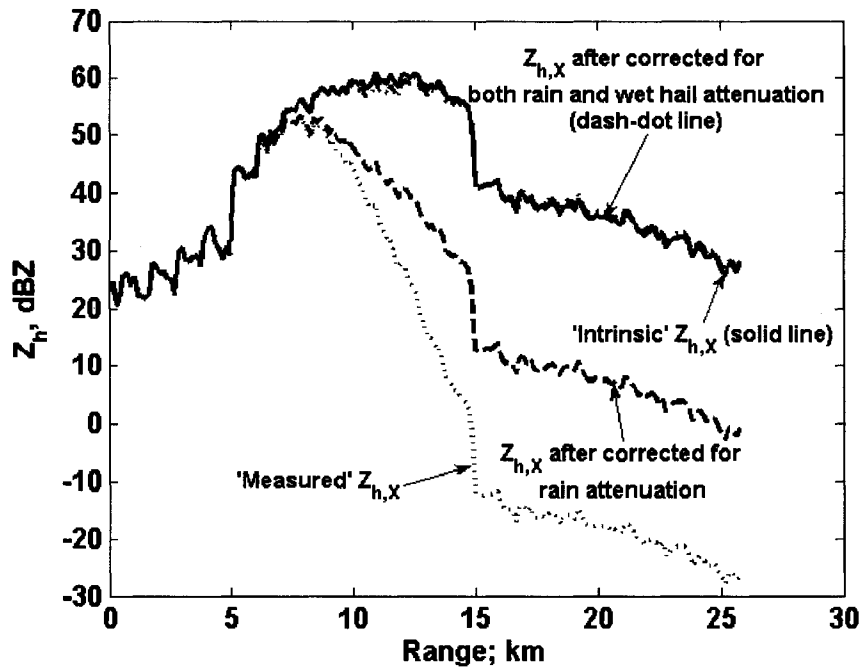


Figure 5.6 Profiles of the attenuated (or 'measured') $Z_h(X)$, the $Z_h(X)$ after correction for rain attenuation, the $Z_h(X)$ after correction for both rain and wet hail attenuation, and the 'intrinsic' $Z_h(X)$.

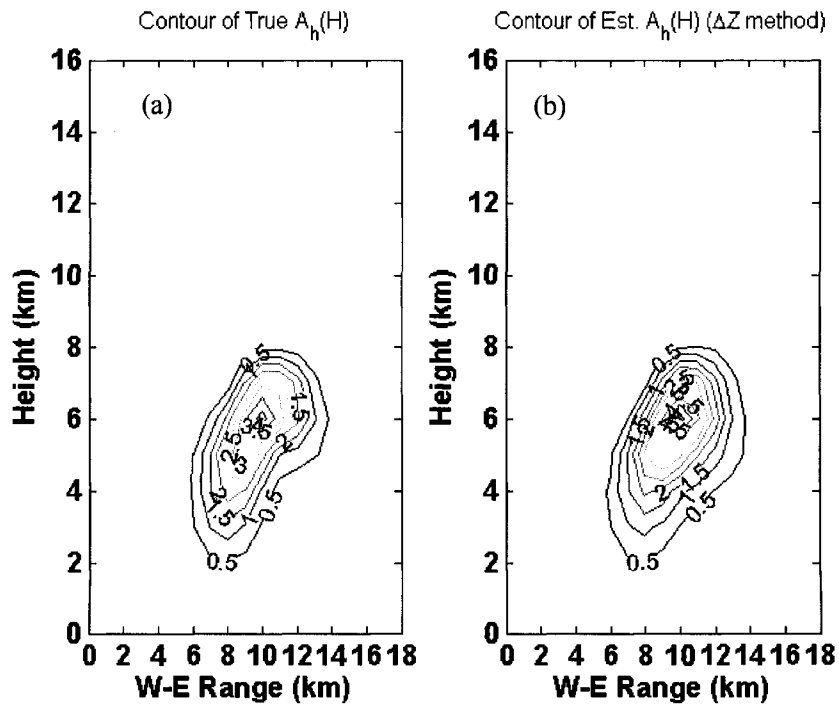


Figure 5.7 Contours of specific attenuation of the wet hail in the vertical section. (a) the 'true' values from the RAMS microphysical output, (b) the retrieved values calculated from the second proposed method.

6 SUMMARY AND SUGGESTIONS FOR FUTURE WORK

6.1 Summary

The objective of this dissertation is to improve the accuracy and efficiency of attenuation-correction procedure for dual-polarization radar systems operated at X-band. The attenuation due to raindrops and wet hail that occurs in heavy convective storms has been studied. For raindrops, we have presented a framework to estimate and correct the attenuation and the differential attenuation accurately based on the consistency between $Z_{h,v}$ and K_{dp} , without knowing *a priori* the coefficients in the $A_{h,v}$ - $Z_{h,v}$ and $A_{h,v}$ - K_{dp} relationships. For wet hail, we have presented a framework to estimate and correct the attenuation separately from the rain attenuation component, provided that constraint information can be obtained through dual-wavelength technique (S, X-band) with matched 3-dB beamwidth antennas or other non-attenuating radar system (e.g., WSR-88D) nearby from which coincident resolution cells can be matched.

Beginning with the introduction chapter, the primary driving force of this work, the CASA IP1 Doppler, dual-polarization X-band radar network has been introduced along with other similar X-band radar systems that have also been studied or simulated herein, i.e., the Doppler, dual-polarization MPX (X-band) radar operated by NIED, Japan and the dual-wavelength (S, X-band) dual-polarization (only at S-band) CP-2 radar operated by BMRC, Australia. Following the introduction, the theoretical background and related work on attenuation estimation and correction have been reviewed systematically.

In chapter 3, we have presented first a simple scheme to construct the path-integrated attenuation in a gate-by-gate manner. It has been found, via simulation, that this scheme has numerical stability difficulty if the total path attenuation exceeds about 10 dB. The simple scheme has been extended to include a constraint from the total differential propagation phase by which the numerical solution becomes stable. A path-integrated attenuation model is constructed using the Hitschfeld and Bordan (1954) method with the constraint. Then a minimization scheme has been used to minimize the cost function constructed with the modeled Φ_{dp} and the measured Φ_{dp} at every gate in the segment that has been identified as rain along a propagation path. It has been shown via simulation, that the consistency between $Z_{h,v}$ and K_{dp} has been maintained. The method formulated herein has shown the ability to adapt to changes in the temperature, raindrop shapes, and to certain classes of DSD studied in the simulation. We have validated the method for a Typhoon event using radar data from the MP-X radar operated by NIED where the correction of Z_h for attenuation agreed, within instrumental errors, with the ground truth value calculated from the measured DSD by three *in situ* Joss disdrometers. We have implemented the method, in real time, for the CASA IP1 network. We have compared the corrected PPI scan of a convective storm with that of the nearby un-attenuated WSR-88D radar and found that the two scans match well. The statistics of the retrieved coefficient α_h in the A_h - K_{dp} relationship and the resulted total path attenuation for several storms that occurred over the testbed in Spring, Summer, and Autumn, 2007 have also been shown. An additional value of the method is that it is independent of the systematic offset that may exist in the measured Z_h of a radar system (i.e., absolute calibration of the h -

channel of the radar).

In chapter 4, the consistency principle studied in chapter 3 has been extended to the vertically polarized variable Z_v and sequentially a path-integrated differential attenuation model has been constructed. The validity of such model has been discussed and it has been shown that if the coefficient α_h in the A_h-K_{dp} relationship is greater than the coefficient α_v in the A_v-K_{dp} relationship, then the model is valid for rain. A more strict condition is also discussed but not used in the actual implementation. The conditions for validity of the model have been met in our simulations. The simulations have also shown that the method has the same ability to adapt changes in the temperature, drop shapes, and certain classes of DSD. We have validated using the same radar data for the Typhoon storm that the corrected Z_{dr} agreed, within instrumental errors, with the ground truth value calculated from DSD data from the didrometers. We have also implemented the method, in real time, for the CASA IP1 network. The statistics of the retrieved coefficient α_v for the same storms studied in chapter 3 have also been shown. It has been shown that the coefficients α_h and α_v are highly correlated and linearly related. An additional value of the method is that it is independent of the systematic offset that may exist in the measured Z_{dr} of a dual-polarization radar system (i.e., relative calibration between the h and v -channels).

In Chapter 5, the wet hail attenuation has been discussed and two preliminary methods to estimate and correct it have been presented. The methods are both based on dual-polarization configuration such that the wet hail can be distinguished from rain and the

estimation of attenuation can be improved. The first method assumes a dual-wavelength dual-polarization configuration which is available with the CP-2 radar. The second method assumes a CASA IP1/WSR-88D configuration where the resolution cells of both systems can potentially be matched to provide constraint information. We have evaluated both methods using a previous supercell event simulated from the microphysical outputs of the CSU-RAMS model. The radar-based retrieved wet hail attenuation field in a vertical cross section of the supercell at the time of maximum reflectivity aloft has been shown to closely correspond to the 'exact' input attenuation field from the RAMS model.

6.2 Suggestions for future work

While the work presented here has been focusing on exploring the dual-polarization radar techniques using simulations and radar measurements for a limited selection of storm regimes, a larger goal of attenuation estimation and correction is to achieve systematic and consistent results for a much larger set of storm regimes using available *in situ* instruments. The concept of the consistency between the observations presented here has been constructed using the dual-polarization techniques but can be extended to include other type of instruments. The minimization technique can also be reused after a desired model (cost function) has been obtained.

The method presented here for the rain attenuation estimation and correction has been studied extensively via theory, simulations, and radar data. However, we have just begun the work for the mixed-phase (rain mixed with wet ice) attenuation estimation and

correction methods therefore only preliminary simulation results have been shown. It is important and invaluable to obtain and make available *a priori* information from natural storms, especially while designing a precipitation sensing system with a cost constraint either on construction cost or launching cost (e.g., for wide-area ground deployment or for space-borne applications). The two preliminary methods developed here for mixed-phase attenuation estimation are our starting point to study the microphysical processes in heavy convective storms for understanding and measuring large families of *A-Z* relationship for wet hail from radar data to obtain the aforementioned *a priori* information.

First, we recommend further studies of the relationship between the wet hail specific attenuation and the reflectivity using the CP-2 radar installed near Brisbane, Australia, over a period of several years so as to obtain statistics from a variety of storm regimes. These results can be analyzed statically over a large region or in vertical cross section to provide insight into the temporal evolution of the vertical attenuation profile in convective storms. This information will be useful to construct a more precise *a priori* range profiling model used in the TRMM or being proposed for the GPM.

Secondly, we recommend additional work on wet hail attenuation correction algorithms for the CASA IP1 or similar X-band radar networks. While the preliminary method developed here for the CASA IP1/WSR-88D configuration is simple, the system engineering aspect between the very different two radar systems has not been addressed. In particular, we have not addressed systematically the potential errors caused by the

timing error and the spatial resolution difference while matching observations from the two systems. The understanding of the errors are important, especially for the study of heavy convection storms, whose evolution is rapid and spatial distribution can vary significantly within a resolution cell (especially for the WSR-88D with much poorer resolution). The study of the system engineering aspect of the problem can be invaluable because of the possibilities of studying wet hail attenuation nationwide in the U.S. These possibilities may be rendered by the dual-polarization upgrade of the WSR-88D network in a few years that will give nationwide coverage along with the anticipated increasing trend of using commercially-available Doppler, dual-polarization X-band radar systems in a network configuration for short range applications.

Appendix A: Derivation of the Hitschfeld and Bordan Method

The intrinsic reflectivity Z_e (in mm^6m^{-3}) is related to the apparent (or measured) reflectivity Z_m (in mm^6m^{-3}) through the specific attenuation A (in dBkm^{-1}) as,

$$Z_e(r) = Z_m(r) \exp\{0.46 \int A(s) ds\} \quad (\text{A.1})$$

Assuming,

$$A(r) = aZ_e^b(r) \quad (\text{A.2})$$

Eq. (A.1) can be rewritten as:

$$Z_e(r) = Z_m(r) \exp\{0.46 \int aZ_e^b(s) ds\} \quad (\text{A.3})$$

Let

$$x(r) = 0.46 \int aZ_e^b(s) ds \quad (\text{A.4})$$

Take the derivative of $x(r)$ with respect to r , we have:

$$\frac{dx(r)}{dr} = 0.46aZ_e^b(r) \quad (\text{A.5})$$

$$Z_e(r) = \left(\frac{1}{0.46a} \cdot \frac{dx(r)}{dr} \right)^{\frac{1}{b}} \quad (\text{A.6})$$

Substitute eqs. (A.6) and (A.4) into eq. (A.3), we have:

$$\left(\frac{1}{0.46a} \cdot \frac{dx(r)}{dr} \right)^{\frac{1}{b}} = Z_m(r) \exp\{x(r)\} \quad (\text{A.7})$$

$$\frac{dx(r)}{\exp\{bx(r)\}} = 0.46aZ_m^b(r)dr \quad (\text{A.8})$$

Let

$$y(r) = \exp\{bx(r)\} \quad (\text{A.9})$$

we have:

$$dx(r) = \frac{dy(r)}{y(r)b} \quad (\text{A.10})$$

Substitute eqs. (A.9) and (A.10) into eq. (A.8), we have:

$$\frac{dy(r)}{y^2(r)} = 0.46abZ_m^b(r)dr \quad (\text{A.11})$$

Eq. (A.11) can be solved through integration. Since:

$$\int_{y(0)}^{y(r)} \frac{dy(r)}{y^2(r)} = \int 0.46abZ_m^b(s)ds \quad (\text{A.12})$$

we have:

$$-\frac{1}{y(r)} + \frac{1}{y(0)} = \int 0.46abZ_m^b(s)ds \quad (\text{A.13})$$

and:

$$\frac{1}{y(r)} = \frac{1}{\exp(bx(r))} = \exp\{-0.46b \int aZ_e^b(s)ds\} \quad (\text{A.14a})$$

$$\frac{1}{y(0)} = 1 \quad (\text{A.14b})$$

Substitute eqs. (A.14a) and (A.14b) into eq. (A.13), we have:

$$-0.46b \int aZ_e^b(s)ds = \log_e(1 - \int 0.46abZ_m^b(s)ds) \quad (\text{A.15})$$

Take derivatives on both sides of eq. (A.15) with respect to r , we have:

$$-0.46abZ_e^b(r) = \frac{-0.46abZ_m^b(r)}{1 - \int 0.46abZ_m^b(s)ds} \quad (\text{A.16})$$

Finally we obtain the solution for $Z_e(r)$ as a function of $Z_m(r)$:

$$Z_e(r) = Z_m(r) \left(1 - 0.46ab \int Z_m^b(s)ds \right)^{\frac{1}{b}} \quad (\text{A.17})$$

Appendix B: Derivation of Testud et al.'s Method

Following Appendix A and change the integral intervals in the integral equation (A.12)

from $[0, r]$ to $[r, r_i]$, we have:

$$-\frac{1}{y(r_i)} + \frac{1}{y(r)} = \int_r^{r_i} 0.46abZ_m^b(s)ds \quad (\text{B.1})$$

From eqs. (A.14.a) and (A.2), we have:

$$\frac{1}{y(r)} = \exp\{-0.46b \int_r^r A(s)ds\} \quad (\text{B.2})$$

Eq. (B.1) can be expanded as:

$$\exp\{-0.46b \int_r^{r_i} A(s)ds\} = \exp\{-0.46b \int_r^r A(s)ds\} + \int_r^{r_i} 0.46abZ_m^b(s)ds \quad (\text{B.3})$$

Take logarithms and then differentiate with respect to r on both sides of (B.3), we have:

$$A(r) = \frac{aZ_m^b(r)}{\exp\{-0.46b \int_r^r A(s)ds\} + \int_r^{r_i} 0.46abZ_m^b(s)ds} \quad (\text{B.4})$$

From eq. (A.1), we know:

$$\exp\{0.46 \int_r^i A(s) ds\} = \frac{Z_e(r_i)}{Z_m(r_i)} \quad (\text{B.5})$$

Substitute eq. (B.5) into eq. (B.4), we have:

$$A(r) = \frac{aZ_m^b(r)}{\left(\frac{Z_e(r_i)}{Z_m(r_i)}\right)^{-b} + \int_r^i 0.46abZ_m^b(s) ds} \quad (\text{B.6a})$$

$$= \frac{Z_m^b(r)aZ_e^b(r_i)}{Z_m^b(r_i) + aZ_e^b(r_i) \int_r^i 0.46bZ_m^b(s) ds} \quad (\text{B.6b})$$

$$= \frac{Z_m^b(r) A(r_i)}{Z_m^b(r_i) + A(r_i) \int_r^i 0.46bZ_m^b(s) ds} \quad (\text{B.6c})$$

Assume:

$$A(r) = \alpha K_{dp}(r) \quad (\text{B.7})$$

Integrate eq. (B.7) from r_0 to r_i , we have:

$$\int_0^i A(s) ds = \int_0^i \alpha K_{dp}(s) ds \quad (\text{B.8a})$$

$$= \int_0^i \alpha \cdot \frac{1}{2} \cdot \frac{d\Phi_{dp}}{ds} \cdot ds \quad (\text{B.8b})$$

$$= \frac{\alpha}{2} [\Phi_{dp}(r_i) - \Phi_{dp}(r_0)] \quad (\text{B.8c})$$

$$= \frac{\alpha}{2} \Delta \Phi_{dp}(r_i, r_0) \quad (\text{B.8d})$$

From eqs. (B.6c) and (B.8d), we have:

$$\int_0^{r_i} \frac{Z_m^b(l)A(r_i)}{Z_m^b(r_i) + A(r_i) \int_0^l 0.46bZ_m^b(s)ds} \cdot dl = \frac{\alpha}{2} \Delta \Phi_{dp}(r_i, r_0) \quad (\text{B.9})$$

Let

$$I(r, r_i) = \int_0^r 0.46bZ_m^b(s)ds \quad (\text{B.10})$$

The integrand in eq. (B.9) is the derivative of a logarithmic function which we can obtain as:

$$\frac{d}{dl} \left\{ \frac{-1}{0.46b} \cdot \log_e [Z_m^b(r_i) + A(r_i)I(l, r_i)] \right\} = \frac{-1}{0.46b} \cdot \frac{A(r_i) \cdot \frac{dI(l, r_i)}{dl}}{Z_m^b(r_i) + A(r_i)I(l, r_i)} \quad (\text{B.11a})$$

$$= \frac{A(r_i)Z_m^b(l)}{Z_m^b(r_i) + A(r_i)I(l, r_i)} \quad (\text{B.11b})$$

Now the left side of eq. (B.9) can be integrated readily as:

$$\int_0^{r_i} \frac{Z_m^b(l)A(r_i)}{Z_m^b(r_i) + A(r_i) \int_0^l 0.46bZ_m^b(s)ds} \cdot dl = \int_0^{r_i} \frac{d}{dl} \left\{ \frac{-1}{0.46b} \cdot \log_e [Z_m^b(r_i) + A(r_i)I(l, r_i)] \right\} \cdot dl \quad (\text{B.12a})$$

$$= \left\{ \frac{-1}{0.46b} \cdot \log_e [Z_m^b(r_i) + A(r_i)I(l, r_i)] \right\} \Big|_0^{r_i} \quad (\text{B.12b})$$

$$= \frac{-1}{0.46b} \left\{ \log_e [Z_m^b(r_i) + A(r_i)I(r_i, r_i)] - \log_e [Z_m^b(r_i) + A(r_i)I(r_0, r_i)] \right\} \quad (\text{B.12c})$$

$$= \frac{-1}{0.46b} \left\{ b \log_e Z_m(r_i) - \log_e [Z_m^b(r_i) + A(r_i)I(r_0, r_i)] \right\} \quad (\text{B.12d})$$

Substitute eq. (B.12d) into eq. (B.9), we have the solution for $A(r)$ at r_i as:

$$A(r_i) = \frac{Z_m^b(r_i) \left\{ \exp\{0.23b\alpha\Delta\Phi_{dp}(r_0, r_i)\} - 1 \right\}}{I(r_0, r_i)} \quad (\text{B.13})$$

Substitute eq. (B.13) into (B.6c), we have the solution for $A(r)$ at any r in the intervals of

$[r_0, r_i]$ as:

$$A(r) = \frac{Z_m^b(r) \left\{ \exp\{0.23b\alpha\Delta\Phi_{dp}(r_0, r_i)\} - 1 \right\}}{I(r_0, r_i) + \left\{ \exp\{0.23b\alpha\Delta\Phi_{dp}(r_0, r_i)\} - 1 \right\} I(r, r_i)} \quad (\text{B.14})$$

Appendix C: Drop shape models used in this dissertation

We used several drop shape models available in the literature, listed as follows:

1. The mixed model using a linear model for large drops and Brandes et al. (2002) for small drops:

$$\begin{cases} \frac{a}{b} = 0.9951 + 0.02510D - 0.03644D^2 + 0.005303D^3 - 0.0002492D^4, \text{ if } D \leq 1.75\text{mm} \\ \frac{a}{b} = (0.9535 + 1.75\beta) - \beta D, \text{ if } D > 1.75\text{mm} \end{cases} \quad (\text{C.1})$$

2. The Pruppacher and Beard (1970) model:

$$\frac{a}{b} = 1.03 - 0.062D \quad (\text{C.2})$$

3. The Beard and Chuang (1987) model:

$$\frac{a}{b} = 1.0048 + 0.0057\left(\frac{D}{10}\right) - 2.628\left(\frac{D}{10}\right)^2 + 3.682\left(\frac{D}{10}\right)^3 - 1.677\left(\frac{D}{10}\right)^4 \quad (\text{C.3})$$

4. The Andsager et al. (1999) model:

$$\begin{cases} \frac{a}{b} = 1.0048 + 0.0057\left(\frac{D}{10}\right) - 2.628\left(\frac{D}{10}\right)^2 + 3.682\left(\frac{D}{10}\right)^3 - 1.677\left(\frac{D}{10}\right)^4, & \text{if } D \leq 1\text{mm or } D > 4\text{mm} \\ \frac{a}{b} = 1.012 - 0.1445\left(\frac{D}{10}\right) - 1.028\left(\frac{D}{10}\right)^2, & \text{otherwise} \end{cases} \quad (\text{C.4})$$

In eqs. (C.1)-(C.4), parameter a is the minor axis of the spheroid raindrop, parameter b is the major axis, and parameter D is the equivalent volume diameter (see Fig. C.1).

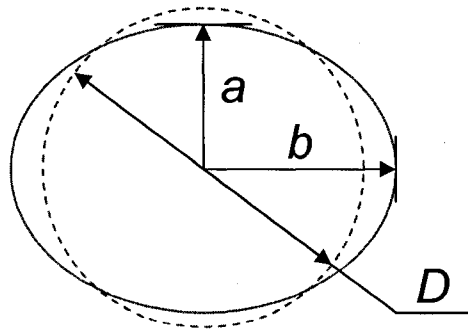


Figure C.1. A spheroid model of a raindrop.

REFERENCES

- Andsager, K., K. V. Beard, and N. F. Laird, 1999: Laboratory measurements of axis ratios for large raindrops. *J. Atmos. Sci.*, **56**, 2673-2683.
- Barber, P. W. and S. C. Hill, 1990: *Light scattering by particles: computational methods*. New Jersey, World Scientific.
- Barge, B. I. and R. G. Humphries, 1980: Identification of rain and hail with polarization and dual-wavelength radar. *Preprints 19th Conf. on Radar Meteorology*, Miami, Amer. Meteor. Soc., 507-516.
- Beard, K. V., and C. Chuang, 1987: A new model for the equilibrium shape of raindrops. *J. Atmos. Sci.*, **44**, 1509-1524.
- Berne, A. and R. Uijlenhoet, 2005: A stochastic model of range profiles of raindrop size distributions: application to radar attenuation correction. *Geo. Research Letters*, 32L10803, 2005
- Bharadwaj, N. and V. Chandrasekar, 2006: Waveform design for first generation CASA testbed. *Preprints IEEE International Geoscience and Remote Sensing Symposium 2006*, Denver, Colorado.
- Brandes, E. A., G. Zhang, and J. Vivekanandan, 2002: Experiments in rainfall estimation with a polarimetric radar in a subtropical environment. *J. Appl. Meteor.*, **41**, 674-684.
- Bringi, V.N., T. A. Seliga, and K. Aydin, 1984: Hail detection with a differential reflectivity radar. *Science*, **225**: 1145-1147.

- Bringi, V. N., V. Chandrasekar, N. Balakrishnan, and D.S. Zrníc 1990: An examination of propagation effects in rainfall on radar measurements at microwave frequencies. *J. Atmos. Oceanic Technol.*, **7**, 829-840.
- Bringi, V.N. and A. Hendry, 1990: Technology of polarization diversity radars for meteorology. In *Radar in Meteorology*. D. Atlas, Ed., 153-190, Boston, MA, American Meteorological Society.
- Bringi, V. N., and V. Chandrasekar, 2001: *Polarimetric Doppler Weather Radar: Principles and Applications*. Cambridge Univ. Press, 636 pp.
- Bringi, V. N., T. D. Keenan, and V. Chandrasekar, 2001: Correcting C-band radar reflectivity and differential reflectivity data for rain attenuation: A self-consistent method with constraints. *IEEE Trans. Geosci. Remote Sens.*, **39**, 1906-1915.
- Chandrasekar, V., S. Lim, N. Bharadwaj, W. Li, D. McLaughlin, V.N. Bringi, and E. Gorgucci, 2004: Principles of networked weather radar operation at attenuating frequencies. *Preprints ERAD 2004*, 109-114.
- Chong, E. K. P. and S. H. Żak, 2001: An introduction to optimization, 2nd edition. John Wiley & Sons, Inc., pp 476.
- Crum, T. D. and R. L. Alberty 1993: The WSR-88D and the WSR-88D operational support facility. *Bulletin of the American Meteorological Society*, **74**, 1669–1687.
- Doviak, R. J. and D.S. Zrníc, 1993: *Doppler Radar and Weather Observations*. 2nd edition, San Diego, CA, Academic Press.

- Gorgucci, E., G. Scarchilli, and V. Chandrasekar, 1999: A procedure to calibrate multiparameter weather radar using properties of the rain medium. *IEEE Trans. Geosci. Remote Sens.*, **17**, 269-276.
- Gorgucci, E., and V. Chandrasekar, 2005: Evaluation of attenuation correction methodology for dual-polarization radars: application to X-band systems. *J. Atmos. And Oceanic Technol.*, **22**, 1195-1206.
- Hitschfeld, W., and J. Bordan, 1954: Errors inherent in the radar measurement of rainfall at attenuating wavelengths. *J. Meteor.*, **11**, 58-67.
- Hogan, R. J., 2007: A variational scheme for retrieving rainfall rate and hail intensity from polarization radar. *J. of Appl. Meteor.*, **46**, 1544-1564.
- Huang, G.J., V.N. Bringi, S. van den Heever, and W. Cotton, 2005: Polarimetric radar signatures from RAMS microphysics. *Preprints 32nd Conference on Radar Meteorology*, October, 24-29, 2005, Albuquerque, NM. American Meteorological Society.
- Hubbert, J., and V. N. Bringi, 1995: An iterative filtering technique for the analysis of copolar differential phase and dual-frequency polarimetric variables. *J. Atmos. Oceanic Technol.*, **12**, 643-648.
- Iguchi, T., T. Kozu, R. Meneghini, J. Awaka, and K. Okamoto, 2000: Rain-Profiling Algorithm for the TRMM Precipitation Radar. *J. Appl. Meteo.*, **39**, 2038-2052.
- Jameson, A. R., 1992: The effect of temperature on attenuation-correction schemes in rain using polarization propagation differential phase shift. *J. Appl. Meteo.*, **31**, 1106-1118.

- Kummerow, C. and L. Giglio, 1994: A passive microwave technique for estimating rainfall and vertical structure information from space. Part I: Algorithm description. *J. Appl. Meteor.*, **33**, 3-18.
- Kummerow, C., J. Simpson, O. Thiele, W. Barnes, A. T. C. Chang, E. Stocker, R. F. Adler, A. Hou, R. Kakar, F. Wentz, P. Ashcroft, T. Koza, Y. Hong, K. Okamoto, T. Iguchi, H. Kuroiwa, E. Im, Z. Haddad, G. Huffman, B. Ferrier, W. S. Olson, E. Zipser, E. A. Smith, T. T. Wilheit, G. North, T. Krishnamurti, and K. Nakamura, 2000: The status of the Tropical Rainfall Measuring Mission (TRMM) after two years in orbit. *J. of Appl. Meteor.*, **39**, 1965–1982.
- Levenberg, K., 1944: A method for the solution of certain problems in least squares. *Quart. Appl. Math.*, **2**, 164-168.
- Lim, S., V. Chandrasekar and D. McLaughlin, 2004: Retrieval of reflectivity in a networked radar environment. *Preprints IEEE International Geoscience and Remote Sensing Symposium 2004*, Anchorage.
- Liu, H. and V. Chandrasekar, 2000: Classification of hydrometeors based on polarimetric radar measurements: development of fuzzy logic and neuro-fuzzy systems and in-situ verification. *J. Atmos. Oceanic Technol.*, **17**, 140-164.
- Liu, Y., V.N. Bringi and M. Maki, 2006: Improved rain attenuation correction algorithms for reflectivity and differential reflectivity with adaptation to drop shape models. *Preprints IEEE International Geoscience and Remote Sensing Symposium 2006*, Denver, Colorado.

- Liu, Y., Y. Wang, V. Chandrasekar, and V. N. Bringi, 2007: Real-time three-dimensional radar mosaic in CASA IP1 testbed. *Preprints IEEE International Geoscience and Remote Sensing Symposium 2007*, Barcelona, Spain.
- L'Ecuyer, T. S. and G. L. Stephens, 2002: An estimation-based precipitation retrieval algorithm for attenuating radars. *J. of Appl. Meteor.*, **41**, 272–285.
- Marquardt, D., 1963: An algorithm for least-squares estimation of nonlinear parameters. *SIAM J. Appl. Math.*, **11**, 431-441.
- Matrosov, S.Y., K.A. Clark, B.E. Martner, and A. Tokay, 2002: X-band polarimetric radar measurements of rainfall. *J. Appl. Meteor.*, **41**, 941-952.
- Matrosov, S. Y., R. Cifelli, P. C. Kennedy, S. Nesbette, V. N. Bringi, and B. E. Martner 2005: On the role of X-band radar in extending longer-wavelength radar polarimetric retrievals to lighter rains. *Preprints 32nd conference on radar meteorology.*, Albuquerque, New Mexico, Amer. Meteor. Soc.
- McLaughlin, D., V. Chandrasekar, K. Droegemeier, S. Frasier, J. Kurose, F. Junyent, B. Philips, S. Cruz-Pol, and J. Colom, 2005: Distributed collaborative adaptive sensing (DCAS) for improved detection, understanding, and prediction of atmosphere hazards. *Preprints 9th Symposium on Integrated Observing and Assimilation Systems for the Atmosphere, Oceans, and Land surface*, San Diego, CA.
- Park, S.-G., V. N. Bringi, V. Chandrasekar, M. Maki and K. Iwanami. 2005: Correction of radar reflectivity and differential reflectivity for rain attenuation at X band. Part I: theoretical and empirical basis. *J. Atmos. and Oceanic Technol.*, **22**, 1621–1632.

- Park, S.-G., M. Maki, K. Iwanami, V. N. Bringi and V. Chandrasekar. 2005: Correction of radar reflectivity and differential reflectivity for rain attenuation at X band. Part II: evaluation and application. *J. Atmos. and Oceanic Technol.*, **22**, 1633–1655.
- Pruppacher, H. R., and K. V. Beard, 1970: A wind tunnel investigation of the internal circulation and shape of water drops falling at terminal velocity in air. *Q. J. R. Meteorol. Soc.*, **96**, 247-256.
- Ryzhkov, A. and D.S. Zrnić, 1995: Precipitation and attenuation measurements at 10 cm wavelength. *J. Appl. Meteor.*, **34**, 2121-2134.
- Sinclair, G., 1950: The transmission and reception of elliptically polarized waves. *Proc. IRE*, **38**, 148-151.
- Seliga, T. A. and V. N. Bringi, 1976: Potential use of radar differential reflectivity measurements at orthogonal polarizations for measuring precipitation. *J. Appl. Meteor.*, **15**, 69-76.
- Smyth, T. J. and A. J. Illingworth, 1998: Correction for attenuation of radar reflectivity using polarization data. *Quart. J. Roy. Meteor. Soc.*, **124**, 2393-2415.
- Stephens, G. L., Deborah G. Vane, Ronald J. Boain, Gerald G. Mace, Kenneth Sassen, Zhien Wang, Anthony J. Illingworth, Ewan J. O'Connor, William B. Rossow, Stephen L. Durden, Steven D. Miller, Richard T. Austin, Angela Benedetti, Cristian Mitrescu, and The CloudSat Science Team, 2002: The CloudSat mission and the A-train. *Bulletin of the American Meteorological Society.*, **83**, 1771–1790.

- Testud, J., E. Le Bouar, E. Obligis, and M. Ali-Mehenni, 2000: The rain profiling algorithm applied to polarimetric weather radar. *J. Atmos. Oceanic Technol.*, **17**, 332-356.
- Tuttle, J.D. and R.E. Rinehart, 1983: Attenuation correction in dual-wavelength analyses. *J. Climate Appl. Meteor.*, **22**, 1914-1921.
- Ulbrich, C. W., 1983: Natural variations in the analytical form of the raindrop size distribution. *J. Climate Appl. Meteor.*, **22**, 1764-1775.
- van den Heever, S.C. and W.R. Cotton, 2004: The impact of hail size on simulated supercell storm, *J. Atmos. Sci.*, **61**, 1596-1609.
- Zrnić, D. S., V. N. Bringi, N. Balakrishnan, K. Aydin, V. Chandrasekar, and J. Hubbert, 1993: Polarimetric measurements in a severe hailstorm. *Monthly Weather Rev.*, **121**, 2223-2238.